

STUDIES OF THE NEUTRON-RICH NUCLEI NEAR $N = 40$ THROUGH β DECAY

By

Scott Allen Suchyta

A DISSERTATION

Submitted to
Michigan State University
in partial fulfillment of the requirements
for the degree of

Chemistry – Doctor of Philosophy

2014

ABSTRACT

STUDIES OF THE NEUTRON-RICH NUCLEI NEAR $N = 40$ THROUGH β DECAY

By

Scott Allen Suchyta

Nuclear structure evolves as a progression is made from stable to exotic nuclei. The energy spacings between the single-particle orbitals that protons and neutrons occupy are not constant and change based on the ratio of protons to neutrons in a nucleus. The promotion of nucleons across an energy gap into a higher shell can drive nuclei from spherical to deformed shapes. When a deformed state arising from the filling of a higher orbital has a similar energy to a spherical state in which there is no occupation of the higher orbital, the situation is known as shape coexistence. Due to nuclear-structure evolution, in radioactive nuclei, the energy of an intruder orbital that originates from a higher shell near stability can become close to the energy of a lower-shell orbital. Therefore, the filling of intruder orbitals is often associated with nuclear deformation and low-energy shape coexistence.

Demonstrating the evolution of nuclear structure, rapid changes have been observed in the properties of neutron-rich nuclei with neutron numbers near 40. A subshell closure has been proposed at $N = 40$ in ${}^{68}_{28}\text{Ni}_{40}$ based on the energy gap between the upper fp shell and the $0g_{9/2}$ orbital. However, collectivity rapidly develops in the ${}^{66}_{26}\text{Fe}_{40}$ and ${}^{64}_{24}\text{Cr}_{40}$ isotopes. Ground-state deformation, largely interpreted in terms of the occupation of the intruder $\nu 0g_{9/2}$ orbital, has accordingly been inferred for ${}^{66}\text{Fe}$ and ${}^{64}\text{Cr}$.

Two separate experiments were performed at the National Superconducting Cyclotron Laboratory that provided insight about the excitation of neutrons out of the fp shell in the neutron-rich nuclei with approximately 40 neutrons and 28 or fewer protons. The nuclei

studied were populated primarily through β decay. Isomeric decays of metastable excited states were also observed. In each experiment, the radioactive ion beam was deposited into a semiconductor detector that was used to detect both the implantation of the ions and their subsequent β decays. The β -decay detector was surrounded by an ancillary array of high-purity Ge detectors for γ -ray detection. The results of both experiments complement prior work and emphasize the important role of the $\nu 0g_{9/2}$ orbital in the low-energy level schemes of the neutron-rich nuclei near $N = 40$.

One experiment investigated the decay of the first excited state in ^{68}Ni populated through the β decay of ^{68}Co , and the analysis of decay events relied heavily on pulse-shape analysis. The $\nu 0g_{9/2}$ orbital has an impact on the low-energy level scheme of ^{68}Ni , and the first excited state is due to the excitation of a pair of neutrons across the $N = 40$ gap. The energy of the first excited state in ^{68}Ni was measured precisely and determined to be significantly lower than the value reported previously. The decay strength of the excited state was also determined precisely. Interpreting within a simple two-level mixing model, the experimental results are consistent with Monte Carlo shell-model calculations that predict shape coexistence between a spherical ^{68}Ni ground state and an oblate first excited state.

A second experiment involved the study of the β decay of $^{61,63}\text{V}$ to the odd- A $^{61,63}\text{Cr}_{37,39}$ isotopes, where data were previously scarce. The inferred level scheme of ^{61}Cr has an increased low-energy level density relative to the neighboring lower mass odd- A Cr isotopes. The change in the level scheme of ^{61}Cr was attributed to the onset of deformation resulting from the excitation of neutrons out of the fp shell. The isomeric decays of metastable states in $^{64,66}_{25}\text{Mn}_{39,41}$ were also investigated. Based on the inferred low-energy level schemes, shape coexistence was proposed, with the ground states of $^{64,66}\text{Mn}$ having deformed shapes but the isomeric states being spherical.

ACKNOWLEDGMENTS

First, I would like to thank my advisor, Sean. Without a doubt, I got the most assistance from you throughout graduate school and this work would not have been possible without you. Thank you for the guidance, career advice, and being there to answer questions during my hundreds of pop-ins into your office.

I have been very fortunate to have great support from my family. Mom and Dad, you have always provided me with an outstanding educational foundation, as well as helped me through every phase of life, and I am very grateful. Eric and Aimee, thank you for listening and being the ones to experience the highs and lows of graduate-school life with me. While simple, it was important for me to temporarily escape the seemingly overwhelming work load.

There are many other people to recognize. I would like to thank Paul, Dave, and Alexandra for serving on my guidance committee. I would also like to thank Bill Walters and Chris Chiara for their help in the preparation of publications. Additionally, I am grateful for the assistance provided by Morten Hjorth-Jensen, Alex Brown, and Taka Otsuka in terms of theoretical interpretations. Further, I must acknowledge my fellow β -group members, in particular Nicki and Chris. Thank you for the time spent preparing for experiments and assistance in general daily research activities. Finally, I would like to give one more thank you to everyone who has made this dissertation possible in the largest or smallest way. Your contribution is appreciated.

TABLE OF CONTENTS

LIST OF TABLES	vii
LIST OF FIGURES	ix
Chapter 1 Introduction	1
1.1 Nuclear shell structure and shell closures	1
1.2 Nuclear structure in the vicinity of shell closures	6
1.3 Evolution of nuclear shell structure	9
1.4 Shape coexistence	11
1.5 Nuclear deformation and collectivity	16
1.6 Nuclear structure of the neutron-rich nuclei with $N \approx 40$ and $Z \leq 28$	19
1.7 Motivations for the measurements	23
1.8 Dissertation outline	25
Chapter 2 Technique	26
2.1 β decay	26
2.2 γ -ray decay	31
2.3 Internal conversion	33
2.4 Internal pair production	35
2.5 $E0$ transitions	35
2.6 β -delayed neutron decay	36
Chapter 3 Experimental Description	38
3.1 Isotope production, separation, identification, and detection	39
3.2 NSCL Digital Data Acquisition System (DDAS)	41
3.3 NSCL experiment e11503	44
3.3.1 Isotope production and delivery	44
3.3.2 Planar Germanium Double-sided Strip Detector (GeDSSD)	48
3.3.3 GeDSSD triggering conditions	49
3.3.4 Correlation	49
3.3.5 Segmented Germanium Array (SeGA)	51
3.3.6 SeGA triggering conditions	52
3.3.7 Calibrations	52
3.3.8 Pulse-shape analysis	59
3.4 NSCL experiment e08020	76
3.4.1 Isotope production and delivery	76
3.4.2 Beta Counting System (BCS)	77

3.4.3	Segmented Germanium Array (SeGA)	80
3.4.4	Triggering conditions	80
3.4.5	Correlation	81
3.4.6	Calibrations	83
Chapter 4	Experimental Results	89
4.1	Identification of the energy peaks observed using pulse-shape analysis	89
4.1.1	Single radioactive decays	89
4.1.2	Sequential radioactive decays	89
4.2	Decay of excited states in ^{68}Ni following β decay of ^{68}Co	96
4.3	Isomeric γ -ray decay in ^{60}V	104
4.4	β decay of ^{60}V to ^{60}Cr	106
4.5	β decay of ^{60}Ti to ^{60}V	115
4.6	β decay of ^{61}V to ^{61}Cr	118
4.7	β decay of ^{62}V to ^{62}Cr	129
4.8	β decay of ^{63}V to ^{63}Cr	135
4.9	Isomeric γ -ray decay in ^{64}V	140
4.10	β decay of ^{64}V to ^{64}Cr	142
4.11	Isomeric γ -ray decay in ^{64}Mn	144
4.12	Isomeric γ -ray decay in ^{66}Mn	148
Chapter 5	Discussion	155
5.1	Shape coexistence in ^{68}Ni	155
5.2	Odd- A Cr isotopes	160
5.3	Odd-odd Mn isotopes	164
Chapter 6	Conclusions and Outlook	167
6.1	Conclusions	167
6.2	Outlook	168
BIBLIOGRAPHY	171

LIST OF TABLES

Table 2.1	β -decay selection rules, adapted from Ref. [1].	29
Table 2.2	Selection rules and multiplicities for the lowest multipolarity γ -ray transitions, adapted from Ref. [1].	32
Table 2.3	Electromagnetic transition rates assuming a single-particle transition from an initial state to a final state, adapted from Ref. [1]. λ is the multipolarity of the transition, E_γ is the γ -ray energy in MeV, and A is the mass number of the nucleus.	33
Table 3.1	Intensity of the 367-keV γ -ray from the decay of ^{67m}Fe reported as the efficiency-corrected number of γ -ray decays divided by the total number of implanted ions when gates are placed on isotopes Fe1, Fe2, Fe3, and Fe4 in Fig. 3.4. γ rays detected up to 500 μs after an ion implantation in the GeDSSD were correlated with the ion.	47
Table 3.2	Total numbers of ions for each isotope that was delivered to the experimental station in experiment e11503.	47
Table 3.3	Total numbers of ions for each isotope that was delivered to the experimental station in experiment e08020.	77
Table 4.1	Theoretical half-lives calculated from Weisskopf estimates for the decay of an excited state in ^{68}Ni by a 2422-keV transition.	103
Table 4.2	Energies and absolute intensities of the γ -ray transitions identified in ^{60}Cr following the β decay of ^{60}V . The energies of the initial and final states between which each transition occurs are also listed. . . .	108
Table 4.3	Half-life of ^{60}V extracted from the β -decay curve additionally requiring the coincident detection of a γ ray with energy $E_{\text{coinc}\gamma}$. The half-lives were determined from fits of the respective decay curves to an exponential plus constant background.	113
Table 4.4	Energies and absolute intensities of the γ -ray transitions identified in ^{61}Cr following the β decay of ^{61}V . The energies of the initial and final states between which each transition occurs are also listed. . . .	122

Table 4.5	Energies and absolute intensities of γ -ray transitions identified in ^{62}Cr following the β decay of ^{62}V . The energies of the initial and final states between which each transition occurs are also listed.	132
Table 4.6	Energies and absolute intensities of the γ -ray transitions identified in ^{63}Cr following the β decay of ^{63}V . The energies of the initial and final states between which each transition occurs are also listed. . . .	136
Table 4.7	Theoretical internal conversion coefficients [2] for 83- and 120-keV transitions in ^{63}Cr and Weisskopf half-life estimates for states in ^{63}Cr depopulated by 83- and 120-keV transitions.	140
Table 4.8	Energies and relative intensities of γ rays detected in the decay of ^{64m}Mn . The listed intensities only take into account γ -ray transitions and do not include any potential contributions from internal conversion. The energies of the initial and final states between which each transition occurs are also given.	144
Table 4.9	Theoretical internal conversion coefficients [2] for 40- and 135-keV transitions in ^{64}Mn and Weisskopf half-life estimates for states in ^{64}Mn depopulated by 40- and 135-keV transitions.	148
Table 4.10	Energies and relative intensities of γ rays detected in the decay of ^{66m}Mn . The listed intensities only take into account γ -ray transitions and do not include any potential contributions from internal conversion. The energies of the initial and final states between which each transition occurs are also given.	149
Table 4.11	Theoretical internal conversion coefficients [2] for 43-, 170-, 251-, and 294-keV transitions in ^{66}Mn and Weisskopf half-life estimates for states in ^{66}Mn depopulated by 43-, 170-, 251-, and 294-keV transitions.	154
Table 5.1	Main valence-neutron configurations of the $1/2_1^-$, $3/2_1^-$, and $5/2_1^-$ levels in $^{55,57,59,61}\text{Cr}$ as determined by the shell-model calculations. Configurations with a probability of 0.10 or greater are shown. In addition to the given occupancies of $1p_{3/2}$, $0f_{5/2}$, and $1p_{1/2}$ orbitals, each listed configuration has a completely filled $0f_{7/2}$ orbital.	161

LIST OF FIGURES

Figure 1.1	(a) First ionization energy as a function of atomic number. Noble-gas elements are labelled along with their atomic numbers. The ionization energies were taken from Ref. [3]. (b) Differential neutron separation energies as a function of neutron number for even-even nuclei. Series of isotopes are connected by lines. The figure was adapted from Ref. [4].	2
Figure 1.2	Energy levels for the Woods-Saxon potential with a spin-orbit potential included. The number of nucleons required to completely fill all levels up to a particular level are shown. Numbers in blue denote shell closures (magic numbers), while gray numbers denote subshell closures. The figure was adapted from Ref. [4]. For interpretation of the references to color in this and all other figures, the reader is referred to the electronic version of this thesis.	5
Figure 1.3	Low-energy level scheme of ^{89}Y . States are labelled on the left by their spins and parities and on the right by their energies in keV. Data were taken from Ref. [5].	7
Figure 1.4	Low-energy level scheme of ^{90}Y . States are labelled on the left by their spins and parities and on the right by their energies in keV. Data were taken from Ref. [6].	9
Figure 1.5	(a) Energy of the first excited 2^+ state $[E(2^+)]$ shown as a function of neutron number for the even-even Ni, Fe, and Cr isotopes. (b) $B(E2)$ value for the transition from the ground state to the first excited 2^+ state shown as a function of neutron number for the even-even Ni, Fe, and Cr isotopes. Data were taken from Refs. [7, 8, 9].	20
Figure 1.6	Energies in keV of the $9/2_1^+$ state in the odd- A $^{53-59}\text{Cr}_{29-35}$ isotopes. The energies were taken from Refs. [10, 11, 12, 13].	21
Figure 3.1	Schematic layout of Coupled Cyclotron Facility at NSCL showing the arrangement of the K500 cyclotron, K1200 cyclotron, and A1900 fragment separator.	40

Figure 3.2	Schematic representation of the trapezoidal trigger filtering performed by DDAS on a detector signal. See text for details.	42
Figure 3.3	Schematic arrangement of the PIN detectors and GeDSSD in experiment e11503.	44
Figure 3.4	Particle-identification plot of the ions delivered to the experimental station in experiment e11503. Selected ions are labelled by their chemical symbol followed by an arbitrary number distinguishing a particular isotope from the other isotopic ions that were delivered to the GeDSSD.	45
Figure 3.5	Profile of ion implantations into the GeDSSD in experiment e11503.	48
Figure 3.6	Profile of decays detected in the GeDSSD in experiment e11503. . .	50
Figure 3.7	GeDSSD strip multiplicities for implant and decay events. The strip multiplicity gated on implants is shown for (a) the front strips and (b) the back strips. The strip multiplicity gated on decays is shown for (c) the front strips and (d) the back strips.	51
Figure 3.8	Schematic arrangement of SeGA around the GeDSSD in experiment e11503.	52
Figure 3.9	Simulated γ -ray efficiency of (a) the GeDSSD and (b) SeGA for γ rays emitted from a nucleus 1 mm deep in the GeDSSD.	53
Figure 3.10	Calibrated energy spectrum of the sum of all 16 back strips of the GeDSSD for the SRM source. The spectrum is shown in the ranges of (a) 0 – 275 keV, (b) 650 – 900 keV, and (c) 1150 – 1350 keV. Peak energies in keV are labelled and were obtained based on a pulse-shape-processing method in which the area underneath the decay signals were determined.	55
Figure 3.11	Residuals of the sum spectrum of all 16 (a) front strips and (b) back strips of the GeDSSD for the energy calibrations performed after experiment e11503.	56
Figure 3.12	Residuals of the 16 individual SeGA detectors for a representative energy calibration performed using background γ rays from a single experimental run during experiment e11503.	57

Figure 3.13	Residuals of the sum spectrum of all 16 SeGA detectors for a representative energy calibration performed using background γ rays from a single experimental run during experiment e11503.	57
Figure 3.14	Residuals of the sum spectrum of all 16 SeGA detectors for background γ -ray lines monitored throughout the duration of experiment e11503. A new energy calibration was applied for each experimental run, with an average run length of approximately an hour.	58
Figure 3.15	Typical pulse shape observed for the detection of a radioactive decay in a strip of the GeDSSD. Signals were recorded using a trace length of $6 \mu\text{s}$ and a delay of $3 \mu\text{s}$	61
Figure 3.16	Typical pulse shape observed in the GeDSSD when two separate decays deposit energy in the same strip within a time period that is short compared to the decay constant of the preamplifier.	61
Figure 3.17	χ_n^2 distribution in the back of the GeDSSD for all decay signals that were fit to Eq. 3.3. The dashed line indicates the cutoff for a “good” fit.	63
Figure 3.18	Examples of recorded traces from the back strips of the GeDSSD for which the fit to Eq. 3.3 yielded a value of χ_n^2 of (a) less than 140 or (b) - (e) greater than 140. The traces are shown in black, while the fits are shown in red. The observed pulse shapes resulted from (a) a single radioactive decay, (b) two sequential radioactive decays, (c) a transient signal induced from charge collection in a neighboring strip, (d) a noisy signal, and (e) a signal in which the preamplifier had not returned to baseline at the start of the signal.	64
Figure 3.19	Residuals for the sum of all 16 back strips of the GeDSSD from the energy calibration based on the determined value of S when γ -ray decay signals from the SRM and ^{137}Cs sources were fit according to Eq. 3.3.	65
Figure 3.20	χ_n^2 distribution in the back of the GeDSSD for all decay signals that were fit to Eq. 3.7 and for which the difference between the two time-offset parameters in the fit was greater than 150 ns. The dashed line indicates the cutoff for a “good” fit.	67

Figure 3.21	Examples of recorded traces from the back strips of the GeDSSD for which the fit to Eq. 3.7 yielded a difference between the two time-offset parameters of greater than 150 ns and the value of χ_n^2 was (a) less than 85 or (b) - (d) greater than 85. The traces are shown in black, while the fits are shown in red. The observed pulse shapes resulted from (a) two sequential radioactive decays, (b) a transient signal induced from charge collection in a neighboring strip, (c) a noisy signal, and (d) a signal in which the preamplifier had not returned to baseline at the start of the signal.	68
Figure 3.22	Time difference between the back-strip signal and the front-strip signal of the GeDSSD for decay events during (a) the calibration run used to construct the ideal trace for each strip and (b) the collection of experimental data during experiment e11503. The displayed time difference is the back time minus the front time. (c)-(d) The ideal trace that is determined for back strip 9 when different gating conditions are applied. (c) The ideal trace that results when a gate from -70 to -40 ns or 20 to 50 ns is placed on the back-front time difference is shown in blue and green, respectively. The region of each gate is indicated by the blue and green dotted lines in (a). (d) The ideal trace that results when gating on back-front time differences from 10 to 40 ns is shown in red and compared to the ideal trace that results when any back-front time difference is allowed, which is shown in black. The region of the gate from 10 to 40 ns is indicated by the red dotted lines in (a) and (b).	69
Figure 3.23	Energy spectrum in the back strips of the GeDSSD for all decay signals that were characterized as being caused by a single radioactive decay based on the results of fitting the decay signal to Eq. 3.3. The energy was determined from the value of parameter S in Eq. 3.4. Peaks are labelled by their energies in keV.	70
Figure 3.24	Energy spectrum in the back strips of the GeDSSD for the second decay of double pulses. The entire energy range from 0 - 1800 keV is shown in (a). Zooms of the regions from 100 - 250 keV and 1450 - 1750 keV are shown in (b) and (c), respectively.	71
Figure 3.25	Two dimensional plot of energy of the second decay versus time difference between the first and second decays for double pulses. The time difference was determined from the difference between the two time-offset parameters found from the fit of the decay signal to Eq. 3.7. Both the energy and time difference were determined using signals in the back strips of the GeDSSD.	72

Figure 3.26	Example of a GeDSSD signal (black) and the associated fit to Eq. 3.7 (red) for a signal in which the time difference between the two separate radioactive decays was determined to be just above 150 ns.	73
Figure 3.27	Centroids for the peaks near (a) 13 (b) 93, (c) 580, and (d) 1600 keV in Fig. 3.24 (a) as a function of the time difference between the first and second decays in increments of 200 ns. The horizontal error bars represent the span of each 200-ns time-difference increment.	74
Figure 3.28	Energy spectrum in the back of the GeDSSD for the second decay of double pulses for which the difference between the time-offset parameters for the two decays was larger than 1200 ns. The entire energy range from 0 - 1800 keV is shown in (a). Zooms of the regions from 100 - 250 keV and 1450 - 1750 keV are shown in (a) and (b), respectively.	75
Figure 3.29	Residuals for the peaks in Fig. 3.24 (a) and Fig. 4.1 that arise from known decays in ^{73}Ge and ^{67}Zn	75
Figure 3.30	(a) Ion position at the image 2 scintillator of the A1900 vs TOF gated on the Cr isotopes. The uncorrected TOF value on the x-axis refers to the raw TOF between PIN01 and the image 2 scintillator. (b) Ion position at the image 2 scintillator vs corrected TOF gated on the Cr isotopes. The corrected TOF on the x-axis refers to the TOF value that is obtained following a coordinate-system rotation of (a).	78
Figure 3.31	Particle-identification plot of the ions delivered to the experimental station in experiment e08020.	79
Figure 3.32	Schematic arrangement of the BCS in experiment e08020.	79
Figure 3.33	Schematic arrangement of SeGA in experiment e08020.	81
Figure 3.34	Representative energy calibration of (a) a front strip and (b) a back strip of the DSSD in experiment e08020. The energies of each strip were gain matched so that the 6.8-MeV α -decay peak occurred at channel 3000 in the calibrated energy spectrum. The 6.8-MeV α -decay peak is marked by a red triangle in each spectrum.	83
Figure 3.35	Residuals of the 16 individual SeGA detectors for the energy calibration performed before experiment e08020.	84
Figure 3.36	Residuals of the sum spectrum of all 16 SeGA detectors for the energy calibration performed before experiment e08020.	84

Figure 3.37	Residuals of the sum spectrum of all 16 SeGA detectors for background γ -ray lines monitored throughout the duration of experiment e08020. A new energy calibration was applied about every 24 hours to account for gain shifts of the SeGA detectors.	86
Figure 3.38	γ -ray peak efficiency curve for all 16 SeGA detectors in experiment e08020. A fourth-order polynomial was used to fit the data.	87
Figure 3.39	(a) Time difference between the detection of a γ ray with an energy between 10 and 60 keV in SeGA and the implantation of an ion in the DSSD gated on implant events. (b) Time difference between the detection of the 123- and 248-keV γ rays in SeGA from the SRM source measurements.	88
Figure 4.1	Energy spectrum in the back of the GeDSSD for the first decay of double pulses for which the energy of the second decay was 14 keV. The single peak is labelled by its energy in keV.	91
Figure 4.2	Energy spectrum in the back strips of the GeDSSD for the second decay of double pulses for a 2-hour background run performed 10 minutes after the end of beam delivery to the GeDSSD in experiment e11503. The entire energy range from 0 - 1800 keV is shown in (a). A zoom of the region from 0 - 200 keV is shown in (b). Peaks are labelled by their energies in keV.	91
Figure 4.3	Energy spectrum in the back of the GeDSSD for the first decay of double pulses that had a second-decay energy of 93 keV.	92
Figure 4.4	γ -ray energy spectrum detected in SeGA in coincidence with the 190-keV peak in the GeDSSD in Fig. 3.24 (b). The spectrum is shown in the ranges of (a) 0 - 500 keV and (b) 500 - 2000 keV. Tentatively identified γ -ray peaks from decays in ^{69}Cu are labelled by approximate energies in keV.	93
Figure 4.5	Energy spectrum in the back of the GeDSSD for the first decay of double pulses that had a second-decay energy of 175 keV. The spectrum is shown in the ranges of (a) 0 - 200 keV and (b) 200 - 2000 keV. The 24-keV transition is marked by its energy.	93
Figure 4.6	Time difference between the first and second decays for double pulses for which the second decay had an energy of 175 keV and the first decay had (a) any energy other than 24 keV (b) an energy of 24 keV.	94

Figure 4.7	Energy spectrum in the back strips of the GeDSSD for signals that were detected within 2 s of a ^{68}Co ion implantation in the GeDSSD and that were characterized as being caused by a single radioactive decay. Peaks are labelled by their energies in keV.	96
Figure 4.8	Energy of the decay occurring second in time for double pulses in the back strips of the GeDSSD that occurred within 2 s of the implantation of a ^{68}Co in the GeDSSD. The determined time difference between the first and second decays was (a) allowed to be any value greater than 150 ns (b) limited to values between 150 and 600 ns. . .	97
Figure 4.9	SeGA energy spectrum observed in coincidence with single decays in the GeDSSD that were detected within 2 s of the implantation of a ^{68}Co ion in the GeDSSD shown in the range of (a) 550 - 600 keV and (b) 1585 - 1635 keV.	99
Figure 4.10	Decay curves showing the time difference between the first and second decays when gates are placed on the (a) 581-keV and (b) 1602-keV peaks in Fig. 4.8(a).	100
Figure 4.11	γ -rays detected by SeGA in coincidence with the peaks in the GeDSSD due to the internal-conversion and pair-production decays of the first excited 0^+ state in ^{68}Ni . The SeGA energy spectrum is shown in the range of (a) 0 - 1000 keV and (b) 1000 - 2500 keV for coincidence with the 581-keV pair-production peak in the GeDSSD. The SeGA energy spectrum is also shown in the range of (c) 0 - 1000 keV and (d) 1000 - 2500 keV for coincidence with the 1602-keV internal-conversion peak in the GeDSSD. The SeGA energy spectrum is shown in (e) in the range of 1000 - 2500 keV for coincidence with both the 581-keV pair production peak and the 1602-keV internal-conversion peak in the GeDSSD.	101
Figure 4.12	Level scheme of ^{68}Ni showing the transitions observed in experiment e11503. States are labelled on the left by their spins and parities and on the right by their energies in keV. Transition energies are given in keV above the transitions.	102
Figure 4.13	Isomeric γ -ray energy spectrum detected within the 10- μs event window for events in which a ^{60}V ion was implanted into the DSSD. . .	104
Figure 4.14	γ - γ coincidence spectra detected within the 10- μs event window for events in which a ^{60}V ion was implanted into the DSSD gated on the (a) 100- and (b) 104-keV transitions.	105

Figure 4.15	Decay curves corresponding to the time difference between the detection of a ^{60}V ion in the DSSD and (a) a 100- or (b) a 104-keV γ ray in SeGA for γ rays that were detected within the 10- μs event window. The fits of the decay curves, labelled by “tot,” included an exponential for the decay of ^{60m}V and a constant background. . . .	106
Figure 4.16	β -delayed γ -ray energy spectrum detected within 500 ms of the implantation of a ^{60}V ion in the DSSD shown in the ranges of (a) 0 - 1500 keV and (b) 1500 - 3200 keV. γ -ray transitions in the daughter ^{60}Cr nucleus are labelled with red triangles and the transition energy in keV. γ -ray transitions in ^{59}Cr that are populated from the β -delayed neutron decay of ^{60}V are marked by gray squares. γ rays emitted following the β decay of a daughter or granddaughter nucleus are indicated by the blue circles.	107
Figure 4.17	Background-subtracted ^{60}V β -delayed γ - γ coincidence spectra gated on the (a) 644-, (b) 817-, (c) 1335-, (d) 1515-, and (e) 1586-keV transitions	109
Figure 4.18	Background-subtracted ^{60}V β -delayed γ - γ coincidence spectra gated on the (a) 1731-, (b) 2008-, (c) 2159-, (d) 2284-, and (e) 3138-keV transitions	110
Figure 4.19	^{60}V decay curve showing fragment- β correlations for β decays detected within 1 s of a ^{60}V ion implantation in the DSSD. The fit to the decay curve, labelled “tot,” included the exponential decay of ^{60}V , the exponential growth and decay of ^{60}Cr and ^{60}Mn , and a constant background.	111
Figure 4.20	^{60}V decay curves from 0 - 1000 ms showing fragment- β correlations for events in which a coincident γ ray with an energy of (a) 644, (b) 817, or (c) 1335 keV was also detected. Each decay curve was fit to an exponential for the decay of ^{60}V and a constant background. . .	111
Figure 4.21	Level scheme of ^{60}Cr populated by the β decay of ^{60}V . States are labelled on the left by their spins and parities and on the right by their energies in keV. γ -ray transition energies in keV are shown above the transitions. The absolute γ -ray intensity of each transition is shown in parentheses after the transition energy. The Q -value for the β decay of ^{60}V to ^{60}Cr was taken from Ref. [14].	112

Figure 4.22	^{60}V β -decay curve for β decays that were correlated with a ^{60}V ion detected in coincidence with a (a) 100- or (b) 104-keV γ ray in SeGA. The fit of each decay curve, labelled “tot,” included the exponential decay of ^{60}V , the exponential growth and decay of ^{60}Cr and ^{60}Mn , and a constant background.	114
Figure 4.23	^{60}V β -decay curve for decays detected in coincidence with a 644-keV γ -ray in SeGA and only for decays that were correlated with a ^{60}V ion implantation in the DSSD that was coincident with a 100- or 104-keV γ -ray in SeGA. The decay curve was fit to an exponential for the decay of ^{60}V and a constant background.	115
Figure 4.24	β -delayed γ -ray energy spectrum detected within 70 ms of the implantation of a ^{60}Ti ion in the DSSD shown in the ranges of (a) 0 - 350 keV and (b) 350 - 1250 keV.	116
Figure 4.25	Decay curve showing fragment- β correlations for β decays that were detected within 250 ms of a ^{60}Ti ion implantation in the DSSD and that were also detected in coincidence with a 112-keV γ ray in SeGA. The decay curve was fit to an exponential for the decay of ^{60}Ti and a constant background.	117
Figure 4.26	β -delayed γ -ray energy spectrum detected within 250 ms of the implantation of a ^{61}V ion in the DSSD shown in the ranges of (a) 0 - 300 keV and (b) 300 - 2400 keV. γ -ray transitions in the daughter ^{61}Cr nucleus are labelled with red triangles and the transition energy in keV. γ -ray transitions in ^{60}Cr that are populated from the β -delayed neutron decay of ^{61}V are marked by gray squares. γ rays emitted following the β decay of a daughter or granddaughter nucleus are indicated by the blue circles.	119
Figure 4.27	Background-subtracted ^{61}V β -delayed γ - γ coincidence spectra gated on the (a) 71-, (b) 98-, (c) 127-, (d) 331-, (e) 408-, (f) 451-, and (g) 467- transitions	120
Figure 4.28	Background-subtracted ^{61}V β -delayed γ - γ coincidence spectra gated on the (a) 677-, (b) 716-, (c) 774-, (d) 929-, (e) 1026-, (f) 1151-, (g) 1965-, and (h) 2164-keV transitions	121

Figure 4.29	^{61}V decay curve showing fragment- β correlations for β decays detected within 1 s of a ^{61}V ion implantation in the DSSD. The fit to the decay curve, labelled “tot,” included the exponential decay of ^{61}V , the exponential growth and decay of ^{61}Cr , ^{61}Mn , ^{60}Cr , and ^{60}Mn , and a constant background.	123
Figure 4.30	^{61}V decay curves from 0 - 500 ms showing fragment- β correlations for decay events in which a coincident γ ray was also detected with an energy of (a) 71, (b) 98, (c) 127, (d) 331, (e) 408, (f) 451, (g) 467, and (h) 677 keV. Each decay curve was fit with an exponential for the decay of ^{61}V and a constant background.	124
Figure 4.31	^{61}V decay curves from 0 - 500 ms showing fragment- β correlations for events in which a coincident γ ray was also detected with an energy of (a) 716, (b) 774, (c) 929, (d) 1026, (e) 1151, (f) 1965, and (g) 2165 keV. Each decay curve was fit with an exponential for the decay of ^{61}V and a constant background.	125
Figure 4.32	Level scheme of ^{61}Cr populated by the β decay of ^{61}V . States are labelled on the left by their spins and parities and on the right by their energies in keV. γ -ray transition energies in keV are shown above the transitions. The absolute γ -ray intensity of each transition is shown in parentheses after the transition energy. The Q -value for the β decay of ^{61}V to ^{61}Cr was taken from Ref. [14].	126
Figure 4.33	β -delayed γ -ray energy spectrum detected within 150 ms of the implantation of a ^{62}V ion in the DSSD shown in the ranges of (a) 0 - 700 keV and (b) 700 - 2300 keV. γ -ray transitions in the daughter ^{62}Cr nucleus are labelled with red triangles and the transition energy in keV. γ -ray transitions in ^{61}Cr that are populated from the β -delayed neutron decay of ^{62}V are marked by gray squares. γ rays emitted following the β decay of a daughter or granddaughter nucleus are indicated by the blue circles.	130
Figure 4.34	Background-subtracted ^{62}V β -delayed γ - γ coincidence spectra gated on the (a) 446-, (b) 730-, (c) 933-, (d) 1058-, (e) 1510-, (f) 1801-, and (g) 2248-keV transitions	131
Figure 4.35	^{62}V decay curve showing fragment- β correlations for β decays detected within 1 s of a ^{62}V ion implantation in the DSSD. The fit to the decay curve, labelled “tot,” included the exponential decay of ^{62}V , the exponential growth and decay of ^{62}Cr , ^{62}Mn , ^{61}Cr , and ^{61}Mn and a constant background.	133

Figure 4.36	^{62}V decay curves from 0 - 350 ms showing fragment- β correlations for decay events in which a coincident γ ray was also detected with an energy of (a) 446, (b) 933, (c) 1510, and (d) 1801 keV. Each decay curve was fit with an exponential for the decay of ^{62}V and a constant background.	134
Figure 4.37	Level scheme of ^{62}Cr populated by the β decay of ^{62}V . States are labelled on the left by their spins and parities and on the right by their energies in keV. γ -ray transition energies in keV are shown above the transitions. The absolute γ -ray intensity of each transition is shown in parentheses after the transition energy. The Q -value for the β decay of ^{62}V to ^{62}Cr was taken from Ref. [14].	135
Figure 4.38	β -delayed γ -ray energy spectrum detected within 150 ms of the implantation of a ^{63}V ion in the DSSD shown in the range of 0 - 1000 keV. γ -ray transitions in the daughter ^{63}Cr nucleus are labelled with red triangles and the transition energy in keV. γ -ray transitions in ^{62}Cr that are populated from the β -delayed neutron decay of ^{63}V are marked by gray squares. γ rays emitted following the β decay of a daughter or granddaughter nucleus are indicated by the blue circles.	136
Figure 4.39	Background-subtracted ^{63}V β -delayed γ - γ coincidence spectra gated on the (a) 83-, (b)120-, and (c)414-keV transitions.	137
Figure 4.40	^{63}V decay curve showing fragment- β correlations for β decays detected within 1 s of a ^{63}V ion implantation in the DSSD. The fit to the decay curve, labelled "tot," included the exponential decay of ^{63}V , the exponential growth and decay of ^{63}Cr , ^{63}Mn , ^{62}Cr , and ^{62}Mn , and a constant background.	137
Figure 4.41	^{63}V decay curves from 0 - 200 ms showing fragment- β correlations for decay events in which a coincident γ ray was also detected with an energy of (a) 83 and (b) 120 keV. Each decay curve was fit with an exponential for the decay of ^{63}V and a constant background.	138
Figure 4.42	Level scheme of ^{63}Cr populated by the β decay of ^{63}V . States are labelled on the left by their spins and parities and on the right by their energies in keV. γ -ray transition energies in keV are shown above the transitions. The absolute γ -ray intensity of each transition is shown in parentheses after the transition energy. The Q -value for the β decay of ^{63}V to ^{63}Cr was taken from Ref. [14].	139

Figure 4.43	Isomeric γ -ray energy spectrum detected within the 10- μ s event window for events in which a ^{64}V ion was deposited in the DSSD. γ rays detected less than 300 ns after the implantation of the ^{64}V are excluded to minimize the contribution from the prompt γ flash that is emitted when the ions are stopped in the detector.	141
Figure 4.44	^{64}V isomeric decay curve gated on 81-keV γ -ray transitions that occurred within the 10- μ s event window and that were detected at least 300 ns after the implantation of the ^{64}V ion in the DSSD. The decay curve is shown with a logarithmic x-axis and a fit to Eq. 4.1 was used to determine the half-life of the isomeric state in ^{64}V	142
Figure 4.45	β -delayed γ -ray energy spectrum detected within 80 ms of the implantation of a ^{64}V ion in the DSSD shown in the range of 0 - 600 keV. The $2_1^+ \rightarrow 0_1^+$ transition in ^{64}Cr is marked by the red triangle and labelled by its energy in keV.	143
Figure 4.46	^{64}V decay curve showing fragment- β correlations for β decays detected within 500 ms of a ^{64}V ion implantation in the DSSD. The fit to the decay curve, labelled “tot,” included the exponential decay of ^{64}V , the exponential growth and decay of ^{64}Cr and ^{64}Mn , and a constant background.	143
Figure 4.47	γ -ray energy spectrum detected within 2 ms of the implantation of a ^{64}Mn ion in the DSSD. Transitions observed following the decay of ^{64m}Mn are labelled with red triangles. Peaks due natural background decays are marked by green diamonds.	144
Figure 4.48	γ - γ coincidence spectra detected within 2 ms of the implantation of a ^{64}Mn ion in the DSSD gated on the (a) 40-keV and (b) 135-keV γ rays.	145
Figure 4.49	Decay curves for ^{64m}Mn showing fragment- γ correlations in which a (a) 40-keV or (b) 135-keV γ ray was detected within 5 ms of the ^{64}Mn fragment. The total fits to the data are labelled by “tot” and are comprised of an exponential for the decay of ^{64m}Mn and a constant background (“bkg”).	146
Figure 4.50	Decay scheme of ^{64m}Mn . States are labelled on the left by their spins and parities and on the right by their energies in keV. The half-life of the isomeric state at 175 keV is indicated.	147

Figure 4.51	γ -ray energy spectrum detected within 4 ms of the implantation of a ^{66}Mn ion in the DSSD. Transitions observed following the decay of ^{66m}Mn are labelled with red triangles. Peaks due natural background decays are marked by green diamonds.	149
Figure 4.52	Background-subtracted γ - γ coincidence spectra detected within 4 ms of the implantation of a ^{66}Mn ion in the DSSD gated on the (a) 170-keV, (b) 251-keV, and (c) 294-keV transitions. The inset of each panel shows a zoom of the region from 0 - 150 keV.	150
Figure 4.53	Decay curves for ^{66m}Mn showing fragment- γ correlations in which a (a) 170-keV, (b) 251-keV, or (c) 294-keV γ ray was detected within 7 ms of the ^{66}Mn fragment. The total fits to the data are labelled by “tot” and are comprised of an exponential for the decay of ^{66m}Mn and a constant background (“bkg”).	152
Figure 4.54	Decay scheme of ^{66m}Mn . States are labelled on the left by their spins and parities and on the right by their energies in keV. The half-life of the isomeric state at 464 keV is indicated.	152
Figure 5.1	Energies of the four lowest energy states in ^{68}Ni as determined by experiment (Exp), Monte Carlo shell-model calculations using the revised A3DA [15] effective interaction (MCSM), and shell-model calculations using the LNPS [16], Lisetskiy [17], jj44b [18], and JUN45 [19] effective interactions. The experimental energies of the 2_1^+ and 0_3^+ states were taken from Ref. [20] and Ref. [21], respectively.	156
Figure 5.2	Potential energy surface for ^{68}Ni calculated by the constrained Hartree-Fock method. The circles on the potential energy surface represent the basis vectors calculated by the MCSM calculation. The location of each circle represents the shape of the basis vector, while the area of the circle denotes the importance of the basis vector in the calculated wave function of the (a) 0_1^+ , (b) 0_2^+ , and (c) 0_3^+ state in ^{68}Ni . The figure was taken from Ref. [22].	158
Figure 5.3	Comparison of known energy levels in $^{55,57}\text{Cr}$ with shell-model calculations. Experimental data were taken from Refs. [11, 12].	162

Figure 5.4 Comparison of known energy levels in $^{59,61}\text{Cr}$ with shell-model calculations. Experimental data for ^{59}Cr were taken from Refs. [23, 24]. The levels reported at 828 and 1084 keV in ^{59}Cr in Ref. [24] are not displayed in the experimental level scheme for ^{59}Cr . Deep-inelastic-scattering data suggests that the 518-keV γ -ray transition [24] was incorrectly placed in the level scheme [25]. The energy of the 525-keV level in the experimental ^{59}Cr level scheme is shown in parentheses to indicate the tentative nature of its identification [23]. Although a γ -ray cascade was observed, the order of the 841- and 317-keV transitions could not be determined in Ref. [23]. If the order of the transitions is reversed compared to the tentative assignment, the level shown at 525 keV would instead be at 1042 keV. 163

Chapter 1

Introduction

1.1 Nuclear shell structure and shell closures

An important concept for explaining the properties of atomic nuclei is the development of shell structure. Protons and neutrons are understood to fill particular energy levels, with groups of levels having similar energies referred to as shells, and the nuclear structure of a nucleus can be interpreted based on the filling of the shells. Atomic electrons also exhibit properties of shell structure. In atoms, the electrons fill the available atomic energy levels, or orbitals, and orbital filling is critical for determining chemical properties. The effects of atomic shell structure are clearly seen when examining trends in the first ionization energy, the amount of energy needed to remove an electron from an atom. The first ionization energy for atoms across the periodic table is shown in Fig. 1.1(a). Large drops in ionization energy occur immediately following noble-gas elements. In the noble gases, the last occupied atomic orbital is completely filled. Therefore in the elements with an atomic number one greater than a noble gas, the last electron must fill a higher energy orbital, and the energy required to remove the electron from the atom decreases.

The shell structure exhibited by protons and neutrons within the atomic nucleus is very similar. Near the valley of stability, an enhanced stability relative to the neighboring isotopic and isotonic nuclei is observed for the “magic” nuclei, which have neutron or proton numbers of 2, 8, 20, 28, 50, 82, or (for neutrons) 126. The magic nuclei are analogous to the noble

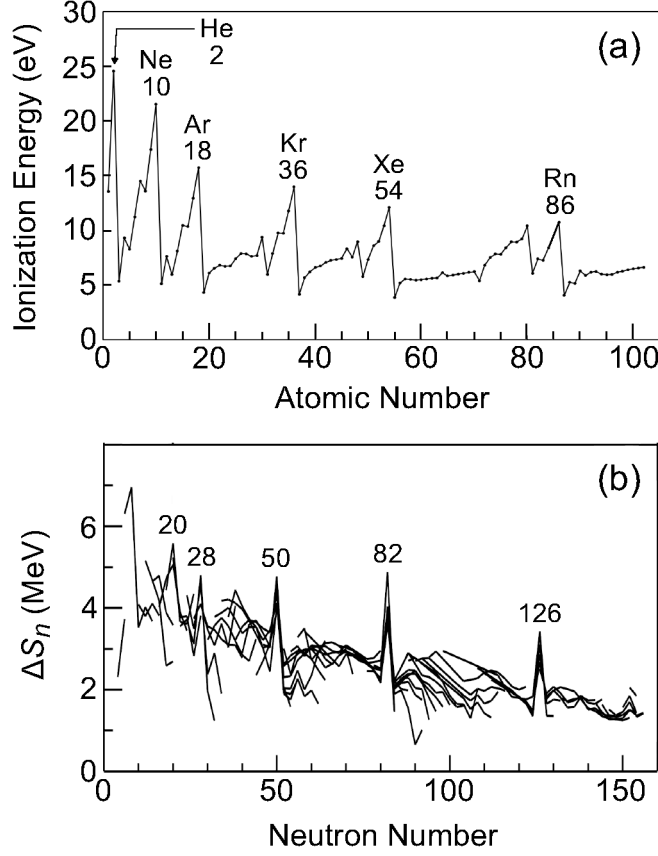


Figure 1.1: (a) First ionization energy as a function of atomic number. Noble-gas elements are labelled along with their atomic numbers. The ionization energies were taken from Ref. [3]. (b) Differential neutron separation energies as a function of neutron number for even-even nuclei. Series of isotopes are connected by lines. The figure was adapted from Ref. [4].

gases and are associated with a completely filled proton or neutron shell. The existence of nuclear shells can be observed in systematic trends in neutron separation energies as a function of neutron number. The one-neutron separation energy, S_n , is defined in terms of nuclear binding energy, BE, such that

$$S_n = \text{BE}(N, Z) - \text{BE}(N - 1, Z) \quad (1.1)$$

where Z is the atomic number and N is the neutron number. In other words, the one-neutron separation energy is the difference in binding energy between a particular nucleus

and the neighboring isotope with just one fewer neutron, which represents the energy required to remove a single neutron. The difference in one-neutron separation energies between neighboring isotopes, ΔS_n , can thus be expressed as

$$\Delta S_n = \text{BE}(N, Z) - \text{BE}(N - 1, Z) - [\text{BE}(N + 1, Z) - \text{BE}(N, Z)]. \quad (1.2)$$

ΔS_n is also called the differential neutron separation energy and is plotted as a function of neutron number for nuclei with even numbers of protons and neutrons in Fig. 1.1(b). Peaks are located at the magic numbers, indicative of the shell structure of neutrons within a nucleus. Corresponding peaks are found at an identical set of magic numbers in a plot of differential one-proton separation energy across the chart of the nuclides, demonstrating that shell structure also exists for the protons in a nucleus. The effects of shell structure can similarly be observed in trends in two-neutron (two-proton) separation energy, S_{2n} (S_{2p}), which represents the energy needed to remove a pair of neutrons (protons) from a nucleus. S_{2n} is defined in the same manner as S_n , where

$$S_{2n} = \text{BE}(N, Z) - \text{BE}(N - 2, Z). \quad (1.3)$$

The corresponding differential two-neutron separation energy is given by

$$\Delta S_{2n} = \text{BE}(N, Z) - \text{BE}(N - 2, Z) - [\text{BE}(N + 2, Z) - \text{BE}(N, Z)]. \quad (1.4)$$

Peaks are seen at the same magic numbers in a plot of ΔS_{2n} (ΔS_{2p}) versus N (Z) as in Fig. 1.1(b). ΔS_{2n} (ΔS_{2p}) is not influenced by differences that may exist between nuclei with even and odd numbers of nucleons.

The interactions between the nucleons in nuclei are expressed as a nuclear potential, but the exact form of the potential is not entirely understood. A relatively simple approximation that can be used for the nuclear potential is the harmonic-oscillator potential. However, this potential is not very realistic, particularly since it goes to infinity at large distances. A better description of the nuclear potential is given by the Woods-Saxon potential, which has the form

$$V(r) = \frac{-V_0}{1 + \left[\exp\left(\frac{r-R}{a}\right) \right]} \quad (1.5)$$

where r is the distance from the center of the nucleus, V_0 is the depth of the potential, R is the mean nuclear radius, and a is the diffuseness of the nucleus. Using the nuclear potentials described above, only the magic numbers at and below 20 can be reproduced. To correctly predict the higher magic numbers, another term in the nuclear potential is needed.

The additional component that must be added to the nuclear potential to reproduce the experimentally observed magic numbers is the spin-orbit potential. Including the spin-orbit term removes the ℓ -degeneracy of states, and states split in energy based on their total angular momentum, \vec{j} , where $\vec{j} = \vec{\ell} + \vec{s}$ and $\vec{\ell}$ is the orbital angular momentum and \vec{s} is the intrinsic nucleon spin. States with a parallel coupling of $\vec{\ell}$ and \vec{s} move lower in energy, while states with an antiparallel coupling of $\vec{\ell}$ and \vec{s} increase in energy. The schematic shell structure that results from using the Woods-Saxon potential with the spin-orbit force is shown in Fig. 1.2 for nucleon numbers up to 64. Large energy gaps between adjacent levels are present for nucleon numbers of 2, 8, 20, 28, and 50, which correspond to the experimentally known magic numbers. Such large energy gaps between the levels that the nucleons fill are known as shell gaps. Smaller but still significant gaps between energy levels, like the one at nucleon number 40 in Fig. 1.2, are referred to as subshell gaps.

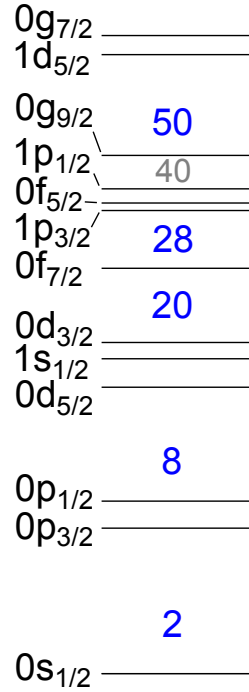


Figure 1.2: Energy levels for the Woods-Saxon potential with a spin-orbit potential included. The number of nucleons required to completely fill all levels up to a particular level are shown. Numbers in blue denote shell closures (magic numbers), while gray numbers denote subshell closures. The figure was adapted from Ref. [4]. For interpretation of the references to color in this and all other figures, the reader is referred to the electronic version of this thesis.

While shell closures are very important for understanding many nuclear properties, nuclear orbital energies evolve as Z and N change. Therefore, the energy gaps between adjacent levels that protons and neutrons fill are not constant, and away from the valley of stability, the traditional shell closures can disappear and new ones can emerge. An example of the breakdown of a traditional shell closure is found in the $N = 20$ isotones near ${}^{32}_{12}\text{Mg}_{20}$, which is located at the “island of inversion” [26, 27, 28, 29]. The spacing between the $\nu 0d_{3/2}$ and $\nu 0f_{7/2}$ levels is substantially reduced in ${}^{32}\text{Mg}$ compared to stable isotonic ${}^{36}_{16}\text{S}_{20}$, resulting in a diminished $N = 20$ shell gap [16, 29, 30]. Given that the levels available to nucleons are not fixed in energy, it is very important to understand how nuclear structure evolves as proton and neutron numbers change in nuclei. More details specifically regarding the evolution of

nuclear shell structure are presented in Section 1.3. First though, a framework is introduced for interpreting the structure of nuclei near closed shells.

1.2 Nuclear structure in the vicinity of shell closures

A simple model especially useful for describing nuclei one particle (or one hole) away from a shell closure is the independent particle model. Within this model, a nucleon moves within a potential that is defined by the other nucleons. Nucleons sequentially fill the single-particle orbitals that are determined from the potential and each nucleon does not interact with the other nucleons. When two nucleons fill the same orbital, they pair to a total angular momentum and parity of 0^+ . The completely filled orbitals comprise an inert “core” that does not contribute to the low-energy level structure. Consequently, the nuclear properties are determined by a single valence particle (hole). In this model, the ground-state spin of a nucleus corresponds to the total angular momentum of the single-particle state that the valence nucleon (hole) occupies and the ground-state parity is $(-1)^\ell$, where ℓ is the orbital angular momentum of the orbital that the valence nucleon (hole) occupies. Excited states result from promoting the valence particle (hole) to different single-particle orbitals, and the spin and parity of an excited state is similarly determined based on the orbital that the promoted particle (hole) occupies.

The application of the independent particle model can be illustrated with the example of ${}^{89}_{39}\text{Y}_{50}$. The independent particle model predicts that a single proton hole occupies the $1p_{1/2}$ orbital below $Z = 40$ in the ${}^{89}\text{Y}$ ground state. The experimental low-energy level scheme of ${}^{89}\text{Y}$ is shown in Fig. 1.3. In agreement with the independent particle model, the ground state has a spin and parity of $1/2^-$. The 1507- and 1745-keV excited states correspond to

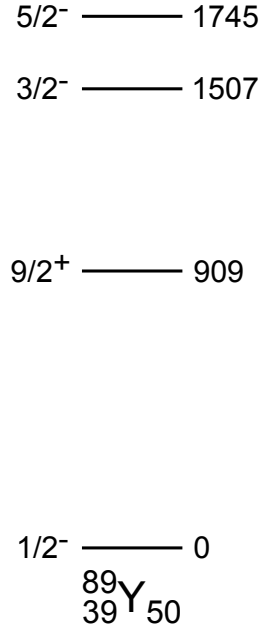


Figure 1.3: Low-energy level scheme of ${}^{89}\text{Y}$. States are labelled on the left by their spins and parities and on the right by their energies in keV. Data were taken from Ref. [5].

states in which the proton hole is found in the $1p_{3/2}$ and $0f_{5/2}$ orbitals, respectively. Within the independent particle model, ${}^{89}\text{Y}$ could also be represented as a single proton outside of a ${}^{88}_{38}\text{Sr}_{50}$ core. Like before, the ground state is predicted to have a spin and parity of $1/2^-$. The $9/2^+$ state at 909-keV results from the promotion of the valence proton to the $0g_{9/2}$ single-particle state. Spectroscopic factors, defined as the probability for finding a particular single-particle configuration in a given nuclear state [31], extracted from comparisons of nucleon-transfer-reaction cross sections to theoretical calculations indicate high degrees of purity for the single-particle configurations described above in the low-energy states of ${}^{89}\text{Y}$ [32, 33, 34, 35, 36].

The framework of the independent particle model can be extended in a very straightforward manner to treat nuclei a few nucleons away from a closed shell. An additional “residual” potential accounting for nucleon-nucleon interactions is included in this model. As with the independent particle model, completely occupied levels form a core, which is

determined based on the large energy gaps between the single-particle orbitals and does not contribute to the nuclear properties. However, interactions between the valence nucleons outside the core are added to the nuclear potential and are often very important for accurately describing the low-energy level schemes of nuclei located a few nucleons from a shell closure.

A single proton and a single neutron occupying the single-particle orbitals with total angular momenta j_1 and j_2 , respectively, couple to form a multiplet of nuclear states with total angular momentum, J , that can range from $|j_1 - j_2| \leq J \leq |j_1 + j_2|$. The states of the multiplet with the lowest and highest possible J values will typically have the lowest energies, while those with intermediate values of J will have the highest energies [37]. Conversely, if a proton hole is coupled with a neutron particle, or vice versa, the minimum energy of a state in the multiplet occurs for an intermediate value of J , and the states of the multiplet with the largest and smallest possible J values have the highest energies [37]. As an example, states generated from the coupling of a single proton with a single neutron are observed at low energy in the level scheme of ${}^{90}_{39}\text{Y}_{51}$, which is shown in Fig. 1.4. ${}^{90}\text{Y}$ has the same proton configuration as ${}^{89}\text{Y}$ but has a single neutron beyond the $N = 50$ shell closure. The proton in the $1p_{1/2}$ single-particle state can couple with a neutron in the $1d_{5/2}$ single-particle state to produce two states with spins and parities of 2^- and 3^- , which correspond to the experimentally observed ground and first excited states in ${}^{90}\text{Y}$, respectively. If the proton is elevated to the $0g_{9/2}$ orbital, the proton can couple with the neutron in the $1d_{5/2}$ to produce a multiplet of states with spins and parities ranging from 2^+ to 7^+ . The states of the multiplet with the largest and smallest possible spins would be expected to have the lowest energy [37], and accordingly, the second and third excited states at 682 and 777 keV in ${}^{90}\text{Y}$ are 7^+ and 2^+ states, respectively.

2^+ ——— 777
 7^+ ——— 682

3^- ——— 203
 2^- ——— 0
 ${}^{90}_{39}\text{Y}_{51}$

Figure 1.4: Low-energy level scheme of ${}^{90}\text{Y}$. States are labelled on the left by their spins and parities and on the right by their energies in keV. Data were taken from Ref. [6].

Using the framework described above, nuclear shell-model calculations are commonly carried out with a large number of inert-core nucleons and a comparatively small number of valence nucleons. The single-particle orbitals included in the calculation that the valence nucleons can fill comprise the model space. Effective-shell model interactions are then developed within a particular model space to reproduce the nuclear properties of nuclei in a certain region of the chart of the nuclides.

1.3 Evolution of nuclear shell structure

An important contributor to the reordering of single-particle states is the proton-neutron tensor monopole force [38], which is a component of the residual nucleon-nucleon interaction in the nuclear potential. As the number of protons or neutrons in a nucleus changes, the tensor monopole force can alter the effective single-particle energy (ESPE) of a nucleon occupying a single-particle orbital. The ESPE reflects the average effects from the other nucleons on the nucleon occupying the particular single-particle orbital [39].

The tensor monopole force affects ESPE in a systematic way. The trend can be understood by assuming a proton and a neutron occupy the single-particle states with orbital

angular momenta ℓ and ℓ' , respectively. The proton orbital therefore has a total angular momentum of $j_{>} = \ell + 1/2$ or $j_{<} = \ell - 1/2$ and the neutron orbital has total angular momentum of $j'_{>} = \ell' + 1/2$ or $j'_{<} = \ell' - 1/2$. The tensor force between $j_{>}$ and $j'_{<}$ (or $j_{<}$ and $j'_{>}$) is attractive, while that between $j_{>}$ and $j'_{>}$ (or $j_{<}$ and $j'_{<}$) is repulsive [38], and the attraction or repulsion is maximized when $\ell = \ell'$ [39]. Thus, due to the tensor force, as protons (neutrons) are added or removed from a single-particle state, the energy gaps and possibly the ordering between the neutron (proton) single-particle states may change. The change in the ESPE of the j' (j) orbital in terms of the number of protons (neutrons) in the j (j') orbital is linear. Therefore, for exotic nuclei that have many neutron (proton) particles or holes in the j' (j) orbital relative to a stable isotope (isotone), the impact of the tensor force can be large. The role of the tensor force has been identified, for example, at $N = 20$ in the nuclei located at the island of inversion. Starting from $^{34}\text{Si}_{20}$, as protons are removed from the $0d_{5/2}$ orbital, the attractive interaction between protons in the $0d_{5/2}$ orbital and neutrons in the $0d_{3/2}$ orbital decreases. Consequently, the energy spacing between the neutron $0d_{3/2}$ and $0f_{7/2}$ single-particle states shrinks, reducing the size the $N = 20$ shell closure [16, 29, 30].

As nuclear structure evolves, the energy of a single-particle state originating from a higher major shell in a stable nucleus may become similar to the energy of single-particle states that originate from a lower major shell. Such a single-particle state that originates from the higher shell and that has the opposite parity of the other single-particle states near the Fermi surface is known as an “intruder” orbital. Nuclear states that are associated with filling nucleons in the intruder orbital rather than an orbital originating from the lower shell are similarly referred to as intruder states. Once again drawing reference to the island of inversion, the ground state in $^{32}_{12}\text{Mg}_{20}$ is an intruder state and characterized by two neutrons occupying

the $0f_{7/2}$ orbital with two corresponding neutron holes in the $0d_{3/2}$ orbital [40, 41]. As is further explained in the following sections, intruder states are often connected to ground-state deformation or shape coexistence since the occupation of the intruder orbital typically drives a nucleus toward non-spherical shapes.

1.4 Shape coexistence

In closed-shell nuclei, which are generally spherical, there is a large energy gap between the last occupied single-particle state and first unoccupied single-particle state. However, the excitation of a pair (or several pairs) of nucleons across the energy gap is possible and can cause the nucleus to adopt a deformed shape. While there is an energy cost associated with promoting the nucleons across the gap, there may also be an energy stabilization based on the residual interactions between pairs of valence nucleons in the higher energy single-particle level, as well as the residual interactions between nucleons in the higher energy single-particle state and any other valence nucleons. If the stabilization gained from the residual interactions is similar to the energy required to excite the pair(s) of nucleons across the energy gap, the state can have a similar energy to and “coexist” with the spherical state based on the closed-shell configuration. Shape coexistence is not isolated to stable nuclei, but occurs quite commonly across the chart of the nuclides [42]. Indeed, in many nuclei it has been inferred that at low energies, there is a competition between spherical states stabilized by large energy gaps between single-particle orbitals and prolate and/or oblate states in which a low energy results from the nucleus adopting a quadrupole deformation. An example nucleus in which low-energy shape coexistence occurs is ^{186}Pb [43]. While the ground state of ^{186}Pb is spherical, the 532-keV first excited state and 650-keV second excited

state have been identified as oblate- and prolate-deformed, respectively [43].

The lowest energy state that typically results from the excitation of pairs of nucleons across an energy gap in even-even nuclei is a 0^+ state. Therefore, the presence of a low-energy excited 0^+ state in an even-even nucleus is often taken as a first indication of shape coexistence, and studying the decay properties of excited 0^+ states can be important for investigating shape coexistence. Particularly important are decays between two 0^+ states, which occur via electric monopole ($E0$) transitions. The intensity of an $E0$ transition is characterized by the dimensionless electric monopole transition strength, $\rho^2(E0)$. In a given nucleus, $\rho^2(E0)$ is deduced from the half-life of the decaying state, the branching ratio for the decay of the state by the $E0$ transition, and the energy of the $E0$ transition.

For an $E0$ transition between initial state, $|i\rangle$, and final state, $|f\rangle$, $\rho^2(E0)$ can be written

$$\rho^2(E0) = \left| \frac{\langle f | \hat{T}(E0) | i \rangle}{eR^2} \right|^2 \quad (1.6)$$

where e is the unit of electrical charge and R is the mean nuclear radius, which can be approximated by $R = 1.2A^{1/3}$ [44]. $\hat{T}(E0)$ is the electric monopole operator defined by

$$\hat{T}(E0) = \sum_n e_n r_n^2 \quad (1.7)$$

where for the n th nucleon, e_n is the effective charge and r_n is the position relative to the center of mass of the nucleus [44].

It can be theoretically shown that $\rho^2(E0)$ connects to differences in deformation. To demonstrate the relationship between $\rho^2(E0)$ and shape coexistence, a simple two-level-mixing model will be adopted here. Within such a model, the 0^+ states $|0_i^+\rangle$ and $|0_f^+\rangle$

can be described as a linear combination of two different nucleon configurations that each have a spin and parity of 0^+ but that have different shapes. Assuming a spherical nucleon configuration, $|0_s^+\rangle$, and a deformed nucleon configuration, $|0_d^+\rangle$, the states $|0_i^+\rangle$ and $|0_f^+\rangle$ can be expressed as

$$|0_i^+\rangle = a|0_s^+\rangle + b|0_d^+\rangle \quad (1.8)$$

$$|0_f^+\rangle = -b|0_s^+\rangle + a|0_d^+\rangle \quad (1.9)$$

where a and b are the mixing amplitudes and $b = \sqrt{1 - a^2}$. For the case of maximal mixing, $a = b = 1/\sqrt{2}$. In this model, $\rho^2(E0)$ is thus

$$\rho^2(E0) = \left(\frac{1}{eR^2} \left[ab(\langle 0_s^+ | \hat{T}(E0) | 0_s^+ \rangle - \langle 0_d^+ | \hat{T}(E0) | 0_d^+ \rangle) + (a^2 - b^2) \langle 0_d^+ | \hat{T}(E0) | 0_s^+ \rangle \right] \right)^2 \quad (1.10)$$

[44]. If only weak mixing occurs between $|0_s^+\rangle$ and $|0_d^+\rangle$ in $|0_i^+\rangle$ and $|0_f^+\rangle$, ab is approximately zero due the small values of the mixing amplitudes, and $\langle 0_d^+ | \hat{T}(E0) | 0_s^+ \rangle$ is also approximately zero because of the poor overlap between $|0_d^+\rangle$ and $|0_s^+\rangle$, which have different shapes. Therefore, $\rho^2(E0)$ is small in the case of weak mixing. If instead strong mixing occurs, $a^2 - b^2 \approx 0$, so

$$\rho^2(E0) \approx \left(\frac{1}{eR^2} \left[ab(\langle 0_s^+ | \hat{T}(E0) | 0_s^+ \rangle - \langle 0_d^+ | \hat{T}(E0) | 0_d^+ \rangle) \right] \right)^2. \quad (1.11)$$

Given the definition of $\hat{T}(E0)$ in Eq. 1.7, which is independent of level mixing, $\rho^2(E0)$ is proportional to the difference in mean-square radii between $|0_s^+\rangle$ and $|0_d^+\rangle$ and can be written

$$\rho^2(E0) \approx \frac{Z^2}{e^2 R^4} a^2 b^2 [\Delta \langle r^2 \rangle]^2 \quad (1.12)$$

where $\Delta \langle r^2 \rangle$ is the difference in mean-square radii between the two configurations. Higher

values of $\rho^2(E0)$ result when there is a larger difference in shape between the configurations. Assuming axial deformations, $\rho^2(E0)$ can also be expressed in terms of the difference in deformation parameters between the configurations such that

$$\rho^2(E0) \approx \frac{1}{4} \left(\frac{3}{4\pi} \right)^2 Z^2 a^2 b^2 (\Delta\beta^2)^2 \quad (1.13)$$

where $\Delta\beta^2$ is the difference in the squares of the deformation parameters of $|0_s^+\rangle$ and $|0_d^+\rangle$. Given a spherical $|0_s^+\rangle$ with $\beta = 0$, the value of $\rho^2(E0)$ gives an indication of the degree of deformation of $|0_d^+\rangle$.

The usefulness of the simple framework described above can be illustrated with ${}^{90}_{40}\text{Zr}_{50}$. The first excited state in ${}^{90}\text{Zr}$ is at 1761 keV and has a spin and parity of 0^+ [6]. Within a two-level mixing model and considering only the last two valence protons, the ground state, $|0_1^+\rangle$, and first excited state, $|0_2^+\rangle$ can be expressed

$$|0_1^+\rangle = a|0^+, (1p_{1/2})^2(0g_{9/2})^0\rangle + b|0^+, (1p_{1/2})^0(0g_{9/2})^2\rangle \quad (1.14)$$

$$|0_2^+\rangle = -b|0^+, (1p_{1/2})^2(0g_{9/2})^0\rangle + a|0^+, (1p_{1/2})^0(0g_{9/2})^2\rangle \quad (1.15)$$

where $|0^+, (1p_{1/2})^2(0g_{9/2})^0\rangle$ represents the nucleon configuration where the last two valence protons are in the $1p_{1/2}$ orbital and $|0^+, (1p_{1/2})^0(0g_{9/2})^2\rangle$ represents the nucleon configuration where the last two valence protons are excited across the $Z = 40$ subshell gap into the $0g_{9/2}$ orbital. Using this framework and assuming strong mixing between the two configurations

$$\langle 0_1^+ | \hat{T}(E0) | 0_2^+ \rangle = 2eab \left[\langle r^2 \rangle_{1p_{1/2}} - \langle r^2 \rangle_{0g_{9/2}} \right] \quad (1.16)$$

where $\langle r^2 \rangle_{1p_{1/2}}$ and $\langle r^2 \rangle_{0g_{9/2}}$ are the mean-square radii of the $1p_{1/2}$ and $0g_{9/2}$ single-particle orbitals, respectively [44]. From comparisons of measured differential cross sections in nucleon transfer reactions with theoretical calculations, respective values of 4.64 ± 0.02 and 4.79 ± 0.03 fm have been inferred for $\langle r^2 \rangle_{1p_{1/2}}^{1/2}$ and $\langle r^2 \rangle_{0g_{9/2}}^{1/2}$ [45] and respective values of 0.75 ± 0.06 and 0.66 ± 0.09 have been inferred for a and b [33, 46, 47]. Using these values, $\rho^2(E0)$ is calculated to be $2.5 \pm 0.6 \times 10^{-3}$, which compares favorably to the experimental value of $3.30 \pm 0.17 \times 10^{-3}$.

A useful example nucleus for demonstrating the possible range of values for $\rho^2(E0)$ is ^{58}Ni , which has both one of the smallest and largest known $\rho^2(E0)$ values. ^{58}Ni has two excited 0^+ states at 2942 and 3531 keV. The $\rho^2(E0)$ values for the transitions from the 2942 and 3531-keV states to the ground state are 6.2×10^{-6} and 80, respectively [44]. In both the 3531-keV state and ground state, two different configurations have been proposed to be strongly mixed, one configuration where all the valence protons occupy the $0f_{7/2}$ orbital and another configuration where two protons are excited out of the $0f_{7/2}$ orbital and into the next shell [44]. Consistent with this interpretation, the value of $\rho^2(E0)$ for the transition between the 3531-keV and ground states is large [44]. The 2942-keV state on the other hand has been attributed to neutron excitations; specifically, the excitation of the pair of valence neutrons (which are outside the $0f_{7/2}$ orbital) in ^{58}Ni within the upper fp single-particle states (the $1p_{3/2}$, $0f_{5/2}$, and $1p_{3/2}$ orbitals). These neutron-pair excitations occur in the same shell that the valence neutrons occupy in the ground configuration, resulting in essentially the same mean-square radii for the excited and ground configurations. The small value of $\rho^2(E0)$ for the transition between the 2942-keV and ground states is consistent with this explanation [44].

1.5 Nuclear deformation and collectivity

Within the independent particle model, single-particle excitations, which are characterized by the promotion of a single nucleon to a higher single-particle level, are very important. A fundamentally different type of nuclear excitation is a collective excitation. Distinct from single-particle excitations, collective excitations involve several or all of the nucleons in a nucleus. Common examples of collective motion include the rotation of a deformed nucleus and shape vibrations. Nuclear deformation is closely tied to collectivity in that deformed nuclei exhibit enhanced collective behavior.

For nuclei with quadrupole (axial) deformations, the degree of deformation can be quantified by the dimensionless deformation parameter, β , which describes an ellipsoid and is expressed as

$$\beta = \frac{4}{3} \sqrt{\frac{\pi}{5}} \frac{a - b}{R_{\text{av}}} \quad (1.17)$$

where a and b are the lengths of the semimajor and semiminor axes, respectively, of the ellipsoid and R_{av} is given by $R_{\text{av}}^2 = \frac{1}{2}(a^2 + b^2)$. A value of zero for β indicates the nucleus is spherical, and as the magnitude of β increases, the nucleus becomes more deformed. A positive β signifies a prolate shape, while a negative β denotes an oblate shape.

The energy of the first excited 2^+ state in even-even nuclei is often used as an indication of collectivity. Relative to the 0^+ ground state in an even-even nucleus at a shell closure, in order to form a 2^+ state, a pair of nucleons must be broken and one of the nucleons must be excited across the large energy gap responsible for the shell closure. A large amount of energy is required, resulting in a high energy for the 2^+ state. Away from a shell closure, where there may be unoccupied low-energy single-particle states, collective interactions among many nucleons can give rise to an excited 2^+ state, resulting in a lowered energy of the 2_1^+

state. Therefore, by comparing the energy of the 2_1^+ state in a nucleus to the energy of the 2_1^+ state in the neighboring isotopic or isotonic nuclei, inferences about the extent to which the particular nucleus behaves collectively can be made. A low energy of the first excited 2^+ state is associated with an increased collectivity. On the other hand, a high energy of first excited 2^+ state is characteristic of a spherical closed-shell nucleus, which behaves less collectively. A simple, empirically-derived estimate for relating the energy of the first excited 2^+ state, $E(2^+)$, to the quadrupole deformation parameter is given by

$$E(2^+) \approx \frac{1225}{A^{7/3}\beta^2} \text{ MeV} \quad (1.18)$$

where A is the number of nucleons [48]. In a similar manner, the reduced electric quadrupole transition strength, $B(E2)$, from the first excited 2^+ state to the ground state is also used to deduce enhanced collectivity in even-even nuclei. A large $B(E2)$ value signifies a highly collective transition, while a small $B(E2)$ value corresponds to a low degree of collectivity.

Inferences about nuclear deformation in an even-even nucleus can be made based on the ratio of the energy of the first excited 4^+ state to the energy of the first excited 2^+ state, $R_{4/2}$. For vibrational excitation about a spherical shape within a harmonic-oscillator model, the energy of each vibrational state, E_{vib} , is given by

$$E_{\text{vib}} = (N + 1/2)\hbar\omega_0 \quad (1.19)$$

where \hbar is Plank's constant divided by 2π , ω_0 is the fundamental frequency of the vibration, and N is the number of quanta required to make the vibrational excitation. The states within a vibrational band are thus equally spaced and $R_{4/2} = 2$. For the rotation of an

axially-deformed nucleus within the rigid-rotor model, the energy of a state in a rotational band is

$$E_{rot} = \frac{J(J+1)\hbar^2}{2I} \quad (1.20)$$

where J is the rotational quantum number and I is the moment of inertia. Therefore, $R_{4/2} = 3.33$ for a rotational band. $R_{4/2}$ is deduced from experimental data to infer the extent of deformation in a nucleus, with values near 2 indicating a spherical nucleus and values near 3.33 suggesting deformation.

Insight into the nuclear structure of axially deformed nuclei can be gained by considering the energy of the single-particle states that result when a deformed nuclear potential is assumed, which is described by the Nilsson model. Within this model, the j -degeneracy of states originating from a spherical single-particle states in the independent particle model is removed, and the spherical single-particle state splits into $(2j+1)/2$ levels that are characterized by Ω , the projection of the orbital angular momentum onto the nuclear symmetry axis. As an example, the $0g_{9/2}$ orbital splits into five levels with $\Omega = 1/2, 3/2, 5/2, 7/2,$ and $9/2$, and each level is filled by a maximum of two nucleons. As the quadrupole deformation parameter of a nucleus changes, the energies of the levels change. For a spherical nucleus, all levels originating from a spherical single-particle state are degenerate, just like in the independent particle model. However, for a prolate- (oblate-) deformed nucleus, levels with the lowest (highest) values of Ω decrease the most in energy, while levels with the highest (lowest) values of Ω increase the most in energy. In an odd- A nucleus, the spin of a state is determined by the value of Ω for the orbital filled by the single odd nucleon. Thus, by comparing the sequence of spins and parities for the lowest energy states in a deformed odd- A nucleus with predictions from the Nilsson model, inferences can be drawn about whether

the nucleus is prolate or oblate.

1.6 Nuclear structure of the neutron-rich nuclei with

$$N \approx 40 \text{ and } Z \leq 28$$

Extensive experimental and theoretical work has recently been performed on the neutron-rich nuclei with approximately 40 neutrons and 28 or fewer protons. The focus has been to understand the dramatic changes in nuclear structure that occur in this region.

A subshell closure was originally proposed at $N = 40$ based on spectroscopic information in ${}^{68}_{28}\text{Ni}_{40}$ and attributed to a large energy gap between the upper fp -shell orbitals and the $g_{9/2}$ orbital [20, 49]. The energy of the 2_1^+ state and the $B(E2; 0_1^+ \rightarrow 2_1^+)$ value along the even-even Ni isotopic chain are shown in Figs. 1.5(a) and (b), respectively. The high $E(2^+)$ value [20] and the correspondingly low $B(E2; 0_1^+ \rightarrow 2_1^+)$ value [50] in ${}^{68}_{28}\text{Ni}_{40}$ relative to the neighboring even-even Ni isotopes can be viewed as an indication of an $N = 40$ subshell closure. The $E(2^+)$ and $B(E2; 0_1^+ \rightarrow 2_1^+)$ values are also plotted for the even-even Fe and Cr isotopes in Fig. 1.5. Based on the experimental data, collectivity has been inferred to rapidly develop in the Fe and Cr isotopes. $E(2^+)$ monotonically decreases along the even-even Fe [51] and Cr [52] isotopic chains as neutron number increases and reaches 40. Similarly, the $B(E2)$ value increases as $N = 40$ is approached for the Fe [53] and Cr isotopes [8, 9]. Consistent with the spectroscopic data, the two-neutron separation energies for the even-even Ni, Cu, and Zn isotopes, which were derived from mass measurements, do not drop between $N = 40$ and $N = 42$ as would be expected for a subshell closure [54]. Thus, the mass measurements have not revealed evidence for a robust $N = 40$ subshell closure, but instead point to a relatively weak effect isolated to the Ni isotopes [54].

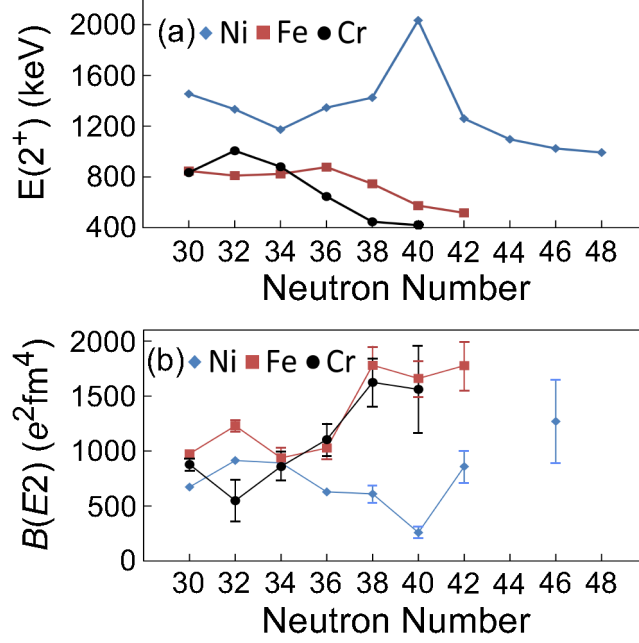


Figure 1.5: (a) Energy of the first excited 2^+ state [$E(2^+)$] shown as a function of neutron number for the even-even Ni, Fe, and Cr isotopes. (b) $B(E2)$ value for the transition from the ground state to the first excited 2^+ state shown as a function of neutron number for the even-even Ni, Fe, and Cr isotopes. Data were taken from Refs. [7, 8, 9].

The relatively low $E(2^+)$ and high $B(E2; 0_1^+ \rightarrow 2_1^+)$ values at $N = 40$ in the Fe and Cr isotopes have been used to infer deformation, leading to a proposed transition from a spherical ground state in ^{68}Ni to prolate-deformed ground states in ^{66}Fe and ^{64}Cr [52, 53]. The deformation has largely been interpreted in terms of the influence of the $\nu g_{9/2}$ orbital and the importance of the proton-neutron tensor monopole force between protons in the $f_{7/2}$ orbital and neutrons in the $f_{5/2}$ orbital [16, 55]. As protons are removed from the $f_{7/2}$ orbital in ^{68}Ni , the attractive interaction between the $f_{7/2}$ protons and the $f_{5/2}$ neutrons decreases. The ESPE of the $\nu f_{5/2}$ orbital therefore increases relative to the ESPEs of the $\nu p_{3/2}$ and $\nu p_{1/2}$ orbitals and the ESPE of the $\nu f_{5/2}$ orbital is elevated above that of the $\nu p_{1/2}$ orbital. The increase in energy of the $\nu f_{5/2}$ orbital reduces the energy gap to the $\nu g_{9/2}$ orbital and the contribution of excitations of neutrons out of the fp shell becomes more important, leading to the inferred ground-state deformation in the neutron-rich Fe and

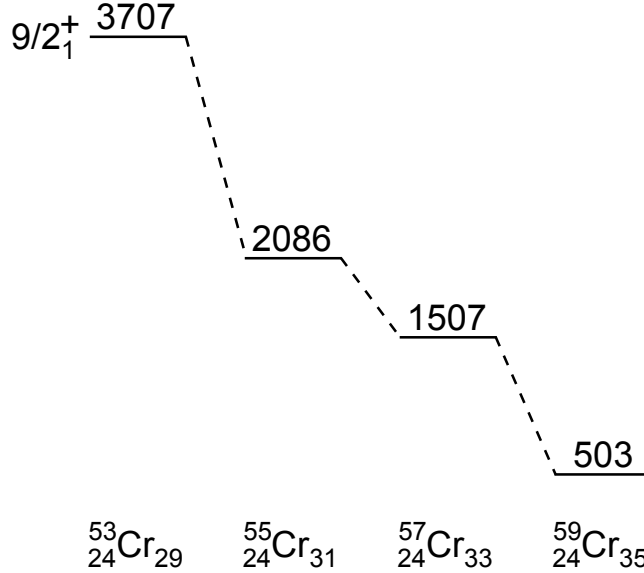


Figure 1.6: Energies in keV of the $9/2_1^+$ state in the odd- A ${}^{53-59}\text{Cr}_{29-35}$ isotopes. The energies were taken from Refs. [10, 11, 12, 13].

Cr isotopes near $N = 40$ [16, 55].

Evidence for the importance of the $\nu g_{9/2}$ orbital has also been identified in neutron-rich odd- A isotopes in the region. The energies of the $9/2_1^+$ states in odd- A ${}^{53-59}\text{Cr}_{29-35}$ are shown in Fig. 1.6. As neutron number increases, the energy of the $9/2_1^+$ state rapidly decreases, going from 3707 keV in ${}^{53}\text{Cr}$ [10] to just 503 keV ${}^{59}\text{Cr}$ [13], highlighting the increased importance of the $g_{9/2}$ orbital as $N = 40$ is approached. The proton-neutron tensor monopole force likely places a role. The attraction between protons excited into the $f_{5/2}$ orbital and neutrons in the $g_{9/2}$ orbital is proportional to the number of neutrons in the $g_{9/2}$ intruder orbital, which increases with increasing neutron number. Thus, the ESPE of the $\nu g_{9/2}$ single-particle orbital decreases as neutron-richness grows [56]. However, the nature of the $9/2_1^+$ state and the evolution of nuclear structure across the neutron-rich odd- A Cr isotopic chain is not completely understood. In ${}^{55,57}\text{Cr}$, the $9/2_1^+$ state has been interpreted as a member of a rotational band associated with prolate deformation that is built on an $1/2^+$ state caused by the excitation of a neutron into the $\Omega^\pi = 1/2^+$ level originating

from the spherical $g_{9/2}$ single-particle state [12]. The $9/2_1^+$ state in ^{59}Cr is isomeric, with a half-life of $96 \mu\text{s}$ [13], and has been proposed to be due to the excitation of a neutron into the $\Omega^\pi = 9/2^+$ level originating from the spherical $g_{9/2}$ single-particle state, which would be expected for an oblate deformation [12, 24]. A similar trend has been observed for the energy of the $9/2_1^+$ state in the odd- A Fe isotopes. The energy of the $9/2_1^+$ state is 2456 keV in $^{57}\text{Fe}_{31}$ [57] and drops to 394 keV in $^{65}\text{Fe}_{39}$ [58].

Theoretically, it is known that the $\nu 0g_{9/2}$ orbital must be included in the model space of shell-model calculations to accurately reproduce the level schemes of the even-even Cr and Fe nuclei with $Z < 28$ and neutron numbers above about 34 [59, 60, 61, 62]. The inclusion of the $\nu 1d_{5/2}$ orbital in the calculations is also important [63]. It was found that shell-model calculations performed in the fp shell using the GXPF1A effective interaction could adequately predict the level schemes of $^{56,58}\text{Cr}_{32,34}$ but fail to reliably calculate the level scheme of $^{60}\text{Cr}_{36}$, especially for higher energy and higher spin states [59]. Further, to accurately calculate the energy of the first excited 2^+ state and the $B(E2; 0_1^+ \rightarrow 2_1^+)$ value in $^{60,62,64}\text{Cr}$, it was found to be necessary to include both the $\nu g_{9/2}$ and $\nu d_{5/2}$ orbitals in the model space [63]. A similar trend has been identified in the even-even Fe isotopes. Shell-model calculations carried out in the fp shell can reproduce the level scheme of $^{60}\text{Fe}_{34}$ quite well [61]. However, sizable discrepancies between calculations performed in the fp shell and experiment result for $^{62}\text{Fe}_{36}$ and even larger discrepancies are seen for $^{64}\text{Fe}_{38}$ [61, 62]. For ^{62}Fe , shell-model calculations allowing for neutron excitations into the $g_{9/2}$ orbital match experimental data much more closely than identical calculations in which neutron excitations into the $g_{9/2}$ orbital were not permitted [61]. For $^{64,66}\text{Fe}$, the $\nu d_{5/2}$ orbital must also be included in the model space to reliably calculate the energy of the first excited 2^+ state [63].

The occurrence of shape coexistence has been proposed in the neutron-rich nuclei near

$N = 40$. Just one proton removed from ^{68}Ni , a 496-ms half-life isomeric state has been identified at 492 keV in $^{67}_{27}\text{Co}_{40}$. The isomer has tentatively been identified as a prolate-deformed $1/2^-$ state that coexists with a spherical $7/2^-$ ground state in which one hole is found in the $\pi f_{7/2}$ orbital [64]. Similar features have been reported for the neighboring lower mass, odd- A Co isotope, whereby shape coexistence between a spherical $7/2^-$ ground state and a 1095-keV prolate-deformed $1/2^-$ excited state has also been proposed in ^{65}Co [65]. Further, the trend of coexistence has been inferred to persist in odd-odd Co isotopes. Shape coexistence has been suggested between the two lowest energy states in $^{66,68}\text{Co}_{39,41}$, with one of the states arising from the coupling of protons and neutrons in spherical single-particle orbitals and the other coming from the deformed coupling of protons and neutrons occupying Nilsson-model orbitals [66].

1.7 Motivations for the measurements

The objective for this thesis work was to more fully understand the nuclear structure of neutron-rich nuclei with about 40 neutrons and 28 or fewer protons. Particularly, a more complete knowledge of the importance of the $\nu g_{9/2}$ orbital in the low-energy level schemes of these nuclei was desired.

Two separate experiments were performed. In one experiment, ^{68}Ni was studied. To more clearly explain the objectives and results of the experiment studying ^{68}Ni , details known about the nuclear structure of ^{68}Ni before the present experiment was performed are summarized here. The level scheme of ^{68}Ni populated by β decay was proposed in Ref. [21]. Further, a detailed ^{68}Ni level scheme determined from quasielastic and deep-inelastic reactions is given in Ref. [67]. Unlike most even-even nuclei, whose first excited state has

a spin and parity of 2^+ , the spin and parity of the first excited state in ^{68}Ni is 0^+ [49]. Prior to the current study, the energy of the first excited state ($1770 \pm 30\text{keV}$ [49]) was not known very precisely. Differences between the excitation energies measured for states above the 0_2^+ state in Ref. [49] and subsequent experiments (Ref. [20] for instance) suggested that the energy calibration of Ref. [49] was not correct, so the energy determined for the first excited 0^+ state was suspect. Theoretically, the first excited 0^+ state has primarily been identified to be due to the excitation of neutrons across the $N = 40$ gap [16, 68]. There is also a low-energy second excited 0^+ state at 2511 keV in ^{68}Ni [21, 69]. The second excited 0^+ state has been proposed to result from the excitation of protons across the $Z = 28$ gap [16, 68]. Another 0^+ state was claimed at 2202 keV in Ref. [70] but was not observed in subsequent experiment work [69]. The present experiment aimed to study the decay of the first excited 0^+ state of ^{68}Ni in detail, with the intent of identifying its energy accurately and more precisely, and recomputing $\rho^2(E0)$ for its decay. Given the presence of low-energy excited 0^+ states can be taken as a first indication of shape coexistence, a greater knowledge of the decay of the excited 0^+ state could provide evidence for shape coexistence in ^{68}Ni , especially since an improved energy determination would result in a more precisely known value of $\rho^2(E0)$ for the transition from the excited 0^+ state to the ground state. It should be noted that results that complement the present experiment have been presented in Ref. [71], in which relative $B(E2)$ values for the decay of the second excited 2^+ state to the ground, first excited, and second excited 0^+ states in ^{68}Ni were deduced and in which the energy of the first excited 0^+ state in ^{68}Ni was independently determined.

The purpose of the second experiment was to study the β decay of neutron-rich V isotopes to the daughter Cr isotopes. Little was known about the low-energy level schemes of the odd- A Cr isotopes beyond $N = 35$. It was believed that by studying increasingly neutron-

rich odd- A Cr isotopes, further insight could be gained into the evolution of nuclear structure and the importance of the $\nu g_{9/2}$ orbital. In the experiment, the nuclei $^{55-57}\text{Sc}$, $^{56-61}\text{Ti}$, $^{58-64}\text{V}$, $^{61-66}\text{Cr}$, $^{63-68}\text{Mn}$, and $^{67-70}\text{Fe}$ were produced and delivered to the experimental station.

1.8 Dissertation outline

The organization of the remainder of this dissertation is summarized here. The techniques that were used in the present studies are described in Chapter 2, with the main focus on β - and electromagnetic-decay spectroscopy. The details about the two experiments that were performed are found in Chapter 3. Information regarding the production of the isotopes studied, the detectors used, the calibrations performed, and the data-analysis techniques applied are given. The experimental results are reported in Chapter 4. The main results deal with the decay of the first excited state in ^{68}Ni , the β decay of $^{61,63}\text{V}$ to $^{61,63}\text{Cr}$, and isomeric decays in V and Mn isotopes. The interpretation of the experimental results are discussed in Chapter 5, with a primary concentration on the impact of the $\nu g_{9/2}$ orbital on the low-energy level schemes and shape coexistence. Finally, concluding remarks and an outlook are provided in Chapter 6.

Chapter 2

Technique

The present experiments utilized β -decay spectroscopy. In β decay, a parent nucleus decays to a daughter nucleus, typically populating excited states in the daughter that subsequently decay to the ground state by emitting electromagnetic radiation. From the so-called “ β -delayed” electromagnetic radiations, one can construct a decay scheme for the decay of the parent to the daughter and often infer nuclear properties. Complementary information from the isomeric decays of metastable excited states was also obtained in the experiments. This chapter describes β , γ , internal-conversion, and internal-pair-production decays, focussing on the details most relevant for β -decay experiments and inferring nuclear properties.

2.1 β decay

Three different decay processes, β^- , β^+ , and electron capture (EC), are classified as β decays and can be written

$$\beta^- : {}^A_Z X_N \rightarrow {}^A_{Z+1} Y_{N-1}^+ + \beta^- + \bar{\nu} + Q_\beta \quad (2.1)$$

$$\beta^+ : {}^A_Z X_N \rightarrow {}^A_{Z-1} Y_{N+1}^- + \beta^+ + \nu + Q_\beta \quad (2.2)$$

$$\text{EC} : {}^A_Z X_N + e^- \rightarrow {}^A_{Z-1} Y_{N+1}^- + \nu + Q_\beta \quad (2.3)$$

where β^\pm is a beta particle, ν is a neutrino, $\bar{\nu}$ is an antineutrino, e^- is an orbital electron, and Q_β is the energy released (i.e. the difference in mass-energy between the initial state

of the parent nucleus and the final state of the daughter nucleus). In a nucleus with an excess of neutrons (protons), β^- (β^+ or EC) decay converts a neutron (proton) to a proton (neutron). All three β -decay processes keep the total number of nucleons constant, so successive β decays occur along an isobaric chain toward stability.

For neutron deficient nuclei, both β^+ decay and EC are possible. In β^+ decay, a positron (the β^+ particle) and a neutrino are emitted. The decay energy is shared among the β^+ particle, the neutrino, and the recoiling daughter nucleus, but the energy of the recoiling daughter is small. Given the rest mass-energy of electrons and positrons is 0.511 MeV, the difference in energy between the parent and daughter must be greater than 1.022 MeV for β^+ decay to occur. In a medium, the emitted positron will lose energy and, after reaching thermal energies, will annihilate with an electron, creating two 0.511-MeV photons. The neutrino, however, which has a very small mass and no charge, is difficult to detect. Since the energy of the recoiling daughter nucleus in β^+ decay (and also in β^- and EC decay) is small, it is not routinely detected, but can be measured using specialized techniques [72].

EC is possible for all Q_β values greater than zero and occurs when a proton in a nucleus captures an orbital electron. The daughter nucleus has one fewer proton than the parent and monoenergetic neutrinos are emitted. The innermost electrons have the highest probability of being captured, and the EC process leaves a vacancy in a normally filled electron shell. Vacancies are typically filled by outer orbital electrons, resulting in the emission of x rays or Auger electrons. Since neutrinos are very difficult to detect, EC is generally studied by monitoring the x rays or Auger electrons.

The decay mode of interest in the present experiments is β^- decay, which is possible if Q_β is greater than zero. In β^- decay, a neutron becomes a proton, and a β^- particle and an antineutrino are emitted. Analogous to β^+ decay, the decay energy is shared between

the β^- particle, the antineutrino, and the recoiling daughter nucleus. The energy of the β^- particle can range from zero to Q_β (neglecting the small contributions from the neutrino mass and recoiling daughter energy). The β^- particle will interact electromagnetically with the atomic electrons within the material of a detector and is commonly detected in this manner.

A fundamental property of β decay is the rate at which it occurs. β decay follows first-order kinetics, meaning the decay rate is proportional to the number of radioactive nuclei present. The decay rate, $\frac{dN}{dt}$, can be written

$$\frac{dN}{dt} = -\lambda N \quad (2.4)$$

where λ is the decay constant. The number of β -decaying nuclei, N , at time, t , is given by

$$N = N_0 e^{-\lambda t} \quad (2.5)$$

where N_0 is the number of nuclei at $t = 0$. The decay constant is closely related to the β -decay half-life, $T_{1/2}$, which can be expressed

$$T_{1/2} = \frac{\ln 2}{\lambda}. \quad (2.6)$$

The half-life is the amount of time required for half of the radioactive nuclei in a sample to decay.

β -decay selection rules govern the decay of a parent nucleus to a daughter nucleus. In β^- decay, the created β particle and antineutrino each have an intrinsic spin, S , equal to $1/2$. In the case that the spins of the created particles have an antiparallel alignment (couple

Table 2.1: β -decay selection rules, adapted from Ref. [1].

Transition Type	Δl	ΔJ	$\Delta\pi$	$\log ft$
Superallowed	0	0	No	2.9 - 3.7
Allowed	0	0,1	No	4.4 - 6.0
First forbidden	1	0,1,2	Yes	6 - 10
Second forbidden	2	1,2,3	No	10 - 13
Third forbidden	3	2,3,4	Yes	≥ 15

to $S = 0$), the decay is referred to as Fermi decay. The other scenario, in which the spins have a parallel alignment (couple to $S = 1$), is known as Gamow-Teller decay. Regardless if the decay is of Fermi or Gamow-Teller nature, “allowed” β^- decay occurs when the β particle and antineutrino are emitted with zero orbital angular momentum ($\Delta l = 0$) relative to the nucleus. “Forbidden” β^- decays involve higher Δl values. First, second, third,... forbidden decays refer to decays where $\Delta l = 1, 2, 3, \dots$. Unlike the name suggests, forbidden decays do occur, but with a much lower likelihood than allowed decays. For each level of forbiddenness, the probability of decay decreases by approximately a factor of 10^4 . Since $\Delta l = 0$ for an allowed decay, allowed Fermi decays require that the change in nuclear spin, ΔJ , between the parent and daughter nucleus be zero. For allowed Gamow-Teller decay, $\Delta J = 0, 1$ are possible. Note $\Delta J = 0$ is allowed for both Fermi and Gamow-Teller decays, and most decays have mixed Fermi and Gamow-Teller character. However, if the final and initial states both have a nuclear spin of 0, only Fermi decay is possible. These special decays are called “superallowed” and have a high probability of occurring. The change in parity, $\Delta\pi$, between the initial and final state in β decay is $\Delta\pi = (-1)^{\Delta l}$. Thus, there is no change in parity in allowed decay. The β -decay selection rules are summarized in Table 2.1.

β -decay branching ratios can be used to compare decays to different states in the daughter nucleus and serve as a guide for deducing if decays to particular states are allowed. The

partial decay constant, λ_f , to final state f is determined by

$$\lambda_f = \lambda BR_f \quad (2.7)$$

where BR_f is the branching ratio to state f . The decay constant can be understood as the sum of the decay constants for the decays to all possible final states and can be written

$$\lambda = \sum_f \lambda_f. \quad (2.8)$$

The partial half-life, $T_{1/2}^{partial,f}$, for the decay to state f is similarly defined as

$$T_{1/2}^{partial,f} = \frac{\ln 2}{\lambda_f}. \quad (2.9)$$

Expressing the partial half-life in units of seconds, the comparative half-life, ft , can be computed from the partial half-life. The Fermi integral, f , is a constant for a given β decay and accounts for the dependence of the decay rate on the Coulomb interaction, the atomic number of the daughter nucleus, and the maximum β -decay energy, E_{max} . Tabulations of the Fermi integral exist [73]. A useful empirical approximation for β^- decay is

$$\log f_{\beta^-} = 4.0 \log E_{max} + 0.78 + 0.02Z - 0.005(Z - 1) \log E_{max} \quad (2.10)$$

[74]. The comparative half-life removes the energy dependence of the decay rate for the decay of the parent to the daughter and is used as a guide for identifying the degree to which a particular decay is allowed or forbidden (see Table 2.1). ft ranges over many orders of magnitude, so it is commonly reported as $\log ft$.

2.2 γ -ray decay

β decay often leaves the daughter nucleus in an excited state, which then decays by emitting electromagnetic radiation of which γ rays predominate. This process is known as β -delayed γ -ray decay. γ -ray transitions connect initial and final states in a single nucleus, and the γ ray carries an integer number of angular momentum units, which is the multipolarity, λ , of the transition. The multipolarity can range from

$$|(J_i - J_f)| \leq \lambda \leq (J_i + J_f) \quad (2.11)$$

where J_i and J_f are the nuclear spins of the initial and final states, respectively. γ rays must carry at least one unit of angular momentum, so $\lambda = 0$ γ -ray transitions do not occur. The emission of the γ ray is associated with the change in the overall distribution of protons and neutrons in the nucleus. A shift in the charge distribution gives rise to an electric field and a shift in the current distribution gives rise to a magnetic field. The parity of the γ ray is determined by the specific type of transition that occurs, and the change in parity, $\Delta\pi$, for electric and magnetic transitions can be expressed as

$$\Delta\pi(E\lambda) = (-1)^\lambda \quad (2.12)$$

$$\Delta\pi(M\lambda) = (-1)^{\lambda+1} . \quad (2.13)$$

The four lowest multipolarity γ -ray transitions are listed in Table 2.2.

Table 2.2: Selection rules and multiplicities for the lowest multipolarity γ -ray transitions, adapted from Ref. [1].

Name	Radiation Type	λ	$\Delta\pi$
Electric dipole	$E1$	1	Yes
Magnetic dipole	$M1$	1	No
Electric quadrupole	$E2$	2	No
Magnetic quadrupole	$M2$	2	Yes
Electric octupole	$E3$	3	Yes
Magnetic octupole	$M3$	3	No
Electric hexadecapole	$E4$	4	No
Magnetic hexadecapole	$M4$	4	Yes

The transition rate, \mathcal{W} , of a γ -ray transition is given by

$$\mathcal{W}(E\lambda) = \alpha\hbar c \frac{8\pi(\lambda+1)}{\lambda[(2\lambda+1)!!]^2} \frac{1}{\hbar} \left(\frac{E_\gamma}{\hbar c}\right)^{2\lambda+1} B(E\lambda) \quad (2.14)$$

$$\mathcal{W}(M\lambda) = \alpha\hbar c \left(\frac{\hbar c}{2m_p c^2}\right)^2 \frac{8\pi(\lambda+1)}{\lambda[(2\lambda+1)!!]^2} \frac{1}{\hbar} \left(\frac{E_\gamma}{\hbar c}\right)^{2\lambda+1} B(M\lambda) \quad (2.15)$$

[75] where α is the fine structure constant, \hbar is Plank's constant divided by 2π , c is the speed of light, m_p is the mass of the proton, E_γ is the energy of the transition, and \mathcal{W} has dimensions of $\frac{1}{\text{time}}$. $B(E\lambda)$ and $B(M\lambda)$ are the reduced electric and magnetic transition probabilities, respectively, which contain the information about the wave functions of the initial and final states. Expressions for the reduced transition probabilities are useful for predicting the rates of electromagnetic transitions. However, $B(E\lambda)$ and $B(M\lambda)$ have strong nuclear-model dependences. Within the single-particle limit, which assumes the γ -ray decay results from the transition of a single nucleon, $B(E\lambda)$ and $B(M\lambda)$ are expressed as

$$B_W(E\lambda) = \frac{1.2^{2\lambda}}{4\pi} \left[\frac{3}{(\lambda+3)}\right]^2 A^{2\lambda/3} e^2 (\text{fm})^{2\lambda} \quad (2.16)$$

Table 2.3: Electromagnetic transition rates assuming a single-particle transition from an initial state to a final state, adapted from Ref. [1]. λ is the multipolarity of the transition, E_γ is the γ -ray energy in MeV, and A is the mass number of the nucleus.

λ	$E\lambda$ transition rate (s^{-1})	$M\lambda$ transition rate (s^{-1})
1	$1.03 \times 10^{14} A^{2/3} E_\gamma^3$	$3.15 \times 10^{13} E_\gamma^3$
2	$7.28 \times 10^7 A^{4/3} E_\gamma^5$	$2.24 \times 10^7 A^{2/3} E_\gamma^5$
3	$3.39 \times 10^1 A^2 E_\gamma^7$	$1.04 \times 10^1 A^{4/3} E_\gamma^7$
4	$1.07 \times 10^{-5} A^{8/3} E_\gamma^9$	$3.27 \times 10^{-6} A^2 E_\gamma^9$

$$B_W(M\lambda) = \frac{10}{\pi} (1.2)^{(2\lambda-2)} \left[\frac{3}{(\lambda+3)} \right]^2 A^{(2\lambda-2)/3} \left(\frac{\hbar}{2m_p c} \right)^2 e^2 (\text{fm})^{2\lambda-2}. \quad (2.17)$$

[75]. The values calculated by these two equations are referred to as Weisskopf single-particle estimates for the reduced transition probability. The transition rates obtained when using Weisskopf estimates for the reduced transition probabilities are shown in Table 2.3 for multipolarities from one to four. Transition rate decreases as multipolarity increases. Thus, γ -ray decay favors low multipolarities assuming a constant energy for the γ -ray transition.

2.3 Internal conversion

It is also possible for an excited nuclear state to decay by internal conversion, which competes with γ -ray decay. In internal conversion, the excited nucleus interacts electromagnetically with an atomic electron, resulting in the ejection of the electron. A vacancy is left in the orbital from which the electron was ejected, and x rays or Auger electrons are usually emitted as vacancies are filled by outer atomic electrons. The internal-conversion electron is monoenergetic and its energy, E_{IC} , is given by

$$E_{IC} = (E_i - E_f) - E_{BE} \quad (2.18)$$

where E_i and E_f are the energies of the initial and final states, respectively, and E_{BE} is the electron binding energy.

The likelihood that a state decays by internal conversion is commonly characterized by the internal conversion coefficient, α , which is defined as

$$\alpha = \frac{\text{number of internal-conversion decays}}{\text{number of } \gamma\text{-ray decays}} = \frac{\lambda_{IC}}{\lambda_\gamma} \quad (2.19)$$

where λ_{IC} and λ_γ are the partial decay constants for internal-conversion and γ -ray decay, respectively. It is possible for an electron to be ejected from the K, L, M... electron shells.

Thus, the total internal conversion coefficient, α_{total} , is

$$\alpha_{\text{total}} = \alpha_K + \alpha_L + \alpha_M + \dots \quad (2.20)$$

However, since K-shell electrons have the highest probability of being found at the nucleus, a K-shell electron is typically ejected, and α_{total} is dominated by α_K . Theoretically calculated internal conversion coefficients have been tabulated for varying atomic numbers, multipolarities, and transition energies [2]. An approximate value of α for a transition that may occur by either γ -ray decay or internal conversion can be obtained from

$$\alpha(E\lambda) = \frac{Z^3}{n^3} \left(\frac{\lambda}{\lambda + 1} \right) \left(\frac{e^2}{4\pi\epsilon_0\hbar c} \right)^4 \left(\frac{2m_e c^2}{E} \right)^{\lambda+5/2} \quad (2.21)$$

$$\alpha(M\lambda) = \frac{Z^3}{n^3} \left(\frac{e^2}{4\pi\epsilon_0\hbar c} \right)^4 \left(\frac{2m_e c^2}{E} \right)^{\lambda+3/2} \quad (2.22)$$

[1] where λ is the multipolarity, n is the principal quantum number of the bound electron that is ejected, m_e is the mass of the electron, and E is the energy of the transition. Inter-

nal conversion is most important in heavy nuclei and for low-energy transitions with high multipolarities.

2.4 Internal pair production

Internal pair production is another electromagnetic-decay process by which an excited nuclear state can decay. Rather than emitting a γ ray or ejecting an internal-conversion electron, an electron-positron pair is created in pair production. In order to produce the electron-positron pair, a transition energy of at least 1.022 MeV is required. The excess transition energy above 1.022 MeV goes into kinetic energy that is shared by the positron and electron. Within a detector medium, the positron will annihilate with an electron, and two 511-keV photons are created as secondary radiations. The probability of internal pair production is usually several orders of magnitude lower than the probability of γ -ray decay. Therefore, internal pair production is generally only important when γ -ray decay does not occur, for instance in the decay of an excited 0^+ state to a lower energy 0^+ state.

2.5 $E0$ transitions

For electromagnetic transitions that connect two states with identical spins and parities, electric monopole ($E0$) transitions can occur. $E0$ transitions between two 0^+ states can only proceed via internal conversion or internal pair production. There is no competition with γ -ray decay since γ rays must carry at least one unit of angular momentum. While higher multipolarity γ -ray decay typically dominates over $E0$ decay when the initial and final states have equal nuclear spins that are greater than zero, only $E0$ transitions are possible between two 0^+ states.

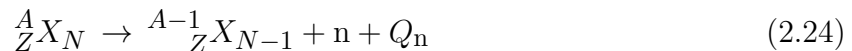
The probability of an $E0$ transition, $\lambda(E0)$, can be expressed as

$$\lambda(E0) = \lambda_{IC}(E0) + \lambda_{\pi}(E0) = \frac{\ln 2}{T_{1/2}(E0)} = \rho^2(E0) \times [\Omega_{IC}(E0) + \Omega_{\pi}(E0)] \quad (2.23)$$

where $\lambda_{IC}(E0)$ and $\lambda_{\pi}(E0)$ are the partial transition probabilities for internal conversion and internal pair production, respectively, and $T_{1/2}(E0)$ is the partial half-life for the decay of the state by the $E0$ transition. $\Omega_{IC}(E0)$ and $\Omega_{\pi}(E0)$ are the “electronic factors” [76] for internal conversion and pair production, respectively, expressed in units of s^{-1} . The electronic factors depend on the transition energy and atomic number, but can be approximated well independently of nuclear properties, and tabulations of the electronic factors exist [2]. $\rho^2(E0)$ is the dimensionless quantity called the electric monopole transition strength, which contains all the information about the final and initial states. Because the value of $\rho^2(E0)$ is often between 10^{-3} and 10^{-1} , it is commonly reported as $10^3 \rho^2(E0)$. Databases of $\rho^2(E0)$ values between 0^+ states across the chart of the nuclides are available [77].

2.6 β -delayed neutron decay

For neutron-rich nuclei, the probability for β -delayed neutron decay exists. As the name suggests, neutron decay results in the spontaneous emission of a neutron, and the process can be written



where Q_n represents the difference in mass-energy between the final and initial states. In β decay when there is a large difference in mass-energy between the ground states of the parent and daughter nuclei, the β decay can populate excited states in the daughter nucleus

with energies higher than the neutron separation energy. When such an excited state above the separation energy is populated, the state decays rapidly by emitting a neutron, and the process is known as β -delayed neutron decay. In β -delayed neutron decay, excited states can be populated in the $^{A-1}Y_{N-1}$ daughter, which can then undergo electromagnetic decay.

Chapter 3

Experimental Description

In this chapter, the two experiments performed at the National Superconducting Cyclotron Laboratory (NSCL) are described. The first is experiment e11503, for which the primary interest was studying the decay of the first excited state in ^{68}Ni following its population in the β decay of ^{68}Co . Details about experiment e11503, particularly the results for the decay of the first excited state in ^{68}Ni , have been published in Ref. [78]. The other experiment described in this chapter is experiment e08020. The main focus of experiment e08020 was the β decay of neutron-rich V isotopes to Cr isotopes. Isomeric decays of V and Mn isotopes were also studied. Experiment e08020 has led to publications focussing on the β decay of $^{61,63}\text{V}$ to $^{61,63}\text{Cr}$ [79], the β and isomeric γ -ray decay of ^{64}V [80], and the isomeric γ -ray decay of $^{64,66}\text{Mn}$ [81]. The rest of this chapter is organized as follows. First, an overview of the radionuclide-production and separation methods used is given. Then, general explanations of particle identification and the detection techniques common to NSCL experiments e11503 and e08020 are provided. More detailed descriptions of each experiment follow, which include information about isotope production/delivery, detector arrangements, detector calibrations, triggering conditions, and the correlation of β decays with particular ions.

3.1 Isotope production, separation, identification, and detection

The vast majority of radioisotopes are not abundant on Earth. Therefore in order to study their properties, radioactive nuclei are produced artificially. NSCL uses the method of projectile fragmentation to produce radioisotopes. In projectile fragmentation, a stable primary beam is accelerated to an energy of order 100 MeV/nucleon and interacts with a thin, stationary production target, typically Be. The process starts at NSCL with a stable isotope being ionized in an electron cyclotron resonance ion source and accelerated by the K500 and K1200 cyclotrons, which are schematically shown in Fig. 3.1. Fragmentation removes nucleons from the projectile, producing a wide range of stable and radioactive products. The momentum transfer is relatively small and the secondary reaction products emerge from the target forward focussed with energies near the energy of the primary beam [1]. A fragment separator is then used to select particular secondary beam products for study.

Fragment separation at NSCL is performed by the A1900 [82]. The A1900 separates ions based on magnetic rigidity, $B\rho$, which is equal to momentum, p , divided by atomic charge, q . At the first stage of the separator, a magnetic rigidity selection is made, which, since the incoming ions have nearly the same velocity, selects ions with approximately the same mass to charge ratio. At image 2, the intermediate dispersive image of the A1900, the ions pass through a wedge shaped energy degrader. Energy loss in the wedge is proportional to the square of the atomic number of the ion, Z^2 , so ions of different Z experience different energy losses and further separation is achieved by a second $B\rho$ selection after the wedge, with the best separation occurring when all ions are fully stripped of electrons. Slits at each of the three intermediate images of the A1900 control the momentum acceptance, $\Delta p/p$, which has

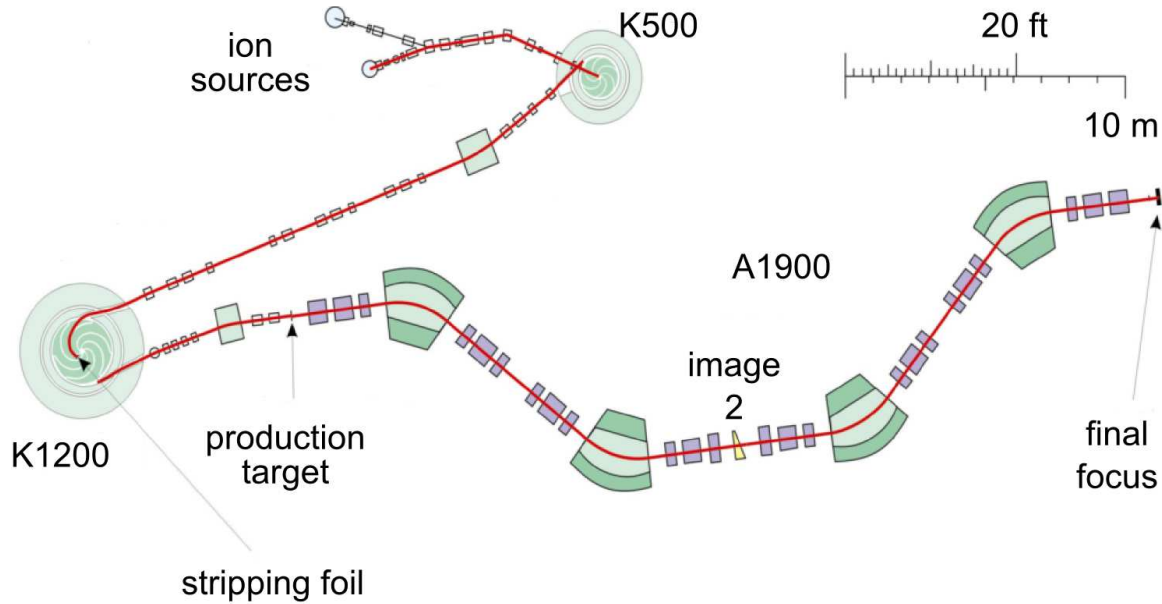


Figure 3.1: Schematic layout of Coupled Cyclotron Facility at NSCL showing the arrangement of the K500 cyclotron, K1200 cyclotron, and A1900 fragment separator.

a maximum value of 5%.

If the maximum momentum acceptance of the A1900 is used, ions entering the A1900 that have the same Z and N but different momenta will take different paths through the separator and travel different distances, resulting in different times of flight (TOF) through the A1900. TOF is commonly used for particle identification at NSCL, since, for a constant fragment momentum and path length, TOF is proportional to mass. If a large A1900 momentum acceptance is selected, the TOF resolution is typically not adequate to distinguish between different isotopes. However, corrections can be made to improve particle identification from a knowledge of ion position at a dispersive image of the A1900. The position is commonly measured with a thin plastic scintillator placed at image 2. Position is determined for each ion as it passes through the scintillator based on the time difference between the arrival of the scintillation photons at two different photomultiplier tubes located at opposite ends of the scintillator. TOF can be corrected based on the determined position to account for the

different flight paths taken through the separator.

In addition to TOF, the energy loss of an ion as it passes through a detector is often measured for particle identification at NSCL, since the energy loss is proportional to the atomic number of the ion. Combining the energy-loss measurement, which is sensitive to Z , and the TOF measurement, which is sensitive to A , both elemental and isotopic identification can be obtained.

Although there were differences between the particular detectors and the physical arrangements of the detectors in experiments e11503 and e08020, the same general detection techniques were used. In each experiment, the secondary ions transported through the A1900 were delivered to the experimental end station where they passed through multiple Si PIN detectors. Particle identification was performed on an event-by-event basis using energy-loss and TOF methods. The energy loss was measured in one of the PIN detectors. The PIN signal also served as the start for the TOF measurement. The stop signal for TOF was obtained from one of two sources: either the cyclotron RF signal or the plastic scintillator at image 2 of the A1900. After passing through the PIN detectors, the secondary ions were stopped in a semiconductor detector (either Si or Ge), which detected both the implantation of the secondary ions and their subsequent β decays. Further, an array of high-purity Ge detectors surrounded the β -decay detector for β -delayed and isomeric γ -ray detection.

3.2 NSCL Digital Data Acquisition System (DDAS)

In both experiments, all detector signals were read out using the NSCL Digital Data Acquisition System (DDAS) [83, 84]. DDAS digitized signals at a rate of 100 megasamples/s via 12-bit Flash Analog to Digital Converters. The digitized signals, or traces, can be recorded,

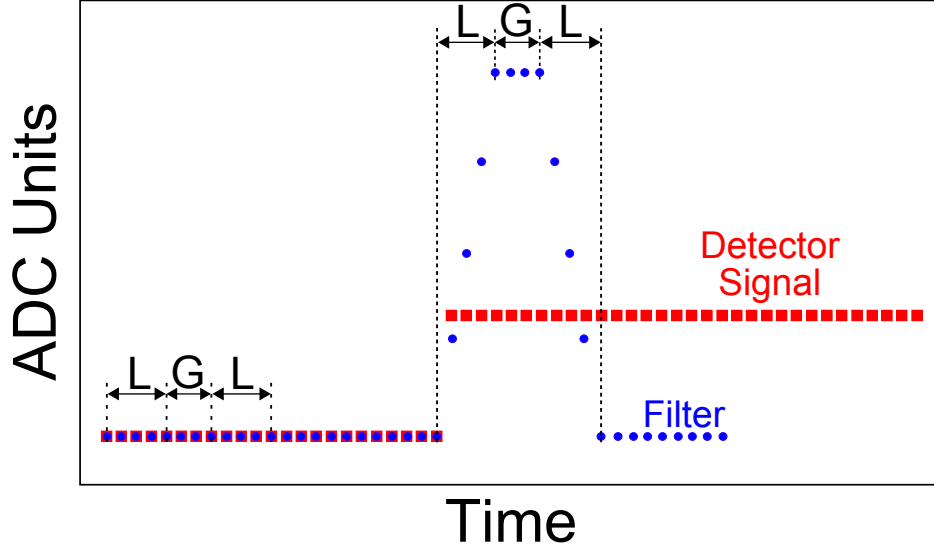


Figure 3.2: Schematic representation of the trapezoidal trigger filtering performed by DDAS on a detector signal. See text for details.

enabling offline pulse-shape analysis of the experimental data. The application of a pulse-shape processing algorithm on recorded traces from experiment e11503 is described in Section 3.3.8.

DDAS utilizes a trapezoidal filter to perform triggering. The general application of the DDAS trapezoidal trigger filter on a step pulse is represented schematically in Fig. 3.2. From the value of the digitized detector signal, S , the trigger-filter value, F , at time, t , is calculated by

$$F[t] = \sum_{i=t-L+1}^t S[i] - \sum_{j=t-2L-G+1}^{t-L-G} S[j] \quad (3.1)$$

where L is the filter length and G is the filter gap. In other words, using Fig. 3.2 as a reference, the filter is calculated along the digitization points by subtracting the sum of the trace values within the first range spanned by L (before the gap) from the sum of the trace values within the second range spanned by L (after the gap).

The trigger filter is also referred to as the “fast” filter. Accordingly, the fast filter uses

relatively small values of L and G to quickly identify the rising edge of the detector signal. A trigger occurs when the value of the fast filter becomes larger than the specified threshold, and the digitization point at which this occurs is the triggering time. DDAS also uses a trapezoidal filter to determine energy. The energy filter uses larger values of L and G than the trigger filter. The trigger filter can be susceptible to noise, especially if the triggering threshold is set too low, but using large values of L and G for the energy filter has the effect of averaging out noise. An additional feature of the energy filter is that it accounts for the preamplifier decay constant [85], which needs to be optimized for each detector channel. The energy is determined from the value of the energy filter at a known distance from the triggering point.

Although DDAS only digitizes every 10 ns, timing precision below 10 ns is obtained from an internal Constant Fraction Discrimination (CFD) algorithm. The CFD signal is computed from the fast filter signal with the equation

$$CFD[t + D] = F[t + D] - \frac{F[t]}{2^{(W+1)}} \quad (3.2)$$

where $CFD[t + D]$ is the CFD signal, D is the CFD delay length, and W is a scaling factor. Linear interpolation is used to determine the zero-crossing location when the CFD signal changes from a positive to a negative value. The time of the signal is then determined from this zero-crossing location.

In both experiments e11503 and e08020, all signals were given a time stamp according to the time determined by DDAS. Physics events comprised of signals from multiple detectors were then constructed in software based on the time stamps. All signals occurring within a 10- μ s time period, referred to as the “event window,” were grouped together as an event.

3.3 NSCL experiment e11503

3.3.1 Isotope production and delivery

The fragmentation of a 130 MeV/nucleon ^{76}Ge beam in a 423-mg/cm 2 ^9Be target was used to produce the secondary radioactive ion beam in experiment e11503. The secondary beam passed through a 20-mg/cm 2 kapton wedge and the 250- μm thick position-sensitive scintillator detector that were placed at the intermediate dispersive image of the A1900. A small momentum acceptance of 0.5% was used for the A1900. The ions of interest were delivered to the experimental station, passed through two Si PIN detectors with respective thicknesses of 303 and 488 μm , and then were deposited into a planar Ge double-sided strip detector (GeDSSD) [86]. The GeDSSD is electrically segmented, with 16 5-mm wide strips on the front of the detector and 16 perpendicular 5-mm wide strips on the back of the detector. The crystal of the GeDSSD is self-contained within a cryostat, which has a 1-mm thick aluminum entrance window. There is also a 0.143-mm thick Al infrared-radiation shield between the cryostat and the Ge crystal. The GeDSSD was placed a short distance downstream from a thin kapton exit window at the end of the beam line. Thus, the ions

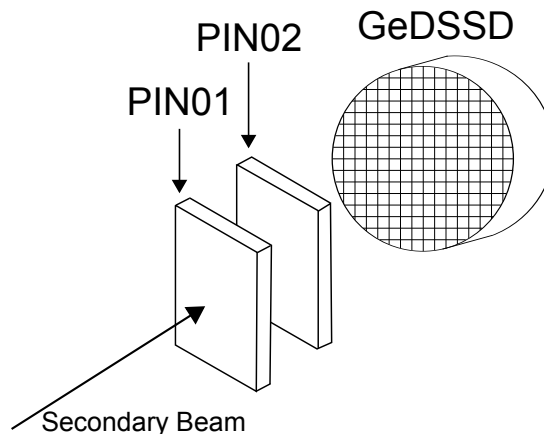


Figure 3.3: Schematic arrangement of the PIN detectors and GeDSSD in experiment e11503.

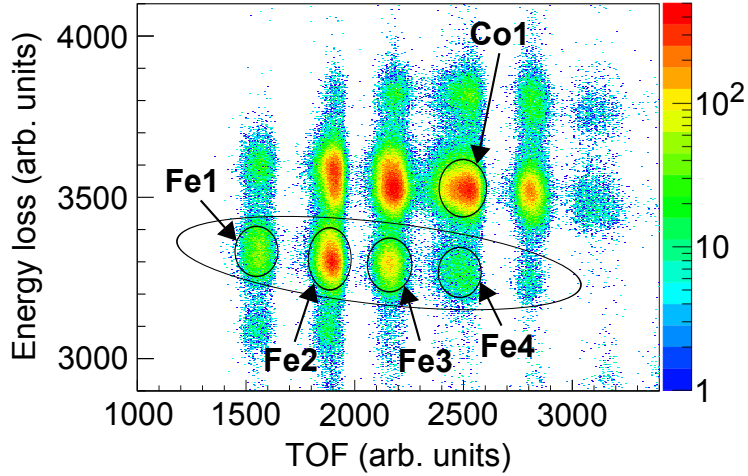


Figure 3.4: Particle-identification plot of the ions delivered to the experimental station in experiment e11503. Selected ions are labelled by their chemical symbol followed by an arbitrary number distinguishing a particular isotope from the other isotopic ions that were delivered to the GeDSSD.

passed through the kapton window, about 2 cm of air, the entrance window of the cryostat, and the Al thermal shield before stopping approximately 1-mm deep in the GeDSSD crystal.

The schematic arrangement of the PINs and GeDSSD in experiment e11503 is shown in Fig. 3.3. Energy loss in PIN01 and TOF between the cyclotron RF signal and PIN01 were used for the particle-identification plot shown in Fig. 3.4. The primary ion of interest was ^{68}Co , which β decays to ^{68}Ni .

Despite many attempts, a complete understanding of the particle identification in experiment e11503 was not obtained. The circled isotopic chain in Fig. 3.4, which includes the isotopes labelled Fe1, Fe2, Fe3, and Fe4, corresponds to the Fe isotopes. This identification was based on the correlation of the 367-keV γ ray from the decay of the 62- μs half-life isomeric state in ^{67}Fe [13, 87] with the fragments. Contrary to what would be expected, the 367-keV γ ray was correlated with isotopes Fe1, Fe2, Fe3, and Fe4, rather than just a single isotope, and this correlation was observed regardless of if the γ rays were restricted to being detected during the 10- μs event window or if the γ rays were allowed to be detected up to

hundreds of microseconds after the ion implantation in the GeDSSD. The intensity of the 367-keV γ ray normalized to the number of implanted ions with gates placed on isotopes Fe1-4 in Fig. 3.4 is shown in Table 3.1 for γ rays detected within 500 μ s of the implantation of the ion. The 367-keV γ ray, however, was not correlated with any ions outside of the Fe isotopic chain. For instance, no correlation was observed when a gate was placed on Co1 in Fig. 3.4. Thus, the correlation of the 367-keV γ -ray with ion implantations was not randomly distributed over all ions. There also did not seem to be a random TOF distribution given the apparent isotopic separation in the particle identification plot. The same results are obtained if TOF is measured between PIN01 and the scintillator at image 2 of the A1900 instead of between PIN01 and the cyclotron RF signal. Fe2 was most strongly associated with the 367-keV γ ray, so it is proposed to be ^{67}Fe , but the association with the other Fe isotopes was significant, so the identification is tentative. It was expected that essentially all of the ions delivered to the GeDSSD were fully stripped of electrons. LISE++ calculations [88] predict that the delivery of the fully stripped ions was approximately three orders of magnitude greater than the delivery of ions with a single electron. Hence, contamination from multiple charge states of the different ions was not expected to be a problem. Charge-state contamination was not observed in experiment e08020 (see Section 3.4.1), which used the same primary beam and target material as experiment e11503, and the secondary beam delivered to the experimental end station was comprised of ions with similar masses. The root cause of the particle-identification issue in experiment e11503 was not discovered. The numbers of the tentatively identified isotopes that were delivered to the GeDSSD are shown in Table 3.2.

Even if an ideal particle identification had been obtained, its utility in studying the decay of the first excited state in ^{68}Ni following ^{68}Co β decay would have been very limited

Table 3.1: Intensity of the 367-keV γ -ray from the decay of ^{67m}Fe reported as the efficiency-corrected number of γ -ray decays divided by the total number of implanted ions when gates are placed on isotopes Fe1, Fe2, Fe3, and Fe4 in Fig. 3.4. γ rays detected up to 500 μs after an ion implantation in the GeDSSD were correlated with the ion.

Isotope gate	Intensity of 367-keV γ -ray (%)
Fe1	15.1 ± 1.5
Fe2	25.1 ± 1.3
Fe3	22.3 ± 2.1
Fe4	12.7 ± 3.3

Table 3.2: Total numbers of ions for each isotope that was delivered to the experimental station in experiment e11503.

Isotope	Number of ions	Isotope	Number of ions	Isotope	Number of ions
^{64}Mn	9040	^{68}Fe	48849	^{71}Co	21057
^{65}Mn	4875	^{66}Co	6576	^{69}Ni	2943
^{64}Fe	3180	^{67}Co	95528	^{70}Ni	17388
^{65}Fe	21465	^{68}Co	303421	^{71}Ni	27786
^{66}Fe	80121	^{69}Co	334051	^{72}Ni	12690
^{67}Fe	202726	^{70}Co	218324	^{73}Ni	2303

in this experiment. The ions stopped in the GeDSSD in e11503 were distributed across approximately 25 pixels. The implantation profile is shown in Fig. 3.5. The total rate at which the ions were delivered to the GeDSSD was about 50Hz, or roughly 2 Hz pixel⁻¹, though the implant distribution was not entirely uniform. Since the average time between successive ion implantations in a pixel of the GeDSSD, about 500 ms, was short compared to the 1.6-s half-life of ^{68}Co [21], each ^{68}Co β decay could not be reliably correlated with the ion-implantation event when the ^{68}Co ion was internally deposited in the GeDSSD. Thus, the implant-decay correlations (described further in Section 3.3.4) for ^{68}Co were not very meaningful. Identifying the decay of the first excited state in ^{68}Ni as belonging to ^{68}Ni had to rely on pulse-shape processing.

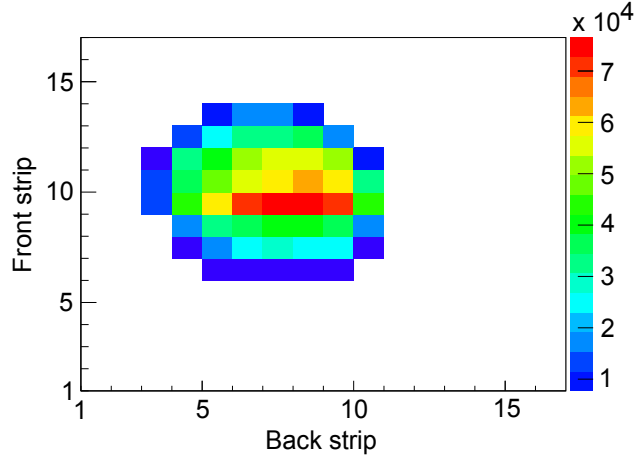


Figure 3.5: Profile of ion implantations into the GeDSSD in experiment e11503.

3.3.2 Planar Germanium Double-sided Strip Detector (GeDSSD)

As previously mentioned, the ions delivered to the experimental station were stopped in the 1-cm thick GeDSSD, which is described in detail in Ref. [86]. In order to measure both high-energy deposition (the stopping of an ion within the GeDSSD) and low-energy deposition (a β or γ -ray decay), each GeDSSD strip is connected to two preamplifiers. The pair of preamplifiers have different gain ranges, with the low-gain preamplifiers suitable for the range of 0 - 30 GeV (ion implantations into the detector) and the high-gain preamplifiers suitable for the range of 0 - 15 MeV (β and γ -ray decays). Due to the increased thickness of the detector and the higher atomic number of Ge relative to Si, an advantage of the GeDSSD compared to conventional Si DSSDs is an improved β -decay detection efficiency. Efficiencies of at least 55% have been demonstrated for the GeDSSD [86], while Si DSSDs usually have efficiencies around 30%.

3.3.3 GeDSSD triggering conditions

The readout of the GeDSSD was gated, requiring an energy deposition to be registered in both the front and back sides of the detector. The gate was a logical AND signal that was constructed from two logical OR signals. The first OR signal was produced when an energy above threshold was detected in any of the 16 strips on the front of the GeDSSD, and the second OR signal was similarly produced when an energy above threshold was detected in a back strip. Separate gates were used for ion implantations and decays. Thus, a front-back coincidence of the low-gain preamplifier signals was required for reading out signals due to ion implantations in the GeDSSD, while a front-back coincidence of the high-gain preamplifier signals was required for reading out signals due to decays. This triggering scheme reduces the contribution of readout signals that are due to noise. Signal traces were recorded for all the front and back strips that had energy depositions above threshold. All traces had a length of $6\ \mu\text{s}$ with a delay of $3\ \mu\text{s}$. Typical thresholds for the high- and low-gain preamplifier signals were approximately 5 keV and 50 MeV, respectively. The triggering rates for the high- and low-gain preamplifiers of each strip were all below about 100 and 50 Hz, respectively.

3.3.4 Correlation

The GeDSSD was used to detect both the implantation of the radioactive ions deposited into the detector, as well as the subsequent decays of those ions. In order for a physics event to be considered an implant, a signal was required in each of the two upstream PIN detectors and a low-gain signal was required in at least one strip on both the front and the back of the GeDSSD. The location of the ion implantation was set as the pixel corresponding to the intersection of the front strip with the maximum energy deposition and the back strip with

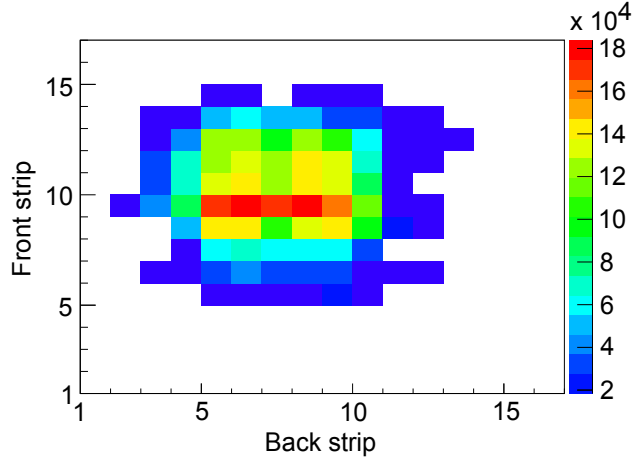


Figure 3.6: Profile of decays detected in the GeDSSD in experiment e11503.

the maximum energy deposition. The implantation profile in experiment e11503 is shown in Fig. 3.5. A decay was defined as a valid high-gain signal in a minimum of one front strip and one back strip of the GeDSSD, no signal in either PIN detector, and no low-gain signal in any front or back strips of the GeDSSD. To be considered valid, the energy of the high-gain signal in the GeDSSD had to be above a threshold set in software, which was 20 keV for a typical strip. Just like for implant events, the pixel where the decay event occurred was set as the intersection of the front strip with maximal energy deposition and the back strip with maximal energy deposition. The decay profile in the GeDSSD is shown in Fig. 3.6. As expected, the distribution of decays is similar to the distribution of ion implantations in the GeDSSD. The strip multiplicities on the front and the back of the GeDSSD are shown for both implant and decay events in Fig. 3.7.

In general, decays were correlated with ion implantations that occurred in the same pixel of the GeDSSD based on the timing information of the decay and the ion implantation. However, as noted previously, the high overall rate of ion implantations in the GeDSSD prevented contamination-free implant-decay correlations for the β -decaying isotope of interest ^{68}Co .

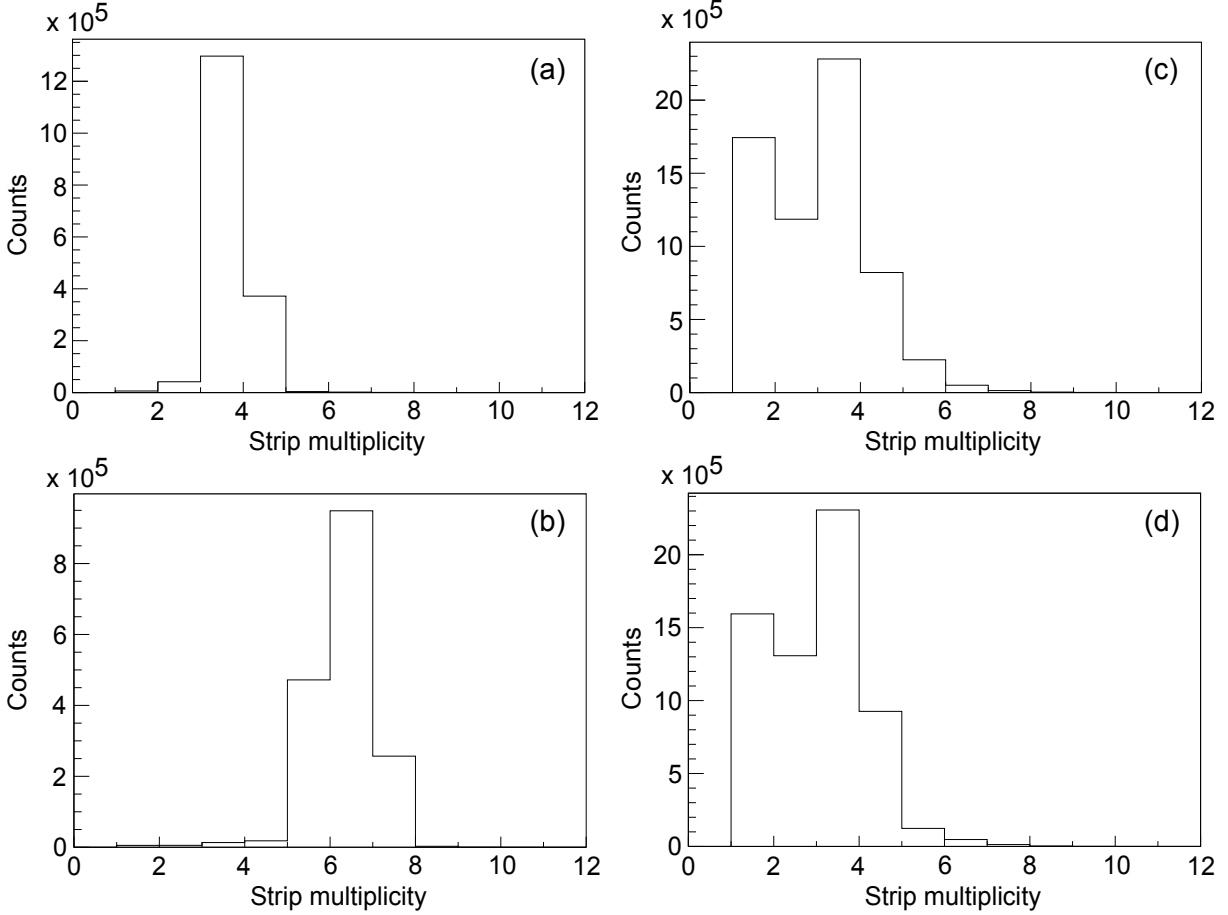


Figure 3.7: GeDSSD strip multiplicities for implant and decay events. The strip multiplicity gated on implants is shown for (a) the front strips and (b) the back strips. The strip multiplicity gated on decays is shown for (c) the front strips and (d) the back strips.

3.3.5 Segmented Germanium Array (SeGA)

The Segmented Germanium Array (SeGA) [89] surrounded the GeDSSD and was used to detect γ rays. SeGA was arranged in two rings of eight detectors each. The detector rings were placed immediately upstream and downstream of the GeDSSD, and the arrangement is shown schematically in Fig. 3.8. In comparison to the traditional beta-SeGA setup that was used in experiment e08020 and is described in Section 3.4.3, a spacer was added in experiment e11503 to allow enough room for the GeDSSD. For the traditional beta-SeGA configuration, the two rings of SeGA are equidistant from the center of the DSSD, with a

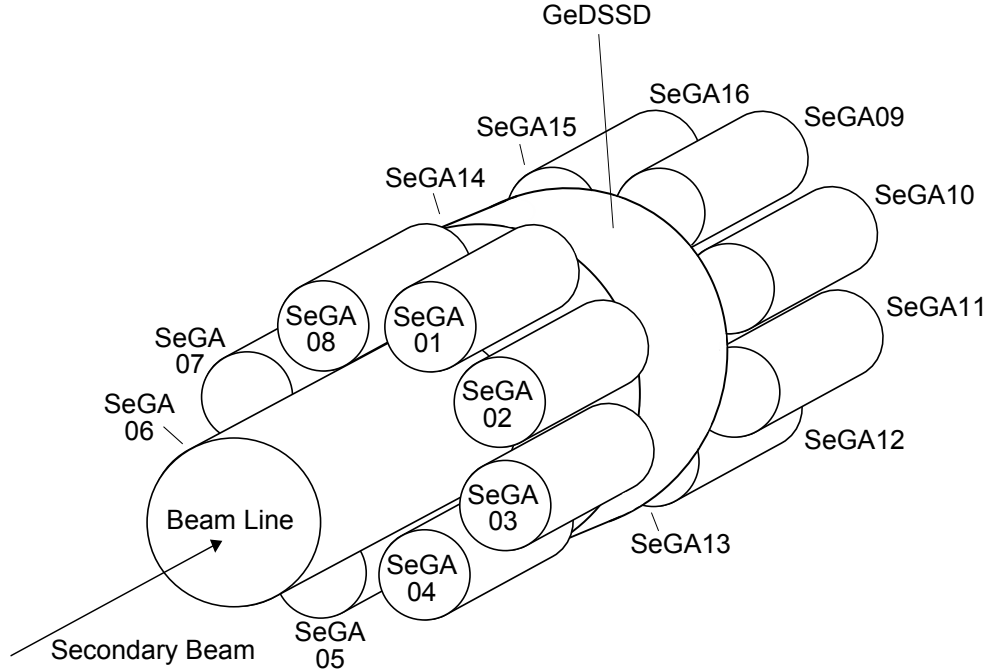


Figure 3.8: Schematic arrangement of SeGA around the GeDSSD in experiment e11503.

distance from the center to each SeGA detector of 8.6 cm. In experiment e11503, one of the rings was located farther away from the GeDSSD than the other, with distances of 13.7 and 14.7 cm from the center of the GeDSSD to the detectors in the respective rings.

3.3.6 SeGA triggering conditions

Unlike the GeDSSD, the reading out of data from SeGA was ungated. All energy depositions above threshold in SeGA were recorded. However, no signal traces were recorded for SeGA. The approximate threshold and triggering rate for each detector of SeGA was 10 keV and 150 Hz, respectively.

3.3.7 Calibrations

γ -ray energy and efficiency calibrations were performed for the GeDSSD and SeGA in experiment e11503. Since the GeDSSD crystal is self-contained within the cryostat, radioactive

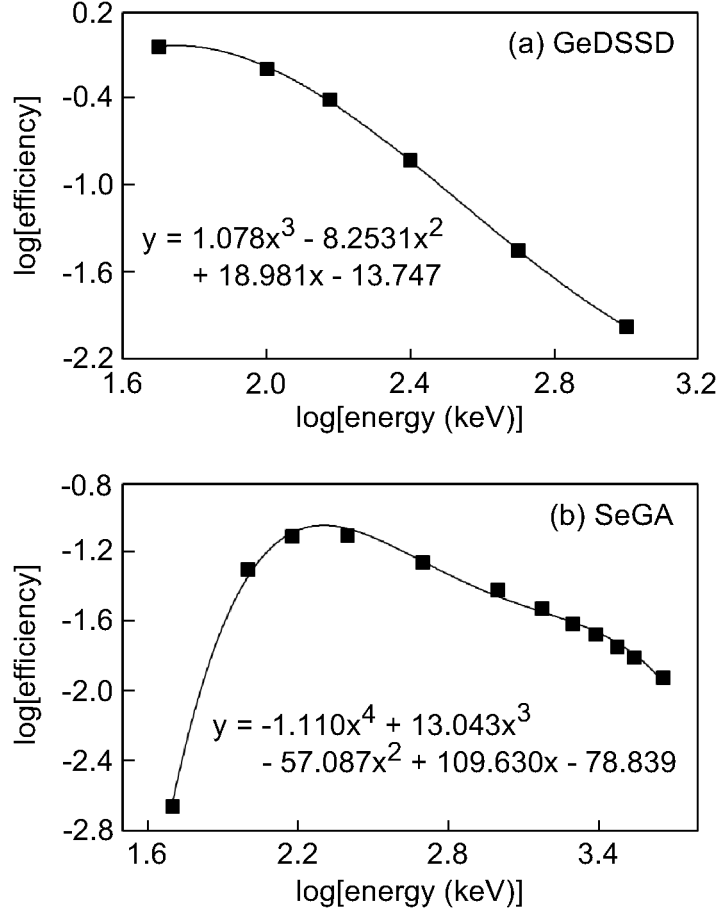


Figure 3.9: Simulated γ -ray efficiency of (a) the GeDSSD and (b) SeGA for γ rays emitted from a nucleus 1 mm deep in the GeDSSD.

sources could not be placed at the location from which γ rays were emitted in the experiment. To determine the efficiency of detecting the γ rays that were emitted from within the GeDSSD after ions had been deposited, and subsequently decayed, simulations were required. The simulations are described in Ref. [86]. To ensure the simulations were valid, a radioactive source was placed at various locations external to the GeDSSD and it was checked that the measured γ -ray efficiency matched the simulated efficiency. The simulated γ -ray efficiencies of the GeDSSD and SeGA are shown in Figs. 3.9(a) and (b), respectively, on a log-log scale for γ rays emitted from a nucleus deposited 1 mm deep into the GeDSSD. The GeDSSD and SeGA efficiency curves were fit to fourth- and fifth-order polynomials,

respectively, and results of the fits are shown in Figs. 3.9(a) and (b).

The energy calibrations for the GeDSSD strips were carried out after the experiment. The detector suffered radiation damage when it was bombarded by the ion beam [86], so a calibration performed after the experiment was more appropriate for the damaged strips. However, only the signals from the front strips were significantly deteriorated. When a radioactive decay deposits energy in the GeDSSD, the generated holes travel toward the front of the detector, while electrons migrate to the back. Radiation damage causes charge-carrier trapping, resulting in incomplete charge collection. For the GeDSSD, radiation damage preferentially leads to hole trapping [90], so the front-strip signals were the most strongly influenced by the bombardment with the ion beam. Conversely, the back strips were largely unaffected by the bombardment since radiation-damage caused trapping of the electrons traveling to the back of the detector is less prevalent, and the back strips had the same energy resolution prior to and following the experiment. Therefore, more precise energy measurements could be made using the back strips than the front strips.

Linear energy calibrations were performed for the front and back strips of the GeDSSD using two different γ -ray sources. The two sources were a ^{137}Cs source and a NIST Standard Reference Material (SRM) source containing ^{125}Sb , ^{154}Eu , and ^{155}Eu (NIST SRM 4275C-69, NSCL source Z7309). Due to the low efficiency of the GeDSSD for high-energy γ rays and the inability to place a radioactive source very near the GeDSSD crystal inside of its cryostat, only the 43- and 123-keV γ rays from the SRM source and the 662-keV γ ray from the ^{137}Cs source were used for the calibration. Uncalibrated energies for each strip were obtained from pulse-shape analysis based on the area underneath the recorded decay signals. The signal traces were recorded with a trace length of $6\ \mu\text{s}$ and a delay of $3\ \mu\text{s}$. A constant baseline was determined for each signal by averaging the value of the trace at each

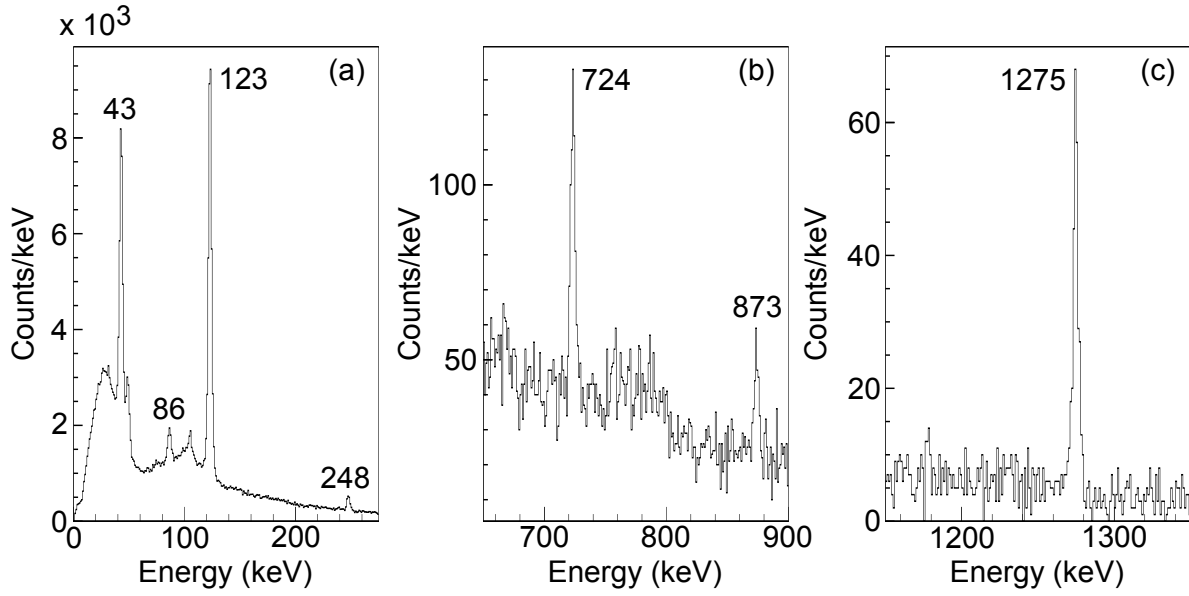


Figure 3.10: Calibrated energy spectrum of the sum of all 16 back strips of the GeDSSD for the SRM source. The spectrum is shown in the ranges of (a) 0 – 275 keV, (b) 650 – 900 keV, and (c) 1150 – 1350 keV. Peak energies in keV are labelled and were obtained based on a pulse-shape-processing method in which the area underneath the decay signals were determined.

digitization point between 1.0 and 2.5 μs . All trace values at the digitization points between 2.5 and 5.0 μs were then summed to determine the total area underneath the pulse in this region. The constant background was multiplied by the length of the summing region and subtracted from the total area underneath the pulse to determine the uncalibrated pulse area due to the radioactive decay. The centroids of the full-energy peaks of the 43-, 123-, and 662-keV γ rays were found from Gaussian fits to the peaks in the uncalibrated energy spectra. A linear energy calibration was then constructed for each strip from the three known γ -ray energies and the measured centroid positions. The calibrated energy spectrum for the sum of all 16 back strips of the GeDSSD is shown as an example in Fig. 3.10. In the energy spectra of the sum of all strips, additional full-energy peaks from the SRM source are observable at 86, 248, 724, 873, and 1275 keV. The residuals, or the difference in energy between the known γ -ray energy and the calibrated energy, are shown for the sum of all

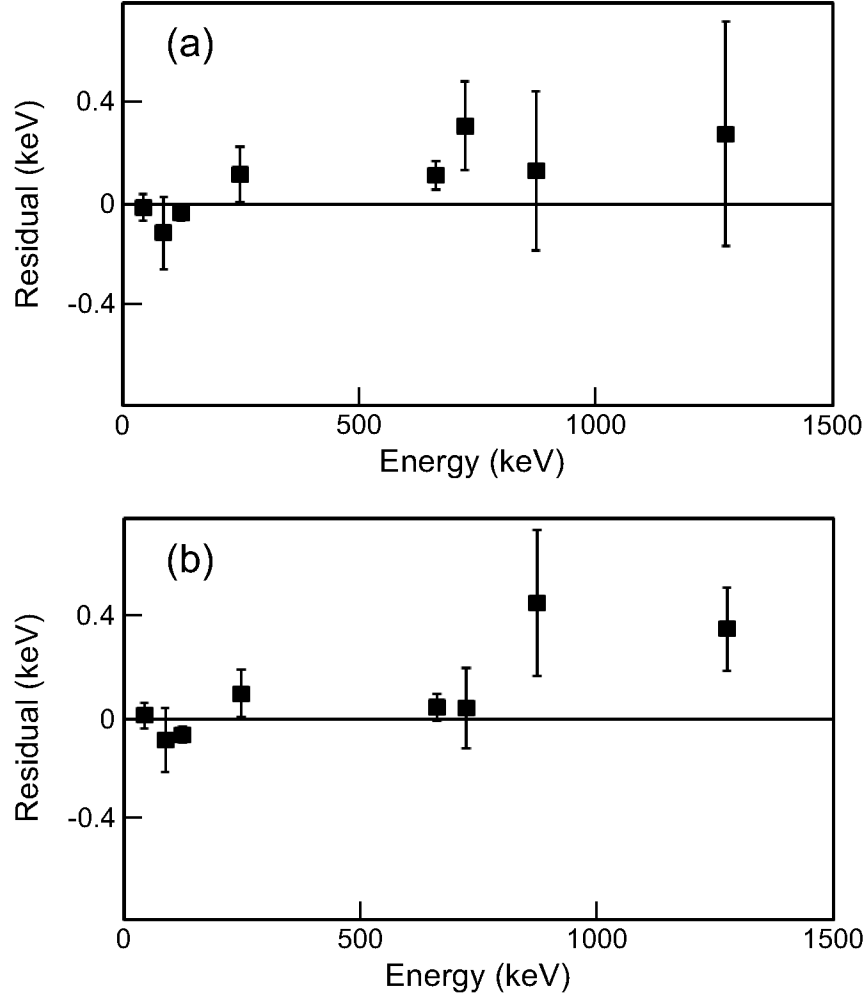


Figure 3.11: Residuals of the sum spectrum of all 16 (a) front strips and (b) back strips of the GeDSSD for the energy calibrations performed after experiment e11503.

16 front strips and the sum of all 16 back strips in Figs. 3.11(a) and (b), respectively. For both the front and back strips, the residuals slightly increase with increasing γ -ray energy, indicating systematic error in the calibration procedure. This energy calibration was only used for localizing β and electromagnetic decays to a particular pixel in the GeDSSD based on which front and back strips had the most energy deposited into them. The results for the energies of the internal-conversion and internal-pair-production decays of the first excited state in ^{68}Ni that were measured in the GeDSSD (Section 4.2) were derived from a different pulse-shape analysis technique described in Section 3.3.8.

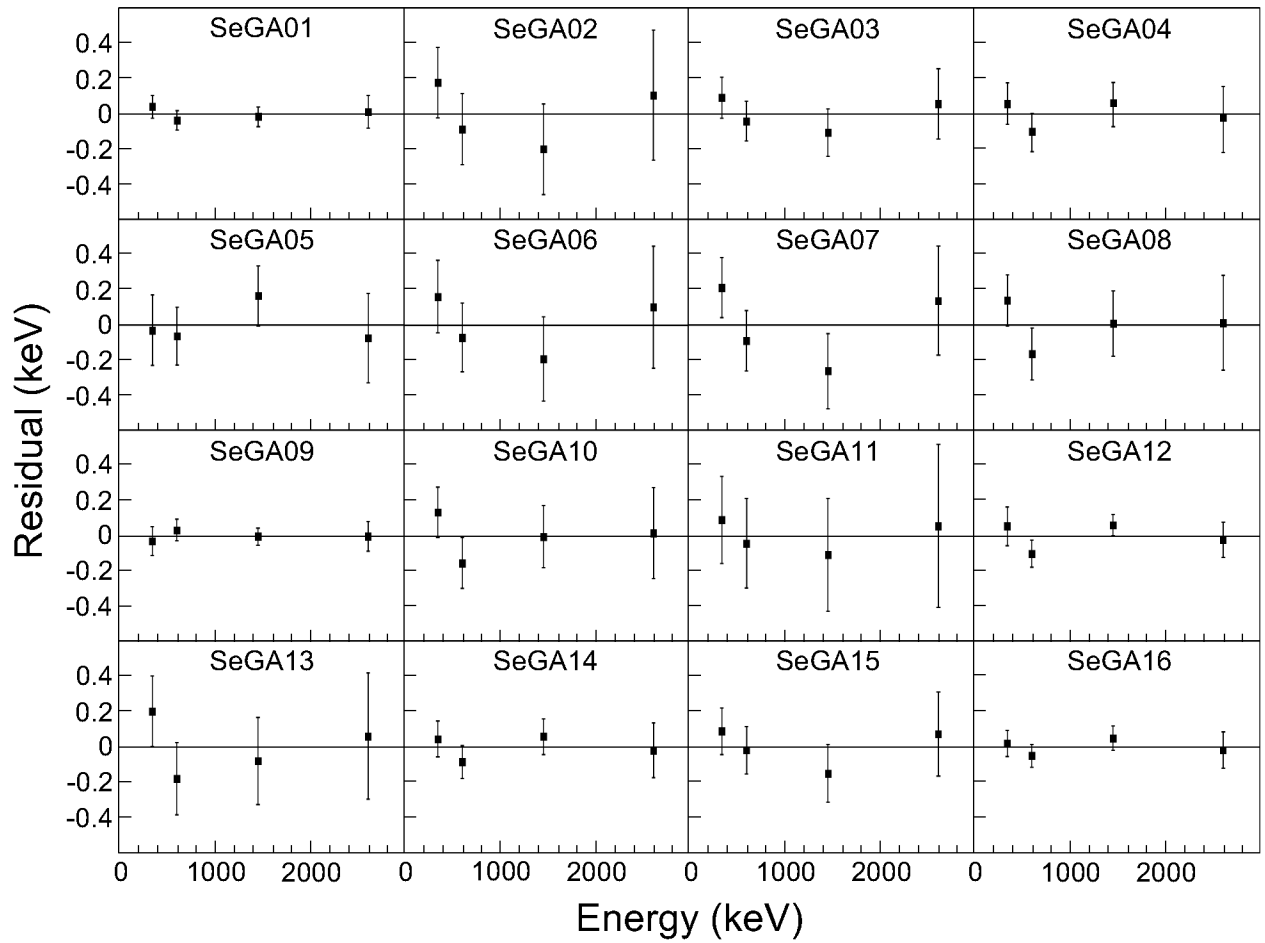


Figure 3.12: Residuals of the 16 individual SeGA detectors for a representative energy calibration performed using background γ rays from a single experimental run during experiment e11503.

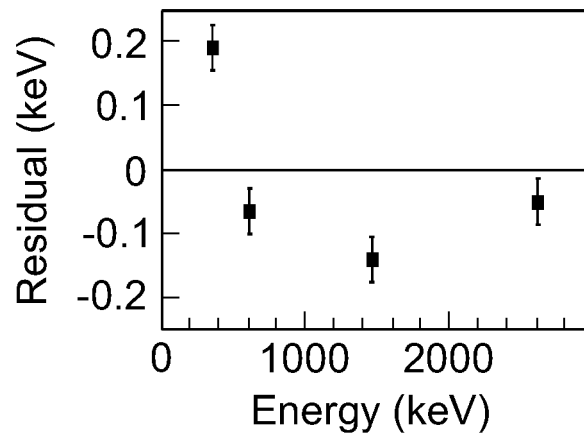


Figure 3.13: Residuals of the sum spectrum of all 16 SeGA detectors for a representative energy calibration performed using background γ rays from a single experimental run during experiment e11503.

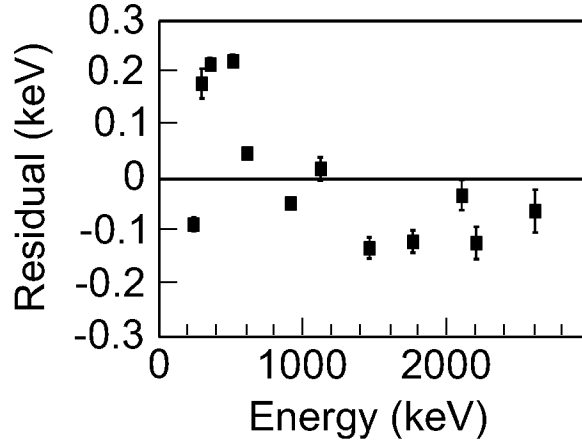


Figure 3.14: Residuals of the sum spectrum of all 16 SeGA detectors for background γ -ray lines monitored throughout the duration of experiment e11503. A new energy calibration was applied for each experimental run, with an average run length of approximately an hour.

SeGA energy calibrations were performed run-by-run using the energies of background γ rays. As before, the γ -ray energies were determined from the centroids of Gaussian fits to the full-energy peaks. For every experimental run (average run length \sim 1hour) a linear calibration of known γ -ray energy versus centroid location was constructed from four background lines. Specifically, the 352-keV γ ray in ^{214}Pb and 609-keV γ ray in ^{214}Bi from the ^{238}U decay chain, the 1461-keV γ ray from ^{40}K , and the 2615-keV γ ray in ^{208}Tl from the ^{232}Th decay chain were used. The residuals are shown for each SeGA detector for a representative run of experiment e11503 in Fig. 3.12. The residuals for the sum spectrum of all 16 SeGA detectors for the same run are shown in Fig. 3.13. The energies of many background γ rays were monitored throughout e11503 to ensure a good energy calibration was achieved. The residuals for the sum spectrum of all 16 SeGA detectors for the background γ rays over the entire course of experiment e11503 are shown in Fig. 3.14. Based on Fig. 3.14, the systematic uncertainty from the energy calibration was conservatively approximated to be ± 0.3 keV.

3.3.8 Pulse-shape analysis

The analysis of the experimental data from experiment e11503 relied on digital pulse-shape processing. Specifically, pulse-shape analysis was required to study the decay of the first excited state in ^{68}Ni . The first excited state in ^{68}Ni can be populated by the β decay of ^{68}Co [21]. Since the first excited state has a spin and parity of 0^+ , a transition to the 0^+ ground state can occur via internal conversion or internal pair production. The emitted internal-conversion electron or electron-positron pair has a small range in Ge and deposits energy in the same location of the GeDSSD as the β -decay electron. In a traditional analog system, the energies would sum, preventing the observation of the $E0$ decay of the excited state in ^{68}Ni . However, taking advantage of the half-life of the isomeric first excited state in ^{68}Ni , from recorded GeDSSD signal traces, pulse-shape processing was used to recover the signature of the $E0$ decay. The applied technique was adapted from Ref. [91]. The method is generally applicable for detecting separate radioactivities that deposit energy in the same strip of the GeDSSD within a time that is short compared to the decay time of the preamplifier, which is around $40\ \mu\text{s}$ for a typical strip.

The typical pulse shape observed when a radioactive decay deposits energy in a strip of the GeDSSD is shown in Fig. 3.15. As mentioned previously, a trace length of $6\ \mu\text{s}$ with a $3\ \mu\text{s}$ delay was used for all strips. In order to carry out the pulse-shape analysis, the expected response of each strip was determined. The expected response, or “ideal pulse,” for each strip was generated using the 662-keV γ ray of a ^{137}Cs source. A baseline was calculated for each trace by averaging the pulse height at each digitization point from 1.0 to $2.5\ \mu\text{s}$. The original trace was then adjusted by subtracting the background and normalizing based on the area underneath the pulse. Approximately 500 adjusted traces were averaged for each

strip, creating the ideal pulses for the GeDSSD strips. The traces used for the creation of the ideal pulses were averaged using the 10-ns time-bin resolution with which DDAS records traces. No further time alignment was performed. While all traces had a triggering time of $3\ \mu\text{s}$ from DDAS, the precise time at which the signal crossed threshold could have occurred at any time during the 10-ns time bin. Therefore, the described technique produces ideal pulses with slightly slower initial rises than the actual experimental signals, but the effect is less than one 10-ns time bin.

Most of the decay signals detected in experiment e11503 had a pulse shape very similar to the one in Fig. 3.15. However, a small subset of the decay signals had a qualitatively different shape and resembled the trace shown in Fig. 3.16. The characteristic “stair-step” shape of the pulse in Fig. 3.16 results when two separate decays deposit energy in the same strip of the GeDSSD within a time period that is short compared to the decay constant of the detector preamplifier. The pulse-shape-analysis algorithm described below was used to distinguish between the two different pulse shapes in Figs. 3.15 and 3.16 and to characterize the decays giving rise to the different signals. The analysis technique was applied separately to strips on the front and back of the detector. As expected, qualitatively identical results were obtained from each side of the detector. The following paragraphs that explain the pulse-shape-processing methods show various spectra measured in the back strips, since the energy resolution is superior to that of the front strips, but the analysis procedure for the front strips was the same. In fact, the results presented in Ref. [78] were from the front of the GeDSSD because the front-strip analysis was performed first.

For each decay event, the signal recorded in the back strip where the most energy was deposited was fit using the ideal pulse for that strip. The value of the fit, SingleFit, at each

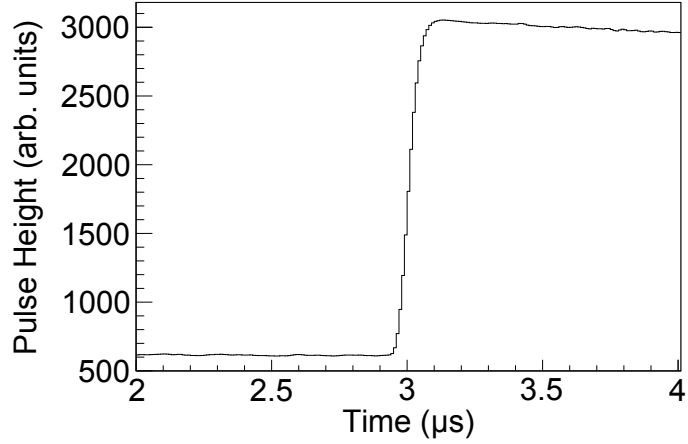


Figure 3.15: Typical pulse shape observed for the detection of a radioactive decay in a strip of the GeDSSD. Signals were recorded using a trace length of $6 \mu\text{s}$ and a delay of $3 \mu\text{s}$

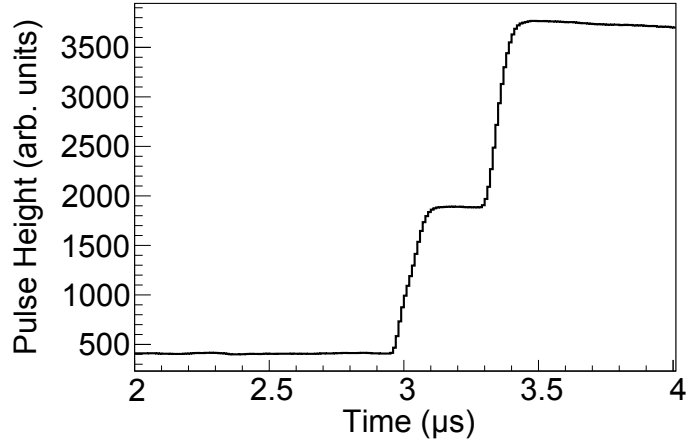


Figure 3.16: Typical pulse shape observed in the GeDSSD when two separate decays deposit energy in the same strip within a time period that is short compared to the decay constant of the preamplifier.

digitization point, i , is determined from

$$\text{SingleFit}[i] = B + \text{SinglePulse}[i] \quad (3.3)$$

where B is a constant baseline and $\text{SinglePulse}[i]$ is the value of the ideal pulse for a particular

strip which has been offset in time and scaled appropriately. SinglePulse[i] is given by

$$\text{SinglePulse}[i] = S (\text{idealpulse}[i_P] + I[i_P]) \quad (3.4)$$

where S is the scaling constant and $\text{idealpulse}[i_P] + I[i_P]$ describes the ideal pulse that has been offset in time. From the time-offset (phase) parameter, P , i_P is defined to be the value of $i - P$ rounded down to the nearest integer. The interpolation term, $I[i_P]$, is calculated from

$$I[i_P] = (i - P - i_P)(\text{idealpulse}[i_P + 1] - \text{idealpulse}[i_P]) . \quad (3.5)$$

Thus, the fit depends on three parameters, the baseline (B), scale (S), and time offset (P). B was fixed and determined by averaging the value of the experimental signal from 1.0 to 2.5 μs , while S and P were varied freely.

The quality of the fit was evaluated based on the difference between the fit and the experimental decay signal in the range from 1 – 5 μs . The quantity χ^2 was defined as

$$\chi^2 = \sum_{i=1\mu\text{s}}^{5\mu\text{s}} (S[i] - \text{SingleFit}[i])^2 \quad (3.6)$$

where i is a digitization point and $S[i]$ is the value of the experimental signal. The value of χ^2 was found to be systematically higher for signals with larger pulse heights compared to signals with smaller pulse heights. Therefore, χ^2 divided by pulse height was used as the metric for comparing the experimental signal with the fit. The normalized χ^2 value will henceforth be referred to as χ_n^2 . The value of χ_n^2 for the fits to the back-strip signals for all decay events in the GeDSSD is shown in Fig. 3.17. Based on the clear change in the structure of the distribution around values of 140, when χ_n^2 was less than 140 the fit was considered

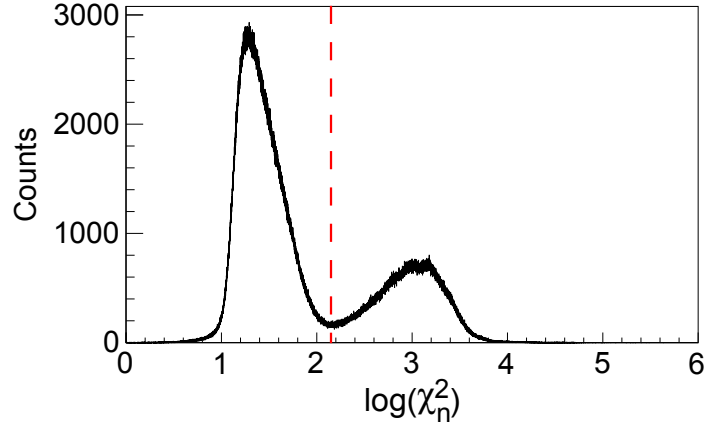


Figure 3.17: χ_n^2 distribution in the back of the GeDSSD for all decay signals that were fit to Eq. 3.3. The dashed line indicates the cutoff for a “good” fit.

“good,” and the signal was attributed to the detection of a single radioactive decay, i.e. a γ -ray or electron decay. An example of a good fit, for which χ_n^2 was 15.3, is shown in Fig. 3.18(a). Some of the signals with values of χ_n^2 greater than 140 were generated when two separate radioactive decays deposited energy in the same strip of the GeDSSD within the $6\text{-}\mu\text{s}$ time period corresponding to the trace length. However, other types of signals also resulted in large χ_n^2 values. The majority of cases in which χ_n^2 was above the cutoff were caused by transient signals that are induced when charge is collected in an adjacent strip. Signals in which the preamplifier had not returned to baseline by the start of the recorded trace, as well as noisy signals, also resulted in large values of χ_n^2 . Examples of signal traces for which the value of χ_n^2 was greater than 140 are shown in Figs. 3.18(b) - (e).

The energy of each decay resulting in a good fit was determined from the value of the parameter S . Applying the pulse-shape-processing method described above to data collected from radioactive-source measurements performed after experiment e11503, a very simple linear energy calibration was performed for each GeDSSD strip using γ rays from the SRM and ^{137}Cs sources. As before, due to the low efficiencies of the individual strips, only the 43- and 123-keV γ rays from the SRM source and the 662-keV γ ray from the ^{137}Cs source

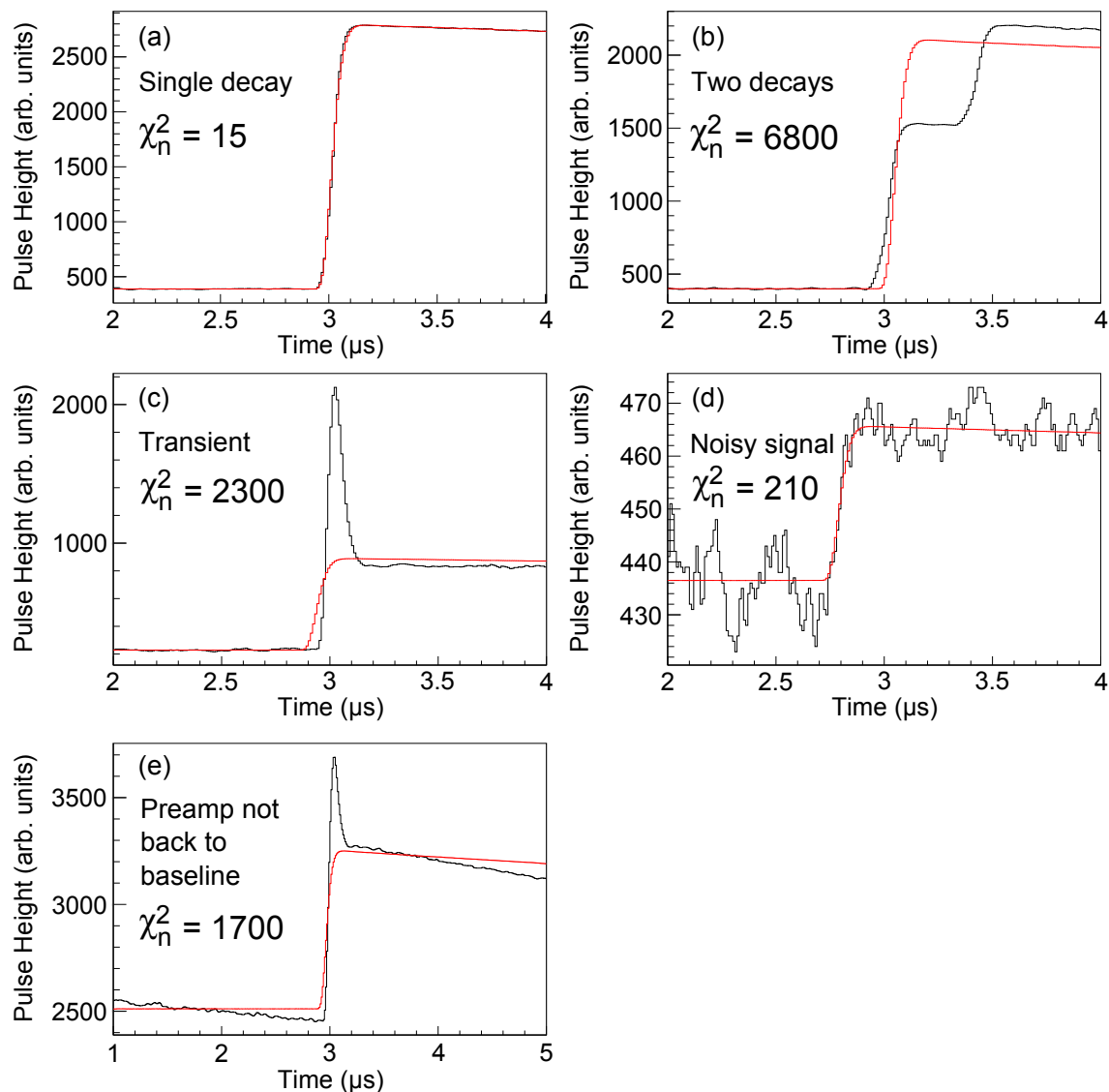


Figure 3.18: Examples of recorded traces from the back strips of the GeDSSD for which the fit to Eq. 3.3 yielded a value of χ_n^2 of (a) less than 140 or (b) - (e) greater than 140. The traces are shown in black, while the fits are shown in red. The observed pulse shapes resulted from (a) a single radioactive decay, (b) two sequential radioactive decays, (c) a transient signal induced from charge collection in a neighboring strip, (d) a noisy signal, and (e) a signal in which the preamplifier had not returned to baseline at the start of the signal.

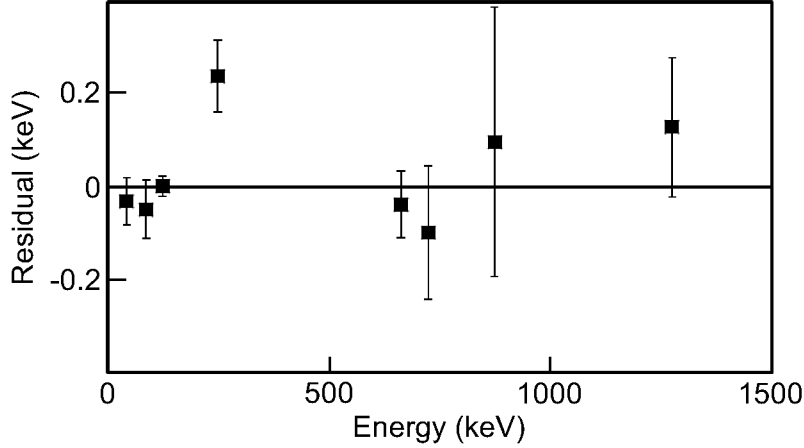


Figure 3.19: Residuals for the sum of all 16 back strips of the GeDSSD from the energy calibration based on the determined value of S when γ -ray decay signals from the SRM and ^{137}Cs sources were fit according to Eq. 3.3.

were used for the calibrations. The residuals for the sum of all strips on the back of the GeDSSD are shown in Fig. 3.19. With the increase in statistics gained when considering all strips compared to just a single strip, the residuals could be determined for the γ -ray peaks at 87, 248, 723, 873, and 1275 keV from the SRM source in addition to the 43- and 123-keV peaks. The systematic uncertainty due to the calibration was approximated as 0.3 keV. The systematic error was combined with the statistical error to determine the total error in the energy of single decays.

If the criteria for a good fit were not met, a second fit was performed. The second fit can be understood as a linear combination of two ideal pulses offset in time, and the value of the fit at each digitization point was determined by

$$\text{DoubleFit}[i] = B + \sum_{j=1}^2 \text{SinglePulse}_j[i] \quad (3.7)$$

where B is the baseline and each SinglePulse_j is given by Eq. 3.4. The fit defined by Eq. 3.7 depends on five parameters, a scaling constant and time offset for the first pulse, a scaling

constant and time offset for the second pulse, and the background. As before, the value of the background parameter was fixed and calculated by averaging the value of the experimental signal from 1.0 to 2.5 μs . The other four parameters were allowed to vary freely.

To qualify a signal as being due to two sequential radioactive decays, the resulting fit characterized by Eq. 3.7 had to meet certain requirements. The first requirement was that the difference between the time offset parameters for SinglePulse[1] and SinglePulse[2] be greater than some specified value. Given the limited digitization rate of the digital system (100 megasamples/s), two decays must be separated in time by several times the time gap between digitization points to resolve one decay from the other. The rise time of the signal is also important in regards to resolving two decays closely spaced in time. The faster the rise time, the easier it is to distinguish between sequential decays. For the present experiment, the minimum allowable time difference between the two decays was set as 150 ns. It was further required that the χ_n^2 value for the difference between the fit described by Eq. 3.7 and the experimental signal be less than 85. The distribution of χ_n^2 for all back-strip experimental decay signals fit to Eq. 3.7 in which the difference between the two time-offset parameters of the fit was greater than 150 ns is shown in Fig. 3.20. For signals corresponding to the detection of two separate radioactive decays, the value of χ_n^2 was less than 85 and fell within the first peak in Fig. 3.20. From this point forward, signals for which the value of χ_n^2 for the difference between the experimental signal and the fit to Eq. 3.7 was below 85 and the difference between the two time-offset parameters in the fit was greater than 150 ns will be referred to as “double” pulses. An example of a double pulse is shown in Fig. 3.21(a). Values of χ_n^2 above 85 resulted from transient signals induced from charge collection in neighboring strips, noisy signals, and signals in which the preamplifier had not returned to baseline at the start of the trace. Examples of traces for which χ_n^2 was greater than 85 are shown in

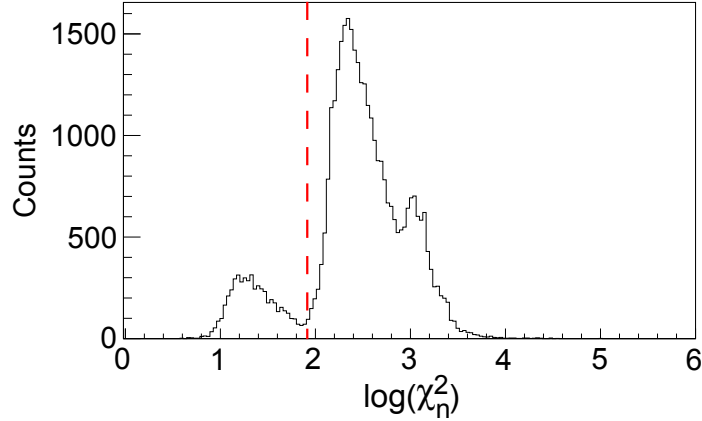


Figure 3.20: χ_n^2 distribution in the back of the GeDSSD for all decay signals that were fit to Eq. 3.7 and for which the difference between the two time-offset parameters in the fit was greater than 150 ns. The dashed line indicates the cutoff for a “good” fit.

Figs. 3.21(b) - (d).

In Fig. 3.21(a) (also in Fig. 3.26), the shape of the fit constructed from the ideal trace is slightly different from the shape of the experimental signal. Namely, the experimental signal begins to rise earlier than the fit. The discrepancy is not caused by fitting to two ideal pulses, but rather, is due to differences in signal shape that occur when decays are detected at different depths in the GeDSSD. The depth of an interaction in the GeDSSD can be approximated based on the time difference between the signals on the front and back sides of the detector. The time difference between the back and front signals for decay events detected during the calibration run with the ^{137}Cs source (which was used to determine the ideal trace for each GeDSSD strip) is shown in Fig. 3.22(a). For comparison, the back-front time difference measured during the experiment is shown in Fig. 3.22(b). With the ^{137}Cs source, the 662-keV γ rays were detected throughout the 1-cm depth of the GeDSSD, resulting in a relatively wide distribution in the back-front time-difference spectrum. During the experiment, however, the ions were deposited in the detector at a depth of approximately 1 mm, so a large number of β decays were detected closer to the front face of the GeDSSD

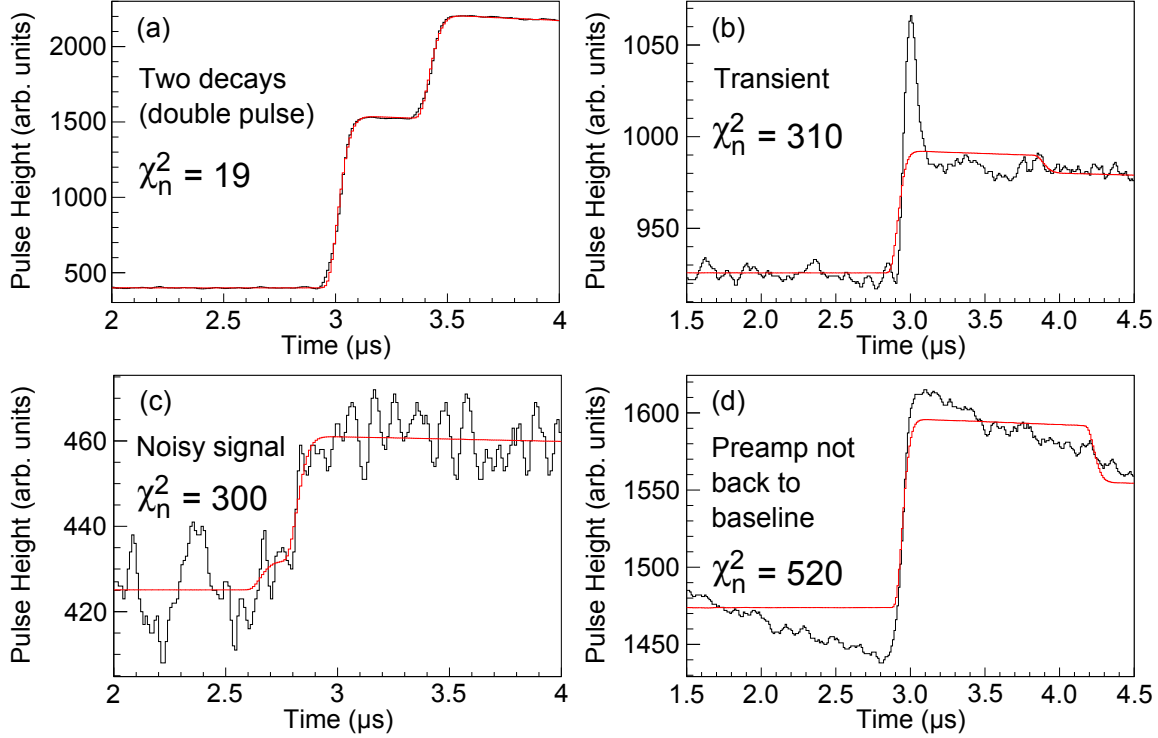


Figure 3.21: Examples of recorded traces from the back strips of the GeDSSD for which the fit to Eq. 3.7 yielded a difference between the two time-offset parameters of greater than 150 ns and the value of χ_n^2 was (a) less than 85 or (b) - (d) greater than 85. The traces are shown in black, while the fits are shown in red. The observed pulse shapes resulted from (a) two sequential radioactive decays, (b) a transient signal induced from charge collection in a neighboring strip, (c) a noisy signal, and (d) a signal in which the preamplifier had not returned to baseline at the start of the signal.

than the back face, resulting in a more strongly peaked time-difference spectrum in which the majority of events have a large difference between the front and the back times. Interactions at different depths produce signals with small differences in shape. As an example, the ideal traces that are determined for back strip 9 when the time difference between the back and front signals of the GeDSSD is restricted to a value between -70 and -40 ns or a value between 20 and 50 ns are shown in blue and green, respectively, in Fig. 3.22(c). The shapes of the rises are different. Therefore, the signals in the experiment, which were primarily detected near the front face of the GeDSSD, did not always have the exact same shape as the ideal pulses, which were determined from signals detected throughout the depth of the GeDSSD.

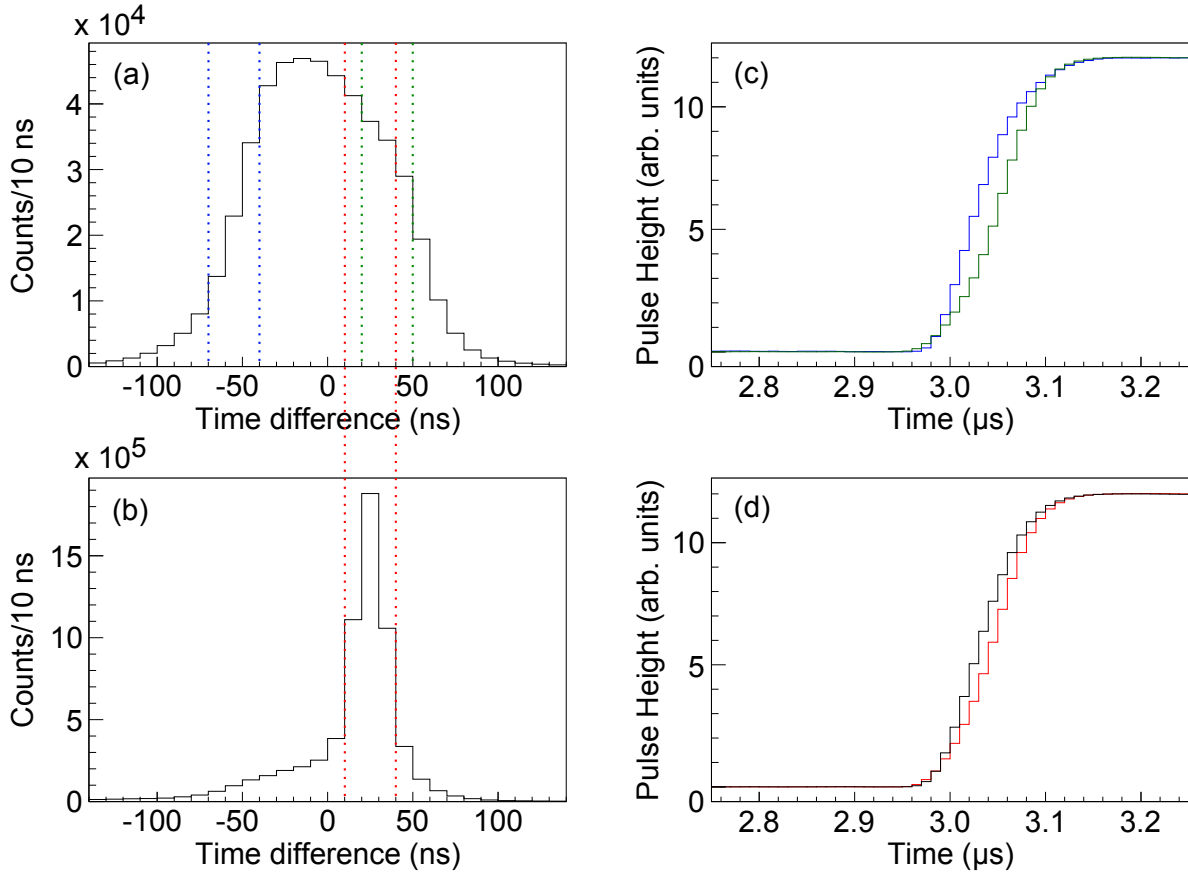


Figure 3.22: Time difference between the back-strip signal and the front-strip signal of the GeDSSD for decay events during (a) the calibration run used to construct the ideal trace for each strip and (b) the collection of experimental data during experiment e11503. The displayed time difference is the back time minus the front time. (c)-(d) The ideal trace that is determined for back strip 9 when different gating conditions are applied. (c) The ideal trace that results when a gate from -70 to -40 ns or 20 to 50 ns is placed on the back-front time difference is shown in blue and green, respectively. The region of each gate is indicated by the blue and green dotted lines in (a). (d) The ideal trace that results when gating on back-front time differences from 10 to 40 ns is shown in red and compared to the ideal trace that results when any back-front time difference is allowed, which is shown in black. The region of the gate from 10 to 40 ns is indicated by the red dotted lines in (a) and (b).

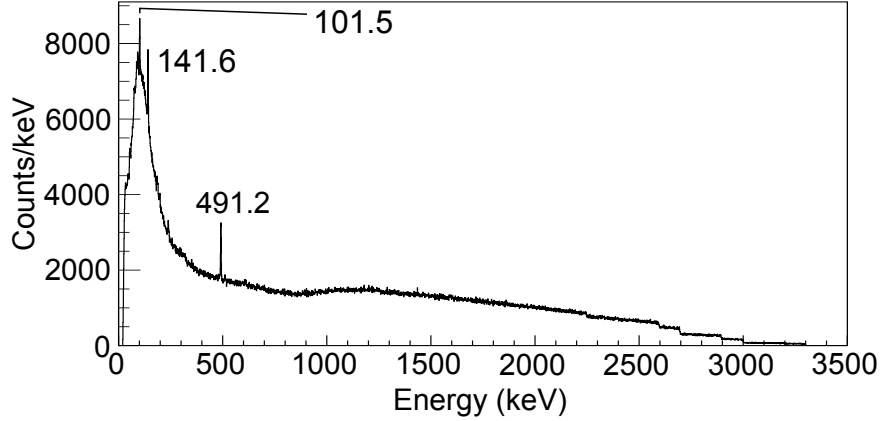


Figure 3.23: Energy spectrum in the back strips of the GeDSSD for all decay signals that were characterized as being caused by a single radioactive decay based on the results of fitting the decay signal to Eq. 3.3. The energy was determined from the value of parameter S in Eq. 3.4. Peaks are labelled by their energies in keV.

To emphasize this point, the ideal trace for back strip 9 that was determined using any back-front time difference (which is the ideal trace that was used for the fitting procedure discussed previously) is shown in black in Fig. 3.22(d) and compared to the ideal trace that results when the back-front time difference is restricted to values of 10 to 40 ns (the range for most experimental decay signals). Overall however, the signal-shape difference as a function of depth is a relatively small effect. The analysis based on fitting the experimental signals to the ideal pulses was not significantly affected by interaction depth. Therefore, depth was not taken into account in the pulse-shape processing.

The energy spectrum in the back of the GeDSSD for all decays that were identified as being due to a single radioactive decay from the fit to Eq. 3.3 is shown in Fig. 3.23. In general, a continuous energy distribution is observed, which is characteristic of β decay. Three intense monoenergetic peaks are also present at 101.5 ± 0.3 , 141.6 ± 0.3 , and 491.2 ± 0.3 keV. The particular decays giving rise to these peaks are identified in Section 4.1.1.

The energy spectrum in the back of the GeDSSD for the second decay of all double pulses is shown in Fig. 3.24(a). Four intense peaks near 13, 93, 580, and 1600 keV are evident.

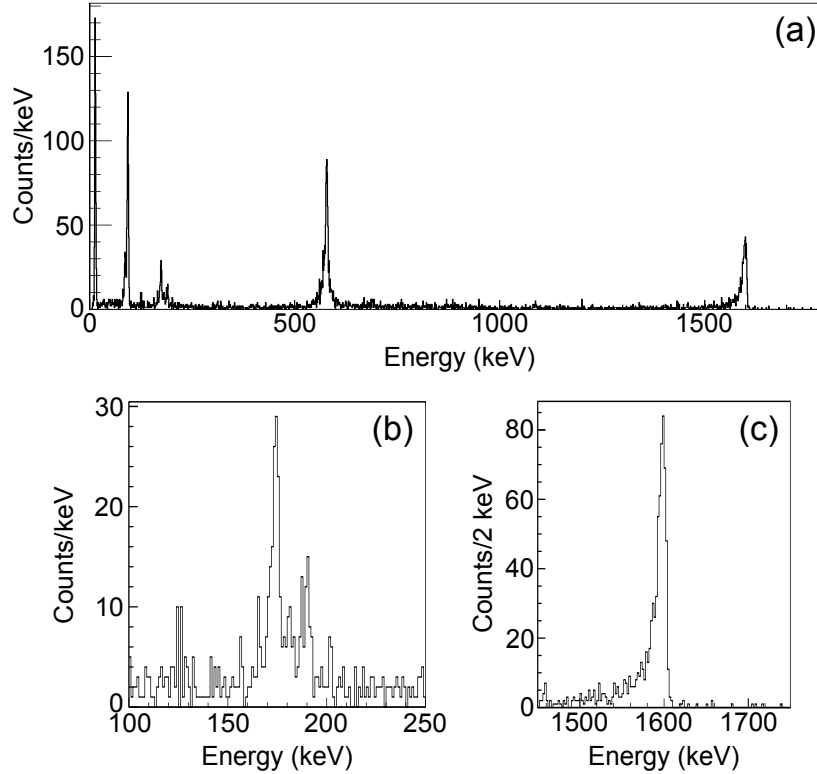


Figure 3.24: Energy spectrum in the back strips of the GeDSSD for the second decay of double pulses. The entire energy range from 0 - 1800 keV is shown in (a). Zooms of the regions from 100 - 250 keV and 1450 - 1750 keV are shown in (b) and (c), respectively.

Two small peaks near 175 and 190 keV are also present and are visualized more clearly in Fig. 3.24(b), which shows an expanded view of the region between 100 and 250 keV. The precise energies of the peaks are discussed in more detail below. The decays responsible for producing the peaks are deduced in Section 4.1.2.

An undesirable feature observed in Fig. 3.24(a) is the low-energy tailing of peaks in the spectrum. An expanded view of the region near 1600 keV is shown in 3.24(c) to more clearly display one of the tails. The cause of the low-energy tailing is evident in Fig. 3.25, which shows the energy of the second decay plotted against the time difference between the first and second decays as determined from the fit of the decay signal to Eq. 3.7 for second-decay energies between 1480 and 1650 keV. When the time difference is small, there is a systematic

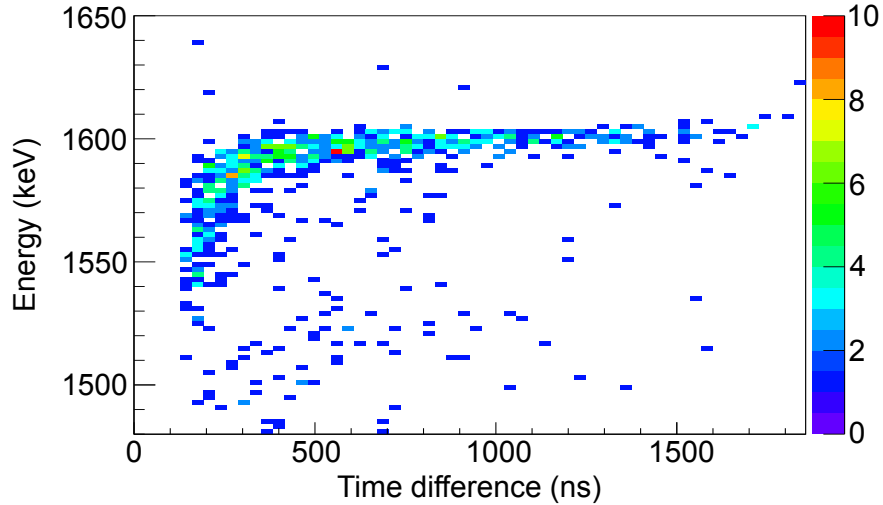


Figure 3.25: Two dimensional plot of energy of the second decay versus time difference between the first and second decays for double pulses. The time difference was determined from the difference between the two time-offset parameters found from the fit of the decay signal to Eq. 3.7. Both the energy and time difference were determined using signals in the back strips of the GeDSSD.

tendency for the fit to underestimate the decay energy. Thus, the low-energy tails for the peaks in Fig. 3.24(a) are due to a limitation of the pulse-shape analysis algorithm in which a poor energy determination results when the two decays are closely spaced in time. An example of the trace and the associated fit for a signal in which the energy of the second decay was determined to be 1555 keV and the time difference between the first and second decays was determined to be 153 ns is shown in Fig. 3.26. The centroids of the energy peaks near 13, 93, 580, and 1600 keV as a function of the time difference between the first and second decays are shown in Figs. 3.27(a), (b), (c), and (d), respectively, for time-difference increments of 200 ns. The energy spectrum of the second decay for events with time differences between the first and second decay of greater than 1200 ns is shown in Fig. 3.28(a). Figs. 3.28(b) and (c) show expanded views of Fig. 3.28(a) in the ranges of 100 - 250 keV and 1450 - 1750 keV, respectively, which are the same energy ranges as in Fig. 3.24(b) and (c). The low-energy tailing is no longer present with the requirement that the

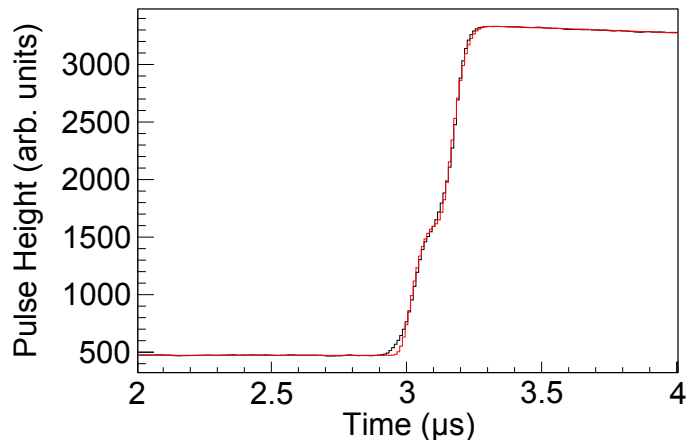


Figure 3.26: Example of a GeDSSD signal (black) and the associated fit to Eq. 3.7 (red) for a signal in which the time difference between the two separate radioactive decays was determined to be just above 150 ns.

time difference between the two decays be greater than 1200 ns.

The four most intense peaks in Fig. 3.28(a) were fit to Gaussians to determine the peak centroids. Energies of 13.7 ± 0.2 , 93.2 ± 0.2 , 580.5 ± 0.5 , and 1601.6 ± 0.5 keV are determined, where the errors are statistical. In Fig. 3.27(c) and (d), the slope of energy as a function of time difference for the 581- and 1602-keV peaks is close to 0 by 1200 ns, but it may not yet be completely flat, especially for the 1602-keV peak. Therefore, a relative energy uncertainty of 0.25% was assumed to account for the uncertainty resulting from the dependence on the time difference.

For decays that have previously been observed, comparing the energies determined from the pulse-shape-processing algorithm for signals that arise from two separate radioactive decays with the known energies can be used to give an indication of the systematic error when the fit to two ideal pulses is performed. The identification of known peaks is described in Section 4.1.2. The difference between the true energy and the energy determined from the pulse-processing routine for the 13.3- and 53.5-keV decays in ^{73}Ge and the 93.3-keV decay ^{67}Zn are shown in Fig. 3.29. Based on the differences, the minimum systematic

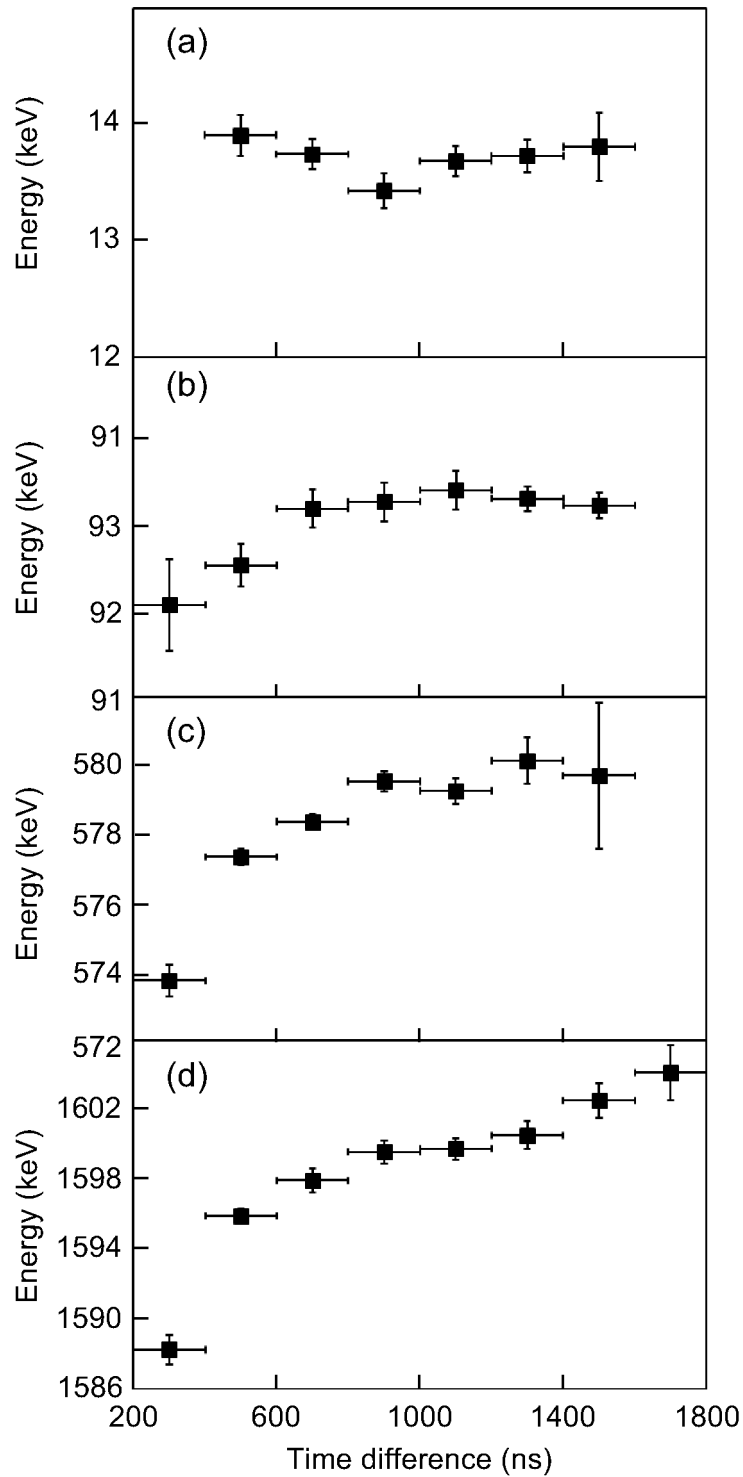


Figure 3.27: Centroids for the peaks near (a) 13 (b) 93, (c) 580, and (d) 1600 keV in Fig. 3.24 (a) as a function of the time difference between the first and second decays in increments of 200 ns. The horizontal error bars represent the span of each 200-ns time-difference increment.

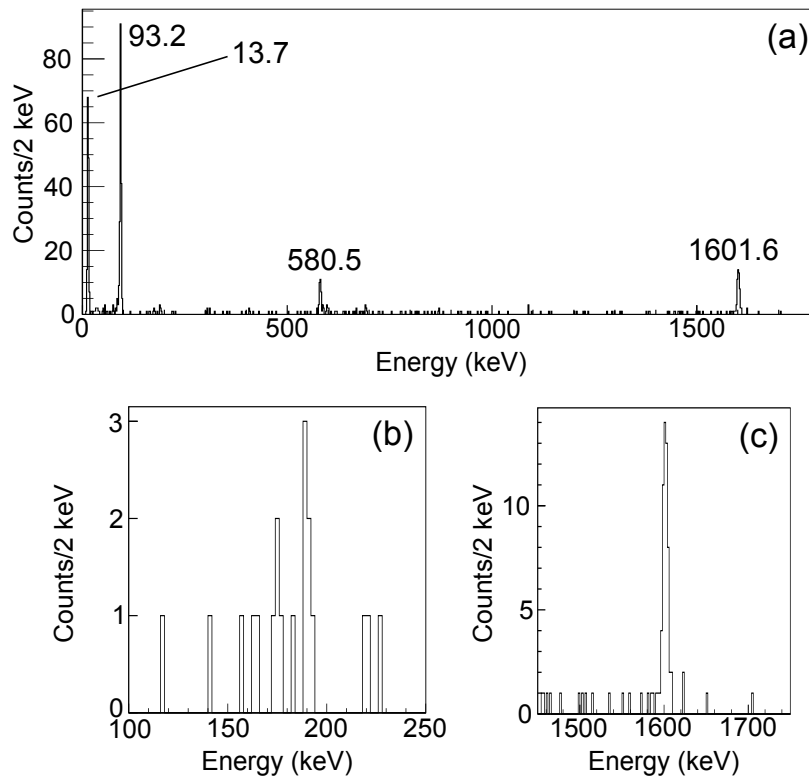


Figure 3.28: Energy spectrum in the back of the GeDSSD for the second decay of double pulses for which the difference between the time-offset parameters for the two decays was larger than 1200 ns. The entire energy range from 0 - 1800 keV is shown in (a). Zooms of the regions from 100 - 250 keV and 1450 - 1750 keV are shown in (a) and (b), respectively.

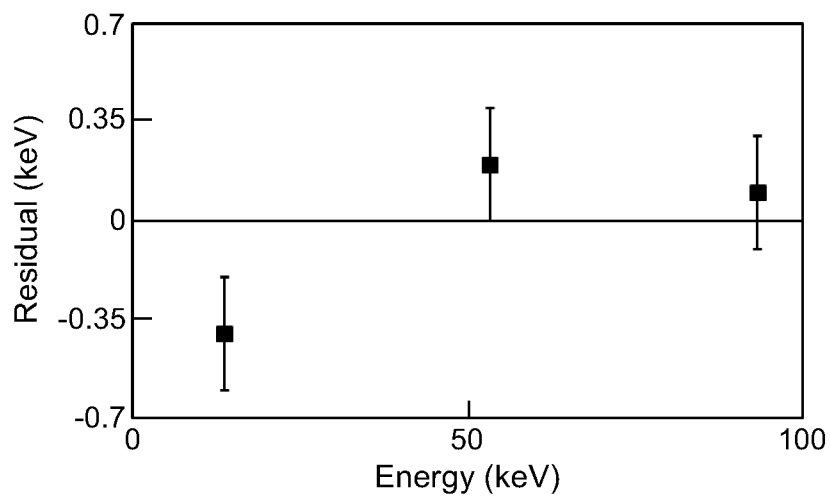


Figure 3.29: Residuals for the peaks in Fig. 3.24 (a) and Fig. 4.1 that arise from known decays in ^{73}Ge and ^{67}Zn .

uncertainty due to the energy calibration for determining the energy of two independent radioactive decays was estimated as 0.7 keV. A comparison over a larger energy range would be desirable, but given the limited data from the experiment, is not possible. Combining the minimum systematic energy uncertainty from the calibration when fitting to two pulses, the uncertainty due to the systematic dependence of energy on the time difference between the two decays, and the statistical uncertainty in the fitting procedure, the energies for the four intense peaks in Figs. 3.24(a) and 3.28(a) are 13.7 ± 0.8 , 93.2 ± 0.8 , 581 ± 2 , and 1602 ± 4 keV.

3.4 NSCL experiment e08020

3.4.1 Isotope production and delivery

Similar to experiment e11503, a ^{76}Ge primary beam, extracted from the K1200 with an energy of 130 MeV/nucleon, was impinged on a 470 mg/cm^2 ^9Be target in experiment e08020, and the produced ions of interest were delivered to the Beta Counting System (BCS) [92]. In order to transport as large of a fraction of the neutron-rich reaction products as possible to the experimental station, the full 5% momentum acceptance of the A1900 was used. The A1900 was tuned for the transmission of ^{64}V , and an Al wedge with a thickness of 45 mg/cm^2 was placed at image 2. Particle identification was performed based on energy loss in PIN01 (see Fig. 3.32) and TOF between the position-sensitive scintillator at image 2 of the A1900 and PIN01. Ion position at the scintillator was used to correct TOF and improve the particle identification. Position is shown as a function of TOF for the Cr isotopes in Fig. 3.30(a). Each band corresponds to a different isotope. Due to the large momentum acceptance used, TOF varied substantially for each isotope, but the systematic relationship between position at the image 2 scintillator and TOF was used to make a TOF correction. This correction was

Table 3.3: Total numbers of ions for each isotope that was delivered to the experimental station in experiment e08020.

Isotope	Number of ions	Isotope	Number of ions	Isotope	Number of ions
⁵⁵ Sc	2244	⁶⁰ V	269672	⁶³ Mn	172
⁵⁶ Sc	4652	⁶¹ V	391643	⁶⁴ Mn	20044
⁵⁷ Sc	1882	⁶² V	78309	⁶⁵ Mn	246859
⁵⁶ Ti	549	⁶³ V	16158	⁶⁶ Mn	209746
⁵⁷ Ti	21061	⁶⁴ V	834	⁶⁷ Mn	66410
⁵⁸ Ti	71280	⁶¹ Cr	12605	⁶⁸ Mn	2583
⁵⁹ Ti	33146	⁶² Cr	264264	⁶⁷ Fe	2109
⁶⁰ Ti	6558	⁶³ Cr	378645	⁶⁸ Fe	15732
⁶¹ Ti	415	⁶⁴ Cr	256268	⁶⁹ Fe	4682
⁵⁸ V	805	⁶⁵ Cr	26405	⁷⁰ Fe	480
⁵⁹ V	76067	⁶⁶ Cr	1432		

accomplished by a coordinate-system rotation. The rotation yielded a “corrected” TOF that was constant for single isotope regardless of the position at which the ion passed through the image 2 scintillator. A plot of position versus the corrected TOF for the Cr isotopes is shown in Fig. 3.30(b). The particle-identification plot, which uses the corrected TOF as the value on the x-axis, is shown in Fig. 3.31. The total numbers of ions delivered to the decay station for each transported isotope are given in Table 3.3.

3.4.2 Beta Counting System (BCS)

The schematic arrangement of the BCS detectors is shown in Fig. 3.32. The central detector was a 995- μm thick, 4 cm by 4 cm Si DSSD, which is electrically segmented into 40 1-mm wide strips on the front of the detector and 40 orthogonal 1-mm wide strips on the back of the detector. As in experiment e11503, the DSSD was used to detect the implantation of the radioactive ions as well as their subsequent β decays and was connected to dual-range preamplifiers. The correlation of β decays with ions is described in Section 3.4.5.

Downstream of the DSSD were five 5 cm by 5 cm Si single-sided strip detectors (SSSDs).

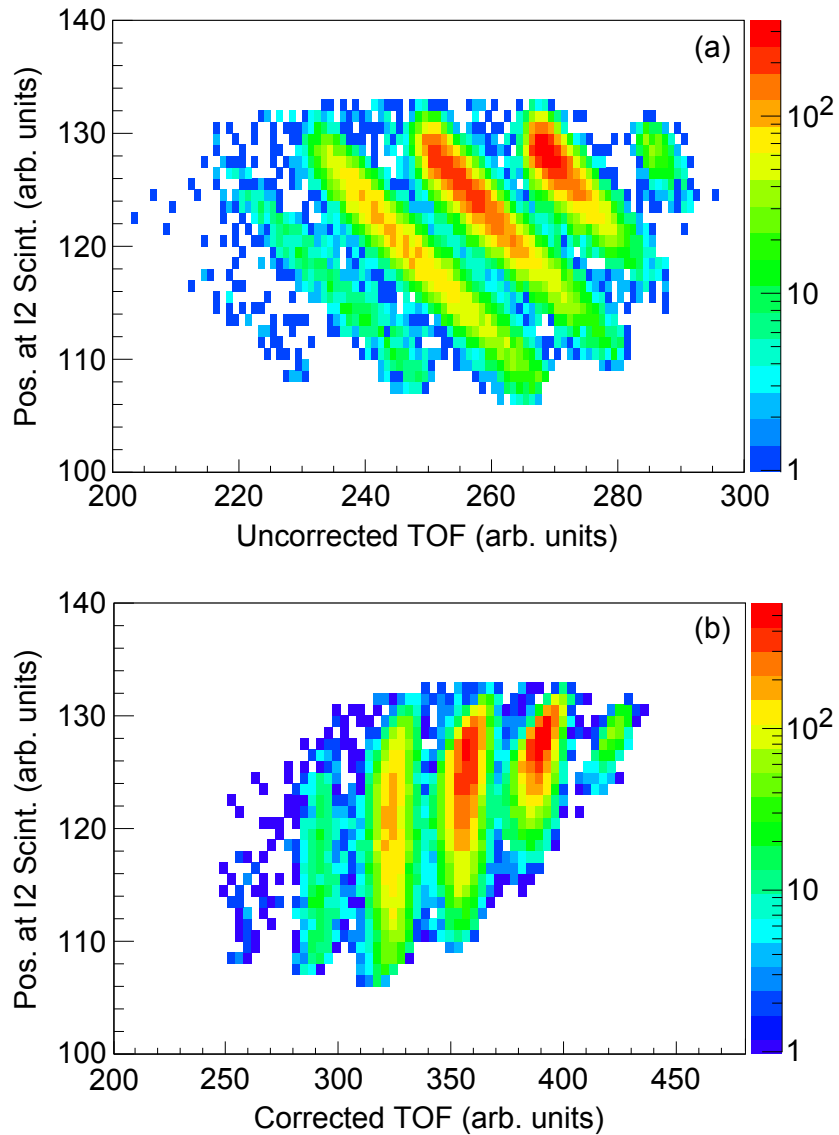


Figure 3.30: (a) Ion position at the image 2 scintillator of the A1900 vs TOF gated on the Cr isotopes. The uncorrected TOF value on the x-axis refers to the raw TOF between PIN01 and the image 2 scintillator. (b) Ion position at the image 2 scintillator vs corrected TOF gated on the Cr isotopes. The corrected TOF on the x-axis refers to the TOF value that is obtained following a coordinate-system rotation of (a).

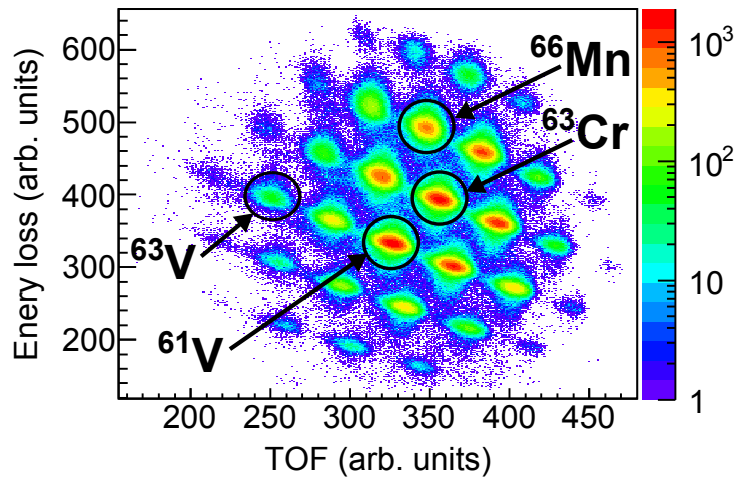


Figure 3.31: Particle-identification plot of the ions delivered to the experimental station in experiment e08020.

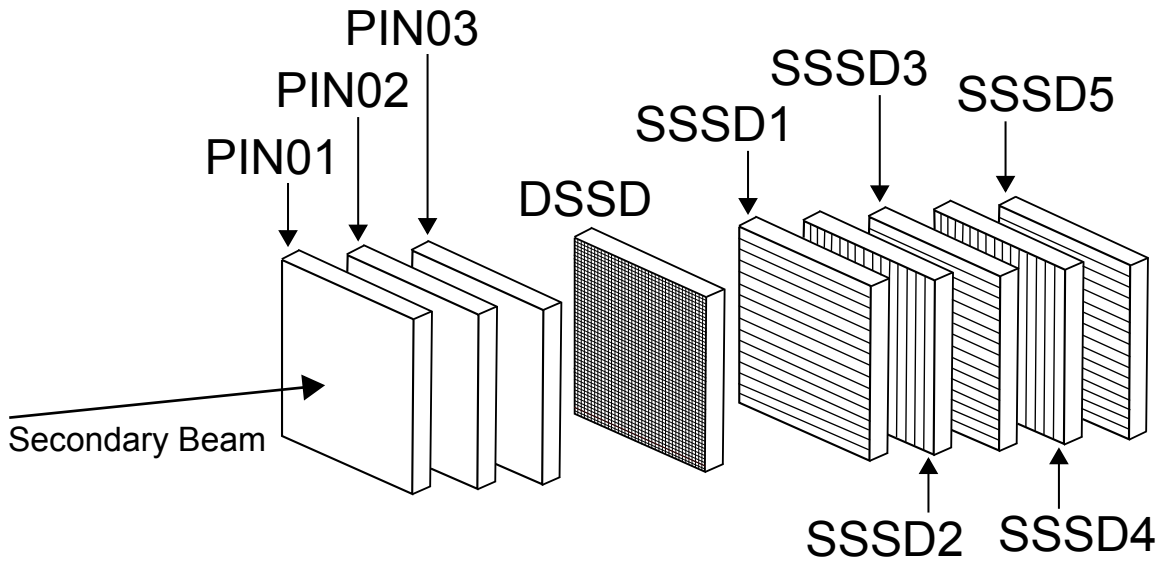


Figure 3.32: Schematic arrangement of the BCS in experiment e08020.

Each SSSD was electrically segmented into 16 strips in one direction. The thicknesses of SSSD1 through SSSD5 were 975 μm , 989 μm , 981 μm , 988 μm , and 997 μm , respectively. Directly upstream relative to the DSSD were three Si PIN detectors. The PIN detectors served as energy degraders, and as mentioned above, PIN01 was used for particle identification. The thicknesses of PIN01, PIN02, and PIN03 were 488 μm , 503 μm , and 996 μm , respectively. Three Al foils, which acted as energy degraders, were placed upstream of the BCS detectors. Two 1-mm thick foils and one 0.25-mm thick foil were used, resulting in a total thickness of 2.25 mm.

3.4.3 Segmented Germanium Array (SeGA)

The arrangement of SeGA in experiment e08020 is shown in Fig. 3.33. The 16 detectors of SeGA were arranged in the standard beta-SeGA configuration in which two concentric rings of eight detectors each are placed at a distance of 8.6 cm from the center of the DSSD. As noted previously, the distance between the two rings of SeGA was smaller than in experiment e11503.

3.4.4 Triggering conditions

The same general triggering conditions were applied in experiment e08020 as in experiment e11503. Experimental data from the DSSD were read out by DDAS and were only recorded when a signal above threshold was detected in both the front and back strips of the DSSD. Typical thresholds for the low- and high-gain preamplifiers of each DSSD strip were 30 MeV and 10 keV, respectively. The respective triggering rates for the low- and high-gain preamplifiers of each strip were less than about 5 and 60 Hz. Unlike experiment e11503,

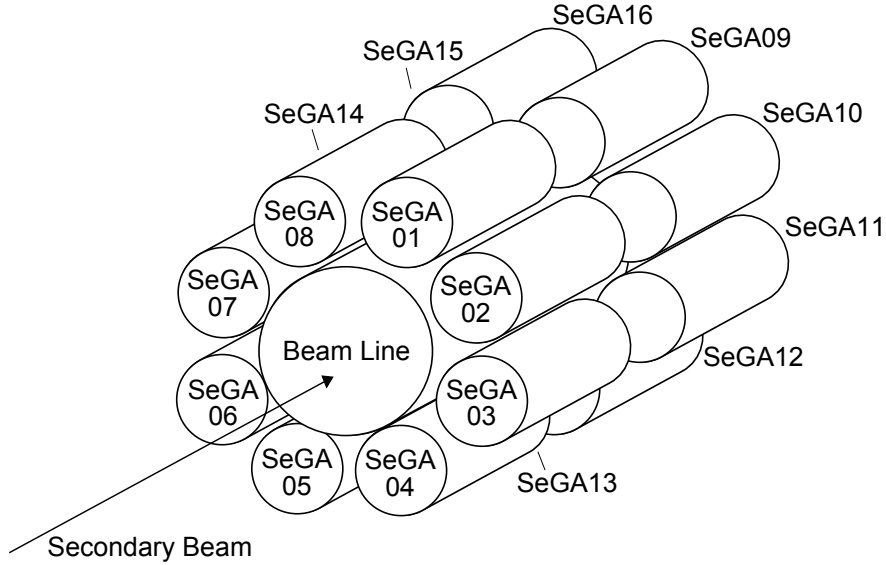


Figure 3.33: Schematic arrangement of SeGA in experiment e08020.

signal traces in the DSSD were not recorded in experiment e08020. Traces were also not recorded for SeGA in experiment e08020, and the readout of data from SeGA by DDAS was ungated.

3.4.5 Correlation

β decays were correlated with implanted ions in the DSSD on an event-by-event basis in software. Like experiment e11503, the requirements for the implantation of an ion were a valid signal in each of the PIN detectors as well as a valid low-gain signal in at least one strip on both the front and back of the DSSD. The energy of the low-gain signals had to be above a threshold set in software, typically about 200 MeV, to be considered valid. Further, implantation events required the absence of a signal in SSSD1. A decay was defined as an event in which there was a high-gain signal in both a front and back strip of the DSSD, but there was no signal in any of the PIN detectors. The high-gain DSSD signals also had to have an energy greater than a threshold that was set in software, which was approximately

50 keV for each strip. The locations of ion implantations and decays were identified in the exact same manner as in experiment e11503 (see Section 3.3.4).

Decay events were correlated with preceding ion implantations using spatial and temporal information. Since the total implantation rate was low in the experiment (less than 10 Hz over the entire DSSD), implant-decay correlations were made between decays and implants that occurred in the same pixel of the DSSD and between decays and implants that occurred in nearest-neighbor pixels. If consecutive ion implantations occur within a short time period, ambiguity could arise in terms of with which ion a particular decay should be correlated. To minimize the potential ambiguity, a minimum time of 1 s between back-to-back implants was required for making implant-decay correlations. Further, it was checked that the decay happened within a specified amount of time, referred to as the correlation time, after the ion implantation. The correlation time was set for each nucleus of interest to be long enough to detect almost all of the β decays of the implanted nucleus but also short enough to minimize the chance of correlating the ion implantation with a background event or a daughter or granddaughter β decay in the decay chain of the implanted nucleus.

β -decay curves were constructed by histogramming the time difference between a decay event and the implantation of a particular nucleus in the DSSD with which the decay was correlated. The half-life of the parent nucleus was determined from a fit to the decay curve. The decay-curve fits accounted for the exponential decay of the parent nucleus, as well as the growth and decay of daughter and granddaughter activities. From the fit, the number of β decays of the parent nucleus was also determined based on the area underneath the component of the fit due to the decay of the parent nucleus. To measure absolute β -delayed γ -ray intensities, the number of counts in the peaks of SeGA γ -ray energy spectra gated on those decays that followed the implantation of particular nuclei in the DSSD were measured.

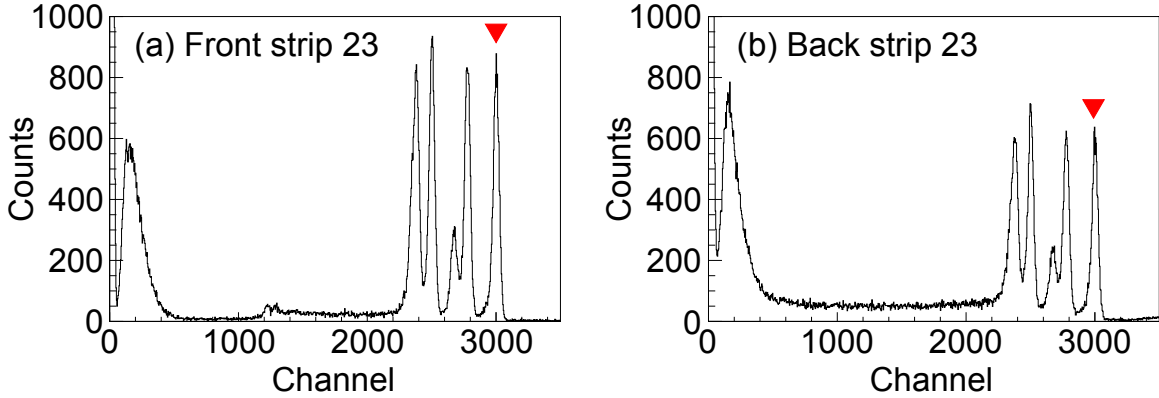


Figure 3.34: Representative energy calibration of (a) a front strip and (b) a back strip of the DSSD in experiment e08020. The energies of each strip were gain matched so that the 6.8-MeV α -decay peak occurred at channel 3000 in the calibrated energy spectrum. The 6.8-MeV α -decay peak is marked by a red triangle in each spectrum.

First, relative intensities of β -delayed γ -ray transitions were calculated based on the detected number of counts in the peaks and the calibrated SeGA efficiency. By normalizing to the number of parent β decays determined from the decay-curve fit, absolute β -delayed γ -ray intensities were then calculated for the transitions in the daughter nucleus populated by the β decay of the parent nucleus.

3.4.6 Calibrations

Each silicon detector of the BCS was calibrated before experiment e08020 using a ^{228}Th source. For the DSSD, a gain-matching procedure was performed in software for each front and back strip such that the energy of the 6.8-MeV peak from the α decay of ^{216}Po in the decay chain of ^{228}Th was placed at channel 3000 in the 12-bit calibrated energy spectrum. Calibrated energy spectra are shown for a representative strip on the front and back of the detector in Fig. 3.34.

Prior to experiment e08020, both energy and efficiency calibrations were performed for SeGA. Two γ -ray sources were used. The first was the SRM source described in Section

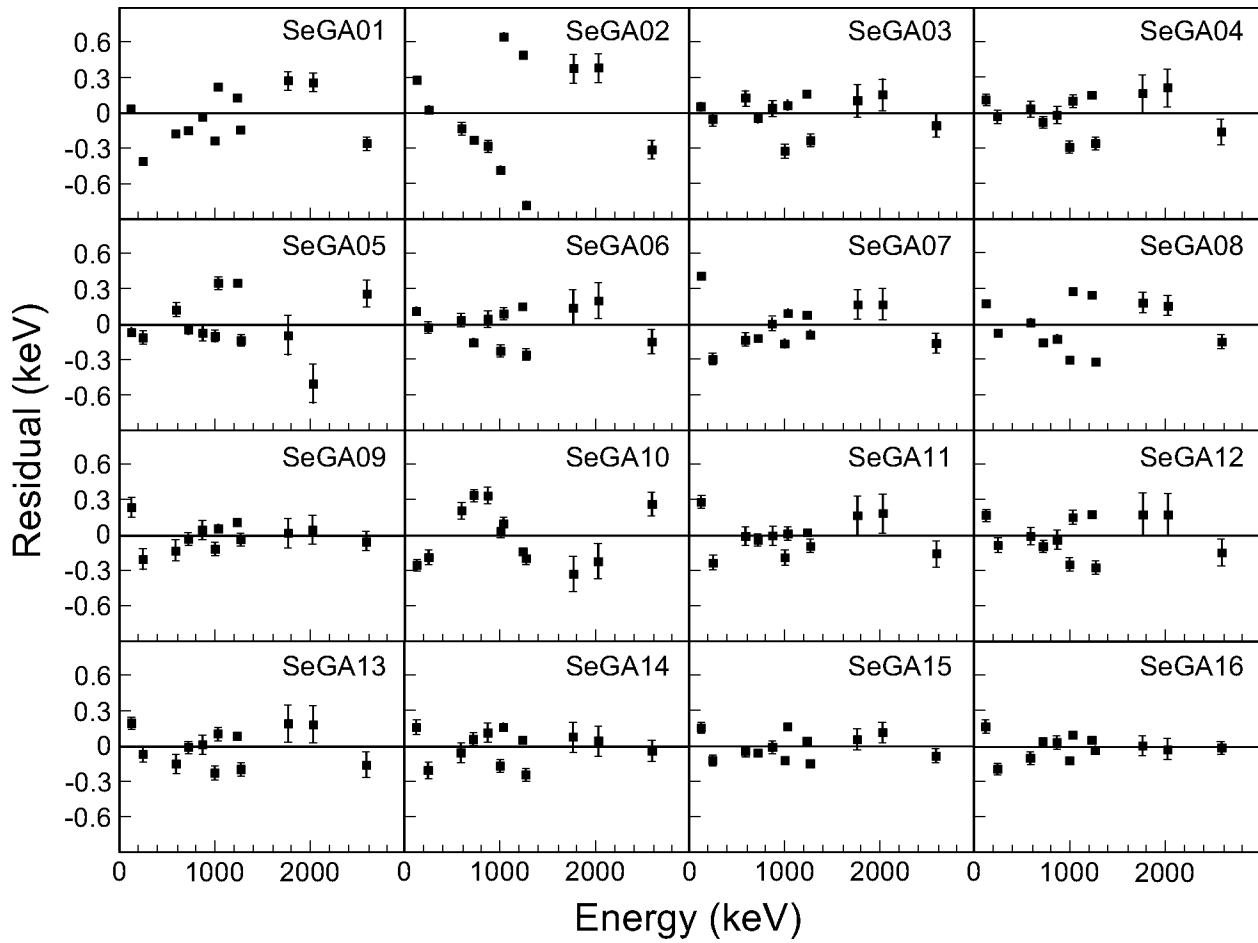


Figure 3.35: Residuals of the 16 individual SeGA detectors for the energy calibration performed before experiment e08020.

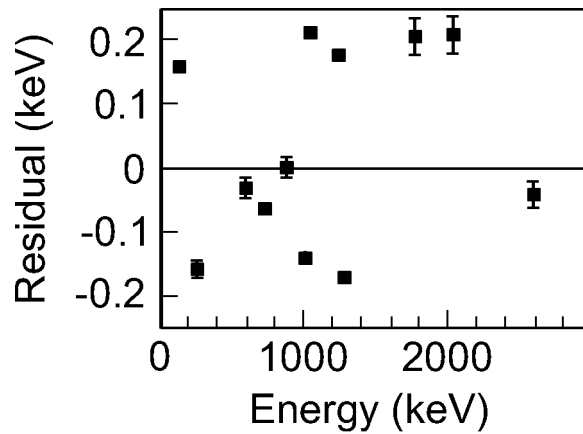


Figure 3.36: Residuals of the sum spectrum of all 16 SeGA detectors for the energy calibration performed before experiment e08020.

3.3.7 and the second a ^{56}Co source. The SRM source was used for low energies, up to 1596 keV, while the ^{56}Co source was used for high energies, up to 2599 keV. Sources were placed at the DSSD position for calibration measurements. The energies of the γ -ray transitions were determined from the centroids of Gaussian fits to the full-energy peaks. A second-order polynomial fit of known γ -ray energy versus centroid channel position was used to construct energy calibrations. The residuals are shown for each individual SeGA detector in the pre-experiment energy calibration in Fig. 3.35. The residuals for the summed energy spectrum of all 16 detectors are shown in Fig. 3.36. Small gain shifts occurred during the course of the experiment. Over a 24-hour time period, the gain shift for each detector was typically about 0.03% or less. To ensure good energy resolutions, the detectors were periodically recalibrated. The calibrations were performed using γ -rays emitted in the decay of common background sources, namely ^{40}K , ^{238}U , and ^{232}Th . A new calibration was performed approximately every 24 hours. While the data could have been used to recalibrate run-by-run, this was not necessary. The residuals of the summed energy spectrum of all 16 SeGA detectors for several background γ -rays for the entire experiment are shown in Fig. 3.37 with all the energy calibrations are applied. Based on Fig. 3.37, a conservative estimate of 0.3 keV was used for the systematic uncertainty associated with the energy calibration in the experiment. The uncertainties in the energies of the experimentally detected isomeric and β -delayed γ rays were then determined by adding in quadrature the uncertainty in the calibration and the uncertainty in the location of the peak centroid.

The known emission rates of the γ rays between 40 and 1600 keV from the SRM-source measurement were used to determine the absolute γ -ray peak efficiencies of SeGA. The number of counts in each Gaussian peak was divided by the known total number of γ rays emitted at that energy to determine the absolute efficiency. Relative efficiencies for detecting

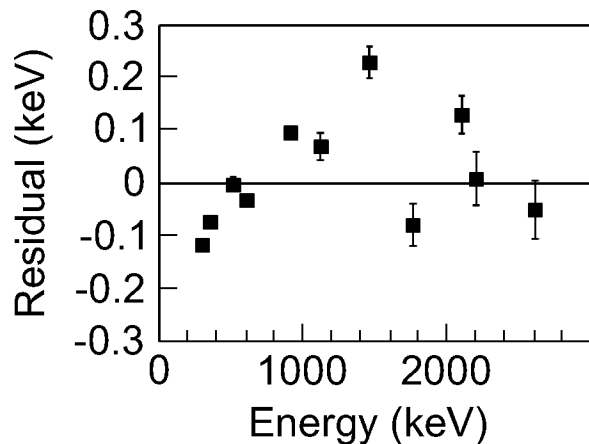


Figure 3.37: Residuals of the sum spectrum of all 16 SeGA detectors for background γ -ray lines monitored throughout the duration of experiment e08020. A new energy calibration was applied about every 24 hours to account for gain shifts of the SeGA detectors.

the γ rays from the ^{56}Co source were found by determining the number of counts in each peak. Absolute efficiencies for detecting the ^{56}Co γ rays were then extracted by matching the absolute efficiency for detecting the 1238-keV γ ray from the ^{56}Co source with the absolute efficiency for detecting the 1275-keV γ ray from the SRM source. A plot of the logarithm of the absolute peak efficiency of all 16 detectors versus the logarithm of energy (in keV) was made and fit with a fourth-order polynomial. The results of the fit are shown in Fig. 3.38.

A simple SeGA time-alignment calibration was also performed. For each SeGA detector, the time difference between the detection of a γ ray with an energy between 10 and 60 keV and the arrival of an ion at the DSSD was plotted for implant events. The majority of the γ rays in this energy range corresponded to prompt γ rays emitted when ions are stopped in the DSSD. The timing of each SeGA detector was adjusted so that peak of the time-difference distribution occurred at 0 ns. The time-difference spectrum for the sum of all 16 SeGA detectors is shown in Fig. 3.39(a). The full-width at half maximum of the distribution is approximately 200 ns.

Following the time-alignment calibration, the timing resolution for detecting two γ rays

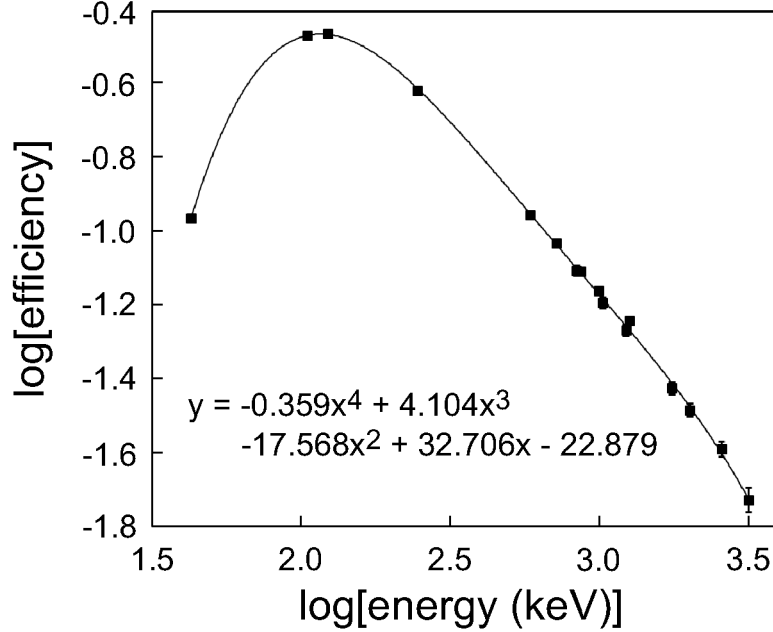


Figure 3.38: γ -ray peak efficiency curve for all 16 SeGA detectors in experiment e08020. A fourth-order polynomial was used to fit the data.

in separate detectors of SeGA was evaluated using the SRM source. The time difference between the detection of the 123- and 248-keV γ rays was measured. The 248-keV γ ray emitted from the SRM source feeds a 123-keV level in ^{154}Gd , which in turn decays to the ground state via the 123-keV transition [93]. The half-life of the 123-keV state is 1.2 ns, which is short compared to the time resolution of SeGA, so it can be ignored in this context. The spectrum of the time difference between the detection of the 123- and 248-keV γ rays is shown in Fig. 3.39(b). The distribution has a Gaussian shape and is centered approximately at 0 ns. The full-width at half maximum of the distribution is about 230 ns. To deduce a half-life based on the measurement of γ rays, the shape of the experimental time-difference spectrum being analyzed had to be significantly different from the shape the would be expected from the intrinsic time resolution of SeGA, limiting the half-lives that could be resolved to roughly 150 ns or greater, but the achievable limit for measuring half-lives also depends on the statistics.

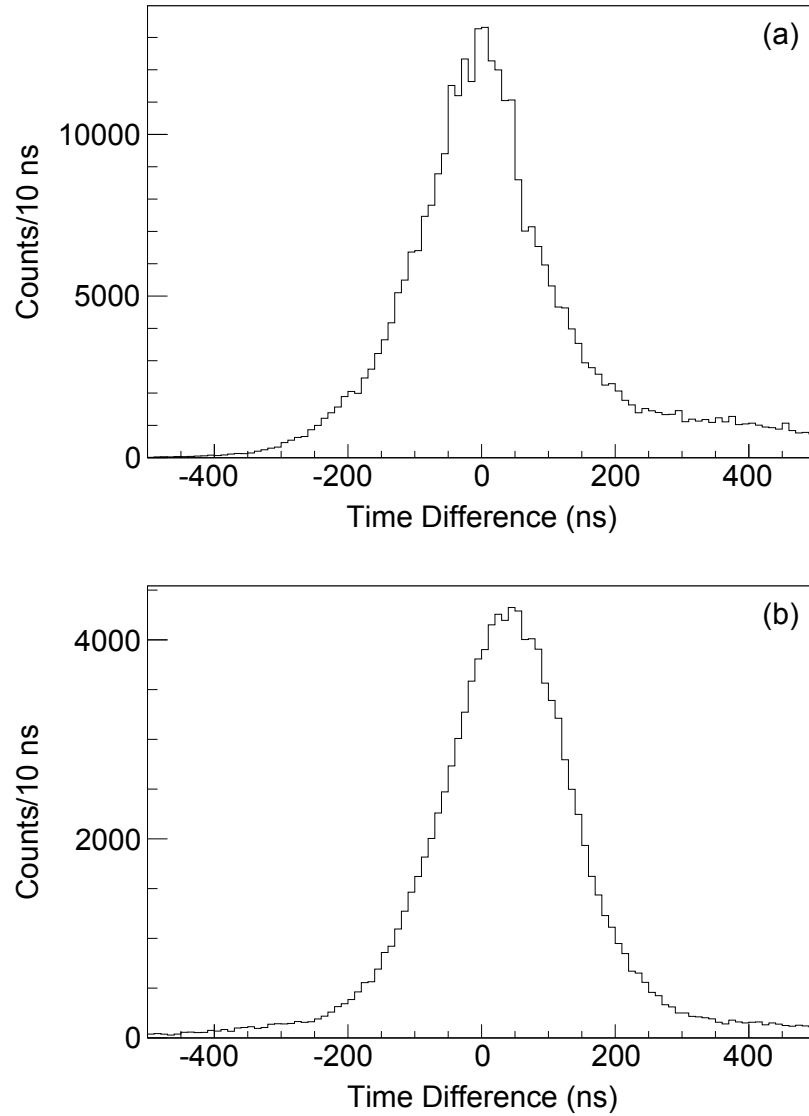


Figure 3.39: (a) Time difference between the detection of a γ ray with an energy between 10 and 60 keV in SeGA and the implantation of an ion in the DSSD gated on implant events. (b) Time difference between the detection of the 123- and 248-keV γ rays in SeGA from the SRM source measurements.

Chapter 4

Experimental Results

4.1 Identification of the energy peaks observed using pulse-shape analysis

The pulse-shape-processing techniques used to analyze the decay signals in experiment e11503 are described in Section 3.3.8. The particular decays giving rise to the peaks observed in the pulse-shape-processing energy spectra are identified below.

4.1.1 Single radioactive decays

The energy spectrum of all signals generated from a single radioactive decay in the GeDSSD is shown in Fig. 3.23. The continuous energy distribution in the spectrum signifies β decay. The peak at 491 keV is due to the γ -ray decay of the 496-ms isomeric $1/2^-$ state in ^{67}Co [64], a nucleus which was delivered to the decay station in the experiment. The 102- and 142-keV peaks arise from the γ -ray decay of two different isomeric states in ^{70}Cu that have half-lives of 33 and 6.6 s, respectively [94]. ^{70}Cu was populated in the β -decay chain of ^{70}Co .

4.1.2 Sequential radioactive decays

The energy spectrum of all signals that were identified as double pulses is shown in Fig. 3.24. The 14-keV peak in Fig. 3.24(a) is due to the isomeric decay of ^{73}Ge , which was

populated in the β -decay chain of ^{73}Ni . The first excited state in ^{73}Ge has an energy of 13.3 keV and a half-life of 2.92 μs [95]. Given the transition from the first excited state to the ground state has $E2$ character, at such a low energy, the transition occurs almost exclusively through internal conversion, with $\alpha = 1100$ [95]. The 14-keV peak in Fig. 3.24(a) therefore corresponds to the simultaneous detection of the energy from the internal-conversion electron and the energies from the cascade of x rays or Auger electrons that are emitted when the atomic-electron vacancy left from internal conversion is filled. The low-energy x rays or Auger electrons have a very small range in the GeDSSD and are detected in the same pixel of the detector as the conversion electron. The energies of the conversion electron and x rays or Auger electrons sum to give the total energy of 14 keV. The first excited state in ^{73}Ge is fed from another 499-ms half-life isomeric state at 66.6 keV [95]. The energy spectrum of the first decay of double pulses for which the second-decay energy was 14 keV is shown in Fig. 4.1. A single monoenergetic peak is evident at 53.3 ± 0.2 keV (error bar is statistical), which is due to the transition from the 66.6-keV isomeric state in ^{73}Ge to the first excited state. The nucleus that β decays to ^{73}Ge in the decay chain of ^{73}Ni is ^{73}Ga . Since ^{73}Ga has a half-life of 4.86 hours [95], the signature of the isomeric decay of ^{73}Ge could still be observed after beam delivery to the GeDSSD had ceased. The GeDSSD energy spectrum of the second decay of double pulses is shown for a 2-hour background run performed about 10 minutes after the conclusion of beam delivery in Fig. 4.2. Accordingly, the peak at 14-keV peak is present due to the long half-life of ^{73}Ga .

The 93-keV peak in Fig. 3.24(a) is caused by the isomeric decay of ^{67}Zn . The β -decay chains originating from ^{67}Fe and ^{67}Co resulted in the production of ^{67}Zn . ^{67}Zn has an isomeric state at 93.3 keV with a half-life of 9.07 μs that decays to the ground state [96]. The isomer can be populated either directly or indirectly by β decay. The difference in

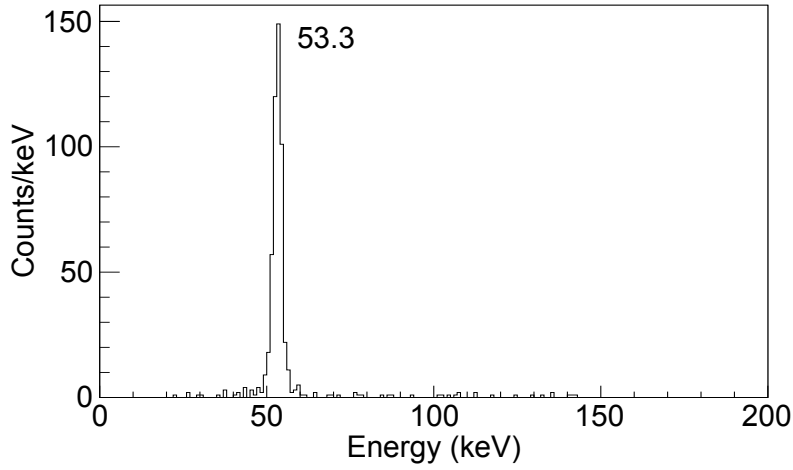


Figure 4.1: Energy spectrum in the back of the GeDSSD for the first decay of double pulses for which the energy of the second decay was 14 keV. The single peak is labelled by its energy in keV.

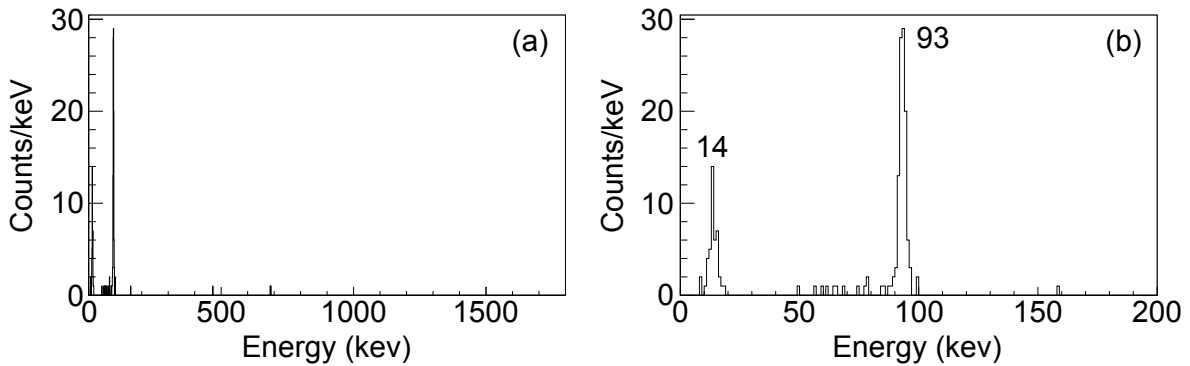


Figure 4.2: Energy spectrum in the back strips of the GeDSSD for the second decay of double pulses for a 2-hour background run performed 10 minutes after the end of beam delivery to the GeDSSD in experiment e11503. The entire energy range from 0 - 1800 keV is shown in (a). A zoom of the region from 0 - 200 keV is shown in (b). Peaks are labelled by their energies in keV.

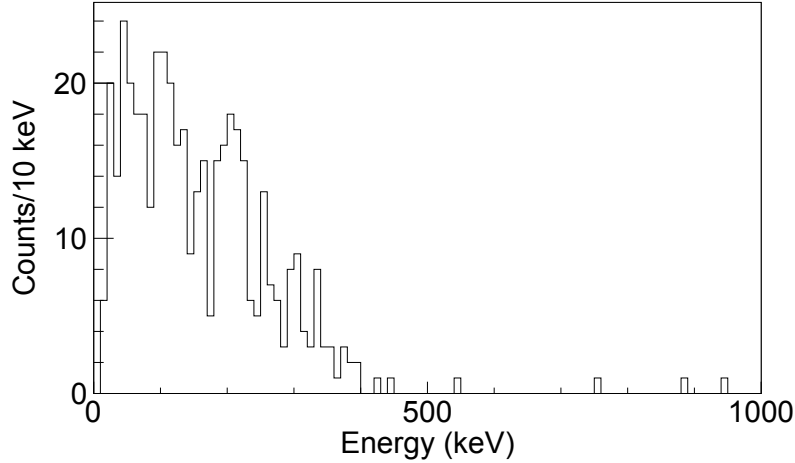


Figure 4.3: Energy spectrum in the back of the GeDSSD for the first decay of double pulses that had a second-decay energy of 93 keV.

the ground-state energies of ^{67}Cu and ^{67}Zn is 562 keV, so the maximum energy that could be deposited in the GeDSSD from a β decay prior to the decay of the isomer is 469 keV. The energy spectrum of the first decay for events in which the second decay had an energy of 93 keV is shown in Fig. 4.3. The spectrum is consistent with what would be expected for measuring β -decay electrons with energies less than 469 keV (and a small background). ^{67}Zn was produced by the β decay of ^{67}Cu , which has a half-life of 61.83 hours. Therefore, the peak at 93 keV is observed in the background energy spectrum of second decays that is shown in Fig. 4.2.

The small peak at 190 keV in Fig. 3.24(b) is most likely due to the decay of ^{69m}Cu , which was populated from the β -decay chains of ^{69}Ni and ^{69}Co . ^{69}Cu has a 357-ns half-life isomeric state at 2742 keV that decays by a 190-keV transition to a 2552-keV state [97]. The 2552-keV state can then decay by the emission of a 681-keV γ ray to populate a 1871-keV state, which subsequently decays to the ground state via a 1871-keV γ ray. The SeGA energy spectrum detected in coincidence with second decays having an energy of 190-keV is shown in Fig. 4.4. The statistics are very low, preventing the identification of precise γ -ray energies,

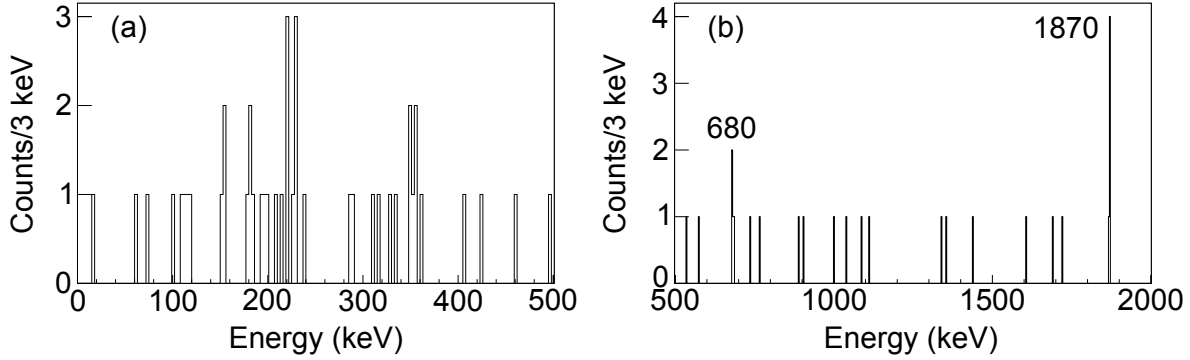


Figure 4.4: γ -ray energy spectrum detected in SeGA in coincidence with the 190-keV peak in the GeDSSD in Fig. 3.24 (b). The spectrum is shown in the ranges of (a) 0 - 500 keV and (b) 500 - 2000 keV. Tentatively identified γ -ray peaks from decays in ^{69}Cu are labelled by approximate energies in keV.

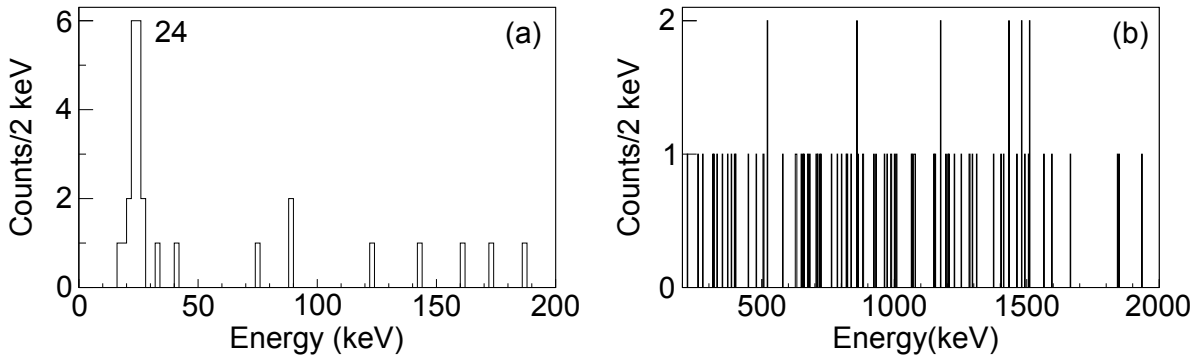


Figure 4.5: Energy spectrum in the back of the GeDSSD for the first decay of double pulses that had a second-decay energy of 175 keV. The spectrum is shown in the ranges of (a) 0 - 200 keV and (b) 200 - 2000 keV. The 24-keV transition is marked by its energy.

but there is evidence for the observation of peaks near 680 and 1870 keV, consistent with the decay scheme of ^{69}Cu .

The relatively weak peak at 175 keV in Fig. 3.24(b) results at least in part from the isomeric decay of ^{71}Ge , which was produced in fragmentation reactions when the secondary ion beam interacted with the crystal of the GeDSSD. The 175-keV first excited state in ^{71}Ge has a half-life of 79 ns [98]. The 175-keV state can be populated by a 23.4-keV transition from a 198-keV state that has a 20.41-ms half-life. The 23-keV transition occurs primarily through internal conversion with $\alpha = 210$ [98]. The energy spectrum of the first decay of

double pulses for which the energy of the second decay was 175 keV is shown in Fig. 4.5. A peak is observed at 24 keV, which is caused by the isomeric decay the 198-keV state in ^{71}Ge . However, the intensity of the 24-keV peak is much weaker than what would be expected if every count in the 175-keV peak in Fig. 3.24(b) was coincident with a 24-keV transition. If an excited state in ^{71}Ge is populated directly from a fragmentation reaction, the state must have a half-life at least of the order of hundreds of microseconds to milliseconds in order for its decay to be observed following the fragmentation reaction. After an interaction with a heavy ion, the high-gain preamplifier signal of the GeDSSD becomes saturated and takes several milliseconds to return to baseline. However, above the 198-keV state, no states in ^{71}Ge have a half-life greater than 1 ns. Therefore, the intensity mismatch between the 24- and 175-keV transitions suggests that additional intensity in the 175-keV peak comes from a different source. In principle, it could be possible for a nucleon(s) to be transferred from the secondary beam to a stable Ge isotope in the GeDSSD crystal to form ^{71}As , which would then undergo electron capture and directly or indirectly populate the 175-keV state in ^{71}Ge . LISE++ calculations [88] predict a cross section on the order of 0.5 mb for the production of ^{71}As . Based on the calculated cross section and the number of ions delivered

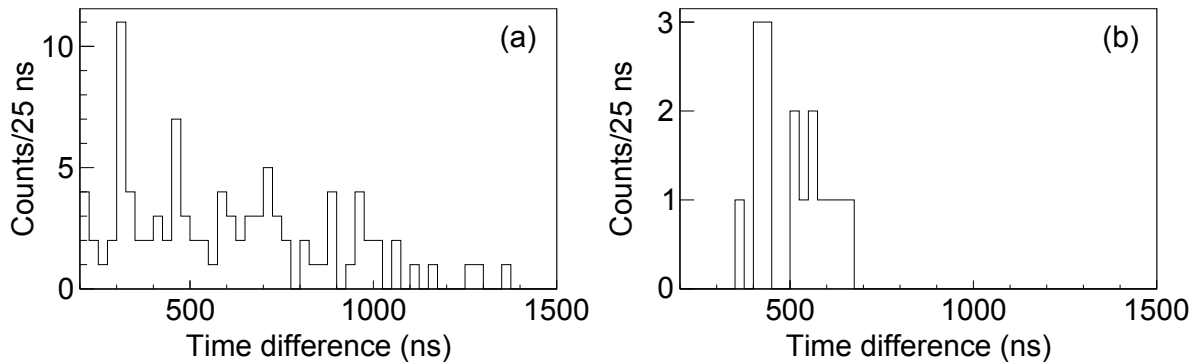


Figure 4.6: Time difference between the first and second decays for double pulses for which the second decay had an energy of 175 keV and the first decay had (a) any energy other than 24 keV (b) an energy of 24 keV.

to the GeDSSD, only a few ^{71}As nuclei would have been expected to have been produced. ^{71}As has a half-life of 65.30 hours, so if a large fraction of the counts at 175 keV in Fig. 3.24(b) are from ^{71}Ge decay populated by ^{71}As electron capture, a 175-keV peak should be observed in Fig. 4.2, which is not the case. Furthermore, the time difference determined between the 175-keV transition and the first decay does not closely match with what would be anticipated if the complete intensity of the 175-keV peak came from the isomeric decay of ^{71}Ge . The time difference between the first and second decays gated on events in which the second decay had an energy of 175 keV and the first decay had any energy except 24 keV is shown in Fig. 4.6(a). The corresponding time-difference spectrum between the first and second decays for which the second decay had an energy of 175 keV and the first decay had an energy of 24 keV is shown in Fig. 4.6(b). As detailed in Section 3.3.8, the minimum allowed time difference was 150 ns. The decay curve requiring the first decay to have an energy of 24 keV appears to have a shorter half-life and roughly be in agreement with the 79-ns half-life that is known for the 175-keV state in ^{71}Ge . However, the decay curve gated on all first-decay energies beside 24 keV seems to have a much longer half-life. To resolve the discrepancies, the isomeric decay of ^{66}Co is also proposed to give rise to counts at 175 keV in Fig. 3.24(b). ^{66}Co has an isomeric state at 175 keV with a half-life of 1.21 μs [13]. The longer half-life as compared to the half-life of the 175-keV state in ^{71}Ge results in the different shape of the decay curve in Fig. 4.6(a) relative to Fig. 4.6(b). In experiment e11503, the isomer in ^{66}Co was populated through the β decay of ^{66}Fe , which explains the energy distribution that is observed at energies greater than 24 keV in Fig. 4.5.

The peaks at 581 and 1602 keV in Fig. 3.24 result from the decay of the first excited state in ^{68}Ni . The results for ^{68}Ni are presented in detail in the next section.

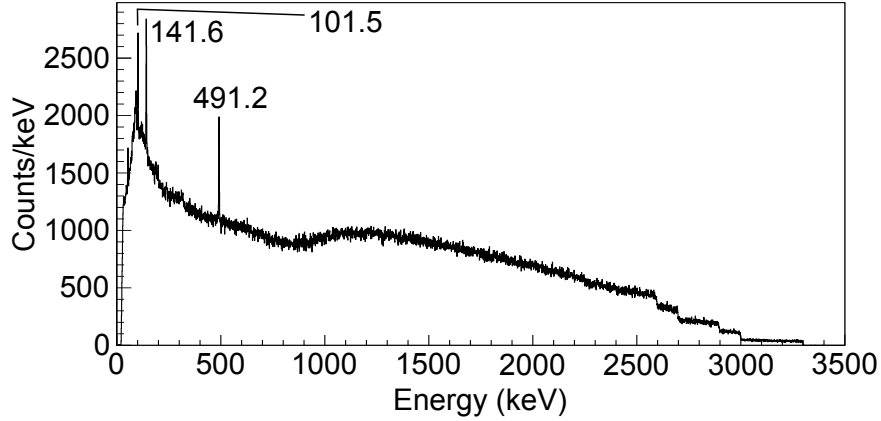


Figure 4.7: Energy spectrum in the back strips of the GeDSSD for signals that were detected within 2 s of a ^{68}Co ion implantation in the GeDSSD and that were characterized as being caused by a single radioactive decay. Peaks are labelled by their energies in keV.

4.2 Decay of excited states in ^{68}Ni following β decay of ^{68}Co

The energy spectrum measured in the back of the GeDSSD for decays occurring within 2 s of the arrival a ^{68}Co ion at the GeDSSD and that were identified as being due to a single radioactive decay is shown in Fig. 4.7. The spectrum is very similar to the one shown in Fig. 3.23 that was measured for all single decays in the GeDSSD. Given the long half-lives of the isomeric states in ^{70}Cu and ^{67}Co that decay by the 102-, 142-, and 491-keV transitions compared to the average time between ion implantations in the GeDSSD in experiment e11503, random correlations would be expected between ^{68}Co ions and these isomeric decays.

The decay of the 0_2^+ state in ^{68}Ni was observed following population by β decay through a selection of experimental decay signals identified as double pulses. The energy spectrum of the second decay of double pulses that were detected within 2 s of a ^{68}Co ion implantation in the GeDSSD is shown in Fig. 4.8(a). The spectrum is similar to the one in Fig. 3.24(a),

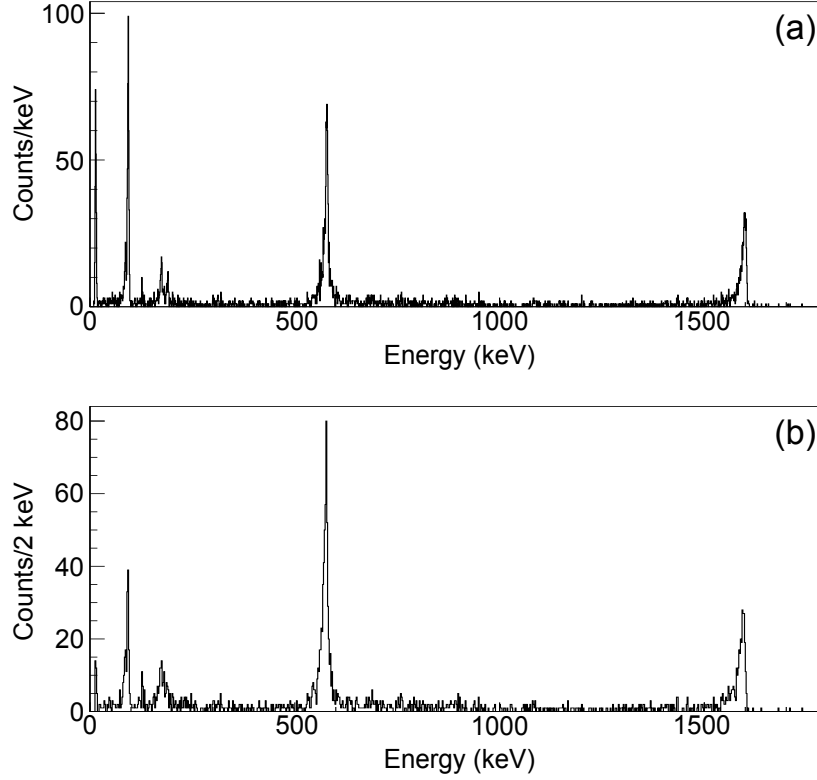


Figure 4.8: Energy of the decay occurring second in time for double pulses in the back strips of the GeDSSD that occurred within 2 s of the implantation of a ^{68}Co in the GeDSSD. The determined time difference between the first and second decays was (a) allowed to be any value greater than 150 ns (b) limited to values between 150 and 600 ns.

which shows the energy of the second decay for all double pulses, but the intensities of the 581- and 1602-keV peaks relative to the 14-keV peak are much larger in Fig. 4.8(a) than in Fig. 3.24(a), and the intensities of the 581- and 1602-keV peaks relative to the 93-keV peak are slightly larger in Fig. 4.8(a). The half-life of the first excited 0^+ state in ^{68}Ni was previously found to be 270 ns [50]. The energy spectrum of the second decay of double pulses that were detected within 2 s of the arrival of a ^{68}Co ion at the GeDSSD and for which the time difference between the first and second decays was less than 600 ns is shown in Fig. 4.8(b). The 581- and 1602-keV peaks are preferentially selected by the time gate, suggesting that the 581- and 1602-keV transitions are consistent with the decay of the first excited 0^+ state in ^{68}Ni . Further evidence that the peaks at 581 and 1602 keV result from the isomeric

decay of the first excited state in ^{68}Ni populated by the β decay of ^{68}Co is given in the following paragraphs.

The β decay of ^{68}Co can directly or indirectly populate the 0_2^+ state in ^{68}Ni . Not all β decays result in the population of the 0_2^+ state. For instance, the 2_1^+ state in ^{68}Ni can be populated in β decay and subsequently decay to the ground state, bypassing the 0_2^+ state [21]. Further, if the 1.6-s β -decaying isomer in ^{68}Co has a ground-state spin and parity of 1^+ [66], direct ground-state feeding of ^{68}Ni is possible. The focus of this work, however, was the decay of the 0_2^+ state in ^{68}Ni populated through β decay. γ -ray decay between the first excited 0^+ state and ground 0^+ state in ^{68}Ni cannot occur, but the decay can instead proceed by either internal conversion or internal pair production. The 1602-keV peak in Fig. 4.8 arises from the internal-conversion decay of the first excited 0^+ state in ^{68}Ni . The energy of 1602 keV results from the simultaneous detection of the conversion electron and the cascade of x rays or Auger electrons that are emitted when the atomic-electron vacancy is filled. The 581-keV peak is caused by the pair-production decay of the first excited 0^+ state. The difference in energy between the internal-conversion and pair-production peaks, 1021 ± 5 keV, matches the energy required to create the electron-positron pair, 1022 keV, in the pair-production decay mode. Neither the 581- nor 1602-keV peaks can be due to the detection of γ rays. At these energies, the γ -ray detection efficiency of the GeDSSD is much lower than that of SeGA. However, no peaks were observed at 581 or 1602 keV in the SeGA energy spectrum measured in coincidence with decays detected within 2 s of a ^{68}Co ion implantation in the GeDSSD. The coincident SeGA energy spectrum is shown in Fig. 4.9. Based on the simulated γ -ray detection efficiencies of the GeDSSD and SeGA, if the 581- and 1602-keV peaks in Fig. 4.8 were caused by γ rays, about 2000 and 3500 counts would be expected at 581 and 1602 keV, respectively, in Fig. 4.9. The peak at 595 keV in

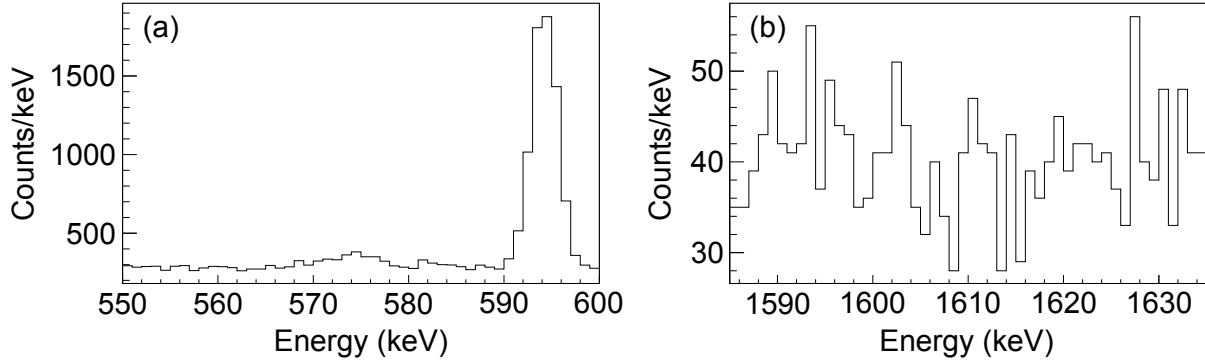


Figure 4.9: SeGA energy spectrum observed in coincidence with single decays in the GeDSSD that were detected within 2 s of the implantation of a ^{68}Co ion in the GeDSSD shown in the range of (a) 550 - 600 keV and (b) 1585 - 1635 keV.

Fig. 4.9 (a), which has an intensity of approximately 5500 counts, is due to a previously observed γ -ray transition in ^{68}Ni that was proposed to connect a state at 3444 keV with the isomeric 5^- state at 2848 keV [21].

The time-difference spectra between the first and second decays with gates placed on the 581- and 1602-keV peaks are shown in Fig. 4.10. When the decay curves are fit to an exponential plus a constant background, half-lives of 270 ± 16 and 285 ± 25 ns are found for the 581- and 1602-keV gates, respectively. The two half-lives are the same within the uncertainties of the measurements and each agrees with the previously determined half-life of 270 ± 5 ns for the first excited 0^+ state in ^{68}Ni . The weighted average of the two half-lives is 274 ± 13 ns.

γ rays were detected by SeGA in coincidence with the internal-conversion and pair-production peaks in the GeDSSD. The SeGA energy spectra coincident with either the 581-keV peak or the 1602-keV peak in the GeDSSD are shown in Fig. 4.11. 511-keV annihilation photons, which are emitted when the positron annihilates following the pair-production decay of the first excited 0^+ state in ^{68}Ni , are coincident with the 581-keV peak in the GeDSSD. The number of detected 511-keV coincidences is consistent with two 511-keV counts for

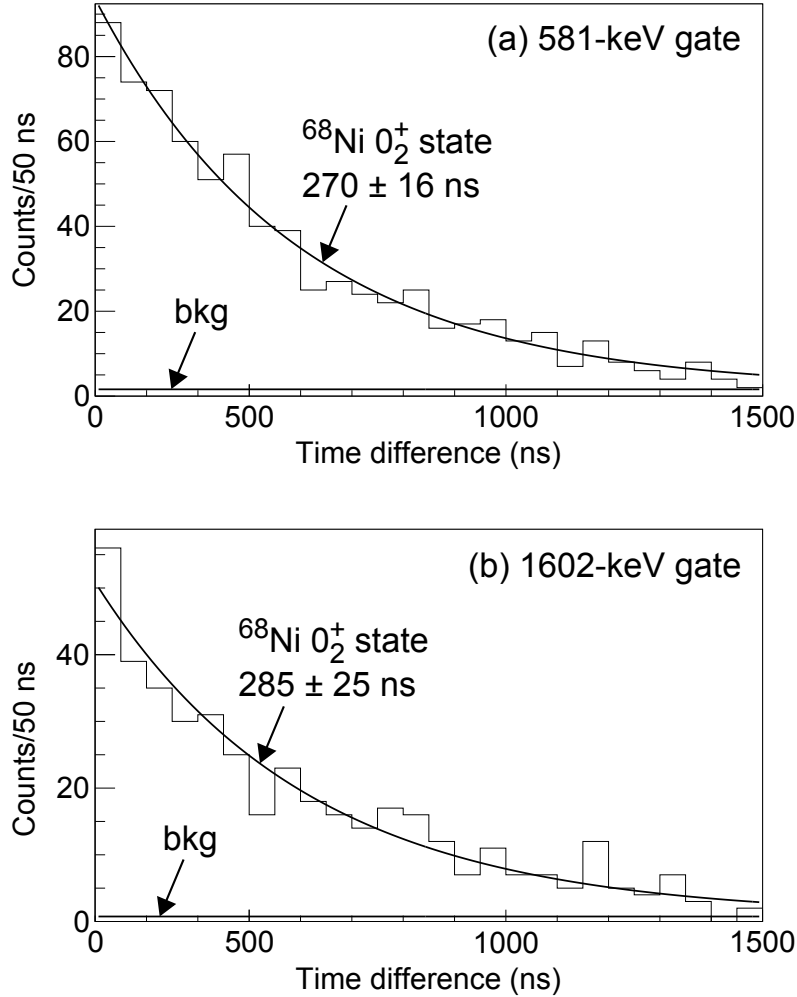


Figure 4.10: Decay curves showing the time difference between the first and second decays when gates are placed on the (a) 581-keV and (b) 1602-keV peaks in Fig. 4.8(a).

every 581-keV count. No coincident peak is detected at 511 keV in SeGA when gating on the 1602-keV internal-conversion peak in the GeDSSD. The coincident SeGA energy spectra in the range of 1000 - 2500 keV are shown in Fig. 4.11(b) and (d) for gates on the 581- and 1602-keV peaks in the GeDSSD, respectively. Two γ rays are coincident with both the 581- and 1602-keV peaks. The SeGA energy spectrum in coincidence with the sum of the 581- and 1602-keV peaks is shown in Fig. 4.11(e). Based on Fig. 4.11(e), energies of 1138.5 ± 1.0 and 2421.8 ± 2.2 keV are determined for the two coincident γ -ray transitions.

The low-energy level scheme of ^{68}Ni displaying the transitions that were detected in

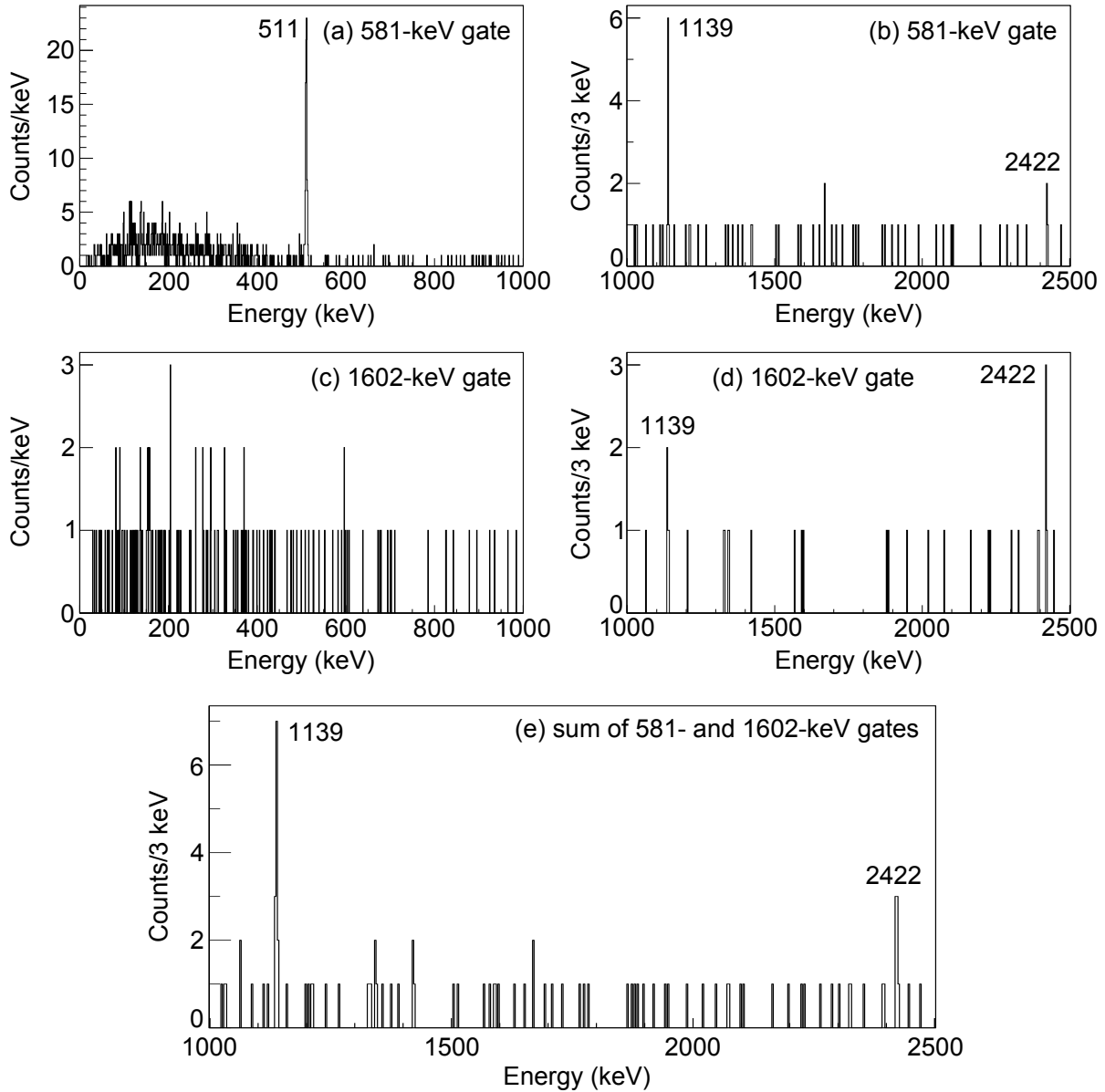


Figure 4.11: γ -rays detected by SeGA in coincidence with the peaks in the GeDSSD due to the internal-conversion and pair-production decays of the first excited 0^+ state in ^{68}Ni . The SeGA energy spectrum is shown in the range of (a) 0 - 1000 keV and (b) 1000 - 2500 keV for coincidence with the 581-keV pair-production peak in the GeDSSD. The SeGA energy spectrum is also shown in the range of (c) 0 - 1000 keV and (d) 1000 - 2500 keV for coincidence with the 1602-keV internal-conversion peak in the GeDSSD. The SeGA energy spectrum is shown in (e) in the range of 1000 - 2500 keV for coincidence with both the 581-keV pair production peak and the 1602-keV internal-conversion peak in the GeDSSD.

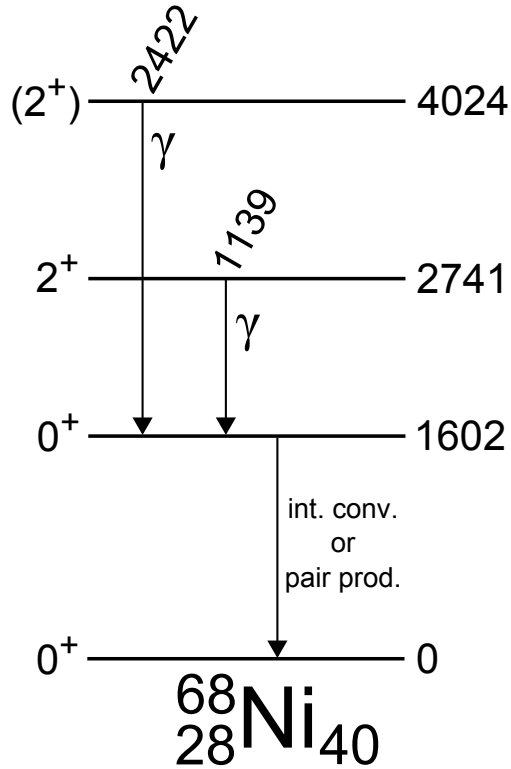


Figure 4.12: Level scheme of ^{68}Ni showing the transitions observed in experiment e11503. States are labelled on the left by their spins and parities and on the right by their energies in keV. Transition energies are given in keV above the transitions.

experiment e11503 are displayed in Fig. 4.12. Both the 1139- and 2422-keV transitions are proposed to directly feed the first excited 0^+ state in ^{68}Ni . An 1139-keV γ -ray was previously observed following the β decay of ^{68}Co , but was tentatively placed feeding the isomeric 5^- state at 2848 keV in ^{68}Ni [21]. However, based on its measured energy and coincidence with the decay of the 0_2^+ state in ^{68}Ni , the 1139-keV γ ray is proposed to depopulate a state with an energy of 2741 ± 4 keV. The determined energy of the state is consistent with that of the second excited 2^+ in ^{68}Ni at 2742.9 keV [69]. Therefore, the 1139-keV γ ray is identified as the transition that connects the 2_2^+ and 0_2^+ states in ^{68}Ni . After the analysis of the data from experiment e11503, the 1139-keV transition was independently verified to feed the first excited 0^+ state in Ref. [71]. If the 2422-keV transition also directly feeds the first excited

Table 4.1: Theoretical half-lives calculated from Weisskopf estimates for the decay of an excited state in ^{68}Ni by a 2422-keV transition.

Radiation Type	$T_{1/2}^{Weisskopf}$ (s)
$E2$	4.1×10^{-13}
$M3$	4.9×10^{-7}
$E4$	2.9×10^{-4}

0^+ state, it depopulates a state with an energy of $4024 \pm 5\text{keV}$. A 4026-keV state was previously proposed to be populated in the β decay ^{68}Co [21], so the 2422-keV transition is identified as occurring between this state and the 0_2^+ state in ^{68}Ni . The 4026-keV state was proposed to have a spin and parity of 2^+ , 3^+ , or 4^+ in Ref. [21]. Assuming one of these spins and parities, a transition to the 0_2^+ state would occur by either an $E2$, $M3$, or $E4$ transition. Weisskopf half-life estimates for the decay of the state via a 2422-keV $E2$, $M3$, or $E4$ transition are shown in Table 4.1. From the theoretical half-lives predicted by the Weisskopf estimates, an $E2$ transition seems most probable, so the 4024-keV state in Fig. 4.12 is tentatively assigned a spin and parity of 2^+ .

From the energy of the $E0$ transition between the first excited 0^+ state and the ground state in ^{68}Ni and the half-life of the excited state, $\rho^2(E0)$ for the transition can be calculated. Using the energy of 1602 ± 4 keV and half-life of 274 ± 13 ns determined in the present experiment, and calculating $\Omega_{IC}(E0)$ and $\Omega_{\pi}(E0)$ from Ref. [2], $\rho^2(E0)$ is found to be $7.4 \pm 0.4 \times 10^{-3}$. If the previously reported literature value [49] for the energy of the 0_2^+ state in ^{68}Ni is instead used to calculate $\rho^2(E0)$, a value of 4.3×10^{-3} is obtained when the half-life of 274 ns is used. Thus, the change in the energy of the first excited 0^+ state results in an increase in the value of $\rho^2(E0)$ by a factor of about 1.7.

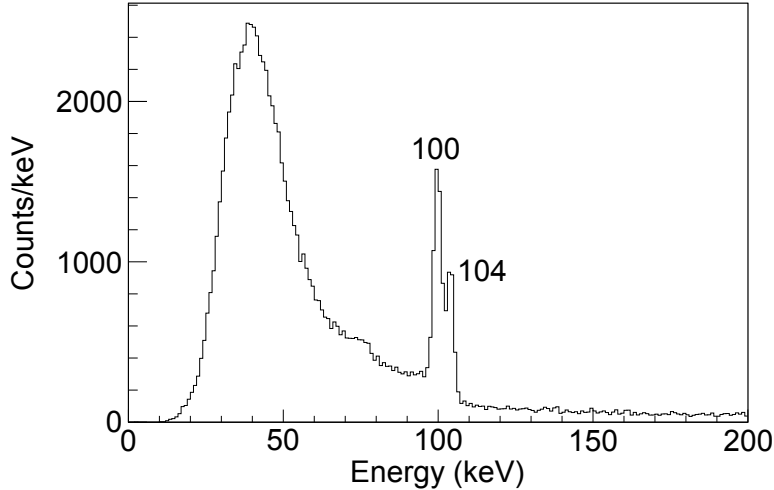


Figure 4.13: Isomeric γ -ray energy spectrum detected within the 10- μ s event window for events in which a ^{60}V ion was implanted into the DSSD.

4.3 Isomeric γ -ray decay in ^{60}V

The SeGA γ -ray energy spectrum observed within the 10- μ s event window for events in which a ^{60}V ion was implanted into the DSSD in experiment e08020 is shown in Fig. 4.13. The very broad feature centered near 40 keV is caused by the prompt flash that is emitted when the ^{60}V ions are stopped in the DSSD. The narrow peaks at 100 and 104 keV in Fig. 4.13 are due to γ rays that are associated with the decay of a metastable state in ^{60}V . The intensities of the 100- and 104-keV γ rays are inferred to approximately 7.7 and 3.5%, respectively, normalized to the total number of detected ^{60}V ions.

The 100- and 104-keV γ -rays were previously reported in a study with much lower statistics [99]. Although γ - γ coincidence measurements were not possible in the earlier work, the 100-keV transition (99-keV in the earlier work) was proposed to feed a 104-keV state (103-keV in the earlier work) [99]. With the increased statistics in the present experiment, γ - γ coincidence spectra were obtained, and the isomeric γ - γ coincidence spectra gated on the 100- and 104-keV transitions are shown in Figs. 4.14(a) and (b), respectively. No coinci-

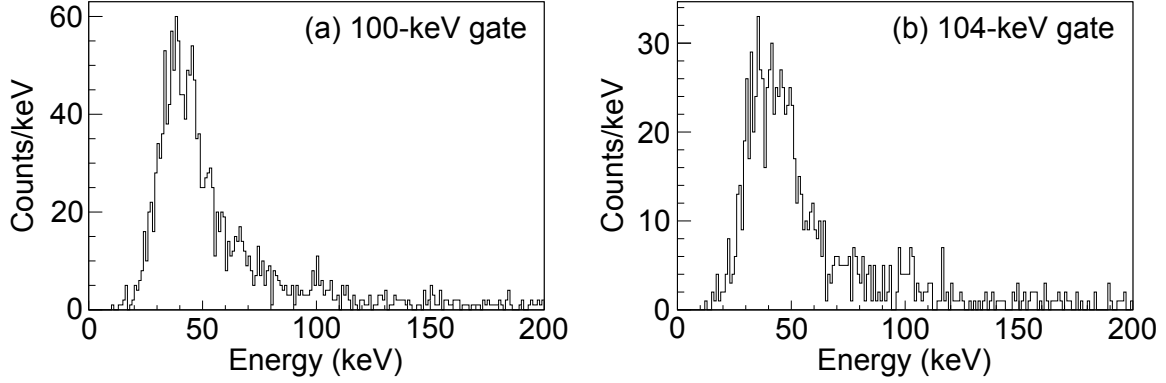


Figure 4.14: γ - γ coincidence spectra detected within the $10\text{-}\mu\text{s}$ event window for events in which a ^{60}V ion was implanted into the DSSD gated on the (a) 100- and (b) 104-keV transitions.

dence relationship between the 100- and 104-keV γ rays is observed, refuting the previously proposed decay scheme.

The time-difference spectra between the implantation of a ^{60}V ion in the DSSD and the detection of a 100- or 104-keV γ ray in SeGA are shown in Figs. 4.15(a) and (b), respectively, for γ rays detected within the $10\text{-}\mu\text{s}$ event window. The shapes of the decay curves result from both the half-life of the decaying isomeric state in ^{60}V and the resolution for measuring time differences between the detection of ions in the DSSD and γ rays in SeGA. The Gaussian-like distribution that is apparent near $0\text{ }\mu\text{s}$ is due to the time resolution, while the long tail of the decay curve is evident because of the decay of the isomer. Since the half-life of the isomeric state was long enough to produce the tails in the decay curves, gated half-lives were extracted by fitting the decay curves in the regions above 500 ns [100]. The fits consisted of an exponential plus a constant background and the results of the fits are shown in Figs. 4.15(a) and (b). Based on the fits, half-lives of 185 ± 8 and $180 \pm 20\text{ ns}$ were determined for the respective 100- and 104-keV gates. Contrary to what was proposed from limited statistics in Ref. [99], the gated half-lives are identical within the errors, suggesting the γ rays are emitted as the result of the decay of a single isomeric state in ^{60}V with a

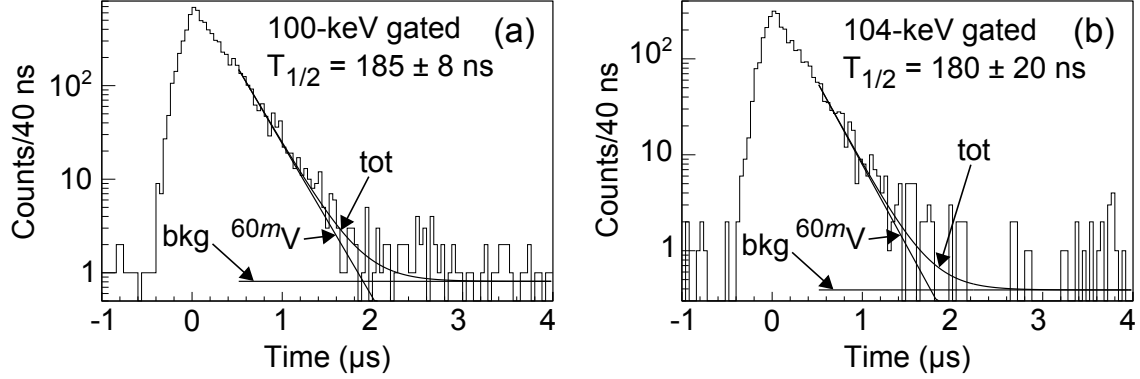


Figure 4.15: Decay curves corresponding to the time difference between the detection of a ^{60}V ion in the DSSD and (a) a 100- or (b) a 104-keV γ ray in SeGA for γ rays that were detected within the 10- μs event window. The fits of the decay curves, labelled by “tot,” included an exponential for the decay of ^{60m}V and a constant background.

half-life of about 185 ns. Additional information about ^{60}V was obtained by studying the β decay of ^{60}V to ^{60}Cr .

4.4 β decay of ^{60}V to ^{60}Cr

The β -delayed γ -ray energy spectrum detected within 500 ms of the implantation of a ^{60}V ion in the DSSD in experiment e08020 is shown in Fig. 4.16. γ -ray transitions were identified in the daughter nucleus ^{60}Cr based on γ -gated β -decay curves, observed γ - γ coincidences, and previous experimental data. The transitions arising from decays in ^{60}Cr are given in Table 4.2 along with their respective absolute intensities. In addition to the γ rays listed in Table 4.2, two transitions at 102 and 208 keV are evident in Fig. 4.16 and are due to γ -ray decays in ^{59}Cr [101], which was populated from the β -delayed neutron decay of ^{60}V . Based on the absolute intensities of the 102- and 208-keV transitions, a lower limit of 5% is determined for the ^{60}V β -delayed neutron-decay branching ratio.

Background-subtracted β -delayed γ - γ coincidence spectra gated on each observed γ -ray transition in ^{60}Cr are shown in Figs. 4.17 and 4.18. The 644-keV transition was found to be

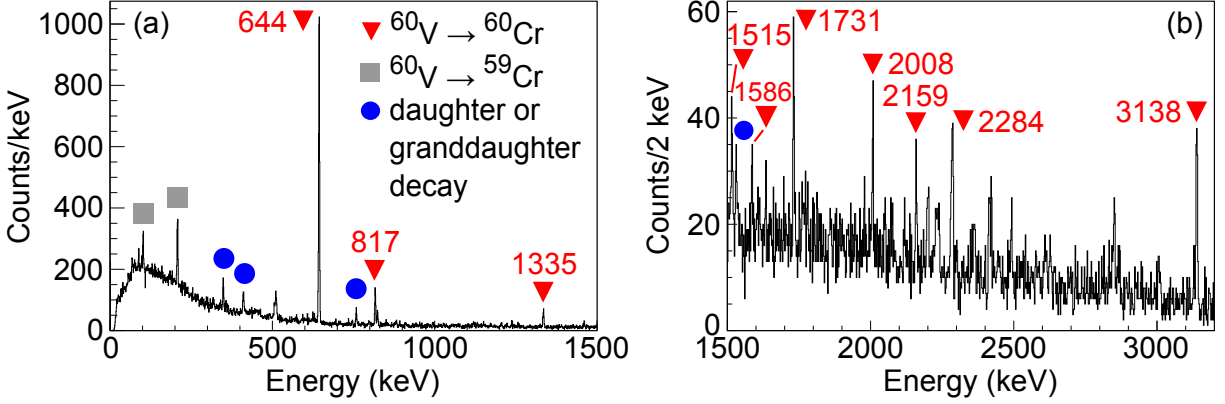


Figure 4.16: β -delayed γ -ray energy spectrum detected within 500 ms of the implantation of a ^{60}V ion in the DSSD shown in the ranges of (a) 0 - 1500 keV and (b) 1500 - 3200 keV. γ -ray transitions in the daughter ^{60}Cr nucleus are labelled with red triangles and the transition energy in keV. γ -ray transitions in ^{59}Cr that are populated from the β -delayed neutron decay of ^{60}V are marked by gray squares. γ rays emitted following the β decay of a daughter or granddaughter nucleus are indicated by the blue circles.

coincident with the 817-, 1335-, and 1731-keV transitions. There are also indications that the 644-keV γ ray is coincident with the 1586-, 2284-, and 3138-keV transitions, though with low confidence. Based on measured absolute intensities, if the 1586-, 2284-, and 3138-keV γ rays each directly feed the state depopulated by the 644-keV γ ray, 4 ± 2 , 11 ± 2 , and 9 ± 2 coincidence counts, respectively, would be expected with the 644-keV γ ray. Neither the 1515-, 2008-, nor 2159-keV γ rays were detected in coincidence with any other transition, but the statistics are very limited due to the low absolute intensities of the transitions.

The β -decay curve observed for decays that occurred within 1 s of the implantation of a ^{60}V ion in the DSSD is shown in Fig 4.19. The decay curve was fit considering the β decay of ^{60}V , ^{60}Cr , and ^{60}Mn and a constant background. The half-lives of ^{60}Cr and ^{60}Mn were fixed at the known literature values of 490 and 280 ms [102], respectively. A half-life of 85 ± 2 ms was extracted for ^{60}V from the decay-curve fit. The inclusion or omission of the small inferred ^{60}V β -delayed neutron-decay branch had no significant impact on the half-life that was determined for ^{60}V and therefore was not included in the fit. It was previously

Table 4.2: Energies and absolute intensities of the γ -ray transitions identified in ^{60}Cr following the β decay of ^{60}V . The energies of the initial and final states between which each transition occurs are also listed.

E_γ (keV)	$I_\gamma^{absolute}$ (%)	Initial State (keV)	Final State (keV)
644.1 ± 0.3	48 ± 2	644	0
817.0 ± 0.3	6.4 ± 0.7	1461	644
1335.0 ± 0.4	5.3 ± 0.7	1979	644
1515.1 ± 0.5	1.1 ± 0.5	2159	644
1585.7 ± 0.7	1.0 ± 0.5	2230	644
1731.2 ± 0.4	2.2 ± 0.7	2375	644
2007.5 ± 0.4^a	2.2 ± 0.7		
2159.4 ± 0.6	1.8 ± 0.8	2159	0
2283.8 ± 0.7	4.1 ± 0.8	2928	644
3138.4 ± 0.5	4.9 ± 0.9	3783	644

^a Transition not placed in ^{60}Cr level scheme

proposed that ^{60}V has multiple β -decaying isomers [103]. The ^{60}V half-life was measured to be 68 ± 4.5 ms in Ref. [103], in contrast to the much larger value of 122 ± 18 ms that was determined in Ref. [101]. Thus, the existence of two β -decaying states, one with a half-life of 68 ms or less and one with a half-life of 122 ms or more, was inferred [103]. Two such β -decaying states could exist if there was a high-spin difference but low-energy difference between the two states. Accordingly, the ^{60}V β -decay half-life was investigated following the β decay of the mother ^{60}Ti nucleus [103]. Since ^{60}Ti has a 0^+ ground state, it was argued that ^{60}Ti β decay should preferentially populate the low-spin β -decaying isomer in ^{60}V . It was determined that in order to obtain a good fit of the ^{60}Ti decay curve, a ^{60}V half-life of 40 ± 15 ms was required. Therefore, the short-lived ^{60}V β -decaying state was proposed to be the low-spin state [103]. The ^{60}V half-life of 85 ± 2 ms observed in the present experiment suggests both β -decaying isomers were populated in nearly equal proportions in fragmentation.

^{60}V β -decay curves additionally requiring the coincident detection of a 644-, 817-, or

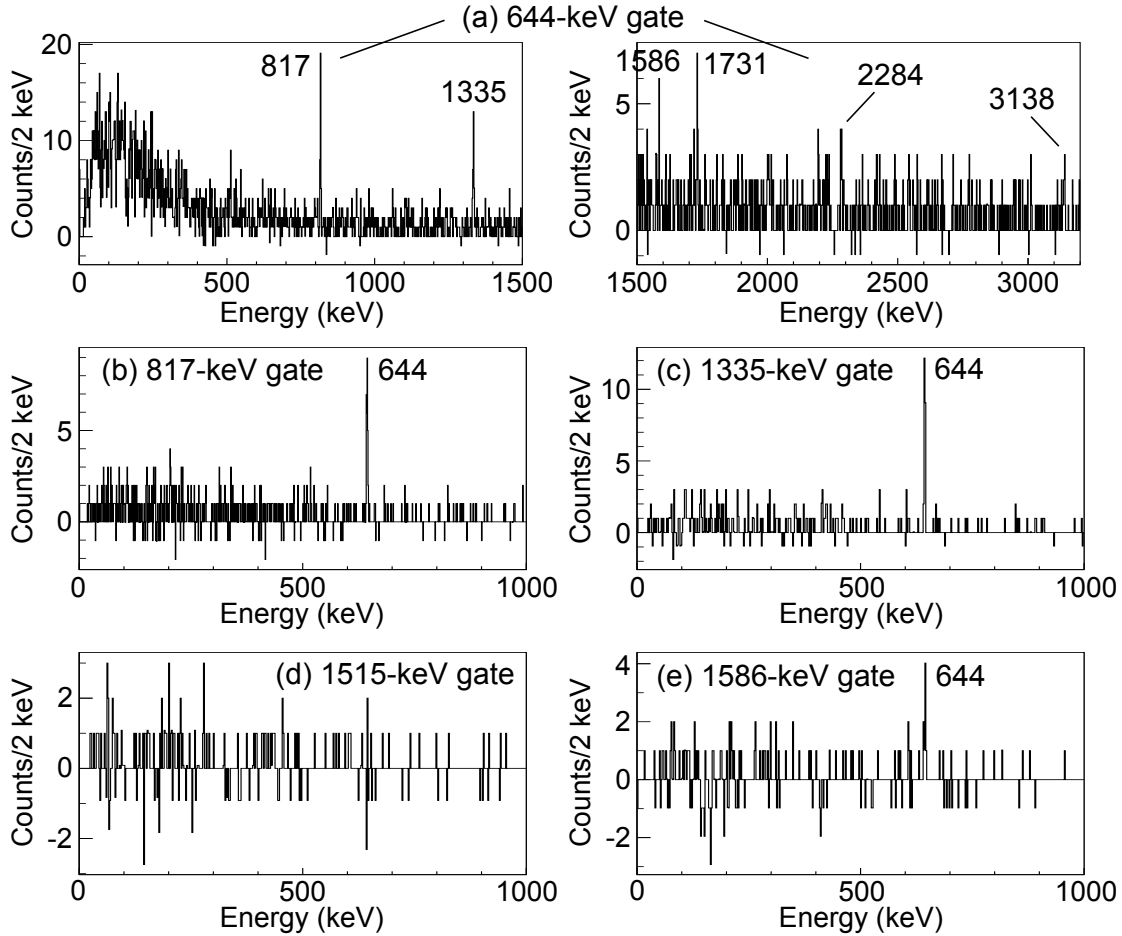


Figure 4.17: Background-subtracted ^{60}V β -delayed γ - γ coincidence spectra gated on the (a) 644-, (b) 817-, (c) 1335-, (d) 1515-, and (e) 1586-keV transitions

1335-keV γ ray in SeGA are shown in Figs. 4.20(a), (b), and (c), respectively. The decay curves were each fit to an exponential for the decay of ^{60}V and a constant background. If a γ -gated half-life was significantly different from the half-life extracted from the ungated ^{60}V decay curve, it could provide evidence that the state depopulated by the gating γ -ray transition is populated by just one of the tentatively identified β -decaying isomers in ^{60}V . However, the gated decay curves shown in Figs 4.20(a), (b), and (c) yield half-lives that are consistent with the one determined from the ungated ^{60}V decay curve in Fig. 4.19, suggesting the states depopulated by the 644-, 817-, and 1335-keV γ rays are either directly or indirectly populated following the decay of both β -decaying isomers in ^{60}V . β -

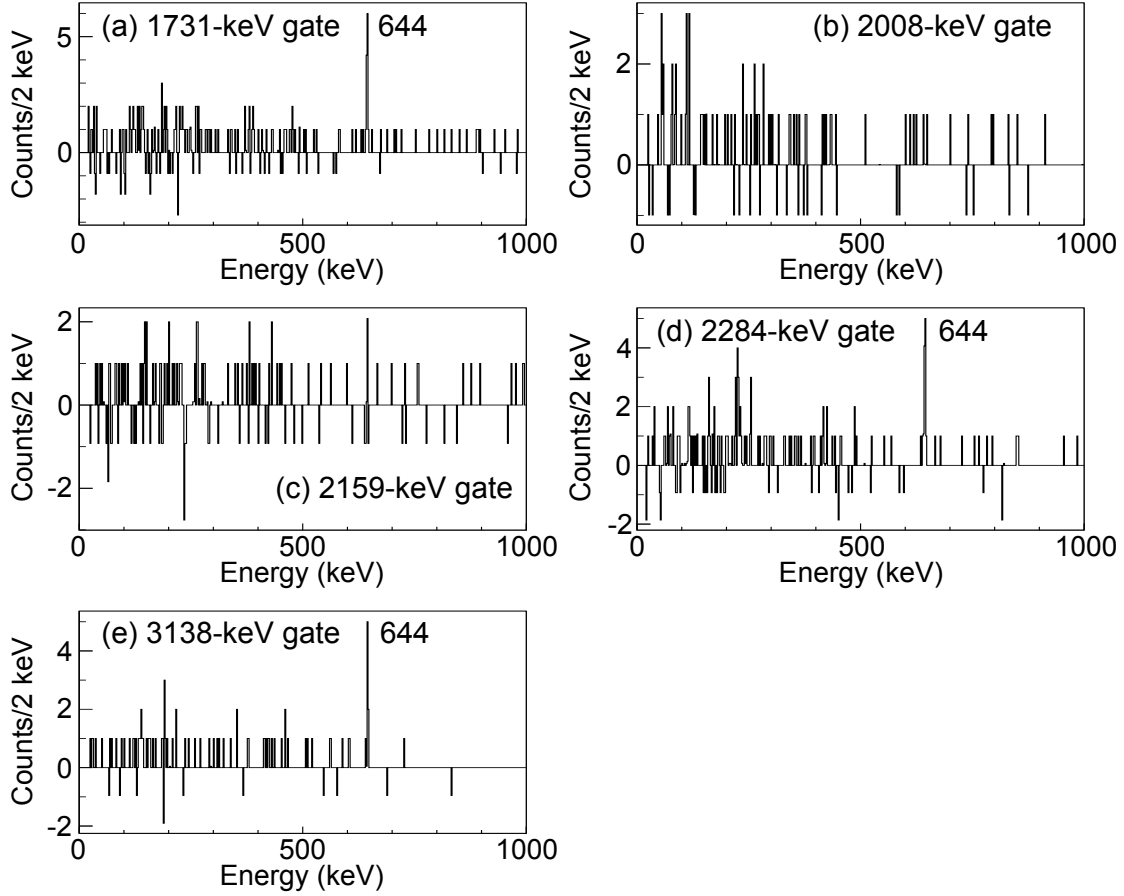


Figure 4.18: Background-subtracted ^{60}V β -delayed γ - γ coincidence spectra gated on the (a) 1731-, (b) 2008-, (c) 2159-, (d) 2284-, and (e) 3138-keV transitions

decay curves requiring the coincident detection of the other γ -ray transitions identified in ^{60}Cr were similarly investigated, but the uncertainties in the determined half-lives are larger. The ^{60}V half-life extracted for all the γ -gated β -decay curves are summarized in Table 4.3. In general, the half-lives are consistent with the half-life determined from the ungated ^{60}V decay curve, though most of the associated uncertainties are large.

The low-energy level scheme of ^{60}Cr populated by the β decay of ^{60}V is shown in Fig. 4.21. The 644-keV γ ray corresponds to the $2_1^+ \rightarrow 0_1^+$ transition in ^{60}Cr [59, 103] and was previously observed following β decay [103]. The 817-keV transition was also observed in an earlier experiment [59] and is the $4_1^+ \rightarrow 2_1^+$ transition in ^{60}Cr . All higher energy transitions

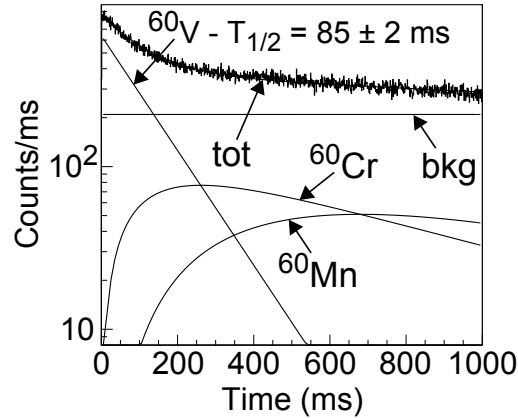


Figure 4.19: ^{60}V decay curve showing fragment- β correlations for β decays detected within 1 s of a ^{60}V ion implantation in the DSSD. The fit to the decay curve, labelled “tot,” included the exponential decay of ^{60}V , the exponential growth and decay of ^{60}Cr and ^{60}Mn , and a constant background.

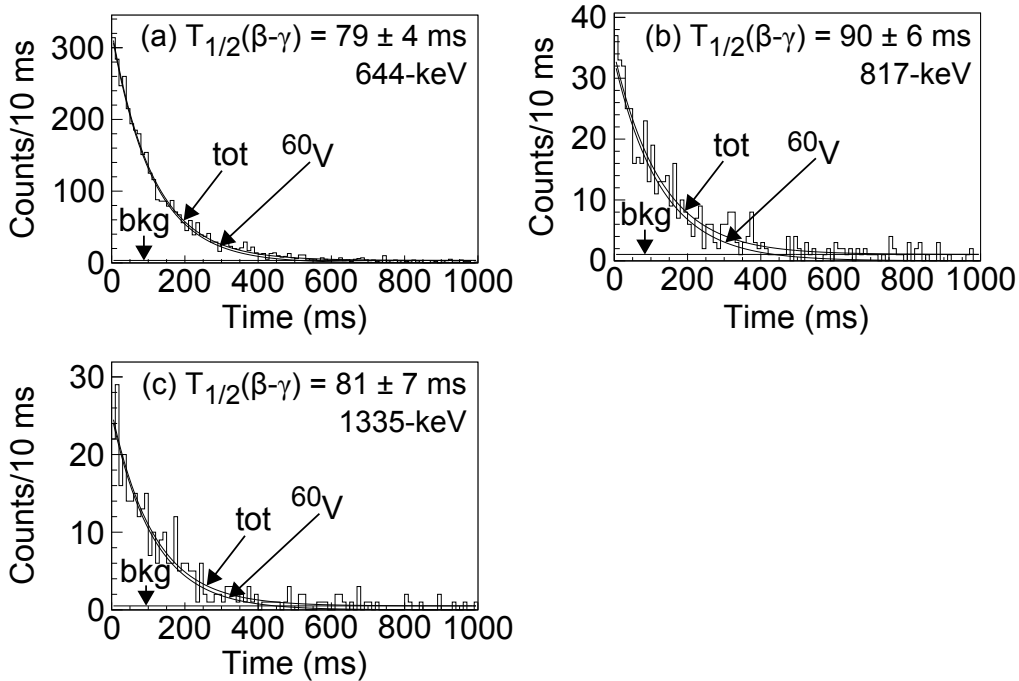


Figure 4.20: ^{60}V decay curves from 0 - 1000 ms showing fragment- β correlations for events in which a coincident γ ray with an energy of (a) 644, (b) 817, or (c) 1335 keV was also detected. Each decay curve was fit to an exponential for the decay of ^{60}V and a constant background.

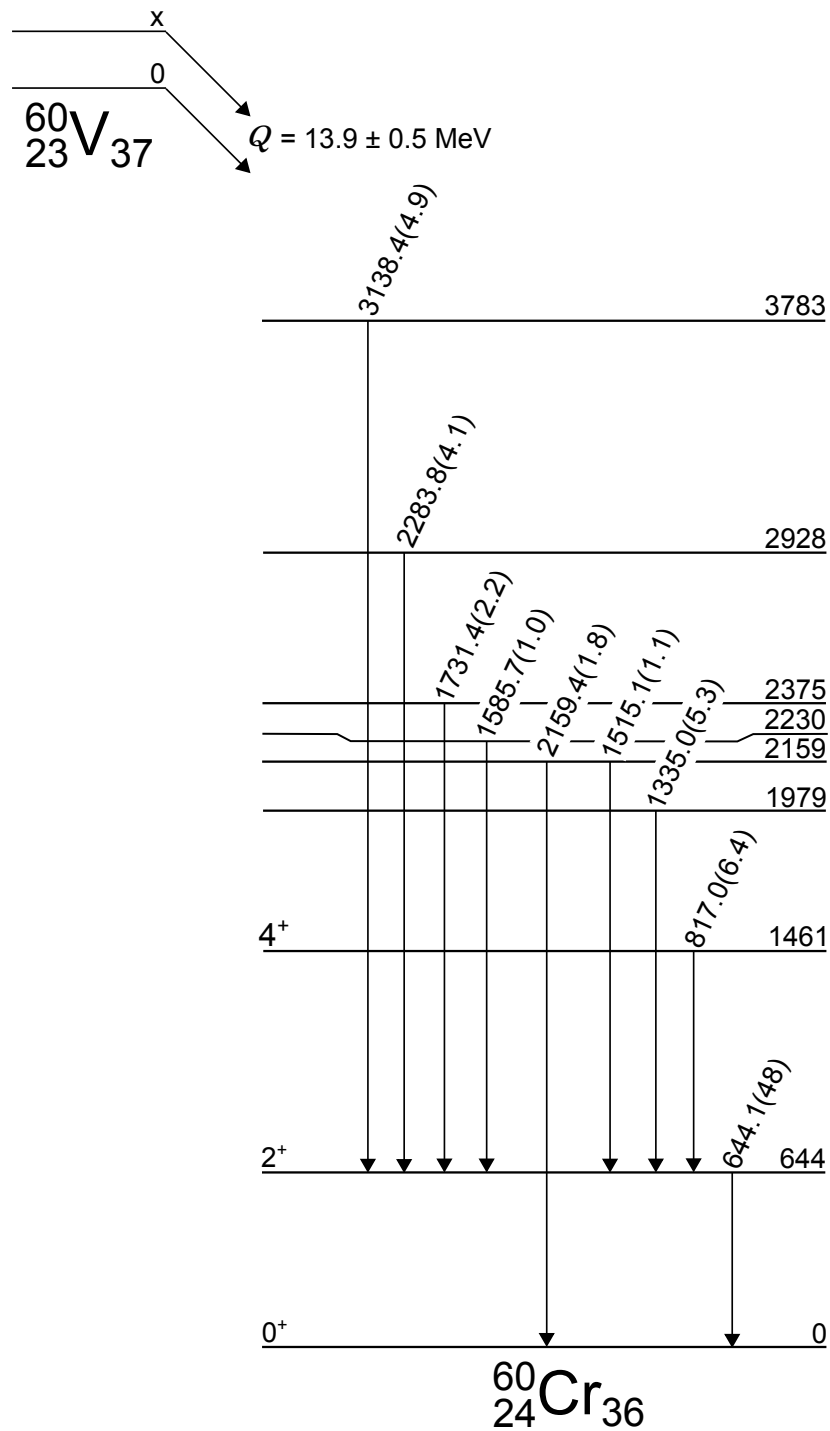


Figure 4.21: Level scheme of ^{60}Cr populated by the β decay of ^{60}V . States are labelled on the left by their spins and parities and on the right by their energies in keV. γ -ray transition energies in keV are shown above the transitions. The absolute γ -ray intensity of each transition is shown in parentheses after the transition energy. The Q -value for the β decay of ^{60}V to ^{60}Cr was taken from Ref. [14].

Table 4.3: Half-life of ^{60}V extracted from the β -decay curve additionally requiring the coincident detection of a γ ray with energy $E_{\text{coinc}\gamma}$. The half-lives were determined from fits of the respective decay curves to an exponential plus constant background.

$E_{\text{coinc}\gamma}$ (keV)	$T_{1/2}$ (ms)
644	79 ± 4
817	90 ± 6
1335	81 ± 7
1515	91 ± 21
1586	57 ± 19
1731	81 ± 15
2008	60 ± 32
2159	95 ± 16
2284	82 ± 10
3138	118 ± 20

in Table 4.2 are observed for the first time in the present study. Tentative placements of the newly observed transitions in the ^{60}Cr level scheme are given in Fig. 4.21. Based on the observed coincidences with the 644-keV γ ray, the 1335- and 1731-keV γ rays are proposed to feed the 2_1^+ state from 1979- and 2375-keV states, respectively. Similarly, from the tentative coincidences between the 644-keV transition and the 1586-, 2284-, and 3138-keV transitions, additional states are proposed at 2230, 2928, and 3783 keV. Although coincidence was not observed between the 644- and 1515-keV γ rays, the 1515-keV transition is proposed to feed the 2_1^+ state. The sum of the 644- and 1515-keV transitions is 2159 keV, identical to the energy of another transition identified in ^{60}Cr . Accordingly, the 2159-keV γ -ray is proposed to directly feed the ground state and be parallel to the 1515-644-keV cascade. Based on the proposed decay scheme, the apparent ground-state feeding of ^{60}Cr from the β decay of ^{60}V is 45%, but this should be regarded as an upper limit, since low-intensity and high-energy γ -ray transitions in ^{60}Cr may have been missed [104].

To study ^{60}V in more detail, ^{60}V β decay was selectively investigated for ^{60}V ions that were in the 185-ns half-life isomeric state when they were deposited into the DSSD. The ^{60}V

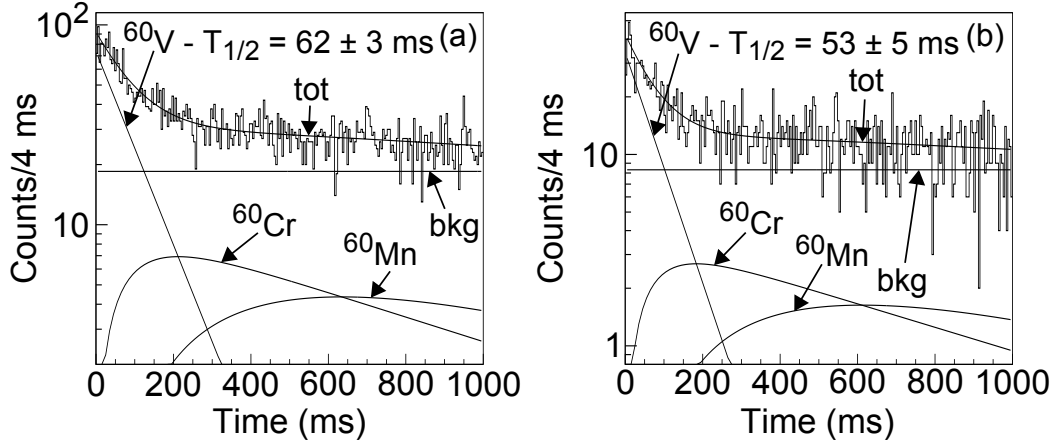


Figure 4.22: ^{60}V β -decay curve for β decays that were correlated with a ^{60}V ion detected in coincidence with a (a) 100- or (b) 104-keV γ ray in SeGA. The fit of each decay curve, labelled “tot,” included the exponential decay of ^{60}V , the exponential growth and decay of ^{60}Cr and ^{60}Mn , and a constant background.

β -decay curves showing only decays that were correlated with a ^{60}V ion that was detected in coincidence with a 100- or 104-keV γ -ray in SeGA are shown in Figs. 4.22(a) and (b), respectively. Half-lives were determined from the decay curves using the same fitting procedure that was applied to the decay curve for all decays detected within 1 s of any ^{60}V ion implantation in the DSSD (see Fig. 4.19). Values of 62 ± 3 and 53 ± 5 ms were obtained for the ^{60}V β -decay half-life following the ^{60}V ions detected in coincidence with 100- and 104-keV γ rays, respectively. The similarity of the half-lives suggests that the 100- and 104-keV γ -ray decays lead to the population of the same β -decaying state in ^{60}V . Furthermore, the half-lives of 62 ± 3 and 53 ± 5 ms are shorter than the value of 85 ± 2 ms determined from the decay curve of β decays following any ^{60}V ion. The shorter half-lives are consistent with the 100- and 104-keV γ rays leading to the population of the low-spin β -decaying isomer in ^{60}V that was proposed in Ref. [103]. The ^{60}V half-life was also investigated for ^{60}V β decays that were coincident with a 644-keV γ ray and that were correlated exclusively with a ^{60}V ion implantation detected in coincidence with a 100- or 104-keV γ ray. The resulting

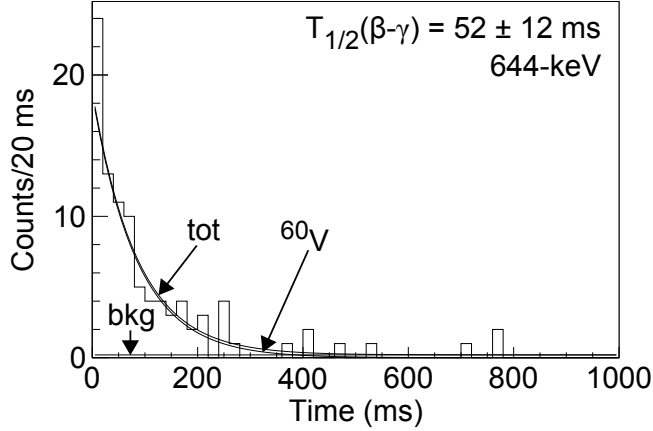


Figure 4.23: ^{60}V β -decay curve for decays detected in coincidence with a 644-keV γ -ray in SeGA and only for decays that were correlated with a ^{60}V ion implantation in the DSSD that was coincident with a 100- or 104-keV γ -ray in SeGA. The decay curve was fit to an exponential for the decay of ^{60}V and a constant background.

spectrum is shown in Fig. 4.23. A half-life of 52 ± 12 ms is determined from the fit to an exponential for the decay of ^{60}V and a constant background. Though the uncertainty is a little larger, this half-life agrees with the half-lives that were extracted for ^{60}V β decay following ^{60}V ion implantations coincident with either a 100- or 104-keV γ ray. In an effort to further investigate the low-energy level scheme of ^{60}V , the β decay of ^{60}Ti to ^{60}V was studied, which is described in the next section.

4.5 β decay of ^{60}Ti to ^{60}V

The ^{60}Ti β -delayed γ -ray energy spectrum is shown in Fig. 4.24. The two most intense peaks in Fig. 4.24 are at energies of 112.4 ± 0.4 and 644.4 ± 0.5 keV. The 644-keV γ ray corresponds to the $2_1^+ \rightarrow 0_1^+$ transition in the ^{60}Cr granddaughter nucleus. The 112-keV γ ray was identified as a transition in ^{60}V from an earlier β -decay experiment, but no placement in the level scheme was proposed [105]. In Fig. 4.24(a), weak peaks may be present at approximately 77, 99, and 102 keV. It is possible that the 99- and 102-keV transitions are

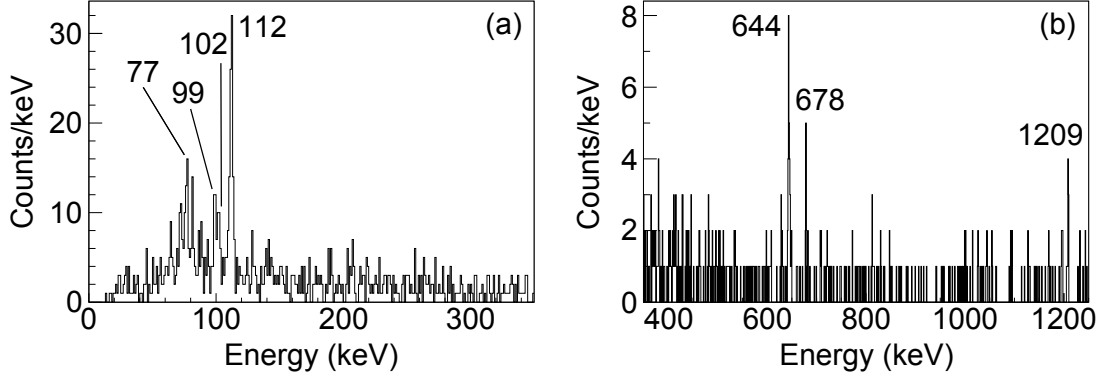


Figure 4.24: β -delayed γ -ray energy spectrum detected within 70 ms of the implantation of a ^{60}Ti ion in the DSSD shown in the ranges of (a) 0 - 350 keV and (b) 350 - 1250 keV.

the same as the transitions associated with the decay of the 185-ns half-life isomeric state in ^{60}V . However, increased statistics would be required for a conclusive determination. Based on very low statistics, it was proposed in Ref. [105] that the 99- and 112-keV transitions have similar absolute intensities. In the present work, the 112-keV transition is observed to be much more intense and have an absolute intensity of $25 \pm 5\%$. From Fig. 4.24(b), transitions with energies of 678 and 1209 keV are also tentatively identified in ^{60}V . Due to the limited statistics, no γ - γ coincidences following ^{60}Ti β decay could be detected.

In fitting an ungated ^{60}Ti β -decay curve to determine the half-life of ^{60}Ti , there is some ambiguity in regard to the half-life that should be used for the ^{60}V daughter nucleus in the fit. As mentioned in the previous section, two different β -decaying states with significantly different half-lives have been proposed in ^{60}V . The simplest expectation is that the β decay of ^{60}Ti , which has a ground state of 0^+ , would preferentially populate the low-spin β -decaying state in ^{60}V [103]. Using this assumption, the ^{60}Ti half-life was determined to be 22 ± 2 ms in Ref. [106] with the ^{60}V half-life fixed at 40 ms [103]. However, based on the large difference in ground-state mass-energy of 10.9 MeV that is expected between ^{60}Ti and ^{60}V from systematics [14], β decays to high-energy excited states in ^{60}V could indirectly

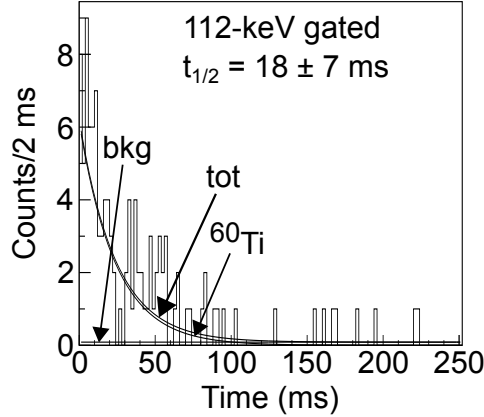


Figure 4.25: Decay curve showing fragment- β correlations for β decays that were detected within 250 ms of a ^{60}Ti ion implantation in the DSSD and that were also detected in coincidence with a 112-keV γ ray in SeGA. The decay curve was fit to an exponential for the decay of ^{60}Ti and a constant background.

feed the high-spin β -decaying isomer [104]. A γ -gated ^{60}Ti decay curve exclusively selects ^{60}Ti β decays, and the ^{60}Ti half-life can be determined without any knowledge about the daughter activity. The ^{60}Ti β -decay curve gated on the 112-keV γ ray is shown in Fig. 4.25. The decay curve was fit to an exponential and a constant background, yielding a half-life of 18 ± 7 ms. The half-life is consistent with the previous determination, but the uncertainty in the γ -gated half-life is large.

Despite the wealth of experimental information, it is difficult to confidently propose and interpret the low-energy level scheme of ^{60}V . The data suggest that the 185-ns half-life γ -decaying isomer feeds the low-spin, short-lived β -decaying isomer. However, the 100- and 104-keV γ rays emitted as a result of the decay of the 185-ns half-life isomer are not in coincidence. It could be inferred that the 185-ns half-life isomeric state is at 104 keV above the low-spin β -decaying isomer. The isomer would thus have two decay branches, one directly to the low-spin β -decaying isomer and another to a 4-keV state that then decays to the low-spin β -decaying isomer via a transition that was not observed because of its low energy. The 185-ns half-life isomer could also have an energy greater than 104 keV above the low-spin

β -decaying isomer. In this scenario, the 185-ns half-life isomer would most likely decay to states at 100 and 104 keV above the β -decaying isomer by transitions that could not be observed in the present experiment. From the available data, it is not possible to distinguish between the different possibilities. For either of the possible decay schemes, a transition depopulating the 185-ns half-life isomeric state would likely be of $M1$ or $E2$ character based on the observed half-life of the isomer and Weisskopf half-life estimates. Further complicating the low-energy level scheme of ^{60}V , the 112-keV γ -ray transition in ^{60}V likely directly feeds the low-spin β -decaying isomer since it is the most strongly populated transition in the β decay of the 0^+ ^{60}Ti ground state. Hence, there seem to be multiple levels at about 100 keV above the low-spin β decaying isomer in ^{60}V . Due to the ambiguities, a low-energy level scheme for ^{60}V cannot confidently be proposed.

4.6 β decay of ^{61}V to ^{61}Cr

The ^{61}V β -delayed γ -ray energy spectrum detected within 250 ms of a ^{61}V ion implantation in the DSSD is shown in Fig. 4.26. γ -ray transitions identified in ^{61}Cr are marked by red triangles and labelled with their energies. Sixteen ^{61}Cr transitions are seen in Fig. 4.26, and two others became apparent in β -delayed γ - γ coincidence spectra. The transitions in ^{61}Cr are also listed in Table 4.4 along with their respective absolute intensities.

Background subtracted β -delayed γ - γ coincidence spectra gated on transitions identified in ^{61}Cr are shown in Figs. 4.27 and 4.28. Based on Fig. 4.27(a), the 71-keV γ -ray transition is coincident with 331- and 1151-keV γ rays. Figs. 4.27(d) and 4.28(f), which are gated on the 331- and 1151-keV transitions, respectively, confirm the coincidences. A low-intensity 645-keV γ ray is also seen in coincidence with the 71-keV transition. The 645-keV peak was

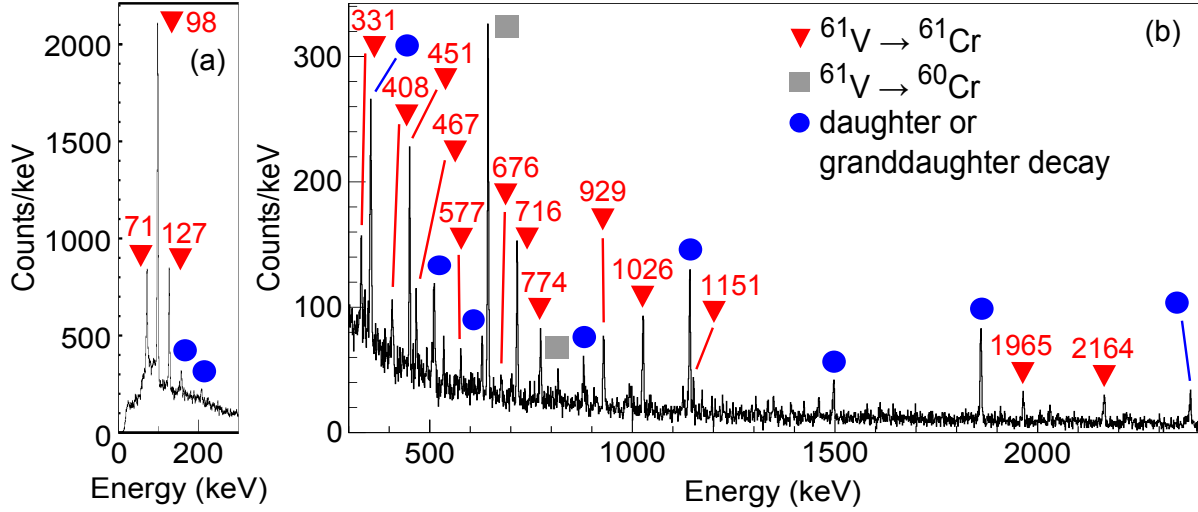


Figure 4.26: β -delayed γ -ray energy spectrum detected within 250 ms of the implantation of a ^{61}V ion in the DSSD shown in the ranges of (a) 0 - 300 keV and (b) 300 - 2400 keV. γ -ray transitions in the daughter ^{61}Cr nucleus are labelled with red triangles and the transition energy in keV. γ -ray transitions in ^{60}Cr that are populated from the β -delayed neutron decay of ^{61}V are marked by gray squares. γ rays emitted following the β decay of a daughter or granddaughter nucleus are indicated by the blue circles.

not seen in the ^{61}V β -delayed γ -ray spectrum (Fig. 4.26) because it was masked by a much more intense 644-keV transition which results from the β -delayed neutron decay of ^{61}V . The 98-keV γ ray is coincident with the 127-, 354-, 408-, 467-, 676-, 929-, 1965-, and 2164-keV γ rays. Similar to the aforementioned low-intensity 645-keV transition, the 354-keV transition was obscured in Fig. 4.26 by a γ ray emitted in the decay of the ^{61}Cr daughter to ^{61}Mn . From Fig. 4.27(c) and (e), the 127-keV transition, which was observed in coincidence with the 98-keV transition, is also coincident the 408-keV transition.

The two transitions marked by gray squares at 644.2 ± 0.3 and 816.7 ± 0.4 keV in Fig. 4.26 are due to the β -delayed neutron decay of ^{61}V . These 644- and 817-keV transitions correspond to the $2_1^+ \rightarrow 0_1^+$ and $4_1^+ \rightarrow 2_1^+$ transitions, respectively, in ^{60}Cr [59]. Absolute intensities of 10.8 ± 0.7 and $0.6 \pm 0.3\%$ were measured for the respective 644- and 817-keV peaks in Fig. 4.26. Based on the intensity of the peak at 645-keV in the ^{61}V γ - γ coincidence

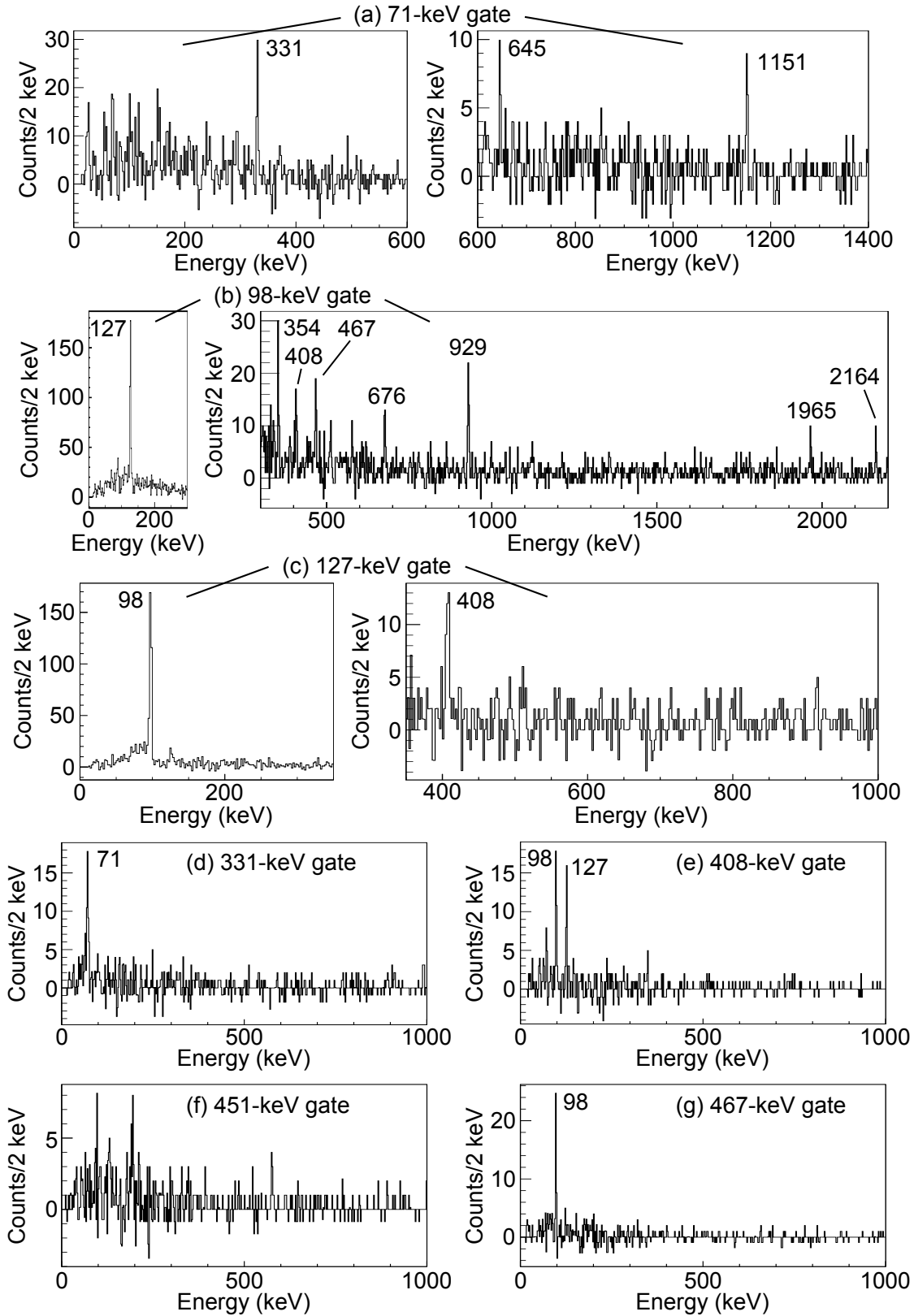


Figure 4.27: Background-subtracted ^{61}V β -delayed γ - γ coincidence spectra gated on the (a) 71-, (b) 98-, (c) 127-, (d) 331-, (e) 408-, (f) 451-, and (g) 467- transitions

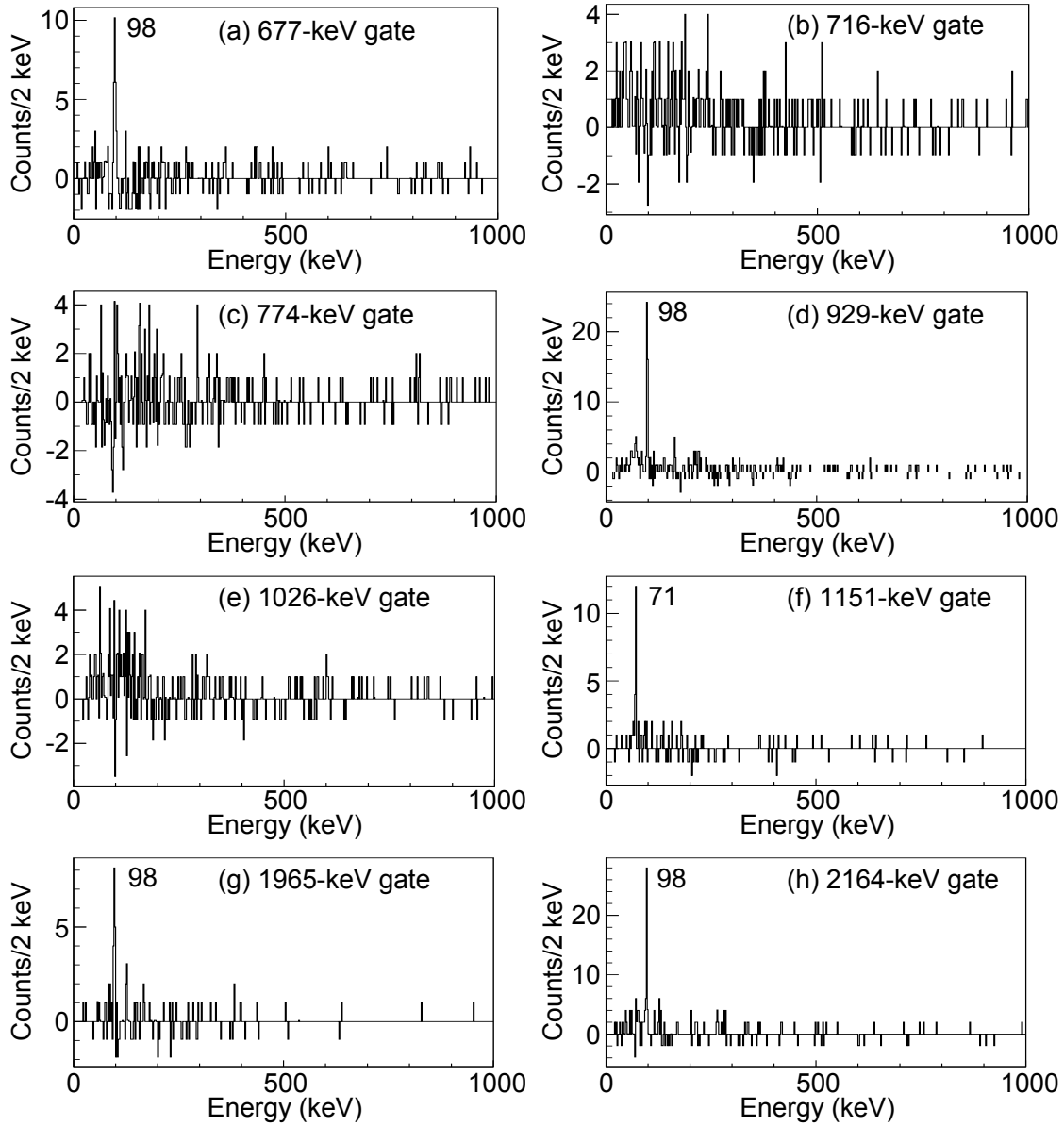


Figure 4.28: Background-subtracted ^{61}V β -delayed γ - γ coincidence spectra gated on the (a) 677-, (b) 716-, (c) 774-, (d) 929-, (e) 1026-, (f) 1151-, (g) 1965-, and (h) 2164-keV transitions

Table 4.4: Energies and absolute intensities of the γ -ray transitions identified in ^{61}Cr following the β decay of ^{61}V . The energies of the initial and final states between which each transition occurs are also listed.

E_γ (keV)	$I_\gamma^{absolute}$ (%)	Initial State (keV)	Final State (keV)
70.8 ± 0.3	9.3 ± 0.8	71	0
97.7 ± 0.3	24.9 ± 0.8	98	0
126.7 ± 0.3	8.1 ± 0.5	224	98
331.0 ± 0.4	1.7 ± 0.5	402	71
353.6 ± 0.5^b	1.2 ± 0.4	451	98
407.6 ± 0.7	1.7 ± 0.7	632	224
450.5 ± 0.3	4.5 ± 0.5	451	0
467.0 ± 0.4	1.5 ± 0.4	565	98
576.7 ± 0.4^a	0.7 ± 0.3		
645.0 ± 0.8^b	1.0 ± 0.4	716	71
676.4 ± 0.6	0.9 ± 0.4	774	98
715.9 ± 0.4	5.1 ± 0.6	716	0
773.7 ± 0.4	2.3 ± 0.5	774	0
929.4 ± 0.4	3.7 ± 0.5	1026	98
1026.3 ± 0.4	4.7 ± 0.6	1026	0
1151.2 ± 0.4	1.4 ± 0.3	1222	71
1964.5 ± 0.4	2.2 ± 0.7	2062	98
2164.0 ± 0.5	2.5 ± 0.8	2262	98

^a Transition not placed in ^{61}Cr level scheme

^b Transition observed in coincidence spectra only

spectrum gated on the 71-keV transition, an intensity of $1.0 \pm 0.4\%$ can be inferred for the low-intensity 645-keV transition in ^{61}Cr that lies below the 644-keV peak caused β -delayed neutron decay. Thus, a minimum β -delayed neutron-decay branching ratio of $9.8 \pm 0.8\%$ is deduced for ^{61}V .

The β -decay curve for ^{61}V from 0 - 1 s is shown in Fig. 4.29. The decay curve was fit considering the exponential decay of ^{61}V , the exponential growth and decay of the β -decay daughter ^{61}Cr and β -decay granddaughter ^{61}Mn , the exponential growth and decay of the β -delayed neutron daughter ^{60}Cr and the β -delayed neutron granddaughter ^{60}Mn , and a constant background. The half-lives of ^{60}Cr , ^{61}Cr , ^{60}Mn , and ^{61}Mn were fixed at 490

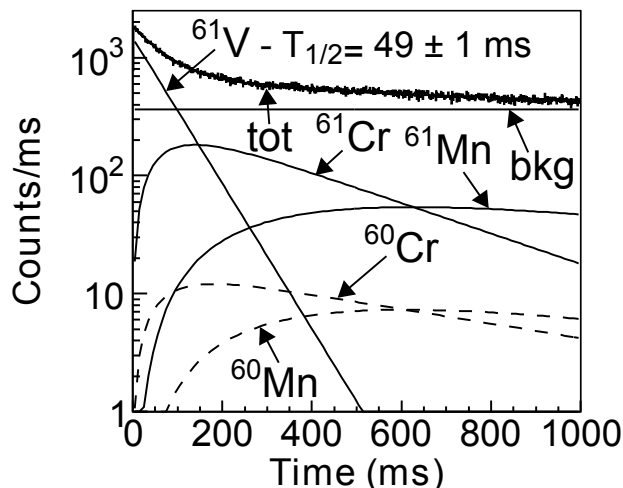


Figure 4.29: ^{61}V decay curve showing fragment- β correlations for β decays detected within 1 s of a ^{61}V ion implantation in the DSSD. The fit to the decay curve, labelled “tot,” included the exponential decay of ^{61}V , the exponential growth and decay of ^{61}Cr , ^{61}Mn , ^{60}Cr , and ^{60}Mn , and a constant background.

[102], 233 [107], 280 [102], and 670 [108] ms, respectively. Further, the fraction of decays due to β -delayed neutron decay was fixed according to the inferred minimum ^{61}V β -delayed neutron-decay branching ratio. A half-life of 49 ± 1 ms is determined for ^{61}V . Varying the magnitude of the β -delayed neutron-decay branching ratio had little effect on the extracted half-life, and increasing the value from 10% to 25% only altered the half-life by about 2 ms. γ -gated decay curves for ^{61}V are shown in Figs. 4.30 and 4.31. The fit of each decay curve included the exponential decay of ^{61}V and a constant background. The half-lives determined from the γ -gated decay curves were consistent with the half-life extracted from the ungated ^{61}V decay curve in Fig. 4.29, confirming the placement of the γ -ray transitions in the ^{61}Cr level scheme.

The low-energy level scheme of ^{61}Cr populated by ^{61}V β decay is shown in Fig. 4.32. A level scheme was previously proposed in Ref. [106] in which four excited states at 97, 310, 450, and 1027 keV were tentatively identified in ^{61}Cr . The present analysis confirms the presence

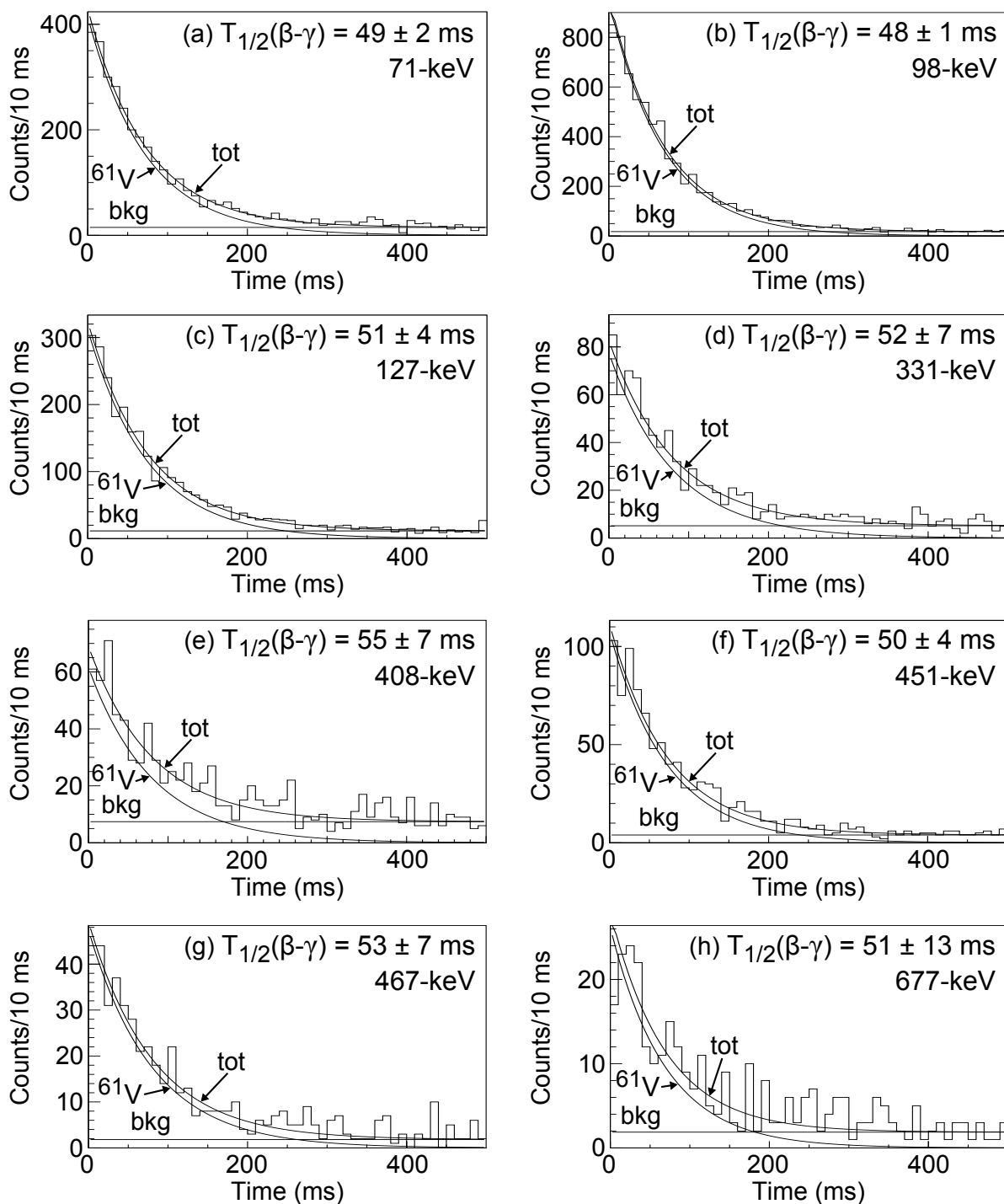


Figure 4.30: ^{61}V decay curves from 0 - 500 ms showing fragment- β correlations for decay events in which a coincident γ ray was also detected with an energy of (a) 71, (b) 98, (c) 127, (d) 331, (e) 408, (f) 451, (g) 467, and (h) 677 keV. Each decay curve was fit with an exponential for the decay of ^{61}V and a constant background.

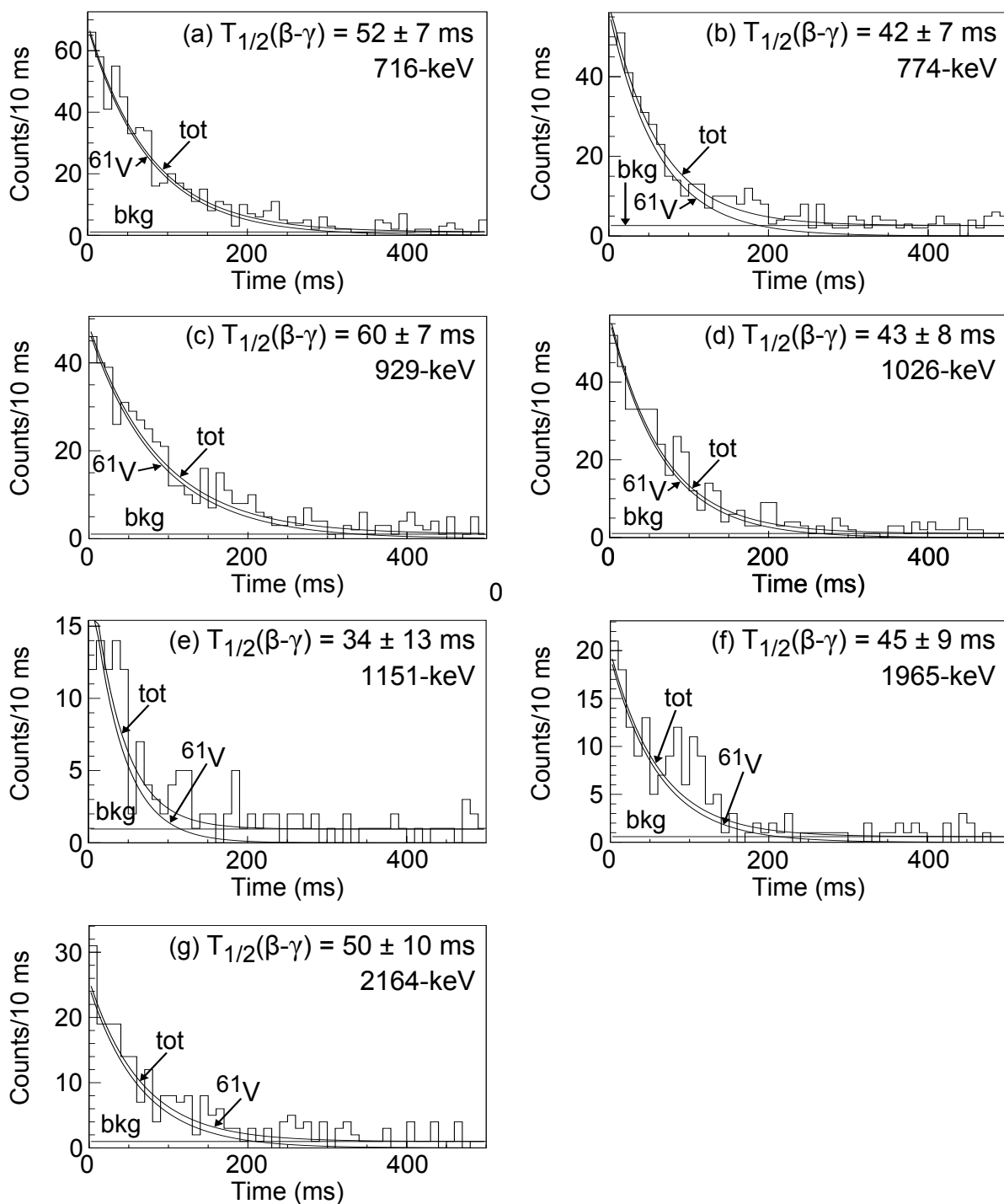


Figure 4.31: ^{61}V decay curves from 0 - 500 ms showing fragment- β correlations for events in which a coincident γ ray was also detected with an energy of (a) 716, (b) 774, (c) 929, (d) 1026, (e) 1151, (f) 1965, and (g) 2165 keV. Each decay curve was fit with an exponential for the decay of ^{61}V and a constant background.

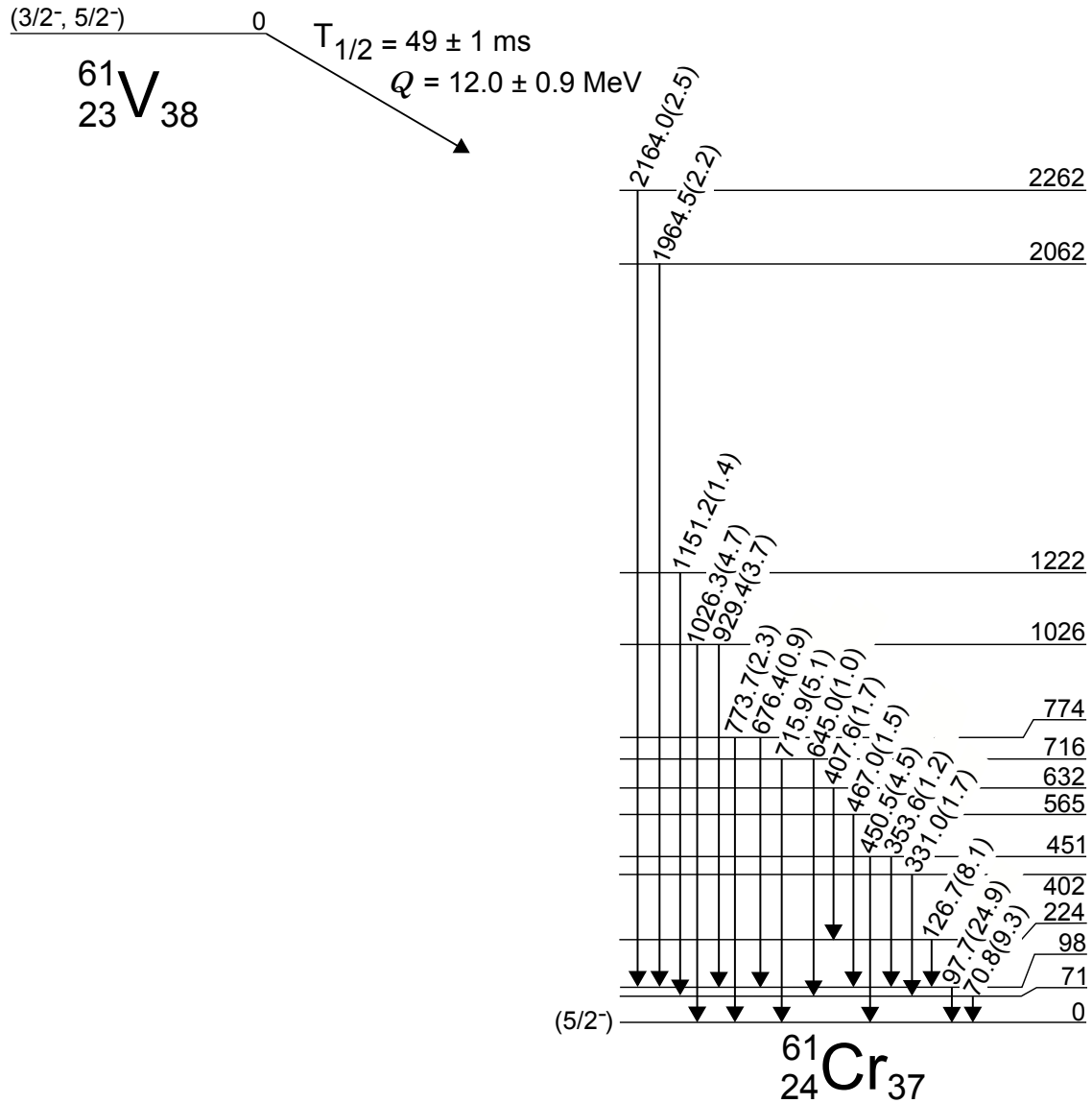


Figure 4.32: Level scheme of ^{61}Cr populated by the β decay of ^{61}V . States are labelled on the left by their spins and parities and on the right by their energies in keV. γ -ray transition energies in keV are shown above the transitions. The absolute γ -ray intensity of each transition is shown in parentheses after the transition energy. The Q -value for the β decay of ^{61}V to ^{61}Cr was taken from Ref. [14].

of the previously identified 97-keV (98-keV presently), 450-keV (451-keV presently), and 1027-keV (1026-keV presently) levels. However, the previously proposed 310-keV state is removed in Fig. 4.32. In Ref. [106], the 717-keV transition (assumed to be the same as the presently identified transition at 716 keV) was proposed to feed the 310-keV state, which in turn was proposed to be depopulated by a 213-keV transition that feeds the 97-keV state. In the current work, no 213-keV transition was observed, resulting in the removal of the 310-keV state. The 716-keV transition is instead assigned as directly feeding the ground state due to the lack of observed coincidence with any other γ ray transition. The 645-keV transition is also proposed to depopulate the 716-keV state and feed the 71-keV state.

Additional γ rays were observed at 71-, 127-, and 329-keV in Ref. [106], but they were not placed in the ^{61}Cr level scheme. With the increased statistics of the current study, their placements are suggested. As no coincidence was observed between the 71-keV γ ray and the 98-, 451-, 716-, or 1027-keV γ rays, the 71-keV transition is proposed to directly feed the ground state. According to Weisskopf estimates and the lack of an observable half-life for the 71-keV state, the 71-keV transition most likely has dipole character. The 331-keV transition depopulates a 402-keV state and feeds the 71-keV state. The 451-keV transition, which is not observed in coincidence with any other transitions, is proposed to directly feed the ground state. The 127-keV transition occurs from a 224-keV state to the 98-keV state. Based on the intensities of the 98- and 127-keV γ rays and the number of detected coincidence counts between the 98- and 127-keV γ rays, an internal conversion coefficient of 0.17 ± 0.13 is deduced for the 98-keV transition, though the relative uncertainty is quite large. The determined value of α is closest to what would be expected for an $M2$ transition, but given the large uncertainty, $E2$ and dipole transitions cannot be excluded. No time delay was observed between the 127- and 98-keV γ rays, which according to Weisskopf estimates,

would suggest a dipole or mixed $M1-E2$ transitions for the 98-keV γ ray.

In total, nine new γ rays were observed in ^{61}Cr and thirteen excited states are tentatively identified in the level scheme shown in Fig. 4.32. Based on the ^{61}V $\gamma-\gamma$ coincidence spectra, additional levels are proposed at 565, 632, 774, 1222, 2062, and 2262 keV in ^{61}Cr . The 565-keV state is depopulated by the 467-keV transition, which feeds the 98-keV state. The 408-keV transition occurs between the 632- and 224-keV levels. Two different γ -ray decays out of the 774-keV state are identified. The first, the 677-keV transition, feeds the 98-keV state, while the second directly populates the ground state. The 1151-keV γ ray is proposed to connect the 1222- and 71-keV states. Finally, the 1965- and 2164-keV transitions each populate the 98-keV level, establishing excited states at energies of 2062 and 2262 keV, respectively.

As no coincidence was observed between any transition coincident with the 71-keV transition and any transition coincident with the 98-keV transition, it might be suggested that one of the 71- or 98-keV transitions feeds the ^{61}Cr ground state while the other transition feeds an isomeric state. Although this possibility was investigated, no further evidence was found to support the presence of an isomer. A search for a β -decaying isomer was made by examining the time delay between selected β -delayed γ rays in ^{61}Cr and the subsequent β decay to ^{61}Mn . The half-life determined for ^{61}Cr when gating on the sum of the 71-, 331-, 716-, and 1151-keV transitions (those transitions which feed either the 71-keV state or the state fed by the 71-keV transition) was 240 ± 60 ms. When gating on the sum of the 98-, 127-, 408-, 451-, 467-, 676-, 774-, 929-, 1026-, 1965-, and 2164-keV transitions (those transitions which feed either the 98-keV state or the state fed by the 98-keV transition) a half-life of 300 ± 50 ms is found. Both half-lives are consistent with the value of 270 ± 30 ms that is determined by gating on the independently produced ^{61}Cr ions in the particle-

identification plot, as well as the literature value of 243 ± 11 ms [108]. Further, a search for a γ -decaying isomer within a time period of up to 10 ms after a ^{61}V β decay was performed, which provided no indication for the existence of an isomer.

As no strong evidence is found in the present data to refute it, the previously proposed ground state spin and parity of $5/2^-$ [106] is retained for ^{61}Cr . In Ref. [106], a large feeding of the ^{61}Cr ground state was proposed in the β decay of ^{61}V . Based on the present results, a maximum ground-state feeding of 40% can be inferred. While the ground-state feeding appears strong, given the large difference in ground-state mass-energies of 12.0 MeV between ^{61}V and ^{61}Cr [14], the electromagnetic decay of high-energy states in ^{61}Cr by high-energy, low-intensity transitions following ^{61}V β decay is possible. Therefore, β -decay feeding to high-energy states in ^{61}Cr may have been missed [104] and only an upper limit is determined for the ^{61}Cr ground-state feeding. The tentative $5/2^-$ ground state is consistent with results for the β decay of ^{61}Cr to ^{61}Mn [107]. $5/2^-$ would be expected to be the ^{61}Cr ground state for modest prolate deformations [106, 109]. As stated in Ref. [106], if ^{61}V is also assumed to be prolate, $3/2^-$ is likely the ground state spin and parity. However, oblate deformation has also been proposed for the neighboring ^{59}V ground state [101]. A ground-state spin and parity of $5/2^-$ in ^{61}V would be expected for an oblate deformation. The observation that the 4_1^+ state in ^{60}Cr is not strongly populated by the β -delayed neutron decay of ^{61}V favors the $3/2^-$ spin and parity for the ^{61}V ground state.

4.7 β decay of ^{62}V to ^{62}Cr

The β -delayed γ -ray energy spectrum detected within 150 ms of the implantation of a ^{62}V ion in the DSSD is shown in Fig. 4.33. The γ rays assigned to transitions in ^{62}Cr are

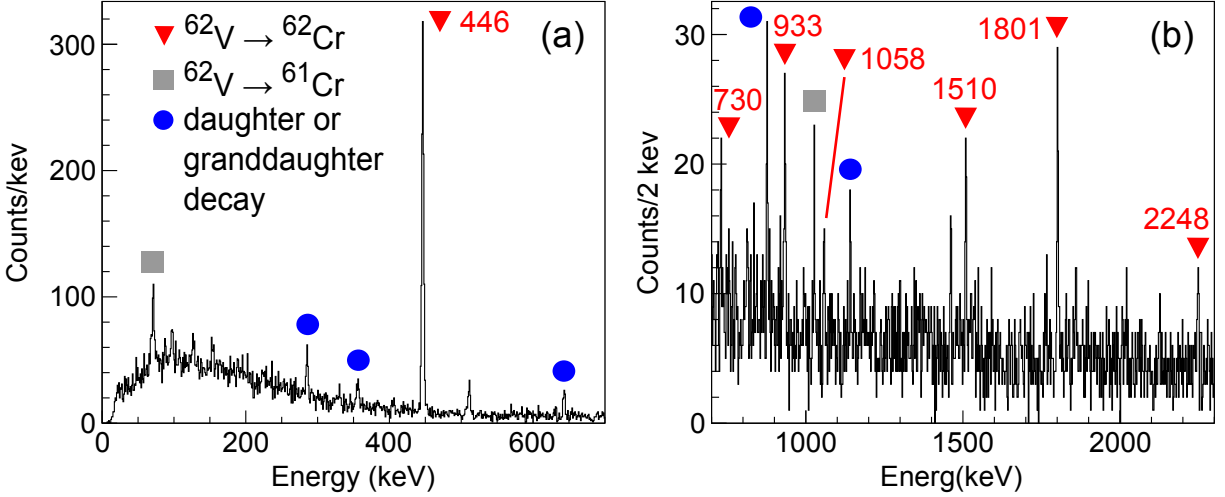


Figure 4.33: β -delayed γ -ray energy spectrum detected within 150 ms of the implantation of a ^{62}V ion in the DSSD shown in the ranges of (a) 0 - 700 keV and (b) 700 - 2300 keV. γ -ray transitions in the daughter ^{62}Cr nucleus are labelled with red triangles and the transition energy in keV. γ -ray transitions in ^{61}Cr that are populated from the β -delayed neutron decay of ^{62}V are marked by gray squares. γ rays emitted following the β decay of a daughter or granddaughter nucleus are indicated by the blue circles.

listed in Table 4.5 with their respective absolute intensities. A total of seven transitions are identified in ^{62}Cr . Two transitions at 71 and 1027 keV with absolute intensities of $5 \pm 2\%$ and $2 \pm 1\%$, respectively, which result from β -delayed neutron decay, are also observed. A minimum β -delayed neutron-decay branch of 7% is thus inferred for ^{62}V . Weak 98- and 127-keV γ -ray transitions in ^{61}Cr may also have been observed, but the statistics are not sufficient to conclusively make this determination. The upper limit for the intensity of the 98- and 127-keV transitions is 2%.

The background-subtracted β -delayed γ - γ coincidence spectra gated on each γ -ray transition in ^{62}Cr are shown in Fig. 4.34. The 446-keV γ ray, which was first reported in Ref. [103], is attributed to the $2_1^+ \rightarrow 0_1^+$ transition in ^{62}Cr . Based on Fig. 4.34, the 1510- and 1801-keV γ rays are coincident with the 446-keV transition. The 730-keV transition has been proposed to correspond to the $4_1^+ \rightarrow 2_1^+$ transition [52, 110], but due to the low absolute

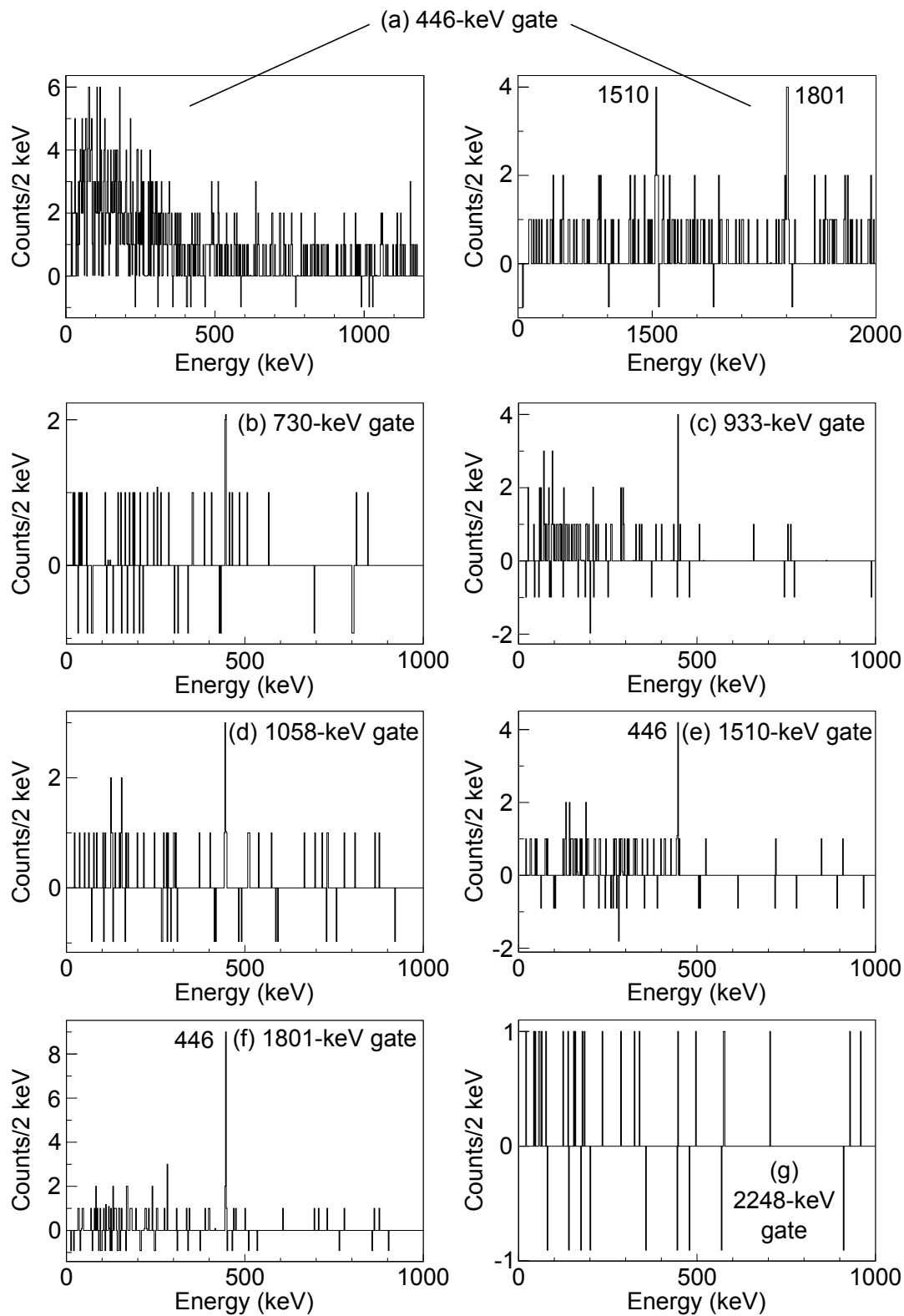


Figure 4.34: Background-subtracted ^{62}V β -delayed γ - γ coincidence spectra gated on the (a) 446-, (b) 730-, (c) 933-, (d) 1058-, (e) 1510-, (f) 1801-, and (g) 2248-keV transitions

Table 4.5: Energies and absolute intensities of γ -ray transitions identified in ^{62}Cr following the β decay of ^{62}V . The energies of the initial and final states between which each transition occurs are also listed.

E_γ (keV)	$I_\gamma^{absolute}$ (%)	Initial State (keV)	Final State (keV)
446.5 ± 0.3	43 ± 3	446	0
730.2 ± 0.6	2.0 ± 0.8	1177	446
933.0 ± 0.7^a	5 ± 2		
1058.3 ± 0.8^a	2.2 ± 0.8		
1509.5 ± 0.6	4 ± 1	1956	446
1801.5 ± 0.5	6 ± 2	2248	446
2248 ± 1	3 ± 1	2248	0

^a γ -ray transition not placed in ^{62}Cr level scheme

intensity of the 730-keV transition, definitive coincidence was not observed between the 446- and 730- keV γ rays in the present experiment. However, based on the observed absolute intensity of the 730-keV γ ray, only 4 ± 2 coincidence counts between the 446- and 730-keV transitions would be expected. While Figs. 4.34(c) and (d) perhaps suggest the 933- and 1058-keV γ rays are coincident with the 446-keV γ ray, peaks sufficiently above background are not observed at 933 or 1058 keV when a gate is placed on the 446-keV γ ray (see Fig. 4.34(a)). Thus, no additional coincidence relationships can confidently be proposed. If the 933- and 1058-keV γ rays both directly populate the state that is depopulated by the 446-keV transition, 8 ± 3 and 3 ± 1 coincidence counts would be expected between the 446-keV γ ray and the 933- and 1058-keV γ rays, respectively.

The ^{62}V β -decay curve is shown in Fig. 4.35. The decay curve was fit considering the decays of ^{62}V , $^{61,62}\text{Cr}$, and $^{61,62}\text{Mn}$ and a constant background. The $A = 61$ nuclei were populated by β -delayed neutron decay, and the fraction of decays from β -delayed neutron decay in the fit was fixed based on the minimum β -delayed neutron-decay branching ratio. In the fit, the half-lives of ^{61}Cr , ^{62}Cr , ^{61}Mn , and ^{62}Mn were fixed according to the literature values of 233 [107], 209 [106], 670 [108], and 92 ms [106], respectively. The ^{62}V half-life is

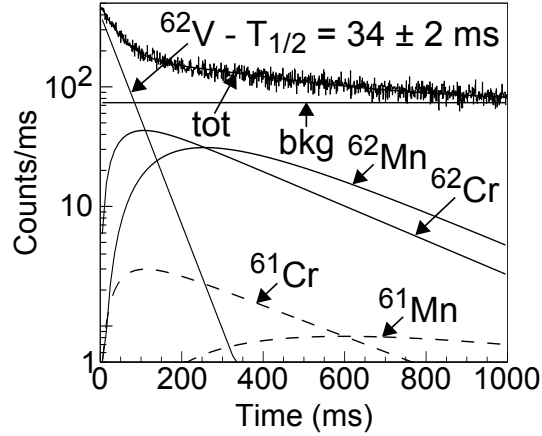


Figure 4.35: ^{62}V decay curve showing fragment- β correlations for β decays detected within 1 s of a ^{62}V ion implantation in the DSSD. The fit to the decay curve, labelled “tot,” included the exponential decay of ^{62}V , the exponential growth and decay of ^{62}Cr , ^{62}Mn , ^{61}Cr , and ^{61}Mn and a constant background.

presently found to be 34 ± 2 ms, which is consistent with previous β -decay studies [103]. The size of the β -delayed neutron-decay branching ratio had only a very minor impact on the extracted half-life. Increasing the branching ratio to 25% changed the determined half-life by just 2 ms. β -decay curves additionally requiring the coincident detection of a 446-, 933-, 1510-, or 1801-keV γ ray in SeGA are shown in Figs. 4.36(a), (b), (c), and (d), respectively. Decay curves gated on the 730-, 1058-, or 2248-keV γ -ray transitions are not shown due to low statistics. The half-lives extracted from fitting the decay curves in Figs. 4.36(a) - (d) to an exponential and a constant background agree with the half-life of 34 ± 2 ms determined from the ungated ^{62}V decay curve.

The tentative low-energy level scheme of ^{62}Cr populated by the β decay of ^{62}V is shown in Fig. 4.37. The 446- and 1177-keV states have previously been identified as the 2_1^+ and 4_1^+ states, respectively, in ^{62}Cr [103, 110]. Based on the observed coincidences between the 446-keV γ ray and the 1510- and 1801-keV γ rays, additional levels are proposed at 1956 and 2248 keV. The 2248-keV transition is identified as directly feeding the ground state and

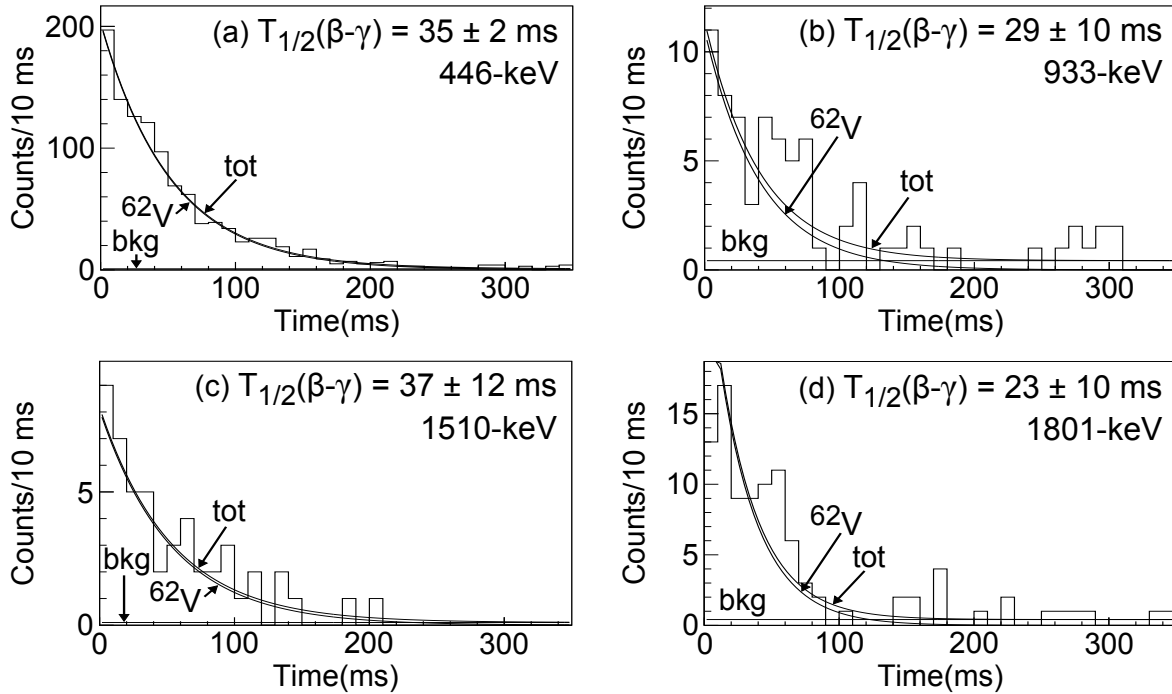


Figure 4.36: ^{62}V decay curves from 0 - 350 ms showing fragment- β correlations for decay events in which a coincident γ ray was also detected with an energy of (a) 446, (b) 933, (c) 1510, and (d) 1801 keV. Each decay curve was fit with an exponential for the decay of ^{62}V and a constant background.

is a parallel decay branch to the 1801-446 keV cascade. The apparent β -decay feeding of the 2248-keV state can be used to infer a $\log ft$ value of 5.6, which favors a spin and parity of 0^+ , 1^+ , or 2^+ for the 2248-keV state based on β -decay selection rules. 0^+ can be excluded because an $E0$ transition cannot occur by γ -ray emission and the 2248-keV γ ray connects the 2248-keV state to the 0^+ ground state. Therefore, the state at 2248 keV in ^{62}Cr is proposed to have a spin and parity of either 1^+ or 2^+ . From the proposed decay scheme, the maximum β -decay feeding of the ^{62}Cr ground state is inferred to be 47%.

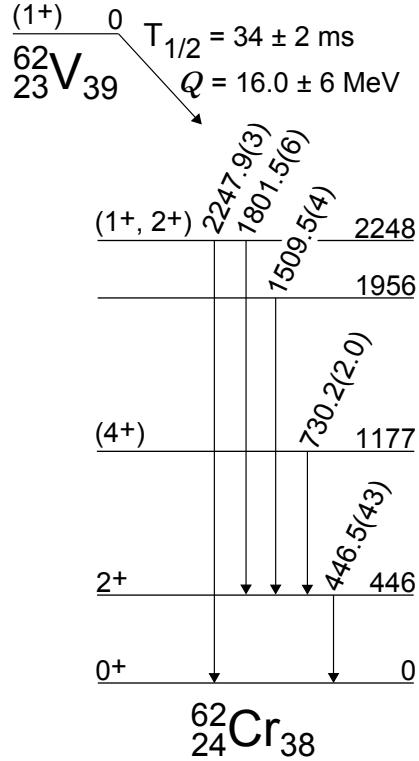


Figure 4.37: Level scheme of ^{62}Cr populated by the β decay of ^{62}V . States are labelled on the left by their spins and parities and on the right by their energies in keV. γ -ray transition energies in keV are shown above the transitions. The absolute γ -ray intensity of each transition is shown in parentheses after the transition energy. The Q -value for the β decay of ^{62}V to ^{62}Cr was taken from Ref. [14].

4.8 β decay of ^{63}V to ^{63}Cr

γ -ray transitions in ^{63}Cr were observed for the first time in experiment e08020. The β -delayed γ -ray energy spectrum detected within 150 ms of the arrival of ^{63}V ion at the DSSD is shown in Fig. 4.38. Three transitions belonging to ^{63}Cr are identified, and their energies and absolute intensities are given in Table 4.6. In addition to the peaks from γ -ray decays in ^{63}Cr , a high-intensity peak due to the $2_1^+ \rightarrow 0_1^+$ transition in ^{62}Cr is observed at 446.7 ± 0.4 keV and occurs following the β -delayed neutron decay of ^{63}V [103]. The absolute intensity of the 446-keV transition in Fig. 4.38 is $29 \pm 4\%$, leading to a minimum of 29% for the ^{63}V β -delayed neutron-decay branching ratio. No peak corresponding to the $4_1^+ \rightarrow 2_1^+$ in ^{62}Cr

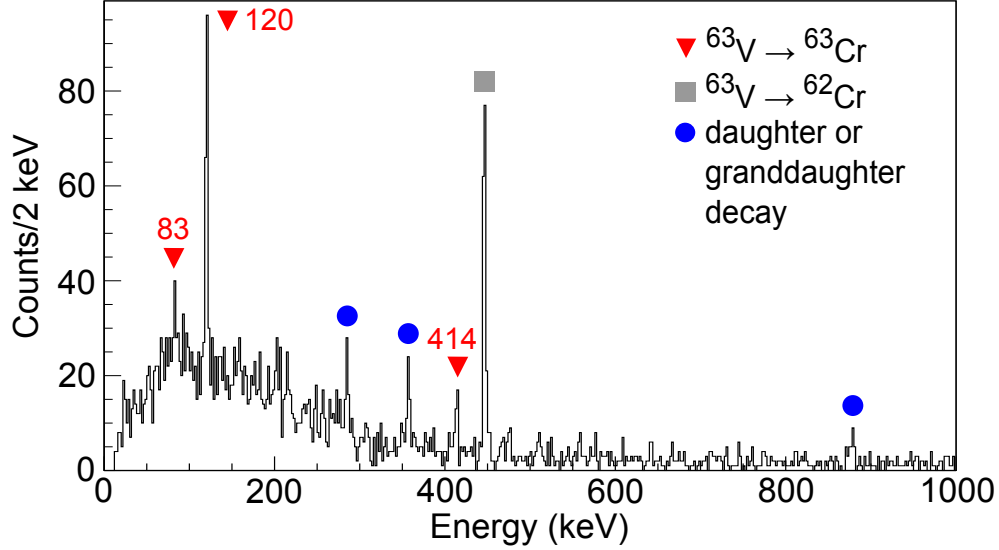


Figure 4.38: β -delayed γ -ray energy spectrum detected within 150 ms of the implantation of a ^{63}V ion in the DSSD shown in the range of 0 - 1000 keV. γ -ray transitions in the daughter ^{63}Cr nucleus are labelled with red triangles and the transition energy in keV. γ -ray transitions in ^{62}Cr that are populated from the β -delayed neutron decay of ^{63}V are marked by gray squares. γ rays emitted following the β decay of a daughter or granddaughter nucleus are indicated by the blue circles.

[52, 110] is present in Fig. 4.38, establishing a limit for the maximum β -delayed neutron-decay branching ratio to the 4_1^+ state of 4%.

The background subtracted ^{63}V β -delayed γ - γ coincidence spectra gated on the 83-, 120-, and 414-keV transitions are shown in Fig. 4.39. Based on Figs. 4.39(a) and (b), the 83- and 120-keV γ rays are coincident. Due to limited statistics, no transitions coincident with the 414-keV transition could be identified.

Table 4.6: Energies and absolute intensities of the γ -ray transitions identified in ^{63}Cr following the β decay of ^{63}V . The energies of the initial and final states between which each transition occurs are also listed.

E_γ (keV)	$I_\gamma^{absolute}$ (%)	Initial State (keV)	Final State (keV)
83.1 ± 0.6	4 ± 2	203	120
120.3 ± 0.4	15 ± 3	120	0
414.0 ± 0.6^a	4 ± 2		

^a Transition not placed in ^{63}Cr level scheme

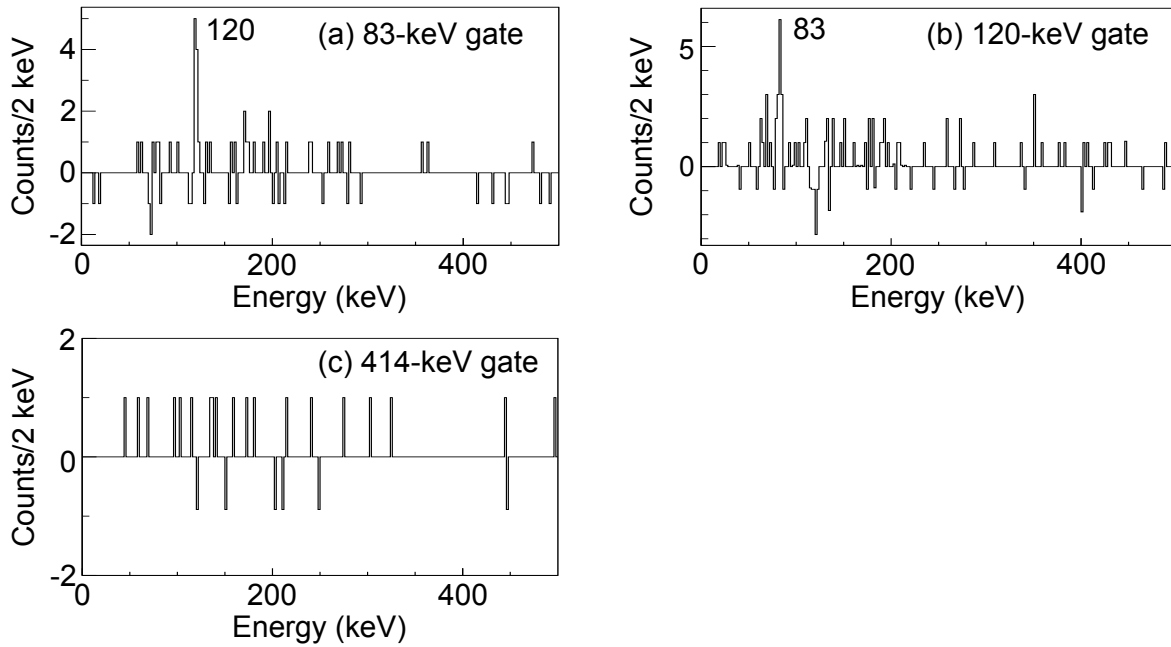


Figure 4.39: Background-subtracted ^{63}V β -delayed γ - γ coincidence spectra gated on the (a) 83-, (b)120-, and (c)414-keV transitions.

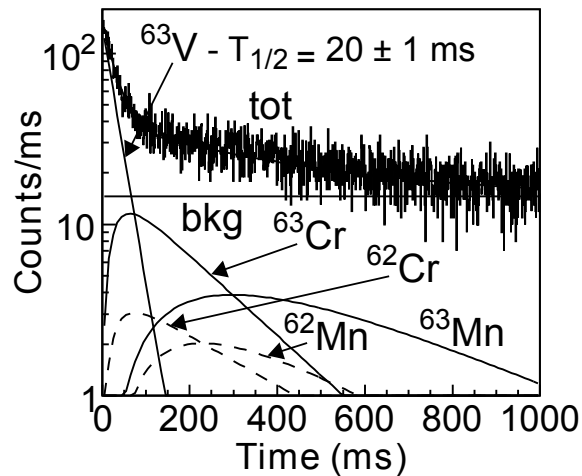


Figure 4.40: ^{63}V decay curve showing fragment- β correlations for β decays detected within 1 s of a ^{63}V ion implantation in the DSSD. The fit to the decay curve, labelled “tot,” included the exponential decay of ^{63}V , the exponential growth and decay of ^{63}Cr , ^{63}Mn , ^{62}Cr , and ^{62}Mn , and a constant background.

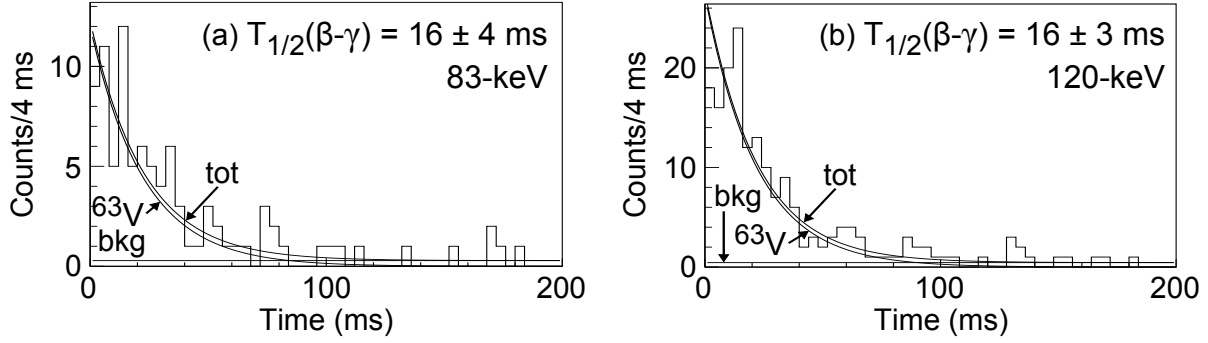


Figure 4.41: ^{63}V decay curves from 0 - 200 ms showing fragment- β correlations for decay events in which a coincident γ ray was also detected with an energy of (a) 83 and (b) 120 keV. Each decay curve was fit with an exponential for the decay of ^{63}V and a constant background.

The ^{63}V decay curve is shown in Fig. 4.40. The fit of the decay curve included contributions from the exponential decay of ^{63}V , the exponential growth and decay of $^{62,63}\text{Cr}$ and $^{62,63}\text{Mn}$, and a constant background. The $A = 62$ nuclei were populated by the β -delayed neutron decay of ^{63}V , and the total percentage of counts due to β -delayed neutron decay in the decay curve was fixed based on the inferred minimum β -delayed neutron-decay branching ratio. The half-lives of $^{62,63}\text{Cr}$ and $^{62,63}\text{Mn}$ were fixed according to literature values of ^{62}Cr - 209 ms [106], ^{63}Cr - 129 ms [106], ^{62}Mn - 92 ms [106], and ^{63}Mn - 275 ms [51]. The half-life extracted for ^{63}V is 20 ± 1 ms. The β -delayed neutron-decay branching ratio used in the fit had minimal bearing on the ^{63}V half-life determination. Changing the branching ratio by a factor of two altered the half-life by less than 1 ms. The primary cause is that the half-lives of ^{62}Cr and ^{63}Cr are both about an order of magnitude longer than the half-life of ^{62}V . The impact of any β -decay daughter/granddaughter or β -delayed-neutron-decay daughter/granddaughter activities in the decay-curve fit are thus very small, especially at short times when most of the ^{63}V decays occur, and the fraction of β -delayed neutron decays is not important. γ -gated ^{63}V β -decay curves, which required the detection of 83- and 120-keV γ rays in coincidence with the β decay are shown in Figs. 4.41(a) and (b), respectively.

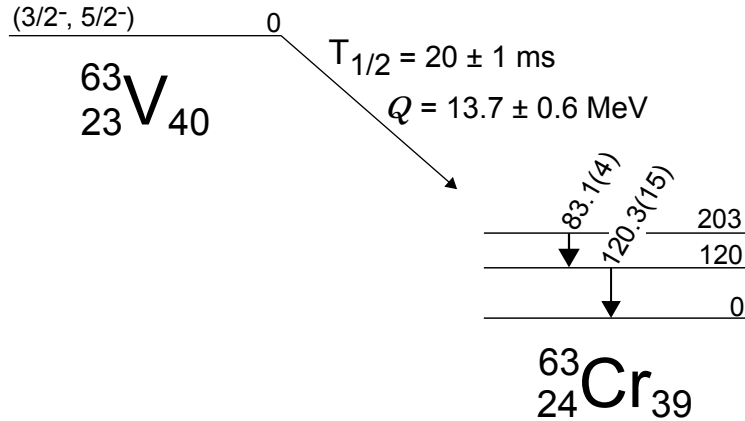


Figure 4.42: Level scheme of ${}^{63}\text{Cr}$ populated by the β decay of ${}^{63}\text{V}$. States are labelled on the left by their spins and parities and on the right by their energies in keV. γ -ray transition energies in keV are shown above the transitions. The absolute γ -ray intensity of each transition is shown in parentheses after the transition energy. The Q -value for the β decay of ${}^{63}\text{V}$ to ${}^{63}\text{Cr}$ was taken from Ref. [14].

Each of the two decay curves was fit based on the exponential decay of ${}^{63}\text{V}$ and a constant background. Half-lives of 16 ± 4 and 16 ± 3 ms result with the gates on the respective 83- and 120-keV transitions, which are consistent with the half-life determined from the ungated ${}^{63}\text{V}$ decay curve. The statistics were insufficient to obtain a meaningful ${}^{63}\text{V}$ half-life when a 414-keV γ ray was required to be detected in coincidence with the ${}^{63}\text{V}$ β decay.

The ${}^{63}\text{Cr}$ level scheme is shown in Fig. 4.42. Based on the observed absolute intensities of the 83- and 120-keV γ rays, the 120-keV transition is proposed to feed the ground state and the 83-keV transition is proposed to depopulate a 203-keV state and feed the 120-keV state. Weisskopf estimates for the decay of states in ${}^{63}\text{Cr}$ by 83- and 120-keV transitions with multipolarities of three or less are shown in Table 4.7. Theoretical calculations of internal conversion coefficients [2] for the transitions are also shown. Based on the Weisskopf estimates and the lack of observable half-lives for the 83- and 120-keV transitions in the present experiment, the 83- and 120-keV transitions are most likely of dipole or collective $E2$ character. It is possible that the ordering of the 83- and 120-keV transitions could be

Table 4.7: Theoretical internal conversion coefficients [2] for 83- and 120-keV transitions in ^{63}Cr and Weisskopf half-life estimates for states in ^{63}Cr depopulated by 83- and 120-keV transitions.

Energy (keV)	Radiation Type	α^{theory}	$T_{1/2}^{Weisskopf}$ (s)
83	<i>E1</i>	0.0621	7.4×10^{-13}
83	<i>M1</i>	0.0425	3.9×10^{-11}
83	<i>E2</i>	0.851	9.6×10^{-6}
83	<i>M2</i>	0.527	5.0×10^{-4}
83	<i>E3</i>	9.89	1.9×10^2
83	<i>M3</i>	6.29	9.8×10^3
120	<i>E1</i>	0.0198	2.4×10^{-13}
120	<i>M1</i>	0.0160	1.3×10^{-11}
120	<i>E2</i>	0.203	1.5×10^{-6}
120	<i>M2</i>	0.144	7.7×10^{-5}
120	<i>E3</i>	1.75	1.4×10^1
120	<i>M3</i>	1.26	7.8×10^2

reversed compared to what is proposed in Fig. 4.42 if the 83-keV transition has an internal conversion coefficient greater than about 1. Taking into account the theoretical values of α shown in Table 4.7 and also considering the Weisskopf estimates, if the reversed ordering is indeed correct, the 120-keV transition is likely an *E2* transition.

4.9 Isomeric γ -ray decay in ^{64}V

An isomer was discovered in ^{64}V in experiment e08020. The isomeric γ -ray energy spectrum detected within the 10- μs event window for those events in which a ^{64}V was implanted in the DSSD is shown in Fig. 4.43. The γ rays were required to be detected at least 300 ns after the implantation of the ^{64}V ion, which reduces the importance of the prompt γ flash emitted when ions are stopped in the detector. An isomeric γ -ray transition with an energy of 81.0 ± 0.7 keV is observed.

Due to the limited statistics, it was not possible to precisely determine a half-life for the

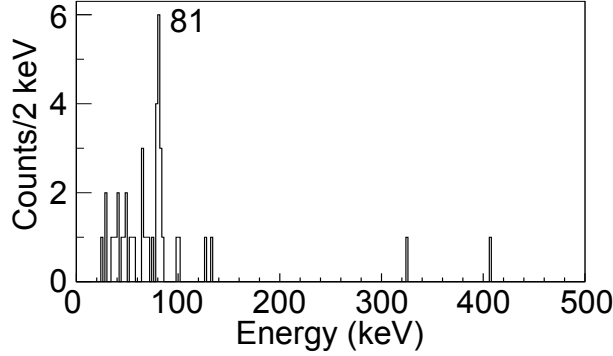


Figure 4.43: Isomeric γ -ray energy spectrum detected within the $10\text{-}\mu\text{s}$ event window for events in which a ^{64}V ion was deposited in the DSSD. γ rays detected less than 300 ns after the implantation of the ^{64}V are excluded to minimize the contribution from the prompt γ flash that is emitted when the ions are stopped in the detector.

isomeric state. However, an upper limit could be set using the methods for low statistics that are described in Ref. [111]. The natural logarithm of the time difference between the detection of the 81-keV γ ray and the ^{64}V ion is shown in Fig. 4.44 for γ rays occurring at least 300 ns after the ion implantation. The decay curve was fit based on the equation

$$\frac{dn}{d\phi} = n\lambda e^{\phi} e^{-\lambda e^{\phi}} \quad (4.1)$$

where n is the number of counts, λ is the decay constant, and

$$\phi = \ln(t) \quad (4.2)$$

[111]. The extracted half-life from the fit is $700 \pm 300\text{ ns}$. Considering the large uncertainty, an upper limit of $1\text{ }\mu\text{s}$ is conservatively reported for the half-life of the ^{64}V isomeric state.

It is difficult to interpret the origin of the isomer in ^{64}V . No isomeric state has been identified in the neighboring odd-odd isotope $^{62}\text{V}_{39}$ to draw systematic comparisons to, though isomers are known in $^{64,66}\text{Mn}_{39,41}$ (see Sections 4.11, 4.12, and 5.3). Deformation is

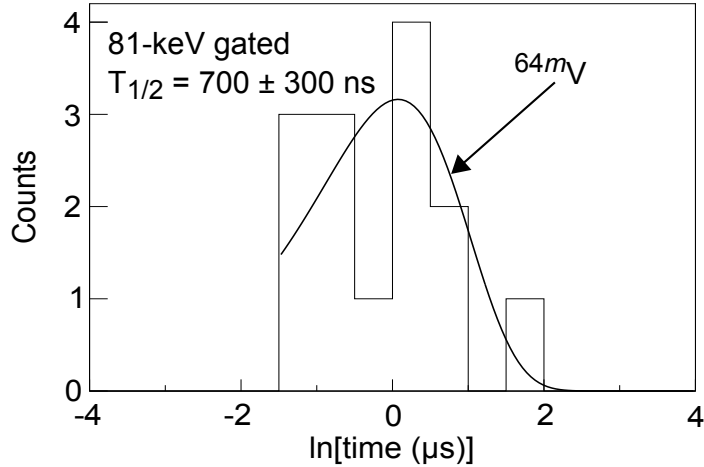


Figure 4.44: ^{64}V isomeric decay curve gated on 81-keV γ -ray transitions that occurred within the 10- μs event window and that were detected at least 300 ns after the implantation of the ^{64}V ion in the DSSD. The decay curve is shown with a logarithmic x-axis and a fit to Eq. 4.1 was used to determine the half-life of the isomeric state in ^{64}V .

likely important in ^{64}V , and a wide range of possible spins and parities could exist for the ground and isomeric states. Further experiments would be needed to deduce more about the low-energy level scheme of ^{64}V .

4.10 β decay of ^{64}V to ^{64}Cr

The β -delayed γ -ray energy spectrum detected within 80 ms of the implantation of a ^{64}V ion in the DSSD in experiment e08020 is shown in Fig. 4.45. The peak at 430 ± 2 keV is identified as the $2_1^+ \rightarrow 0_1^+$ transition in ^{64}Cr . Normalizing to the total number of ^{64}V β decays, the absolute intensity of the 430-keV transition is approximately 20%. The $2_1^+ \rightarrow 0_1^+$ transition was previously reported in two other experiments at energies of 420 ± 7 keV [52] and 435 keV [9] (uncertainty not given, but on order of 15 – 20 keV [112]). The presently determined energy is more precise than the previous values. The improved energy could be useful for future experiments that require the energy of the $2_1^+ \rightarrow 0_1^+$ transition to be used

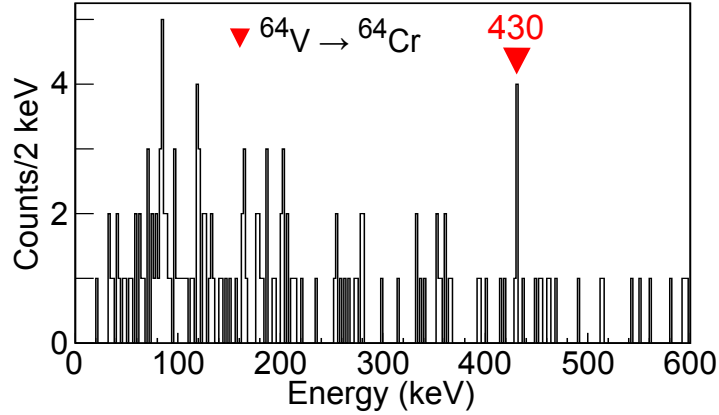


Figure 4.45: β -delayed γ -ray energy spectrum detected within 80 ms of the implantation of a ^{64}V ion in the DSSD shown in the range of 0 - 600 keV. The $2_1^+ \rightarrow 0_1^+$ transition in ^{64}Cr is marked by the red triangle and labelled by its energy energy in keV.

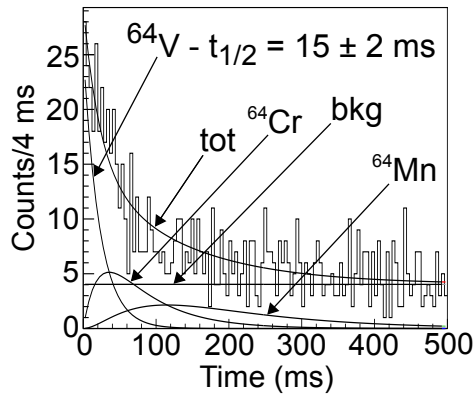


Figure 4.46: ^{64}V decay curve showing fragment- β correlations for β decays detected within 500 ms of a ^{64}V ion implantation in the DSSD. The fit to the decay curve, labelled “tot,” included the exponential decay of ^{64}V , the exponential growth and decay of ^{64}Cr and ^{64}Mn , and a constant background.

as a coincidence gating condition.

The ^{64}V β decay curve is shown in Fig. 4.46. The decay curve was fit including contributions from the decay of ^{64}V , the growth and decay of ^{64}Cr and ^{64}Mn , and a constant background. The half-lives of ^{64}Cr and ^{64}Mn were fixed according to the respective literature half-lives of 43 [106] and 89 ms [51]. The ^{64}V half-life is found to be 15 ± 2 ms. The present half-life is more precise than the value of 19 ± 8 ms determined from an earlier β -decay study.

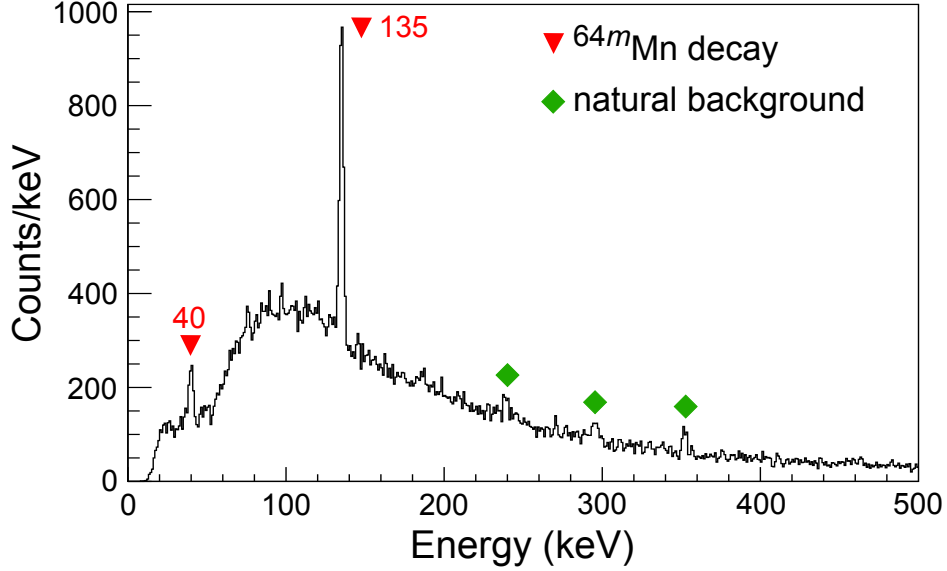


Figure 4.47: γ -ray energy spectrum detected within 2 ms of the implantation of a ^{64}Mn ion in the DSSD. Transitions observed following the decay of ^{64m}Mn are labelled with red triangles. Peaks due natural background decays are marked by green diamonds.

Table 4.8: Energies and relative intensities of γ rays detected in the decay of ^{64m}Mn . The listed intensities only take into account γ -ray transitions and do not include any potential contributions from internal conversion. The energies of the initial and final states between which each transition occurs are also given.

E_γ (keV)	$I_\gamma^{relative}$ (%)	Initial State (keV)	Final State (keV)
39.9 ± 0.4	50 ± 10	40	0
135.1 ± 0.3	100	175	40

4.11 Isomeric γ -ray decay in ^{64}Mn

The isomeric γ -ray energy spectrum detected within 2 ms of the arrival of a ^{64}Mn ion at the experimental end station in e08020 is shown in Fig. 4.47. Two peaks at 40 and 135 keV result from the decay of ^{64m}Mn . The precise energies and relative intensities of the γ -ray transitions that give rise to these peaks are given in Table 4.8. The low-intensity, higher-energy peaks in Fig. 4.47 that are marked by the green diamonds are due to natural background and are visible because the only required condition was the detection of a γ ray within the 2-ms time period after the implantation of a ^{64}Mn ion.

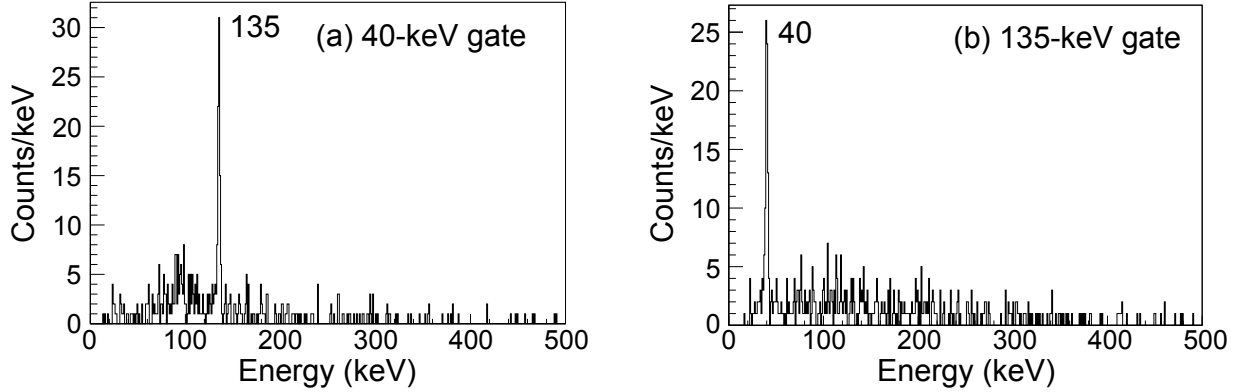


Figure 4.48: γ - γ coincidence spectra detected within 2 ms of the implantation of a ^{64}Mn ion in the DSSD gated on the (a) 40-keV and (b) 135-keV γ rays.

The γ - γ coincidence spectra gated on the 40- and 135-keV transitions in ^{64}Mn are shown in Figs. 4.48(a) and (b), respectively. The γ -decaying isomer in ^{64}Mn was first observed in Ref. [13], in which a 135-keV isomeric γ ray was detected. In a later experiment using conversion-electron spectroscopy, electron peaks with energies of 135 ± 10 and 175 ± 10 keV were detected in the decay of ^{64m}Mn [113]. Two transitions, having energies of 135 and 40 keV, were proposed to be in cascade, with the measured 175-keV peak arising from the sum of the 135- and 40-keV transitions [113]. The observed coincidence between the 40- and 135-keV γ rays in Figs. 4.48(a) and (b) confirms the cascade. No other branches were observed for the decay of the isomer, so it is inferred that the same number of 40- and 135-keV decays occurred. Gating on the 40-keV γ ray, the number of coincident 135-keV γ rays is consistent with one 135-keV γ ray for every 40-keV γ ray within the uncertainty of the measurement, and an upper limit of 0.5 is determined for the value of α for the 135-keV transition. The limit is consistent with the value of 0.15 ± 0.05 that was inferred from conversion-electron spectroscopy in Ref. [113]. On the other hand, if a gate is placed on the 135-keV γ ray in Fig. 4.47, the number of coincident 40-keV γ rays is significantly less than what would be expected if one 40-keV γ ray was detected for each 135-keV γ ray. From the difference

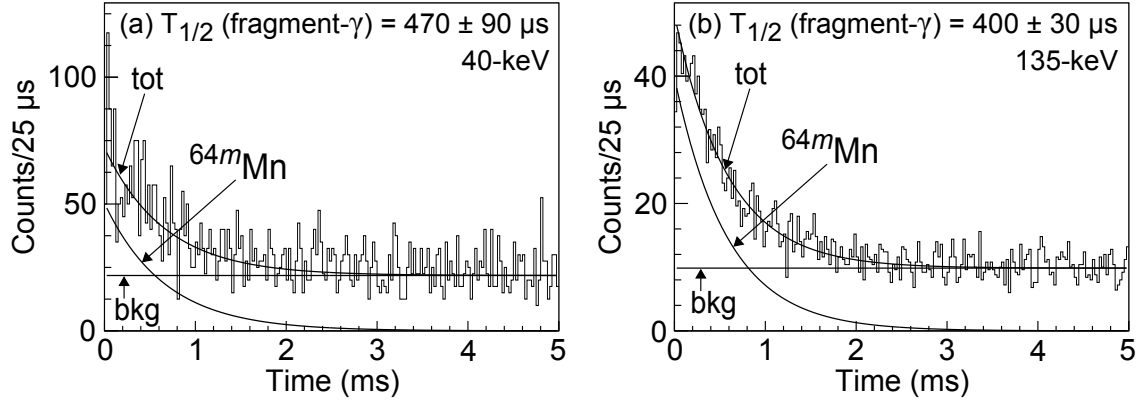


Figure 4.49: Decay curves for ^{64m}Mn showing fragment- γ correlations in which a (a) 40-keV or (b) 135-keV γ ray was detected within 5 ms of the ^{64}Mn fragment. The total fits to the data are labelled by “tot” and are comprised of an exponential for the decay of ^{64m}Mn and a constant background (“bkg”).

between the actual number of detected coincident 40-keV γ rays and what would be expected based on the intensity of the 135-keV peak, an internal conversion coefficient of 1.5 ± 0.6 is inferred for the 40-keV transition. If instead the value of α for the 40-keV transition is extracted from the difference in the total number of detected 40- and 135-keV γ rays, a value 0.9 ± 0.4 is determined. In Ref. [113] when it was first assumed that the 135-keV transition has $M2$ character, the value of α was deduced to be 0.6 ± 0.4 for the 40-keV transition.

Decay curves for ^{64m}Mn displaying the time between the detection of a ^{64}Mn ion in the DSSD and a 40- or 135-keV γ ray in SeGA are shown in Figs. 4.49(a) and (b), respectively. The half-lives determined from the fragment- γ correlations for the 40-keV and 135-keV γ rays were 470 ± 90 and $400 \pm 30 \mu\text{s}$, respectively. The values agree with one another and the weighted average yields a half-life of $410 \pm 30 \mu\text{s}$ for the isomer. ^{64m}Mn had previously been reported to have a slightly longer half-life of $500 \pm 50 \mu\text{s}$ [113].

The tentative decay scheme of ^{64m}Mn is shown in Fig. 4.50. The ordering of the 40- and 135-keV transitions and the tentative spins and parities given in Fig. 4.50 were proposed in Ref. [113] based on the intensities of the observed 135- and 175- keV conversion-electron

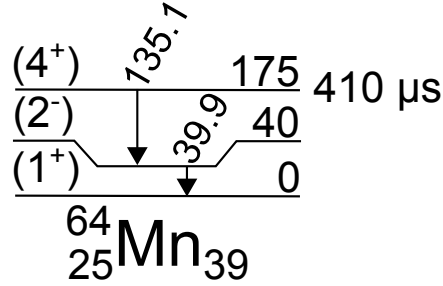


Figure 4.50: Decay scheme of ^{64m}Mn . States are labelled on the left by their spins and parities and on the right by their energies in keV. The half-life of the isomeric state at 175 keV is indicated.

peaks and Weisskopf estimates for the half-life of the isomer. The results of the current experiment are consistent with the previously determined level scheme. Theoretical calculations of internal conversion coefficients [2] for the 40- and 135-keV transitions in ^{64}Mn , as well as Weisskopf half-life estimates, are given in Table 4.9 for transitions with multiplicities less than four. Based on the inferred internal conversion coefficient of the 40-keV transition, it most likely has $E1$ character. The Weisskopf estimate for a 40-keV $E1$ transition is too short to correspond to the transition that depopulates the isomeric state, suggesting that the 135-keV transition instead depopulates the isomer. The value of α measured for the 135-keV transition in Ref. [113] is consistent with a multiplicity of two for the transition. Further, a comparison of the half-life of the isomer with Weisskopf estimates suggests the 135-keV transition is $M2$. Due to inferred strong β -decay feeding of the ^{64}Mn ground state from the 0^+ ground state in ^{64}Cr , 1^+ has been proposed as the ground-state spin and parity of ^{64}Mn [81, 113]. Assuming a 40-keV $E1$ transition and a 135-keV $M2$ transition, 2^- and 4^+ are inferred as the tentative spins and parities of the 40- and 175-keV states, respectively.

Table 4.9: Theoretical internal conversion coefficients [2] for 40- and 135-keV transitions in ^{64}Mn and Weisskopf half-life estimates for states in ^{64}Mn depopulated by 40- and 135-keV transitions.

Energy (keV)	Radiation Type	α^{theory}	$T_{1/2}^{Weisskopf}$ (s)
40	<i>E1</i>	0.634	6.6×10^{-12}
40	<i>M1</i>	0.374	3.4×10^{-10}
40	<i>E2</i>	15.0	3.6×10^{-4}
40	<i>M2</i>	9.1	1.9×10^{-2}
40	<i>E3</i>	320	3.0×10^4
40	<i>M3</i>	203	1.6×10^6
135	<i>E1</i>	0.0154	1.7×10^{-13}
135	<i>M1</i>	0.0138	8.9×10^{-12}
135	<i>E2</i>	0.142	8.3×10^{-7}
135	<i>M2</i>	0.113	4.5×10^{-5}
135	<i>E3</i>	1.11	6.1
135	<i>M3</i>	0.89	3.2×10^2

4.12 Isomeric γ -ray decay in ^{66}Mn

The isomeric γ -ray energy spectrum that was detected within 4 ms of the implantation of a ^{66}Mn ion in the DSSD in experiment e08020 is shown in Fig. 4.51. As in the ^{64}Mn isomeric γ -ray energy spectrum, the peaks marked by green diamonds arise from natural background radiation. The three peaks labelled with the red triangles result from the decay of an isomeric state in ^{66}Mn . The energies and relative intensities of the three γ -ray peaks are shown in Table 4.10. A known background γ ray that is emitted in the decay chain of ^{238}U occurs at 295.2 keV and overlaps in energy with the 294-keV peak in Fig. 4.51. However, the 294-keV transition was also observed in coincidence with the 170-keV transition. Therefore, the reported energy and efficiency of the 294-keV transition in Table 4.10 were determined from the coincidence spectrum.

The background-subtracted isomeric γ - γ coincidence spectra with gates placed on the 170-, 251-, and 294-keV γ -ray transitions in ^{66}Mn are shown in Fig. 4.52(a), (b), and (c),

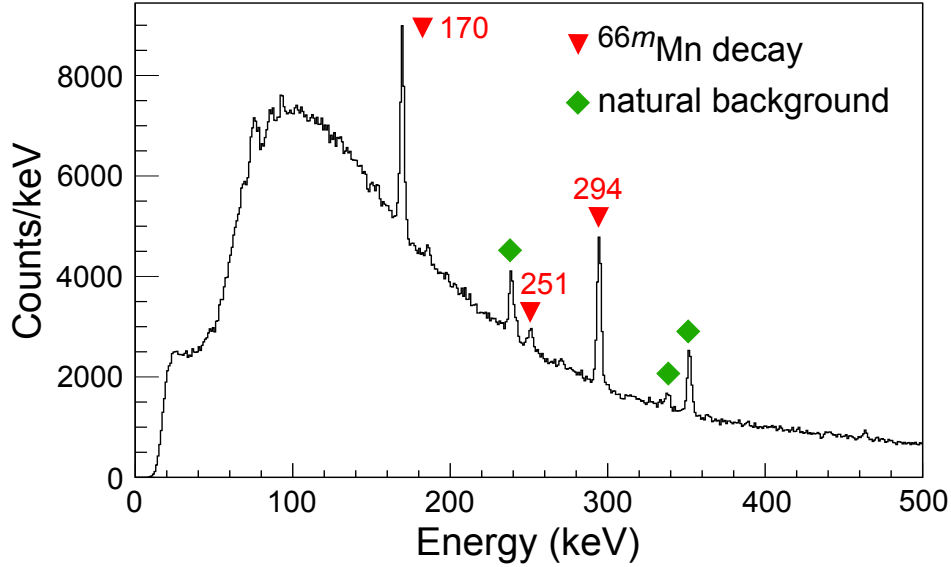


Figure 4.51: γ -ray energy spectrum detected within 4 ms of the implantation of a ^{66}Mn ion in the DSSD. Transitions observed following the decay of ^{66m}Mn are labelled with red triangles. Peaks due natural background decays are marked by green diamonds.

respectively. The ^{66}Mn isomer was first identified in Ref. [113], in which conversion-electron peaks were detected at 170 ± 10 and 294 ± 10 keV. Based on Figs. 4.52(a) and (c), the 170- and 294-keV transitions are coincident. Furthermore, the 251-keV transition, which was observed for the first time, is also coincident with the 170-keV peak. However, the 251- and 294-keV γ rays were not observed in coincidence. Thus, the 251- and 294-keV transitions occur by parallel decay branches, where each decay branch either feeds or is fed

Table 4.10: Energies and relative intensities of γ rays detected in the decay of ^{66m}Mn . The listed intensities only take into account γ -ray transitions and do not include any potential contributions from internal conversion. The energies of the initial and final states between which each transition occurs are also given.

E_γ (keV)	$I_\gamma^{relative}$ (%)	Initial State (keV)	Final State (keV)
42.8 ± 0.5^a	10 ± 2	43	0
169.6 ± 0.3	100	464	295
251.1 ± 0.4	14 ± 4	294	43
294.4 ± 0.3	78 ± 5	294	0

^a Transition only observed in coincidence spectrum

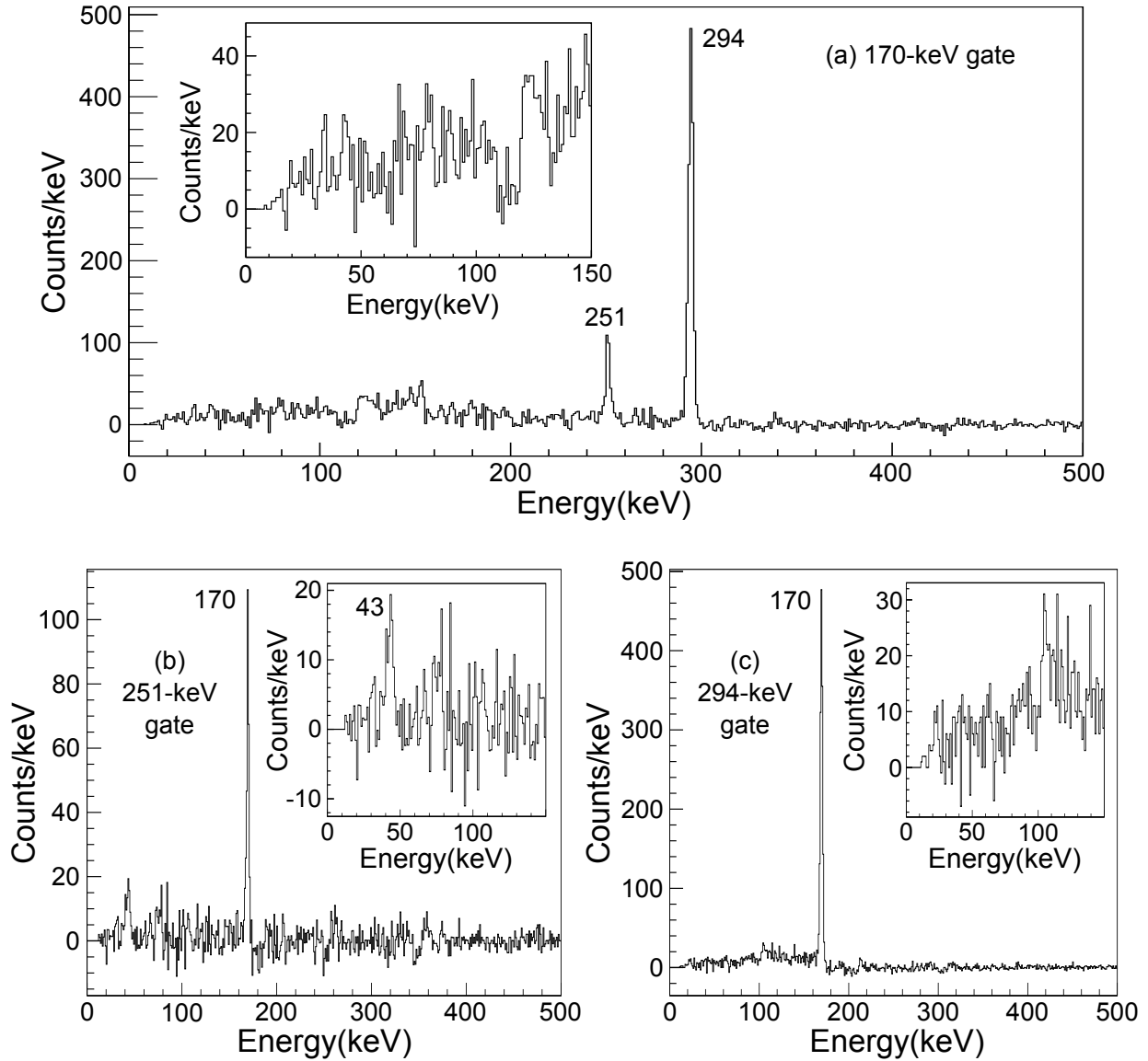


Figure 4.52: Background-subtracted γ - γ coincidence spectra detected within 4 ms of the implantation of a ^{66}Mn ion in the DSSD gated on the (a) 170-keV, (b) 251-keV, and (c) 294-keV transitions. The inset of each panel shows a zoom of the region from 0 - 150 keV.

by the 170-keV transition. Based on Fig. 4.52(b), the 251-keV γ ray appears to be coincident with a low-intensity γ ray at 43 keV. Within the uncertainty, the energy sum of the 43- and 251-keV transitions matches the energy of the 294-keV transition. The apparent coincidence and energy sum suggests the 43- and 251-keV transitions are in cascade. With this decay pattern, coincidence between the 170- and 43-keV would be expected, but a peak at 43 keV is not conclusively identified in Fig. 4.52(a). However, the branch through the 251-43-keV cascade is weak and the 170-keV gate has more background than the 251-keV gate, which could have prevented the observation of coincidence between the 43- and 170-keV γ rays. Despite the lack of definitively observed coincidence between the 170- and 43-keV γ rays, the 43- and 251-keV transitions are proposed to be in cascade based on the apparent coincidence between the 251- and 43-keV γ rays and the match in energy between the 294-keV transition and the sum of the 251- and 43-keV transitions. Based on the inferred number of 251-keV γ -ray decays in the ^{66}Mn isomeric γ -ray spectrum and the observed number of coincidence counts at 43 keV in Fig. 4.52(b), an internal conversion coefficient of 0.7 ± 0.7 is deduced for the 43-keV transition.

The ^{66m}Mn decay curves gated on the 170-, 251-, and 294-keV γ rays are shown in Figs. 4.53(a), (b), and (c), respectively. Fitting each decay curve with an exponential for the decay of ^{66m}Mn plus a constant background, half-lives of 940 ± 40 , 820 ± 120 , and 890 ± 40 μs were determined for the respective decay curves gated on 170-, 251-, and 294-keV transitions. The three half-lives are consistent and yield a weighted average of 910 ± 30 μs , which agrees with, but is more precise than the half-life of 750 ± 250 μs determined previously [113].

The tentatively proposed decay scheme for ^{66m}Mn is shown in Fig. 4.54. As for ^{64}Mn , the ground state of ^{66}Mn has been inferred to have a spin and parity of 1^+ due to an apparent large ground-state feeding in the β decay of ^{66}Cr [81]. Based on the similarities between

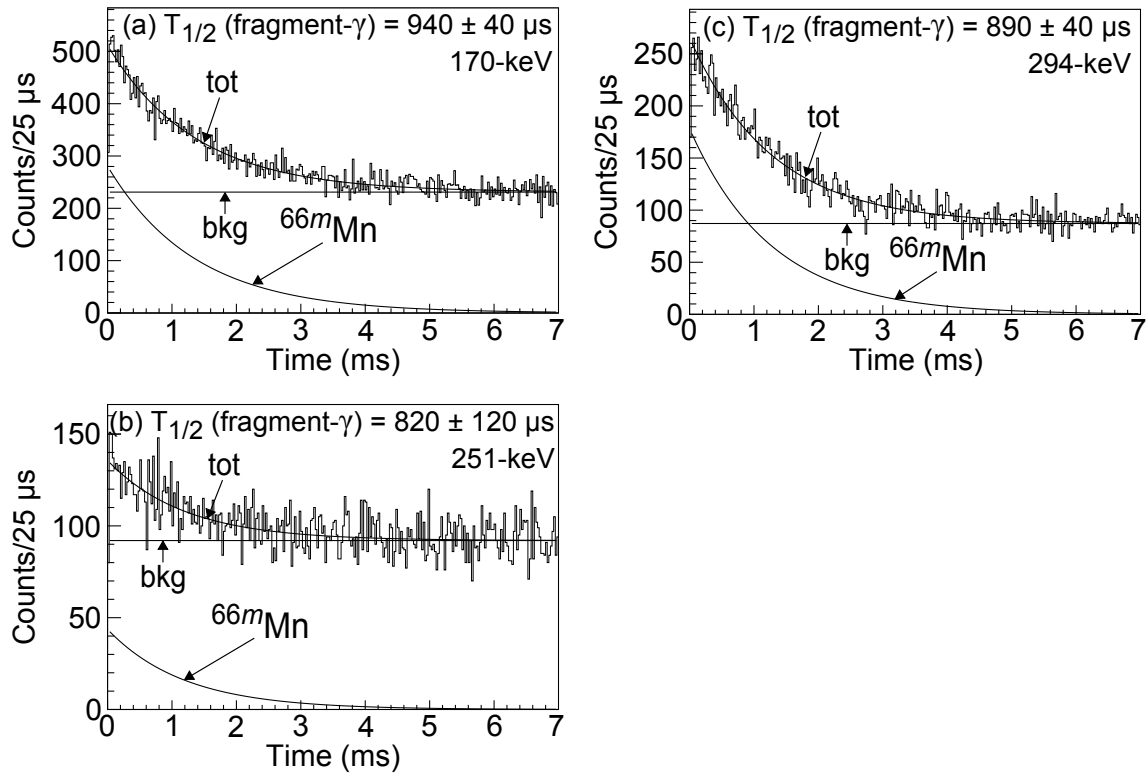


Figure 4.53: Decay curves for ^{66m}Mn showing fragment- γ correlations in which a (a) 170-keV, (b) 251-keV, or (c) 294-keV γ ray was detected within 7 ms of the ^{66}Mn fragment. The total fits to the data are labelled by “tot” and are comprised of an exponential for the decay of ^{66m}Mn and a constant background (“bkg”).

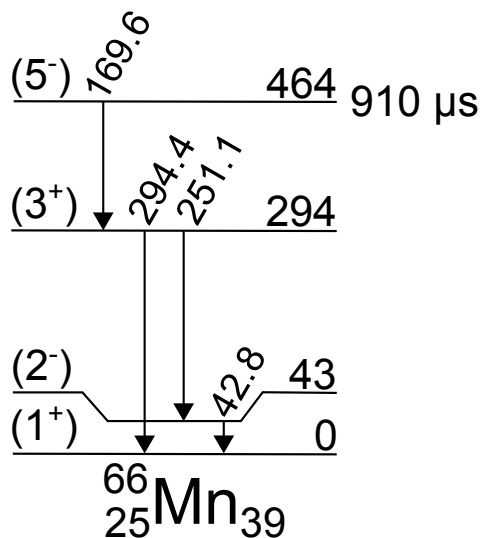


Figure 4.54: Decay scheme of ^{66m}Mn . States are labelled on the left by their spins and parities and on the right by their energies in keV. The half-life of the isomeric state at 464 keV is indicated.

the energies and inferred internal conversion coefficients of the 40- and 43-keV transitions in ^{64}Mn and ^{66}Mn , respectively, the 43-keV transition in ^{66}Mn is tentatively identified as an $E1$ transition that connects a 2^- first excited state with the 1^+ ground state. The 251-keV transition depopulates a 294-keV state and feeds the 43-keV state, and the 294-keV transition feeds the ground state directly. Further insight into the nature of the 251- and 294-keV transitions can be established from Weisskopf estimates of their transition rates. The half-lives calculated based on Weisskopf estimates for states in ^{66}Mn depopulated by 43-, 170-, 251-, and 294-keV transitions are given in Table 4.11. Based on Table 4.11, neither the 251- nor the 294-keV transition should have a multipolarity greater than two in order for the half-life and branching of the 294-keV state to be consistent with the experimental data. Therefore, the spin of the 294-keV state is restricted to three or less with a positive or negative parity.

Low-energy $E1$ transitions are typically strongly hindered relative to Weisskopf estimates, with measured half-lives on the order of six orders of magnitude longer than the Weisskopf estimates [114, 115]. Taking into account the $E1$ hindrance and the observed branching of the 294-keV state, the most likely scenario appears to be a 251-keV $E1$ transition and a 294-keV $E2$ transition that depopulate a 3^+ state at 294 keV. Based on the Weisskopf estimates, the 170-keV transition is proposed to have $E2$ character, leading to a tentative spin and parity of 5^- for the isomer. If however, the 251-keV transition is $E2$ and the 294-keV transition is $E1$, the spins and parities of the 294- and 464-keV states would be 0^- and 2^+ , respectively. In this scenario though, an $M1$ transition would be expected between the 464- and 43-keV states, but none was observed. Therefore, the scheme presented in Fig. 4.54 is proposed for the decay of ^{66m}Mn .

Table 4.11: Theoretical internal conversion coefficients [2] for 43-, 170-, 251-, and 294-keV transitions in ^{66}Mn and Weisskopf half-life estimates for states in ^{66}Mn depopulated by 43-, 170-, 251-, and 294-keV transitions.

Energy (keV)	Radiation Type	α^{theory}	$T_{1/2}^{Weisskopf}$ (s)
43	<i>E1</i>	0.510	5.3×10^{-12}
43	<i>M1</i>	0.305	2.8×10^{-10}
43	<i>E2</i>	11.4	2.5×10^{-4}
43	<i>M2</i>	6.7	1.3×10^{-2}
43	<i>E3</i>	229	1.8×10^4
43	<i>M3</i>	146	9.5×10^5
170	<i>E1</i>	0.0076	8.4×10^{-14}
170	<i>M1</i>	0.0077	4.5×10^{-12}
170	<i>E2</i>	0.0586	2.5×10^{-7}
170	<i>M2</i>	0.0519	1.4×10^{-5}
170	<i>E3</i>	0.383	1.2
170	<i>M3</i>	0.339	6.2×10^1
251	<i>E1</i>	0.00237	2.6×10^{-14}
251	<i>M1</i>	0.00293	1.4×10^{-12}
251	<i>E2</i>	0.0135	3.6×10^{-8}
251	<i>M2</i>	0.0147	1.9×10^{-6}
251	<i>E3</i>	0.066	7.5×10^{-2}
251	<i>M3</i>	0.071	4.0
294	<i>E1</i>	0.00150	1.6×10^{-14}
294	<i>M1</i>	0.00200	8.6×10^{-13}
294	<i>E2</i>	0.0076	1.6×10^{-8}
294	<i>M2</i>	0.0090	8.6×10^{-7}
294	<i>E3</i>	0.0329	2.4×10^{-2}
294	<i>M3</i>	0.0386	1.3

Chapter 5

Discussion

The rapid development of collectivity below ^{68}Ni has been attributed to the influence of the $\nu g_{9/2}$ orbital. The present data set provides a look at the occupancy of the $g_{9/2}$ orbital in nuclei near $N = 40$.

5.1 Shape coexistence in ^{68}Ni

To aid the interpretation of the low-energy level scheme of ^{68}Ni , Monte Carlo shell-model (MCSM) calculations using the A3DA effective interaction with minor revisions [15, 116] have been performed. The calculations were carried out in the $pf g_9 d_5$ model space, which consists of the $0f_{7/2}$, $0f_{5/2}$, $1p_{3/2}$, $1p_{1/2}$, $0g_{9/2}$, and $1d_{5/2}$ orbitals for both protons and neutrons. In comparison to the original A3DA interaction, the single-particle energy of the $\nu 0g_{9/2}$ orbital and the components of the residual nucleon-nucleon interaction arising from the tensor monopole interaction involving the $g_{9/2}$ orbital were modified [15]. The results for MCSM calculations across the Ni isotopic chain are presented in Ref. [22]. Here, the experimental results obtained for ^{68}Ni in experiment e11503 are compared to the MCSM predictions for ^{68}Ni . The energies determined by the MCSM calculation for the three lowest energy excited states in ^{68}Ni are compared to experiment in Fig. 5.1. The results of several additional shell-model calculations using different effective interactions [16, 17, 18, 19] are also shown in Fig. 5.1. All of the calculations shown in Fig. 5.1 were carried out before the

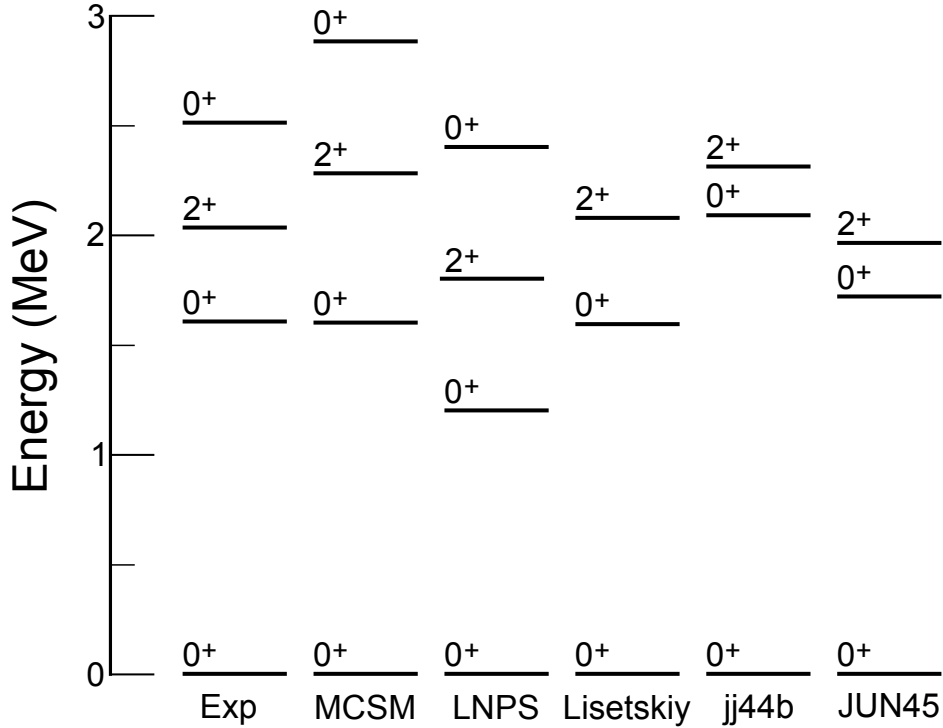


Figure 5.1: Energies of the four lowest energy states in ^{68}Ni as determined by experiment (Exp), Monte Carlo shell-model calculations using the revised A3DA [15] effective interaction (MCSM), and shell-model calculations using the LNPS [16], Lisetskiy [17], jj44b [18], and JUN45 [19] effective interactions. The experimental energies of the 2_1^+ and 0_3^+ states were taken from Ref. [20] and Ref. [21], respectively.

experiment was performed.

An important element of each calculation in Fig. 5.1 is the model space used. The calculations using the Lisetskiy [17], jj44b [18], and JUN45 [19] effective interactions were carried out in a model space encompassing the $1p_{3/2}$, $0f_{5/2}$, $1p_{1/2}$, and $0g_{9/2}$ orbitals for both protons and neutrons. In this model space, there are no valence protons for the Ni isotopes. Therefore, while proton excitations may be implicitly included in the effective interactions based on the fits used to derive the interactions, proton excitation are not included explicitly. The implicit inclusion of proton excitations is likely important for calculations with the Lisetskiy interaction, which was derived based on the Ni isotopes [17]. The LNPS calculation was performed in a model space including the fp shell for protons and the $1p_{3/2}$, $0f_{5/2}$, $1p_{1/2}$,

$0g_{9/2}$, and $1d_{5/2}$ orbitals for neutrons, and the calculated energies shown in Fig. 5.1 were taken from Ref. [16].

The absence of a second excited 0^+ state below 3 MeV in the shell-model calculations using the Lisetskiy, jj44b, and JUN45 interactions can primarily be attributed to the model space. Since the second excited 0^+ state is thought to be due to proton excitations across $Z = 28$ [16, 68], the lack of explicitly included valence proton excitations explains the failure to accurately predict the energy of the second excited 0^+ state with these three calculations. The MCSM and LNPS calculations, which include additional proton degrees of freedom, do predict the presence of three 0^+ states below 3 MeV. All of the interactions can reasonably well calculate the energy of the first excited 0^+ state, which has been attributed to neutron excitations across $N = 40$ [16, 68].

The MCSM calculation suggests that the ground, first excited, and second excited 0^+ states in ^{68}Ni all have different shapes. The results of the MCSM calculation that are indicative of shape coexistence are shown in Fig. 5.2, which was taken from Ref. [22]. In Figs. 5.2(a), (b), and (c), the MCSM basis vectors are shown for the 0_1^+ , 0_2^+ , and 0_3^+ states in ^{68}Ni , respectively, on a constrained Hartree-Fock potential energy surface. Each circle represents a basis vector, with the location of the circle on the potential energy surface denoting the shape of the basis vector and the area of the circle signifying the importance of the basis vector in the wave function of the state. Three local minima, characterized by different shapes, are calculated on the potential energy surface, and the MCSM calculation associates each 0^+ state below 3 MeV in ^{68}Ni with one of the minima. The calculated ground-state wave function has strong overlap with MCSM basis vectors that have very small quadrupole moments, indicating the ground state in ^{68}Ni is spherical. The most important basis vectors in the description of the first excited 0^+ state have oblate shapes nearly identical to the

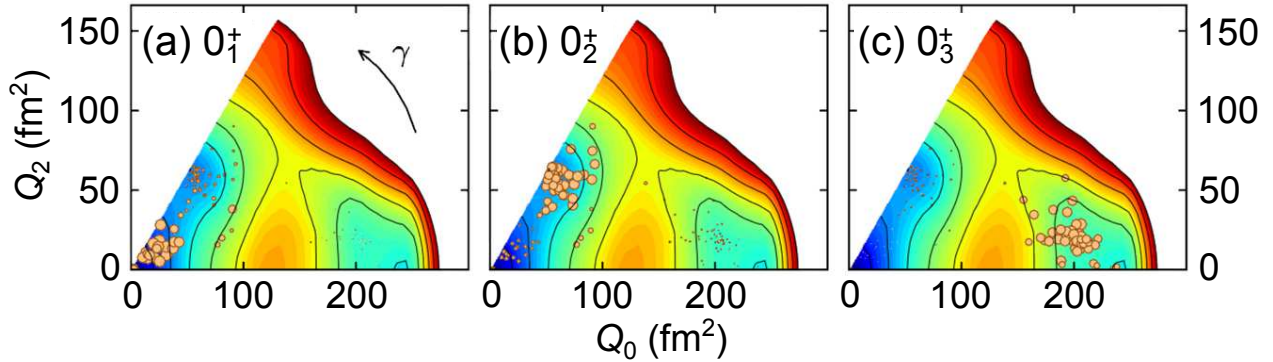


Figure 5.2: Potential energy surface for ^{68}Ni calculated by the constrained Hartree-Fock method. The circles on the potential energy surface represent the basis vectors calculated by the MCSM calculation. The location of each circle represents the shape of the basis vector, while the area of the circle denotes the importance of the basis vector in the calculated wave function of the (a) 0_1^+ , (b) 0_2^+ , and (c) 0_3^+ state in ^{68}Ni . The figure was taken from Ref. [22].

oblate minimum calculated on the potential energy surface, suggesting the first excited 0^+ state is oblate. Similarly, the calculated wave function of the second excited 0^+ state has strong overlap with basis vectors having prolate shapes near the prolate minimum on the potential energy surface. Therefore, the second excited 0^+ state in ^{68}Ni is predicted to be prolate.

According to the MCSM calculation, the first excited 0^+ state in ^{68}Ni has on average 2.4 neutrons and 0.7 protons excited across the $N = 40$ and $Z = 28$ gaps, respectively. Previous theoretical studies have also indicated the importance of neutron excitations out of the fp shell for the first excited 0^+ state [16, 68]. The proton excitations out of the $\pi 0f_{7/2}$ orbital also warrant discussion. Shape coexistence involving proton excitations across $Z = 28$ has been proposed in the isotonic nucleus $^{67}_{27}\text{Co}_{40}$ [64]. Further, it has been suggested that the two β -decaying states in $^{68}\text{Co}_{41}$ have different shapes [66]. Each β -decaying isomer would be expected to preferentially feed daughter states with the same shape. Although the β -decaying-feeding intensities to different ^{68}Ni daughter states were not precisely determined in the present experiment, future β -decay studies could inform the interpretation of shape

coexistence.

While it would be ideal to compare the experimentally determined value of $\rho^2(E0)$ for the $0_2^+ \rightarrow 0_1^+$ transition to a theoretical value, $\rho^2(E0)$ is rather difficult to predict theoretically due to an incomplete knowledge of the appropriate effective charges to use in the calculation. To facilitate comparisons between experiment and theory that go beyond the excitation energies of low-energy states, the ^{68}Ni $\rho^2(E0)$ value can be interpreted using a two-level mixing model. Within the model, strong mixing is assumed between two underlying 0^+ configurations with different shapes in the ground and first excited 0^+ states of ^{68}Ni . The two underlying configurations are a spherical $(f_{5/2}, p)^{12}(g_{9/2})^0$ neutron configuration where no neutrons are excited across the $N = 40$ gap and an oblate $(f_{5/2}, p)^{10}(g_{9/2})^2$ neutron configuration where a pair of neutrons are excited out of the upper fp shell into the $g_{9/2}$ orbital. From the relative $B(E2)$ measurements made in Ref. [71], a large degree of mixing of multi-particle, multi-hole configurations in the ground state of ^{68}Ni was inferred. No transfer reactions have been reported for ^{68}Ni , but $^{90}\text{Zr}_{50}$ can be used as a proton analog of ^{68}Ni , with protons occupying the fp shell and $g_{9/2}$ orbital in ^{90}Zr rather than neutrons, which occupy the fp shell and $g_{9/2}$ orbital in ^{68}Ni . Based on nucleon transfer reactions, strong mixing has been measured between $(f_{5/2}, p)^{12}(g_{9/2})^0$ and $(f_{5/2}, p)^{10}(g_{9/2})^2$ proton configurations in the ground state of ^{90}Zr [33, 46, 47]. Assuming maximal mixing between the spherical and oblate 0^+ configurations in the ground and first excited states of ^{68}Ni , and using Eq. 1.13, from the measured $\rho^2(E0)$ value of 7.4×10^{-3} , the absolute value of the difference in deformation parameter between the oblate and spherical configurations is determined to be 0.16. Similarly, the difference in the absolute value of the intrinsic quadrupole moment between the two configurations can be determined to be 101 efm^2 . The inferred values are consistent with the MCSM predictions, which calculate the oblate-deformed first excited 0^+

state in ^{68}Ni to have a deformation parameter of -0.16 and an intrinsic quadrupole moment of -95 efm^2 .

5.2 Odd- A Cr isotopes

Based on the present analysis of $^{61,63}\text{Cr}_{37,39}$, as $N = 40$ is approached, a significant change is apparent in the low-energy level schemes of the odd- A Cr isotopes, particularly when N exceeds 36. The probable cause is the onset of deformation that occurs due to the occupation of the $\nu 0g_{9/2}$ orbital and to a lesser extent the $\nu 1d_{5/2}$ orbital. Even below $N = 36$, the excitation energy of the $9/2_1^+$ state has been observed to rapidly decrease as N increases along the odd- A Cr isotopic chain (see Fig. 1.6). Notably, the $9/2_1^+$ state energy drops from 3707 keV in $^{53}\text{Cr}_{29}$ to 503 keV in $^{59}\text{Cr}_{35}$.

To investigate the changes to the low-energy level schemes of the odd- A Cr isotopes as an approach is made to $N = 40$, shell-model calculations have been performed with NUSHELLX [117] using the GXPF1A [118] and KB3G [119] effective interactions in the fp model space. The calculated level schemes for $^{55,57}\text{Cr}$ and $^{59,61}\text{Cr}$ are compared to experiment in Figs. 5.3 and 5.4, respectively, for states below 1.5 MeV. For all four nuclei in Figs. 5.3 and 5.4, both the GXPF1A and KB3G interactions predict that the three lowest-energy states are, in some order, $1/2^-$, $3/2^-$, and $5/2^-$ states. Further, the calculated wave functions of the $1/2_1^-$, $3/2_1^-$, and $5/2_1^-$ states can be interpreted relatively simply. The most important neutron configurations calculated for the $1/2_1^-$, $3/2_1^-$, and $5/2_1^-$ states in $^{55,57,59,61}\text{Cr}$ are listed in Table 5.1. For the four isotopes, the GXPF1A and KB3G interactions both calculate configurations with an odd number of neutrons in the $f_{5/2}$ orbital to be the most important configurations in the description of the $5/2_1^-$ state. The calculations predict that the $3/2_1^-$

Table 5.1: Main valence-neutron configurations of the $1/2_1^-$, $3/2_1^-$, and $5/2_1^-$ levels in $^{55,57,59,61}\text{Cr}$ as determined by the shell-model calculations. Configurations with a probability of 0.10 or greater are shown. In addition to the given occupancies of $1p_{3/2}$, $0f_{5/2}$, and $1p_{1/2}$ orbitals, each listed configuration has a completely filled $0f_{7/2}$ orbital.

Isotope	J^π	GXPF1A		KB3G	
		Wave function (neutron)	Prob.	Wave function (neutron)	Prob.
^{55}Cr	$1/2_1^-$	$(1p_{3/2})^2, (0f_{5/2})^1, (1p_{1/2})^0$	0.24	$(1p_{3/2})^2, (0f_{5/2})^1, (1p_{1/2})^0$	0.26
		$(1p_{3/2})^2, (0f_{5/2})^0, (1p_{1/2})^1$	0.22	$(1p_{3/2})^1, (0f_{5/2})^1, (1p_{1/2})^1$	0.18
		$(1p_{3/2})^1, (0f_{5/2})^1, (1p_{1/2})^1$	0.16	$(1p_{3/2})^2, (0f_{5/2})^0, (1p_{1/2})^1$	0.14
	$3/2_1^-$	$(1p_{3/2})^3, (0f_{5/2})^0, (1p_{1/2})^0$	0.47	$(1p_{3/2})^3, (0f_{5/2})^0, (1p_{1/2})^0$	0.37
		$(1p_{3/2})^2, (0f_{5/2})^0, (1p_{1/2})^1$	0.11		
	$5/2_1^-$	$(1p_{3/2})^2, (0f_{5/2})^1, (1p_{1/2})^0$	0.44	$(1p_{3/2})^2, (0f_{5/2})^1, (1p_{1/2})^0$	0.42
		$(1p_{3/2})^1, (0f_{5/2})^1, (1p_{1/2})^1$	0.10		
^{57}Cr	$1/2_1^-$	$(1p_{3/2})^4, (0f_{5/2})^0, (1p_{1/2})^1$	0.51	$(1p_{3/2})^4, (0f_{5/2})^0, (1p_{1/2})^1$	0.19
		$(1p_{3/2})^2, (0f_{5/2})^2, (1p_{1/2})^1$	0.12	$(1p_{3/2})^4, (0f_{5/2})^1, (1p_{1/2})^0$	0.18
				$(1p_{3/2})^3, (0f_{5/2})^2, (1p_{1/2})^0$	0.14
				$(1p_{3/2})^3, (0f_{5/2})^1, (1p_{1/2})^1$	0.10
	$3/2_1^-$	$(1p_{3/2})^3, (0f_{5/2})^2, (1p_{1/2})^0$	0.39	$(1p_{3/2})^3, (0f_{5/2})^2, (1p_{1/2})^0$	0.47
		$(1p_{3/2})^3, (0f_{5/2})^1, (1p_{1/2})^1$	0.12		
	$5/2_1^-$	$(1p_{3/2})^4, (0f_{5/2})^1, (1p_{1/2})^0$	0.45	$(1p_{3/2})^4, (0f_{5/2})^1, (1p_{1/2})^0$	0.38
		$(1p_{3/2})^3, (0f_{5/2})^1, (1p_{1/2})^1$	0.15	$(1p_{3/2})^3, (0f_{5/2})^1, (1p_{1/2})^1$	0.15
			$(1p_{3/2})^2, (0f_{5/2})^1, (1p_{1/2})^2$	0.10	
^{59}Cr	$1/2_1^-$	$(1p_{3/2})^4, (0f_{5/2})^2, (1p_{1/2})^1$	0.63	$(1p_{3/2})^4, (0f_{5/2})^2, (1p_{1/2})^1$	0.60
	$3/2_1^-$	$(1p_{3/2})^4, (0f_{5/2})^2, (1p_{1/2})^1$	0.44	$(1p_{3/2})^4, (0f_{5/2})^3, (1p_{1/2})^0$	0.36
		$(1p_{3/2})^4, (0f_{5/2})^3, (1p_{1/2})^0$	0.12	$(1p_{3/2})^4, (0f_{5/2})^2, (1p_{1/2})^1$	0.22
		$(1p_{3/2})^3, (0f_{5/2})^2, (1p_{1/2})^2$	0.11		
	$5/2_1^-$	$(1p_{3/2})^4, (0f_{5/2})^1, (1p_{1/2})^2$	0.28	$(1p_{3/2})^4, (0f_{5/2})^3, (1p_{1/2})^0$	0.47
		$(1p_{3/2})^4, (0f_{5/2})^3, (1p_{1/2})^0$	0.21	$(1p_{3/2})^3, (0f_{5/2})^3, (1p_{1/2})^1$	0.11
		$(1p_{3/2})^4, (0f_{5/2})^2, (1p_{1/2})^1$	0.15	$(1p_{3/2})^2, (0f_{5/2})^3, (1p_{1/2})^2$	0.10
^{61}Cr	$1/2_1^-$	$(1p_{3/2})^4, (0f_{5/2})^4, (1p_{1/2})^1$	0.76	$(1p_{3/2})^4, (0f_{5/2})^4, (1p_{1/2})^1$	0.75
	$3/2_1^-$	$(1p_{3/2})^4, (0f_{5/2})^3, (1p_{1/2})^2$	0.71	$(1p_{3/2})^4, (0f_{5/2})^4, (1p_{1/2})^1$	0.44
		$(1p_{3/2})^4, (0f_{5/2})^4, (1p_{1/2})^1$	0.13	$(1p_{3/2})^4, (0f_{5/2})^3, (1p_{1/2})^2$	0.33
	$5/2_1^-$	$(1p_{3/2})^4, (0f_{5/2})^3, (1p_{1/2})^2$	0.78	$(1p_{3/2})^4, (0f_{5/2})^3, (1p_{1/2})^2$	0.60
				$(1p_{3/2})^4, (0f_{5/2})^4, (1p_{1/2})^1$	0.10

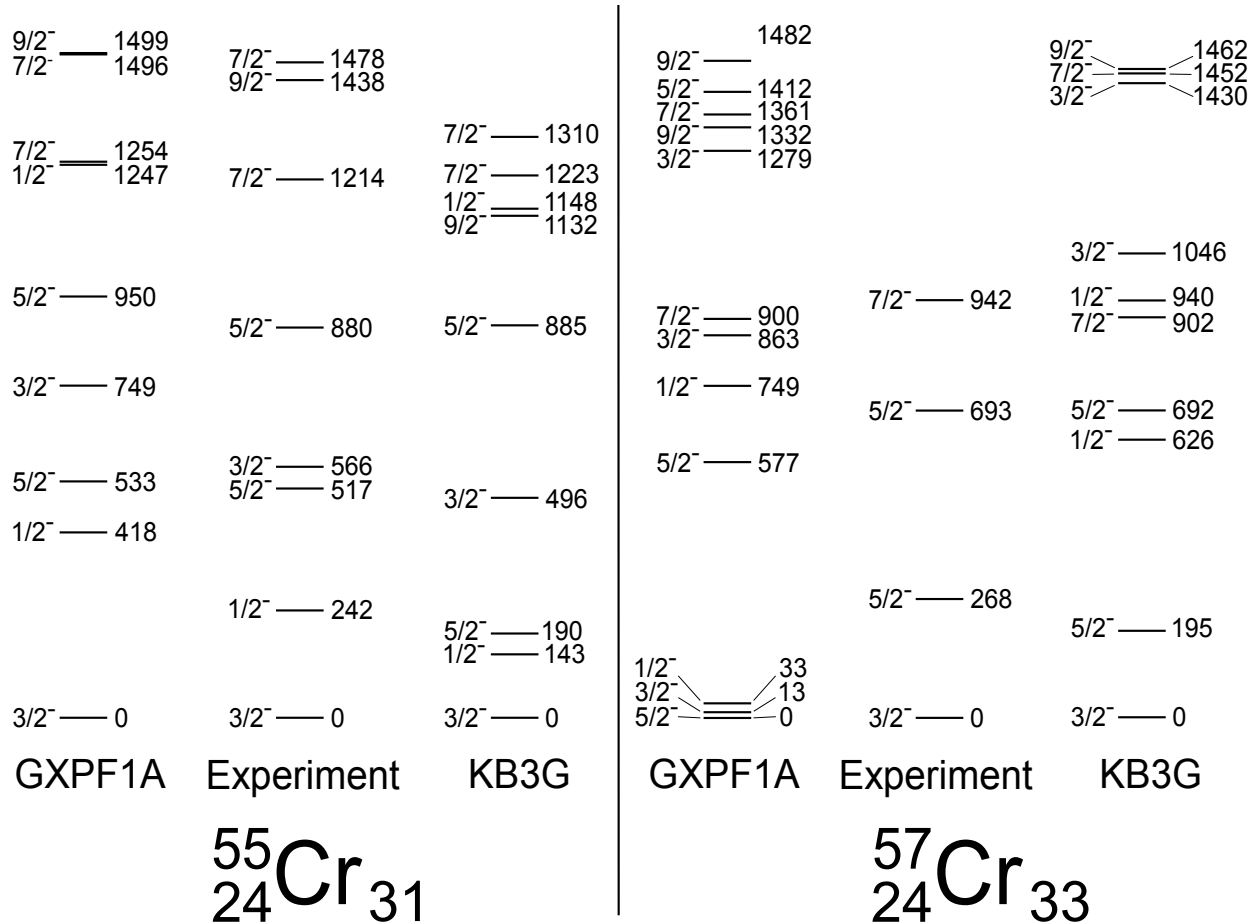


Figure 5.3: Comparison of known energy levels in $^{55,57}\text{Cr}$ with shell-model calculations. Experimental data were taken from Refs. [11, 12].

states in $^{55,57}\text{Cr}$ are dominated by three neutrons occupying the $p_{3/2}$ orbital, but by ^{59}Cr the $p_{3/2}$ orbital is nearly completely filled for the $3/2_1^-$ state, so the odd neutrons are primarily distributed between the $f_{5/2}$ and $p_{1/2}$ orbitals in the $^{59,61}\text{Cr}$ $3/2_1^-$ states. In all the isotopes, configurations with a single neutron in the $p_{1/2}$ orbital are calculated to contribute significantly to the $1/2_1^-$ state wave function. While other configurations may also be quite important in $^{55,57}\text{Cr}$, each interaction clearly predicts the configuration with one neutron in the $p_{1/2}$ orbital to be the dominant component in $^{59,61}\text{Cr}$.

The calculated level scheme of ^{55}Cr qualitatively matches the experimental level scheme quite well and there is a one-to-one correspondence between the measured and calculated

states. There is also a correspondence between each experimentally measured state in ^{57}Cr and the calculations, though the calculations predict the presence of more low-energy states than have actually been observed, perhaps suggesting some low-energy excited states in ^{57}Cr have not yet been discovered. For the three lowest-energy states in ^{59}Cr , there is still general agreement between the theoretical predictions and experiment. However, because the calculations are performed in the fp shell, which does not include the $\nu g_{9/2}$ orbital, the known $9/2^+$ state in ^{59}Cr cannot be reproduced. The calculations do a poor job of reproducing the experimental energy scheme of ^{61}Cr , even at low energies. Although the GXPF1A and KB3G calculations suggest the low-energy level scheme of ^{61}Cr should be similar to that of $^{55,57,59}\text{Cr}$, instead a much higher low-energy level density is observed in ^{61}Cr compared to the neighboring lighter odd- A Cr isotopes. Indeed, in the range of 0 - 800 keV, there are many more experimentally determined energy levels than the calculations predict. The distinct changes in the level scheme of ^{61}Cr are likely due to the onset of deformation that results from the occupation of the $\nu 0g_{9/2}$ and $\nu 1d_{5/2}$ orbitals. Based on the high low-energy level density ^{61}Cr and the inferred deformation, it is probable both negative- and positive-parity states have been observed in the low-energy level scheme of ^{61}Cr . Further, the high low-energy level density arising from deformation could be the reason why no low-energy isomeric states have been observed in $^{61,63}\text{Cr}$ but most other $N = 37$ and $N = 39$ nuclei with 28 or fewer protons are known to have isomers [13, 99, 101, 105, 120, 121, 56, 122, 123, 124].

5.3 Odd-odd Mn isotopes

The low-energy level schemes of the odd-odd $^{64,66}\text{Mn}$ isotopes provide further evidence for the coexistence of spherical and deformed configurations in the neutron-rich region near

$N = 40$. The neighboring odd- A Co and Fe isotopes can provide insight for determining the most important proton and neutron orbitals, respectively, in $^{64,66}\text{Mn}$. While the ground state of ^{67}Co has a spin and parity of $7/2^-$ and has been attributed to the $\pi f_{7/2}^{-1}$ configuration, the isomeric first excited state has tentatively been identified as a prolate-deformed $1/2^-$ state in which a single proton occupies the $1/2^-$ level originating from the spherical proton $p_{3/2}$ single-particle state [64]. The energy of the $1/2^-$ state consistently decreases along the odd- A Co isotopic chain beginning at $N = 36$, falling to just 492 keV in ^{67}Co . For nuclei with fewer protons such as Mn, in which the $1/2^-$ level may have a larger degree of deformation, the deformed $1/2^-$ level could drop even more in energy and become the ground-state proton configuration.

An extreme single-particle-model description would predict the ground states of ^{65}Fe and ^{67}Fe to be $1/2^-$ and $9/2^+$, respectively. Despite these simple expectations, the ground state has tentatively been assigned as $1/2^-$ in both nuclei. To explain the ground-state spin and parity, the low-energy level scheme of ^{67}Fe has been interpreted using a deformation parameter of approximately 0.2 [125]. Assuming a similar deformation in the neutron-rich odd-odd Mn isotopes, the $1/2^-$ level originating from the $\nu p_{1/2}$ state is predicted to be near the Fermi surface for both ^{64}Mn and ^{66}Mn [81]. The $1/2^-$ neutron configuration couples with the $1/2^-$ proton configuration described in the previous paragraph, resulting in a ground state spin and parity of 1^+ for $^{64,66}\text{Mn}$. The preservation of the $1/2^-$ and 1^+ ground states in the Fe and Mn isotopes, respectively, suggests small changes in the separation of the $\nu f_{5/2}$ and $\nu p_{1/2}$ single-particle states occur when transitioning from $N = 39$ to $N = 41$.

The tentatively identified spins and parities of the isomers in ^{64}Mn and ^{66}Mn cannot be explained by coupling a proton in the aforementioned deformed $1/2^-$ orbital with a neutron occupying one of the available lowest-energy deformed neutron orbitals. Furthermore, based

on the deformed coupling rules in Ref. [126] and the low-energy level scheme of ^{64}Mn , 4^+ would not be expected as the spin and parity of the isomer if it arose from the coupling of a proton in the $7/2^-$ level originating from the $f_{7/2}$ single-particle state with a neutron in the $3/2^+$ state originating from the $g_{9/2}$ orbital. However, the spins and parities of the isomeric states in both ^{64}Mn and ^{66}Mn can be explained if shape coexistence is considered. Namely, the 4^+ and 5^- states in ^{64}Mn and ^{66}Mn , respectively, can be attributed to the coupling of a proton in the $f_{7/2}$ spherical single-particle state and a neutron in either the $p_{1/2}$ or $g_{9/2}$ spherical single-particle state.

Chapter 6

Conclusions and Outlook

6.1 Conclusions

The neutron $0g_{9/2}$ orbital influences the low-energy level scheme of ^{68}Ni , leading to a 0^+ state at 1602 keV due to the excitation of a pair of neutrons across the $N = 40$ energy gap. The energy of the first excited 0^+ state in ^{68}Ni was measured precisely and found to be significantly lower than the previously reported value. The $\rho^2(E0)$ value for the decay from the first excited 0^+ state to the ground state was similarly determined. Using a simple mixing model to interpret the data, the experimental results are consistent with MCSM calculations that predict the coexistence of a spherical ground state and an oblate-deformed first excited 0^+ state.

The present study has contributed to the understanding of the nuclear structure of the neutron-rich nuclei near $N = 40$. New information was obtained about the low-energy level schemes of $^{61,63}\text{Cr}$, where data was previously scarce. The increased low-energy level density in ^{61}Cr compared to the neighboring lighter-mass odd- A Cr isotopes provides evidence for the importance of the $\nu g_{9/2}$ orbit at very low energies. The results suggest the onset of deformation in ^{61}Cr and complement previous studies in the even-even Cr isotopes.

Shape coexistence was also proposed in $^{64,66}\text{Mn}$. The low-energy level schemes of the nuclei can be understood if the isomeric states at 175 and 464 keV in ^{64}Mn and ^{66}Mn , respectively, are spherical but the ground states in both nuclei are deformed. Combined with

previous studies of nuclei in the region, the results point toward the common occurrence of low-energy shape coexistence in the neutron-rich nuclei with $N \approx 40$ and $Z \leq 28$.

6.2 Outlook

Further experimental tests of the interpretation of ^{68}Ni provided herein are possible with currently existing techniques. Shell-model calculations predict the $B(E2)$ values for the decay of the 2_1^+ state in ^{68}Ni to the 0_2^+ and 0_1^+ states. Calculations with different effective interactions, for instance the calculations in Refs. [17, 22], yield different relative $B(E2)$ values (different branching ratios) for the decays to the respective 0^+ states. The MCSM calculation in Ref. [22] predicts that the 2_1^+ state is a member of a rotational band built on the 0_2^+ state. Thus, the calculated $B(E2; 2_1^+ \rightarrow 0_2^+)$ value is large compared to what is calculated using the Lisetskiy interaction. A longer experiment with the same detector configuration as experiment e11503 could be capable of measuring the branching ratio for the decays of the 2_1^+ state to the 0_2^+ and 0_1^+ states, which could be compared to theoretical calculations to distinguish between different effective interactions. For the detection of the weak, previously unobserved, transition between 2_1^+ and 0_2^+ states, the detection of the $E0$ decay of the 0_2^+ state in the GeDSSD could be used as a gating condition. It may also be possible to study the decay of the 0_3^+ state in ^{68}Ni . As shown in Fig. 5.2 and further explained in Ref. [22], MCSM calculations suggest the 0_3^+ state has a large prolate deformation. Measuring the value of $\rho^2(E0)$ for the $0_3^+ \rightarrow 0_1^+$ transition could provide valuable insight into the nature of the 0_3^+ state. Determining $\rho^2(E0)$ would require measurements of both the half-life of the 0_3^+ state and the branching ratio for the decay of the 0_3^+ state by the $0_3^+ \rightarrow 0_1^+$ $E0$ transition. Given an upper limit of 15 ns has been established for the half-life [21], it is unlikely that

the pulse-shape-analysis methods presented in Section 3.3.8 would be useful for studying the $E0$ decay of the 0_3^+ state. However, fast-timing measurements, perhaps with scintillator detectors, could be used to determine the half-life of the 0_3^+ state. It may be possible to measure the branching ratio for the $E0$ decay of the 0_3^+ state with the GeDSSD following ^{68}Co β decay, though the summing of energies deposited in the detector from the β decay and the $E0$ decay presents an experimental challenge.

Another question that will be important to investigate is how nuclear structure continues to evolve at and around $N = 40$ in even more neutron-rich systems. The first spectroscopic information for $^{60}_{22}\text{Ti}_{38}$ was very recently reported and points toward decreased collectivity relative to isotonic ^{64}Fe or ^{62}Cr [127]. In the Ca isotopes, a subshell gap between the $\nu p_{1/2}$ and $\nu f_{5/2}$ orbits has been proposed at $N = 34$ [128]. However, studying nuclear structure at $N = 40$ in ^{62}Ti and ^{60}Ca will likely require next-generation rare-isotope facilities.

BIBLIOGRAPHY

BIBLIOGRAPHY

- [1] W. Loveland, D. J. Morrissey, and G. T. Seaborg. *Modern Nuclear Chemistry*. John Wiley & Sons, Inc., New Jersey, 2006.
- [2] T. Kibédi, T. W. Burrows, M. B. Trzhaskovskaya, P. M. Davidson, and C. W. Nestor Jr. *Nucl. Instrum. Methods Phys. Res. A*, 589:202, 2008.
- [3] Crc handbook of chemistry and physics, 94th ed. <http://www.hbcernetbase.com/>, 2013.
- [4] B. A. Brown. *Lecture Notes in Nuclear Structure Physics*. Michigan State University, 2010.
- [5] B. Singh. *Nucl. Data Sheets*, 114:1, 2013.
- [6] E. Browne. *Nucl. Data Sheets*, 82:379, 1997.
- [7] B. Pritychenko, J. Choquette, M. Horoi, B. Karamy, and B. Singh. *At. Data Nucl. Data Tables*, 98:798, 2012.
- [8] T. Baugher, A. Gade, R. V. F. Janssens, S. M. Lenzi, D. Bazin, B. A. Brown, M. P. Carpenter, A. N. Deacon, S. J. Freeman, T. Glasmacher, G. F. Grinyer, F. G. Kondev, S. McDaniel, A. Poves, A. Ratkiewicz, E. A. McCutchan, D. K. Sharp, I. Stefanescu, K. A. Walsh, D. Weisshaar, and S. Zhu. *Phys. Rev. C*, 86:011305, 2012.
- [9] H. L. Crawford, R. M. Clark, P. Fallon, A. O. Macchiavelli, T. Baugher, D. Bazin, C. W. Beausang, J. S. Berryman, D. L. Bleuel, C. M. Campbell, M. Cromaz, G. de Angelis, A. Gade, R. O. Hughes, I. Y. Lee, S. M. Lenzi, F. Nowacki, S. Paschalis, M. Petri, A. Poves, A. Ratkiewicz, T. J. Ross, E. Sahin, D. Weisshaar, K. Wimmer, and R. Winkler. *Phys. Rev. Lett.*, 110:242701, 2013.
- [10] H. Junde. *Nucl. Data Sheets*, 110:2689, 2009.
- [11] H. Junde. *Nucl. Data Sheets*, 109:787, 2008.
- [12] A. N. Deacon, S. J. Freeman, R. V. F. Janssens, F. R. Xu, M. P. Carpenter, I. R. Calderin, P. Chowdhury, N. J. Hammond, T. Lauritsen, C. J. Lister, D. Seweryniak, J. F. Smith, S. L. Tabor, B. J. Varley, and S. Zhu. *Phys. Lett. B*, 622:151, 2005.

- [13] R. Grzywacz, R. Béraud, C. Borcea, A. Emsallem, M. Glogowski, H. Grawe, D. Guillemaud-Mueller, M. Hjorth-Jensen, M. Houry, M. Lewitowicz, A. C. Mueller, A. Nowak, A. Płochocki, M. Pfützner, K. Rykaczewski, M. G. Saint-Laurent, J. E. Sauvestre, M. Schaefer, O. Sorlin, J. Szerypo, W. Trinder, S. Viteritti, and J. Winfield. *Phys. Rev. Lett.*, 81:766, 1998.
- [14] M. Wang, G. Audi, A. H. Wapstra, F. G. Kondev, M. MacCormick, X. Xu, and B. Pfeiffer. *Chin. Phys. C*, 36:1603, 2012.
- [15] N. Shimizu, T. Abe, Y. Tsunoda, Y. Utsuno, T. Yoshida, T. Mizusaki, M. Honma, and T. Otsuka. *Prog. Theor. Exp. Phys.*, 01A205:01A205, 2012.
- [16] S. M. Lenzi, F. Nowacki, A. Poves, and K. Sieja. *Phys. Rev. C*, 82:054301, 2010.
- [17] A. F. Lisetskiy, B. A. Brown, M. Horoi, and H. Grawe. *Phys. Rev. C*, 70:044314, 2004.
- [18] B. Cheal, E. Mané, J. Billowes, M. L. Bissell, K. Blaum, B. A. Brown, F. C. Charwood, K. T. Flanagan, D. H. Forest, C. Geppert, M. Honma, A. Jokinen, M. Kowalska, A. Krieger, J. Krämer, I. D. Moore, R. Neugart, G. Neyens, W. Nörtershäuser, M. Schug, H. H. Stroke, P. Vingerhoets, D. T. Yordanov, and M. Žáková. *Phys. Rev. Lett.*, 104:252502, 2010.
- [19] M. Honma, T. Otsuka, T. Mizusaki, and M. Hjorth-Jensen. *Phys. Rev. C*, 80:064323, 2009.
- [20] R. Broda, B. Fornal, W. Królas, T. Pawlat, D. Bazzacco, S. Lunardi, C. Rossi-Alvarez, R. Menegazzo, G. de Angelis, P. Bednarczyk, J. Rico, D. De Acuña, P. J. Daly, R. H. Mayer, M. Sferrazza, H. Grawe, K. H. Maier, and R. Schubart. *Phys. Rev. Lett.*, 74:868, 1995.
- [21] W. F. Mueller, B. Bruyneel, S. Franchoo, M. Huyse, J. Kurpeta, K. Kruglov, Y. Kudryavtsev, N. V. S. V. Prasad, R. Raabe, I. Reusen, P. Van Duppen, J. Van Roosbroeck, L. Vermeeren, L. Weissman, Z. Janas, M. Karny, T. Kszczot, A. Płochocki, K.-L. Kratz, B. Pfeiffer, H. Grawe, U. Köster, P. Thirolf, and W. B. Walters. *Phys. Rev. C*, 61:054308, 2000.
- [22] Y. Tsunoda, T. Otsuka, N. Shimizu, M. Honma, and Y. Utsuno. *Phys. Rev. C*, 89:031301, 2014.
- [23] S. N. Liddick, P. F. Mantica, R. Broda, B. A. Brown, M. P. Carpenter, A. D. Davies, B. Fornal, M. Horoi, R. V. F. Janssens, A. C. Morton, W. F. Mueller, J. Pavan,

- H. Schatz, A. Stolz, S. L. Tabor, B. E. Tomlin, and M. Wiedeking. *Phys. Rev. C*, 72:054321, 2005.
- [24] S. J. Freeman, R. V. F. Janssens, B. A. Brown, M. P. Carpenter, S. M. Fischer, N. J. Hammond, M. Honma, T. Lauritsen, C. J. Lister, T. L. Khoo, G. Mukherjee, D. Seweryniak, J. F. Smith, B. J. Varley, M. Whitehead, and S. Zhu. *Phys. Rev. C*, 69:064301, 2004.
- [25] J. Harker. private communication, 2013.
- [26] C. Thibault, R. Klapisch, C. Rigaud, A. M. Poskanzer, R. Prieels, L. Lessard, and W. Reisdorf. *Phys. Rev. C*, 12:644, 1975.
- [27] C. Détraz, M. Langevin, D. Guillemaud, M. Epherre, G. Audi, C. Thibault, and F. Touchard. *Nucl. Phys. A*, 394:378, 1983.
- [28] B. H. Wildenthal and W. Chung. *Phys. Rev. C*, 22:2260, 1980.
- [29] E. K. Warburton, J. A. Becker, and B. A. Brown. *Phys. Rev. C*, 41:1147, 1990.
- [30] M. H. Storm, A. Watt, and R. R. Whitehead. *J. Phys. G*, 9:L165, 1983.
- [31] I. J. Thompson and F. M. Nunes. *Nuclear Reactions for Astrophysics*. Cambridge University Press, Cambridge, 2009.
- [32] C. D. Kavaloski, J. S. Lilley, D. C. Shreve, and N. Stein. *Phys. Rev.*, 161:1107, 1967.
- [33] B. M. Preedom, E. Newman, and J. C. Hiebert. *Phys. Rev.*, 166:1156, 1968.
- [34] A. Stuirbrink, G.J. Wagner, K.T. Knöpfle, Liu Ken Pao, G. Mairle, H. Riedesel, K. Schindler, V. Bechtold, and L. Friedrich. *Z. Phys. A*, 297:307, 1980.
- [35] R. Wadsworth, M. D. Cohler, M. J. Smithson, D. L. Watson, F. Jundt, L. Kraus, I. Linck, and J. C. Sens. *J. Phys. G*, 9:1237, 1983.
- [36] K. Bharuth-Ram, A. C. Bawa, and W. R. McMurray. *Phys. Rev. C*, 36:1749, 1987.
- [37] V. Paar. *Nucl. Phys. A*, 331:16, 1979.

- [38] T. Otsuka, T. Suzuki, R. Fujimoto, H. Grawe, and Y. Akaishi. *Phys. Rev. Lett.*, 95:232502, 2005.
- [39] T. Otsuka, R. Fujimoto, Y. Utsuno, B. A. Brown, M. Honma, and T. Mizusaki. *Phys. Rev. Lett.*, 87:082502, 2001.
- [40] E. Caurier, F. Nowacki, A. Poves, and J. Retamosa. *Phys. Rev. C*, 58:2033, 1998.
- [41] B. A. Brown. *Prog. Part. Nucl. Phys.*, 47:517, 2001.
- [42] K. Heyde and J. L. Wood. *Rev. Mod. Phys.*, 83:1467, 2011.
- [43] A. N. Andreyev, M. Huyse, P. Van Duppen, L. Weissman, D. Ackermann, J. Gerl, F. P. Hessberger, S. Hofmann, A. Kleinböhl, G. Münzenberg, S. Reshitko, C. Schlegel, H. Schaffner, P. Cagarda, M. Matos, S. Saro, A. Keenan, C. Moore, C. D. O’Leary, R. D. Page, M. Taylor, H. Kettunen, M. Leino, A. Lavrentiev, R. Wyss, and K. Heyde. *Nature*, 405:430, 2000.
- [44] J. L. Wood, E. F. Zganjar, C. De Coster, and K. Heyde. *Nucl. Phys. A*, 651:323, 1999.
- [45] A. Warwick, R. Chapman, J. L. Durell, J. N. Mo, and S. Sen. *Phys. Lett. B*, 88:55, 1979.
- [46] M. R. Cates, J. B. Ball, and E. Newman. *Phys. Rev.*, 187:1682, 1969.
- [47] A. M. Van Den Berg, A. Saha, G. D. Jones, L. W. Put, and R. H. Siemssen. *Nucl. Phys. A*, 429:1, 1984.
- [48] F. S. Stephens, Diamond R. M., J. R. Leight, T. Kammuri, and K Nakai. *Phys. Rev. Lett.*, 29:438, 1972.
- [49] M. Bernas, Ph. Dessagne, M. Langevin, J. Payet, F. Pougheon, and P. Roussel. *Phys. Lett. B*, 113:279, 1982.
- [50] O. Sorlin, S. Leenhardt, C. Donzaud, J. Duprat, F. Azaiez, F. Nowacki, H. Grawe, Zs. Dombrádi, F. Amorini, A. Astier, D. Baiborodin, M. Belleguic, C. Borcea, C. Bourgeois, D. M. Cullen, Z. Dlouhy, E. Dragulescu, M. Górska, S. Grévy, D. Guillemaud-Mueller, G. Hagemann, B. Herskind, J. Kiener, R. Lemmon, M. Lewitowicz, S. M. Lukyanov, P. Mayet, F. de Oliveira Santos, D. Pantalica, Yu.-E. Penionzhkevich, F. Pougheon, A. Poves, N. Redon, M. G. Saint-Laurent, J. A. Scarpaci, G. Sletten, M. Stanoiu, O. Tarasov, and Ch. Theisen. *Phys. Rev. Lett.*, 88:092501, 2002.

- [51] M. Hannawald, T. Kautzsch, A. Wöhr, W. B. Walters, K.-L. Kratz, V. N. Fedoseyev, V. I. Mishin, W. Böhmer, B. Pfeiffer, V. Sebastian, Y. Jading, U. Köster, J. Lettry, H. L. Ravn, and the ISOLDE Collaboration. *Phys. Rev. Lett.*, 82:1391, 1999.
- [52] A. Gade, R. V. F. Janssens, T. Baugher, D. Bazin, B. A. Brown, M. P. Carpenter, C. J. Chiara, A. N. Deacon, S. J. Freeman, G. F. Grinyer, C. R. Hoffman, B. P. Kay, F. G. Kondev, T. Lauritsen, S. McDaniel, K. Meierbachtol, A. Ratkiewicz, S. R. Stroberg, K. A. Walsh, D. Weisshaar, R. Winkler, and S. Zhu. *Phys. Rev. C*, 81:051304, 2010.
- [53] W. Rother, A. Dewald, H. Iwasaki, S. M. Lenzi, K. Starosta, D. Bazin, T. Baugher, B. A. Brown, H. L. Crawford, C. Fransen, A. Gade, T. N. Ginter, T. Glasmacher, G. F. Grinyer, M. Hackstein, G. Ilie, J. Jolie, S. McDaniel, D. Miller, P. Petkov, Th. Pissulla, A. Ratkiewicz, C. A. Ur, P. Voss, K. A. Walsh, D. Weisshaar, and K.-O. Zell. *Phys. Rev. Lett.*, 106:022502, 2011.
- [54] C. Guénaut, G. Audi, D. Beck, K. Blaum, G. Bollen, P. Delahaye, F. Herfurth, A. Kellerbauer, H.-J. Kluge, J. Libert, D. Lunney, S. Schwarz, L. Schweikhard, and C. Yazidjian. *Phys. Rev. C*, 75:044303, 2007.
- [55] L. Gaudefroy, A. Obertelli, S. Péru, N. Pillet, S. Hilaire, J. P. Delaroche, M. Girod, and J. Libert. *Phys. Rev. C*, 80:064313, 2009.
- [56] S. Lunardi, S. M. Lenzi, F. Della Vedova, E. Farnea, A. Gadea, N. Mărginean, D. Bazzacco, S. Beghini, P. G. Bizzeti, A. M. Bizzeti-Sona, D. Bucurescu, L. Corradi, A. N. Deacon, G. de Angelis, E. Fioretto, S. J. Freeman, M. Ionescu-Bujor, A. Iordachescu, P. Mason, D. Mengoni, G. Montagnoli, D. R. Napoli, F. Nowacki, R. Orlandi, G. Pollarolo, F. Recchia, F. Scarlassara, J. F. Smith, A. M. Stefanini, S. Szilner, C. A. Ur, J. J. Valiente-Dobón, and B. J. Varley. *Phys. Rev. C*, 76:034303, 2007.
- [57] M. R. Bhat. *Nucl. Data Sheets*, 85:415, 1998.
- [58] B. Olaizola, L. M. Fraile, H. Mach, A. Aprahamian, J. A. Briz, J. Cal-González, D. Ghița, U. Köster, W. Kurcewicz, S. R. Leshner, D. Pauwels, E. Picado, A. Poves, D. Radulov, G. S. Simpson, and J. M. Udías. *Phys. Rev. C*, 88:044306, 2013.
- [59] S. Zhu, A. N. Deacon, S. J. Freeman, R. V. F. Janssens, B. Fornal, M. Honma, F. R. Xu, R. Broda, I. R. Calderin, M. P. Carpenter, P. Chowdhury, F. G. Kondev, W. Królas, T. Lauritsen, S. N. Liddick, C. J. Lister, P. F. Mantica, T. Pawlat, D. Seweryniak, J. F. Smith, S. L. Tabor, B. E. Tomlin, B. J. Varley, and J. Wrzesiński. *Phys. Rev. C*, 74:064315, 2006.
- [60] K. Kaneko, Y. Sun, M. Hasegawa, and T. Mizusaki. *Phys. Rev. C*, 78:064312, 2008.

- [61] N. Hoteling, C. J. Chiara, R. Broda, W. B. Walters, R. V. F. Janssens, M. Hjorth-Jensen, M. P. Carpenter, B. Fornal, A. A. Hecht, W. Królas, T. Lauritsen, T. Pawłat, D. Seweryniak, X. Wang, A. Wöhr, J. Wrzesiński, and S. Zhu. *Phys. Rev. C*, 82:044305, 2010.
- [62] N. Hoteling, W. B. Walters, R. V. F. Janssens, R. Broda, M. P. Carpenter, B. Fornal, A. A. Hecht, M. Hjorth-Jensen, W. Królas, T. Lauritsen, T. Pawłat, D. Seweryniak, X. Wang, A. Wöhr, J. Wrzesiński, and S. Zhu. *Phys. Rev. C*, 74:064313, 2006.
- [63] L. Coraggio, A. Covello, A. Gargano, and N. Itaco. *Phys. Rev. C*, 89:024319, 2014.
- [64] D. Pauwels, O. Ivanov, N. Bree, J. Büscher, T. E. Cocolios, J. Gentens, M. Huyse, A. Korgul, Yu. Kudryavtsev, R. Raabe, M. Sawicka, I. Stefanescu, J. Van de Walle, P. Van den Bergh, P. Van Duppen, and W. B. Walters. *Phys. Rev. C*, 78:041307, 2008.
- [65] D. Pauwels, O. Ivanov, N. Bree, J. Büscher, T. E. Cocolios, M. Huyse, Yu. Kudryavtsev, R. Raabe, M. Sawicka, J. Van de Walle, P. Van Duppen, A. Korgul, I. Stefanescu, A. A. Hecht, N. Hoteling, A. Wöhr, W. B. Walters, R. Broda, B. Fornal, W. Krolas, T. Pawlat, J. Wrzesinski, M. P. Carpenter, R. V. F. Janssens, T. Lauritsen, D. Seweryniak, S. Zhu, J. R. Stone, and X. Wang. *Phys. Rev. C*, 79:044309, 2009.
- [66] S. N. Liddick, B. Abromeit, A. Ayres, A. Bey, C. R. Bingham, M. Bolla, L. Cartegni, H. L. Crawford, I. G. Darby, R. Grzywacz, S. Ilyushkin, N. Larson, M. Madurga, D. Miller, S. Padgett, S. Paulauskas, M. M. Rajabali, K. Rykaczewski, and S. Suchyta. *Phys. Rev. C*, 85:014328, 2012.
- [67] R. Broda, T. Pawłat, W. Królas, R. V. F. Janssens, S. Zhu, W. B. Walters, B. Fornal, C. J. Chiara, M. P. Carpenter, N. Hoteling, L. W. Iskra, F. G. Kondev, T. Lauritsen, D. Seweryniak, I. Stefanescu, X. Wang, and J. Wrzesiński. *Phys. Rev. C*, 86:064312, 2012.
- [68] D. Pauwels, J. L. Wood, K. Heyde, M. Huyse, R. Julin, and P. Van Duppen. *Phys. Rev. C*, 82:027304, 2010.
- [69] C. J. Chiara, R. Broda, W. B. Walters, R. V. F. Janssens, M. Albers, M. Alcorta, P. F. Bertone, M. P. Carpenter, C. R. Hoffman, T. Lauritsen, A. M. Rogers, D. Seweryniak, S. Zhu, F. G. Kondev, B. Fornal, W. Królas, J. Wrzesiński, N. Larson, S. N. Liddick, C. Prokop, S. Suchyta, H. M. David, and D. T. Doherty. *Phys. Rev. C*, 86:041304, 2012.
- [70] A. Dijon, E. Clément, G. de France, G. de Angelis, G. Duchêne, J. Dudouet, S. Francoo, A. Gadea, A. Gottardo, T. Hüyük, B. Jacquot, A. Kusoglu, D. Lebhertz,

- G. Lehaut, M. Martini, D. R. Napoli, F. Nowacki, S. Péru, A. Poves, F. Recchia, N. Redon, E. Sahin, C. Schmitt, M. Sferrazza, K. Sieja, O. Stezowski, J. J. Valiente-Dobón, A. Vancraeynest, and Y. Zheng. *Phys. Rev. C*, 85:031301, 2012.
- [71] F. Recchia, C. J. Chiara, R. V. F. Janssens, D. Weisshaar, A. Gade, W. B. Walters, M. Albers, M. Alcorta, V. M. Bader, T. Baugher, D. Bazin, J. S. Berryman, P. F. Bertone, B. A. Brown, C. M. Campbell, M. P. Carpenter, J. Chen, H. L. Crawford, H. M. David, D. T. Doherty, C. R. Hoffman, F. G. Kondev, A. Korichi, C. Langer, N. Larson, T. Lauritsen, S. N. Liddick, E. Lunderberg, A. O. Macchiavelli, S. Noji, C. Prokop, A. M. Rogers, D. Seweryniak, S. R. Stroberg, S. Suchyta, S. Williams, K. Wimmer, and S. Zhu. *Phys. Rev. C*, 88:041302, 2013.
- [72] J. A. Behr and G. Gwinner. *J. Phys. G*, 36:033101, 2009.
- [73] N.B. Gove and M.J. Martin. *At. Data and Nucl. Data Tables*, 10:205, 1971.
- [74] G. Friedlander, J. W. Kennedy, E. S. Macias, and J. M. Miller. *Nuclear and Radiochemistry, 3rd Edition*. John Wiley & Sons, Inc., New York, 1981.
- [75] S. S. M. Wong. *Introductory Nuclear Physics*. WILEY-VCH Verlag GmbH & Co. KGaA, Weinheim, Germany, 2004.
- [76] E. L. Church and J. Weneser. *Phys. Rev.*, 103:1035, 1956.
- [77] T. Kibédi and R. H. Spear. *At. Data and Nucl. Data Tables*, 89:77, 2005.
- [78] S. Suchyta, S. N. Liddick, Y. Tsunoda, T. Otsuka, M. B. Bennett, A. Chemey, M. Honma, N. Larson, C. J. Prokop, S. J. Quinn, N. Shimizu, A. Simon, A. Spyrou, V. Tripathi, Y. Utsuno, and J. M. VonMoss. *Phys. Rev. C*, 89:021301, 2014.
- [79] S. Suchyta, S. N. Liddick, C. J. Chiara, W. B. Walters, M. P. Carpenter, H. L. Crawford, G. F. Grinyer, G. Gürdal, A. Klose, E. A. McCutchan, J. Pereira, and S. Zhu. *Phys. Rev. C*, 89:034317, 2014.
- [80] S. Suchyta, S. N. Liddick, C. J. Chiara, W. B. Walters, M. P. Carpenter, H. L. Crawford, G. F. Grinyer, G. Gürdal, A. Klose, E. A. McCutchan, J. Pereira, and S. Zhu. *Phys. Rev. C*, 89:067303, 2014.
- [81] S. N. Liddick, S. Suchyta, B. Abromeit, A. Ayres, A. Bey, C. R. Bingham, M. Bolla, M. P. Carpenter, L. Cartegni, C. J. Chiara, H. L. Crawford, I. G. Darby, R. Grzywacz,

- G. Gürdal, S. Ilyushkin, N. Larson, M. Madurga, E. A. McCutchan, D. Miller, S. Padgett, S. V. Paulauskas, J. Pereira, M. M. Rajabali, K. Rykaczewski, S. Vinnikova, W. B. Walters, and S. Zhu. *Phys. Rev. C*, 84:061305, 2011.
- [82] D. J. Morrissey, B. M. Sherrill, M. Steiner, A. Stolz, and I. Wiedenhoever. *Nucl. Instrum. Methods Phys. Res. B*, 204:90, 2003.
- [83] K. Starosta, C. Vaman, D. Miller, P. Voss, D. Bazin, T. Glasmacher, H. Crawford, P. Mantica, H. Tan, W. Hennig, M. Walby, A. Fallu-Labruyere, J. Harris, D. Breus, P. Grudberg, and W. K. Warburton. *Nucl. Instrum. Methods Phys. Res. A*, 610:700, 2009.
- [84] C. J. Prokop, S. N. Liddick, B. L. Abromeit, A. T. Chemey, N. R. Larson, S. Suchyta, and J. R. Tompkins. *Nucl. Instrum. Methods Phys. Res., Sect. A*, 741:163, 2014.
- [85] H. Tan, M. Momayezi, A. Fallu-Labruyere, Y. X. Chu, and W.K. Warburton. *IEEE Trans. Nucl. Sci.*, 51:1541, 2004.
- [86] N. Larson, S. N. Liddick, M. Bennett, A. Bowe, A. Chemey, C. Prokop, A. Simon, A. Spyrou, S. Suchyta, S. J. Quinn, S. L. Tabor, P. L. Tai, V. Tripathi, and J. M. VonMoss. *Nucl. Instrum. Methods Phys. Res., Sect. A*, 727:59, 2013.
- [87] J. M. Daugas, M. Sawicka, M. Pfützner, I. Matea, H. Grawe, R. Grzywacz, N. L. Achouri, J. C. Angélique, D. Baiborodin, F. Becker, G. Bélier, R. Bentida, R. Béraud, C. Bingham, C. Borcea, R. Borcea, E. Bouchez, A. Buta, W. N. Catford, E. Dragulescu, A. Emsallem, G. de France, J. Giovinazzo, M. Girod, H. Goutte, G. Gorgiev, K. L. Grzywacz-Jones, F. Hammache, F. Ibrahim, R. C. Lemmon, M. Lewitowicz, M. J. Lopez-Jimenez, P. Mayet, V. Méot, F. Negoita, F. de Oliveira-Santos, O. Perru, P. H. Regan, O. Roig, K. Rykaczewski, M. G. Saint-Laurent, J. E. Sauvestre, G. Sletten, O. Sorlin, M. Stanoiu, I. Stefan, C. Stodel, C. Theisen, D. Verney, and J. Zylicz. *AIP Conf. Proc.*, 831:427, 2006.
- [88] O. B. Tarasov and D. Bazin. *Nucl. Phys. A*, 746:411, 2004.
- [89] W. F. Mueller, J. A. Church, T. Glasmacher, D. Gutknecht, G. Hackman, P. G. Hansen, Z. Hu, K. L. Miller, and P. Quirin. *Nucl. Instrum. Methods Phys. Res. A*, 466:492, 2001.
- [90] E. L. Hull, E. G. Jackson, C. J. Lister, and R. H. Pehl. *Nucl. Instrum. Methods Phys. Res. A*, 762:125, 2014.

- [91] S. N. Liddick, I. G. Darby, and R. K. Grzywacz. *Nucl. Instrum. Methods Phys. Res., Sect. A*, 669:70, 2012.
- [92] J. I. Prisciandaro, A. C. Morton, and P. F. Mantica. *Nucl. Instrum. Methods Phys. Res., Sect. A*, 505:140, 2003.
- [93] C. W. Reich. *Nucl. Data Sheets*, 110:2257, 2009.
- [94] J. K. Tuli. *Nucl. Data Sheets*, 103:389, 2004.
- [95] B. Singh. *Nucl. Data Sheets*, 101:193, 2004.
- [96] H. Junde, H. Xiaolong, and J. K. Tuli. *Nucl. Data Sheets*, 106:159, 2005.
- [97] C. D. Nesaraja. *Nucl. Data Sheets*, 115:1, 2014.
- [98] K. Abusaleem and B. Singh. *Nucl. Data Sheets*, 112:133, 2011.
- [99] J. M. Daugas. PhD thesis, Universite de Caen/Basse-Normandie, 1999.
- [100] H. Mach, R. L. Gill, and M. Moszyński. *Nucl. Instrum. Methods Phys. Res. A*, 280:49, 1989.
- [101] O. Sorlin, C. Donzaud, L. Axelsson, M. Belleguic, R. Béraud, C. Borcea, G. Canchel, E. Chabanat, J. M. Daugas, A. Emsallem, M. Girod, D. Guillemaud-Mueller, K.-L. Kratz, S. Leenhardt, M. Lewitowicz, C. Longour, M. J. Lopez, F. de Oliveira Santos, L. Petizon, B. Pfeiffer, F. Pougheon, M. G. Saint-Laurent, and J. E. Sauvestre. *Nucl. Phys. A*, 669:351, 2000.
- [102] S. N. Liddick, P. F. Mantica, B. A. Brown, M. P. Carpenter, A. D. Davies, M. Horoi, R. V. F. Janssens, A. C. Morton, W. F. Mueller, J. Pavan, H. Schatz, A. Stolz, S. L. Tabor, B. E. Tomlin, and M. Wiedeking. *Phys. Rev. C*, 73:044322, 2006.
- [103] O. Sorlin, C. Donzaud, F. Nowacki, J. C. Angélique, F. Azaiez, C. Bourgeois, V. Chiste, Z. Dlouhy, S. Grévy, D. Guillemaud-Mueller, F. Ibrahim, K.-L. Kratz, M. Lewitowicz, S. M. Lukyanov, J. Mrasek, Yu.-E. Penionzhkevich, F. de Oliveira Santos, B. Pfeiffer, F. Pougheon, A. Poves, M. G. Saint-Laurent, and M. Stanoiu. *Eur. Phys. J. A*, 16:55, 2003.
- [104] J. C. Hardy, L. C. Carraz, B. Jonson, and P. G. Hansen. *Phys. Lett. B*, 71:307, 1977.

- [105] I. Matea. PhD thesis, Universite de Caen/Basse-Normandie, 2002.
- [106] L. Gaudefroy, O. Sorlin, C. Donzaud, J. C. Angélique, F. Azaiez, C. Bourgeois, V. Chiste, Z. Dlouhy, S. Grévy, D. Guillemaud-Mueller, F. Ibrahim, K.-L. Kratz, M. Lewitowicz, S. M. Lukyanov, I. Matea, J. Mrasek, F. Nowacki, F. de Oliveira Santos, Yu.-E. Penionzhkevich, B. Pfeiffer, F. Pougheon, M. G. Saint-Laurent, and M. Stanoiu. *Eur. Phys. J. A*, 23:41, 2005.
- [107] H. L. Crawford, P. F. Mantica, J. S. Berryman, R. Broda, B. Fornal, C. R. Hoffman, N. Hoteling, R. V. F. Janssens, S. M. Lenzi, J. Pereira, J. B. Stoker, S. L. Tabor, W. B. Walters, X. Wang, and S. Zhu. *Phys. Rev. C*, 79:054320, 2009.
- [108] M. R. Bhat. *Nucl. Data Sheets*, 88:417, 1999.
- [109] O. Sorlin, V. Borrel, S. Grévy, D. Guillemaud-Mueller, A. C. Mueller, F. Pougheon, W. Böhmer, K.-L. Kratz, T. Mehren, P. Möller, B. Pfeiffer, T. Rauscher, M. G. Saint-Laurent, R. Anne, M. Lewitowicz, A. Ostrowski, T. Dörfler, and W.-D. Schmidt-Ott. *Nucl. Phys. A*, 632:205, 1998.
- [110] N. Aoi, E. Takeshita, H. Suzuki, S. Takeuchi, S. Ota, H. Baba, S. Bishop, T. Fukui, Y. Hashimoto, H. J. Ong, E. Ideguchi, K. Ieki, N. Imai, M. Ishihara, H. Iwasaki, S. Kanno, Y. Kondo, T. Kubo, K. Kurita, K. Kusaka, T. Minemura, T. Motobayashi, T. Nakabayashi, T. Nakamura, T. Nakao, M. Niikura, T. Okumura, T. K. Ohnishi, H. Sakurai, S. Shimoura, R. Sugo, D. Suzuki, M. K. Suzuki, M. Tamaki, K. Tanaka, Y. Togano, and K. Yamada. *Phys. Rev. Lett.*, 102:012502, 2009.
- [111] K.-H. Schmidt, C.-C. Sahm, K. Pielenz, and H.-G. Clerc. *Z. Phys. A*, 316:19, 1984.
- [112] H. L. Crawford. private communication, 2014.
- [113] L. Gaudefroy. PhD thesis, Universite Paris XI Orsay, 2005.
- [114] A. Bohr and B. R. Mottelson. *Nuclear structure, Vol. 2*. W. A. Benjamin, Inc., New York, 1975.
- [115] I. Hamamoto, J. Höller, and X. Z. Zhang. *Phys. Lett. B*, 226:17, 1989.
- [116] T. Otsuka, M. Honma, T. Mizusaki, N. Shimizu, and Y. Utsuno. *Prog. Part. Nucl. Phys.*, 47:319, 2001.

- [117] B. A. Brown and W. D. M. Rae. <http://www.nscl.msu.edu/~brown/resources/resources.html>.
- [118] M. Honma, T. Otsuka, B. A. Brown, and T. Mizusaki. *Eur. Phys. J. A*, 25:499, 2005.
- [119] A. Poves, J. Sánchez-Solano, E. Caurier, and F. Nowacki. *Nucl. Phys. A*, 694:157, 2001.
- [120] M. Block, C. Bachelet, G. Bollen, M. Facina, C. M. Folden III, C. Guénaut, A. A. Kwiatkowski, D. J. Morrissey, G. K. Pang, A. Prinke, R. Ringle, J. Savory, P. Schury, and S. Schwarz. *Phys. Rev. Lett.*, 100:132501, 2008.
- [121] O. Sorlin, C. Donzau, F. Azaiez, C. Bourgeois, L. Gaudefroy, F. Ibrahim, D. Guillemaud-Mueller, F. Pougheon, M. Lewitowicz, F. de Oliveira Santos, M. G. Saint-Laurent, M. Stanoiu, S. M. Lukyanov, Yu.-E. Penionzhkevich, J. C. Angélique, S. Grévy, K.-L. Kratz, B. Pfeiffer, F. Nowacki, Z. Dlouhy, and J. Mrasek. *Nucl. Phys. A*, 719:193C, 2003.
- [122] J. M. Daugas, T. Faul, H. Grawe, M. Pfützner, R. Grzywacz, M. Lewitowicz, N. L. Achouri, J. C. Angélique, D. Baiborodin, R. Bentida, R. Béraud, C. Borcea, C. R. Bingham, W. N. Catford, A. Emsallem, G. de France, K. L. Grzywacz, R. C. Lemmon, M. J. Lopez Jimenez, F. de Oliveira Santos, P. H. Regan, K. Rykaczewski, J. E. Sauvestre, M. Sawicka, M. Stanoiu, K. Sieja, and F. Nowacki. *Phys. Rev. C*, 81:034304, 2010.
- [123] M. J. Murphy, C. N. Davids, E. B. Norman, and R. C. Pardo. *Phys. Rev. C*, 17:1574, 1978.
- [124] T. Pawlat, R. Broda, W. Królas, A. Maj, M. Ziębliński, H. Grawe, R. Schubart, K. H. Maier, J. Heese, H. Kluge, and M. Schramm. *Nucl. Phys. A*, 574:623, 1994.
- [125] J. M. Daugas, I. Matea, J.-P. Delaroche, M. Pfützner, M. Sawicka, F. Becker, G. Bélier, C. R. Bingham, R. Borcea, E. Bouchez, A. Buta, E. Dragulescu, G. Georgiev, J. Giov-inazzo, M. Girod, H. Grawe, R. Grzywacz, F. Hammache, F. Ibrahim, M. Lewitowicz, J. Libert, P. Mayet, V. Méot, F. Negoita, F. de Oliveira Santos, O. Perru, O. Roig, K. Rykaczewski, M. G. Saint-Laurent, J. E. Sauvestre, O. Sorlin, M. Stanoiu, I. Stefan, Ch. Stodel, Ch. Theisen, D. Verney, and J. Żylicz. *Phys. Rev. C*, 83:054312, 2011.
- [126] C. J. Gallagher and S. A. Moszkowski. *Phys. Rev.*, 111:1282, 1958.
- [127] A. Gade, R. V. F. Janssens, D. Weisshaar, B. A. Brown, E. Lunderberg, M. Albers, V. M. Bader, T. Baugher, D. Bazin, J. S. Berryman, C. M. Campbell, M. P. Carpenter,

C. J. Chiara, H. L. Crawford, M. Cromaz, U. Garg, C. R. Hoffman, F. G. Kondev, C. Langer, T. Lauritsen, I. Y. Lee, S. M. Lenzi, J. T. Matta, F. Nowacki, F. Recchia, K. Sieja, S. R. Stroberg, J. A. Tostevin, S. J. Williams, K. Wimmer, and S. Zhu. *Phys. Rev. Lett.*, 112:112503, 2014.

- [128] D. Steppenbeck, S. Takeuchi, N. Aoi, P. Doornenbal, M. Matsushita, H. Wang, H. Baba, N. Fukuda, S. Go, M. Honma, J. Lee, K. Matsui, S. Michimasa, T. Motobayashi, D. Nishimura, T. Otsuka, H. Sakurai, Y. Shiga, P.-A. Soderstrom, T. Sumikama, H. Suzuki, R. Taniuchi, Y. Utsuno, J. J. Valiente-Dobon, and K. Yoneda. *Nature*, 502:207, 2013.